

TESIS DOCTORAL

AÑO 2021

**E-LITE 360° NEUTRONICS MODEL OF THE
ITER TOKAMAK**

GABRIEL PEDROCHE SÁNCHEZ

**PROGRAMA DE DOCTORADO EN TECNOLOGÍAS
INDUSTRIALES**

DIRECTOR: JAVIER SANZ GOZALO

CODIRECTOR: RAFAEL JUÁREZ MAÑAS

TESIS DOCTORAL

2021

**E-lite 360° neutronics model of the ITER
tokamak**

Gabriel Pedroche Sánchez

Ingeniería Energética

***PROGRAMA DE DOCTORADO EN
TECNOLOGÍAS INDUSTRIALES***

DIRECTOR Javier Sanz Gozalo

CODIRECTOR Rafael Juárez Mañas

ACKNOWLEDGEMENTS

Tras cerrar la redacción de la tesis al completo, quiero por fin dedicar unas líneas a mostrar mi agradecimiento a muchas personas que me han acompañado a lo largo de estos años. Podría escribir otra tesis doctoral entera agradeciendo cosas, pero no lo voy a hacer porque más de un@ me pegaría un tiro. Aún así, aviso de que quiero quedarme lo más a gusto posible escribiendo estas líneas. No obstante, es probable que me olvide de dar las gracias a alguien y/o a algo y pido disculpas de antemano por ello.

Thank you very much to Mike, Eduard, Andrei, Josh, Srini, Shrichand and Yannick for all these years in which I have worked with you for ITER projects. You made my two stays and several visits to IO really enjoyable. Thank you very much Mike for all the laughs and for the support with E-lite. Eduard, thank you for all the references about the tokamak models, which were really useful and interesting, and for all your help and expertise in building the 360° model.

Raúl y Marco, mil gracias también a vosotros por estos años de trabajo en ITER. Es un placer trabajar con gente tan competente y de la que se puede aprender tanto. Gracias por toda vuestra ayuda y recomendaciones a la hora de hacer E-lite, y por compartir vuestras inquietudes en relación a la falta de simetría del B1. Gracias también por los informes para la mención internacional y vuestra buena disposición a la hora de hacerlos. Y Marco, gracias especialmente por todo el apoyo, la comprensión y tu gran paciencia con los Standard Tallies.

Gracias a mis compañeros de TECF3IR. He pasado unos años geniales con vosotros. Duros también, no voy a negarlo, pero muy buenos.

Gracias, Juan, por apiadarte de mí cuando llegué al grupo en aquel verano de 2016, por enseñarme lo que era un cable “ethernet” y por las muchas conversaciones y risas que nos echamos en el día a día. Gracias, Paco, por ser tan genio y por poner a nuestra disposición un cluster tan molón. Tu humor sin filtros y las cenas en tu casa sabes que también me encantan. Pat! Gracias por resolverme tantas y tantas dudas y por ser como eres. De mayor quiero saber tanto como tú. Gracias también por ese pedazo de D1SUNED, sin el cual esta tesis no habría tenido sentido. Mauri, tú también eres grande. Te agradezco tu compañía y las conversaciones durante estos años. Especialmente agradezco tus mensajes de apoyo durante este último, los he valorado muchísimo. Gracias, Javi, por tu infinita ayuda y tus scripts. Me has ayudado siempre que te lo he

pedido, y eso han sido muchas muchas veces. Siempre lo has hecho con muy buena voluntad y te lo agradezco infinito. Gracias también, junto con Pat, por las modificaciones de MCNP, sin las cuales, ya digo, esta tesis no habría sido posible. Toño y Aljaž, mil gracias por todos los ratos y risas que hemos compartido juntos. Me han dado la vida en esas rachas de trabajo sin parar, es decir, me han dado la vida durante todos estos años de tesis. Gracias, Toño, por ser un personajazo con el que no paro de reírme. Aljaž, gracias por tus cositas, sabes que me encantan también. Marco y Pablo, gracias por todo el trabajo juntos en los Mapas y por los ratos compartidos en el nuevo despacho y fuera de él. Juan pequeño y Víctor, también, gracias por las comidas y ratos juntos.

Gracias a todos. He aprendido mucho de cada uno de vosotros y todos me habéis ayudado de muchas maneras. ¡Espero que podamos compartir muchos más años juntos!

Gracias a Marta, a Belén, a Mariví y a Trini por todas las comisiones de servicio.

Gracias a mis tíos y prim@s y a la familia ukraniana.

Gracias a mi hermano, Ale, que te has tragado mucha de la parte dura de mi tesis. Gracias por acompañarme en esta etapa y por ayudarme a llevarla a cabo.

Gracias a mis amigos del Wonkas, de la uni y de teatro. Gracias por toda vuestra paciencia conmigo y por haberme aguantado durante todos estos años. He perdido la cuenta del número de planes en los que me he rajado en el último momento. Y aún así, siempre habéis estado ahí. Me habéis dado la vida también en estos años. Dan, Mario, Guille y Reija, aunque nos vemos cada mil, gracias también. Gracias a Susi y Costa. Gracias a Pablito desde la distancia. Gracias a Andrew. Gracias a Sofitz. Gracias a mis vecinos de Luchana 27. Gracias a Pedro y a Nana. Gracias a mi papi2.

Dentro de este grupo de personas, quiero dar las gracias en especial a Tomy y a Marina, por haber estado siempre al tanto de mis andanzas en la UNED y haber seguido muy de cerca toda mi experiencia. Y gracias en especial también a Elena. Eres la razón por la que conocí a Javier y a TECF3IR, y eso me cambió la vida. También gracias por abrirme las puertas de tu casa cada vez que he ido a Aix y por haberme admitido en tu vida francesa siempre. Guardo muy buenos recuerdos de esa ciudad gracias a ti.

Gracias a Javier. Gracias por haber confiado y creído en mí desde el primer correo que te mandé allá por agosto de 2015. Gracias por todo el apoyo que me

has dado en estos años y todo el seguimiento. Por todas las conversaciones en las que me has mostrado tu visión de las cosas y por todo lo que me has enseñado. Gracias por valorarme siempre, por poner mis intereses por delante y por tenerme siempre en un pedestal. Gracias por toda la paciencia que has tenido conmigo, sobre todo en este último año. No he cumplido ninguno de los deadlines que me has puesto y no me has culpado nunca por ello. En fin, sabes que este último año has sido muy importante para mí. Y sabes que esto que digo no tiene nada de folclórico.

Antes de agradecer a instituciones, proyectos y demás, quiero dar mi más sincero agradecimiento a cuatro personas que han sido mis pilares durante estos años. Sabéis bien lo importante que habéis sido para mí.

Rafa. Gracias por todo. Esta tesis y una gran parte de lo que he aprendido en estos años te lo debo a ti. Que te voy a contar que no sepas. Hemos estado al pie del cañón juntos durante estos años. Gracias por haberme hecho sentir tu máxima prioridad en gran cantidad de momentos. Gracias por tu paciencia. Tú también te has comido muchos deadlines fallidos por mi parte. Gracias por sugerirme la idea de hacer un modelo de 360° cuando yo ya no sabía cómo abordar el modelado de la fuente de los mapas. Gracias por siempre mirar más allá y volar alto (y por llevarme allí contigo). Sin ti, publicar en Nature Energy habría sido algo inconcebible. Gracias por haberte convertido en un gran amigo. Gracias por sacar lo mejor de mí. Gracias por las broncas que nos hemos pegado juntos, los power-walks y las largas conversaciones. Gracias por la Brompton. Gracias por los innumerables papers. Gracias por darme todo el carrete que he necesitado durante este año. En fin, gracias, gracias y gracias. Seguro que me dejo muchas cosas en el tintero.

Clara, guapísima, tú eres otra persona que sabe bien lo que ha sido esta tesis para mí y para nosotros. Gracias por estar siempre a mi lado y apoyarme. Por quererme y aguantarme cuando he estado en lo más alto y en lo más bajo (y levantarme en estos casos). Por escuchar toooodas mis ralladas y mis divagaciones. Por compartir sueños, frustraciones, risas, Netflix y piso. En fin, ya sabes todo lo que te agradezco y lo importante que eres para mí.

Y finalmente, gracias a mis papis, por vuestro apoyo y amor incondicional durante todos estos años. Gracias por darme lo mejor siempre y no esperar nada de mí. Por aguantarme durante estos años, con mis rajadas en Canarias incluidas. Gracias por no parar de escucharme nunca. Gracias por haberme

convertido en quien soy. Os quiero y me encanta la sensación de poder cerrar la tesis en Denia, con el agua de Cortes, y a vuestro lado y el de Ale.

Finalmente, gracias a la UNED, por financiar mi contrato predoctoral (FPI) desde finales de 2016 hasta el 2021. Gracias por poner a mi disposición un despacho y todos los medios necesarios para poder realizar mi tesis. Gracias también por la dotación económica para realizar una estancia de tres meses en Aix-en-Provence.

I would like to mention that this work has been partially supported within the Work Package Education (WP30-EDU) of the EUROfusion programme (Euratom Horizon 2020), under grant for pre-doctoral students. The views and opinions expressed herein do not necessarily reflect those of the European Commission. It has also been supported, as part of the TECF3IR contributions to the development of the “Area of Advanced Neutronics Simulation for Fusion Applications”, by the Spanish MINECO (Ministerio de Economía y Competitividad) under Programa Estatal I+D+I-Retos, Proyecto ENE2015-70733-R; as well as by Programas de Actividades I+D en Tecnologías de la Comunidad de Madrid calls 2013 y 2018 within programas TECHNOFUSIÓN II (S2013/MAE-2745, 2014-2018) and TECHNOFUSIÓN III (S2018-EMT-4437, 2019-2022). I also would like to mention that this work has been supported as well under F4E and ITER contracts to the TECF3IR research group.

The work in this thesis was carried out using an adaption of the C-model which was developed as a collaborative effort between: AMEC Co (International), CCFE (UK), ENEA Frascati (Italy), FDS Team of INEST (PRC), ITER Organization (France), QST (Japan), KIT (Germany), UNED (Spain), University of Wisconsin-Madison (USA), F4E (Europe).

Finally, I want to acknowledge that an important part of the work performed in this thesis was included in an article that was first published in Nature Energy, volume 6, pages 150-157, on the 4th of January 2021 by Springer Nature. The title of the article is: “A full and heterogeneous model of the ITER tokamak for comprehensive nuclear analyses”. Part of the content of this article is reproduced here with permission from Springer Nature.

DISCLAIMER

This thesis reflects the views only of the author, and Fusion for Energy cannot be held responsible for any use which may be made of the information contained herein.

The views and opinions expressed herein do not necessarily reflect the views of the ITER Organization. The content of this thesis does not commit the ITER Organization as nuclear operator.

INDEX

LIST OF FIGURES	i
LIST OF TABLES.....	ix
ABBREVIATIONS.....	xi
ABSTRACT.....	xv
CHAPTER 1 INTRODUCTION	1
1.1 Nuclear fusion as a power source.....	1
1.2 ITER.....	3
1.2.1 General description and objectives.....	3
1.2.2 The facility	5
1.3 Radiation fields in ITER	16
1.3.1 Neutron and photon sources	17
1.3.2 Implications of neutron and photon fields.....	23
1.4 ITER nuclear analysis.....	27
1.4.1 Activation and radiation transport calculations.....	28
1.4.2 Complexity of ITER nuclear analysis.....	29
1.5 Motivation and objectives of this thesis	32
1.6 Structure of this thesis	35
CHAPTER 2 STATE OF THE ART	37
2.1 On the neutronics modelling of ITER geometries	37
2.1.1 The importance of producing detailed geometry models.....	38
2.1.2 Current methodology to model ITER geometries	43
2.1.3 The problematics of modelling ITER geometries	50
2.2 ITER Tokamak reference models	54
2.2.1 General description of the reference models	55
2.2.2 Evolution of the reference models	60
2.2.3 Impact on nuclear responses	68

2.3	Limitations of partial models	69
2.3.1	Shutdown dose rates in port interspaces	70
2.3.2	Radiation mapping in the Tokamak Complex.....	73
2.3.3	Calibration of neutron detectors	78
2.4	Recent computational developments	82
CHAPTER 3	E-LITE.....	85
3.1	E-lite: a 360° model of the ITER Tokamak.....	85
3.2	Methodology.....	89
3.2.1	Assembly of the block structure.....	89
3.2.2	Further modifications of the block structure	92
3.2.3	Allocation of universes.....	103
3.2.4	Materials.....	107
3.2.5	Lost particles debugging.....	107
3.2.6	Plasma source definition	108
3.2.7	Standard Tallies	108
3.3	Computational performance	109
CHAPTER 4	CALCULATIONS AND EVALUATION.....	113
4.1	Shutdown dose rates in port interspaces.....	113
4.1.1	Introduction	113
4.1.2	Methodology.....	114
4.1.3	Results and discussion.....	119
4.1.4	Conclusion.....	124
4.2	Radiation mapping in the Tokamak Complex	125
4.2.1	Introduction	125
4.2.2	Methodology.....	125
4.2.3	Results and discussion.....	126
4.2.4	Conclusion.....	129
4.3	Calibration of neutron detectors	129

4.3.1	Introduction	129
4.3.2	Methodology	130
4.3.3	Results and discussion.....	132
4.3.4	Conclusion.....	135
CHAPTER 5 IMPACT OF THIS THESIS		137
5.1	Impact of E-lite on the ITER project	137
5.2	Other relevant contributions.....	140
5.2.1	D1SUNED: V&V and nuclear data package.....	140
5.2.2	ITER 2020 Radiation Maps.....	142
5.2.3	Other nuclear analyses of relevance.....	144
CHAPTER 6 CONCLUSIONS AND FUTURE WORK		145
6.1	Conclusions	145
6.2	Future work	150
REFERENCES		155
APPENDIX I - RELATIVE ERRORS		173

LIST OF FIGURES

Figure 1-1. Picture of the ITER site (2020). Courtesy of ITER Organization.....	4
Figure 1-2. Vertical cut-view of the ITER Tokamak with the major components indicated. Courtesy of ITER Organization.	5
Figure 1-3. Blanket modules. Courtesy of ITER Organization.....	6
Figure 1-4. Divertor. Courtesy of ITER Organization.	7
Figure 1-5. Vacuum Vessel. Courtesy of ITER Organization.	7
Figure 1-6. Thermal shields. Courtesy of ITER Organization.	8
Figure 1-7. Toroidal (left) and poloidal (right) field systems. These are two of the six magnet systems. Courtesy of ITER Organization.	8
Figure 1-8. Cryostat. Courtesy of ITER Organization.....	9
Figure 1-9. Access ports in the ITER Tokamak.	9
Figure 1-10. Vertical cross-section of the ITER tokamak and the out-bio-shield region. Taken from [11].	10
Figure 1-11. ITER ports allocation.	11
Figure 1-12. Vertical cross-section of the lower part of the tokamak, featuring the TCP port #4.	12
Figure 1-13. Views of the Diagnostics Equatorial Port #11.	12
Figure 1-14. Views of an obsolete concept of TBM port #16.....	13
Figure 1-15. Views of the Neutral Beams.	14
Figure 1-16. Views of an ECH-Upper Launcher.	14
Figure 1-17. Vertical cross-section of a simplified representation of the Tokamak Complex. The Tokamak Building (B11), Diagnostics Building (B74) and Tritium Building (B14) are indicated. The ITER Tokamak would be located at the centre, inside the B11 building. Taken from [23].	15
Figure 1-18. ITER activated water source. The spatial distribution of the ^{16}N concentration (atoms \cdot cm $^{-3}$) is shown.....	19
Figure 1-19. ITER activated water source inside the Tokamak Complex. The spatial distribution of the ^{16}N concentration (atoms \cdot cm $^{-3}$) is shown.	19

Figure 1-20. Example of tritium production ($\text{mg}\cdot\text{cm}^{-3}\cdot\text{d}^{-1}$) map in a TBM concept.	28
Figure 2-1. Schematic view of the double-labyrinth in the space between the port plugs and the blanket and vacuum vessel port extension [75][76]......	40
Figure 2-2. Example of homogenization. Detailed (left) and homogenized (right) models of a blanket module.....	41
Figure 2-3. Cross-sections showing the orientations of the pipes/layers studied in [79]: parallel (left), normal (centre) and at 45° to the flux (right, pipes only).	42
Figure 2-4. Vertical cross-sections of the original CAD (top) and MCNP (bottom) models of EP#11.	44
Figure 2-5. Example of the kind of unnecessary details for the nuclear analysis that are removed.....	46
Figure 2-6. Example of a complex body that has to be split prior to its translation to MCNP format.	46
Figure 2-7. Example of a body (mirror) that is mainly made of sp-lines, which are approximated by planes.	47
Figure 2-8. Example of the kind of clashes that may be present in the original CAD models.....	47
Figure 2-9. MCNP/CAD cell volume deviation (%) per cell as a function of the CAD volume (cm^3).	49
Figure 2-10. Horizontal cross-section of the ITER Tokamak reference model C- model. The model represents 40° of the machine.	56
Figure 2-11. Schematic representation of a horizontal cross-section of a partial model that has reflective boundary conditions (BC). The model features one complete port at the centre and two halves on the laterals. The illustration represents how a radiation particle (in red) is reflected at the boundary.....	56
Figure 2-12. This picture is based on that of Figure 2-11. It illustrates the machine (although here I only included the neighbourhood) that is actually being represented when reflective boundary conditions (BC) are considered. Note how the additional ports and the dashed trajectory are mirrored with respect to the BCs.....	57

Figure 2-13. This picture is similar to that of Figure 2-12. However, here I illustrate the machine that is actually being represented when periodic (instead of reflective) boundary conditions (BC) are considered.	57
Figure 2-14. Horizontal cross-sections of C-model (40°) at B1, L1 and L2 levels. The lower (LP), equatorial (EP) and upper (UP) ports are indicated. The bio-shield is coloured in orange-brown.	59
Figure 2-15. Horizontal cross-sections of an NBI model (80°) at B1, L1 and L2 levels. The lower (LP), equatorial (EP) and upper (UP) ports are indicated. The bio-shield is coloured in pink-purple.	59
Figure 2-16. Vertical and horizontal cross-sections of the BRAND model (2000) of the ITER Tokamak.	61
Figure 2-17. Evolution of the number of cells (blue), surfaces (orange) and materials (grey) of the ITER Tokamak reference models over the years. Note there are two vertical axes.	62
Figure 2-18. Vertical and horizontal cross-sections of the B-lite v2 model (2011) of the ITER Tokamak.	66
Figure 2-19. Horizontal cross-section of the tokamak model representing the NBI region. The model is based on A-lite.	66
Figure 2-20. Vertical and horizontal cross-sections of C-model R181031 (2018) of the ITER Tokamak.	68
Figure 2-21. Examples of radiation cross-talk. On the left-hand side, the vertical cross-talk towards the equatorial port is represented. On the right-hand side, the lateral cross-talk towards the central port is represented.	72
Figure 2-22. Illustration showing the flipping of partial models to relocate the IVVS port as the central port. Taken from [134].	73
Figure 2-23. Vertical cross-section of the Tokamak Complex MCNP model [89]. Taken from [137].	74
Figure 2-24. Horizontal cross-section of the Tokamak Complex MCNP model [89]. Taken from [137].	74
Figure 2-25. Vertical cross-section of tokamak (black) and Tokamak Complex (red) models where it can be seen that the bio-shield is the boundary of both models.	75

Figure 2-26. Schematic representation of how the radiation transmission is coupled between the tokamak and Tokamak Complex models by means of an intermediate source. Taken from [15].	76
Figure 2-27. Mosaic source approach to produce an intermediate plasma source for radiation mapping in the Tokamak Complex [137][139][140].	77
Figure 2-28. Locations where one of the most relevant types of neutron detectors, the neutron flux monitors (NFM), will be placed. Taken from [141].	80
Figure 3-1. Horizontal cross-section of the E-lite model at B1 level.	87
Figure 3-2. Horizontal cross-section of the E-lite model at L1 level.....	87
Figure 3-3. Horizontal cross-section of the E-lite model at L2 level.....	88
Figure 3-4. Vertical cross-section of the E-lite model.	88
Figure 3-5. Horizontal cross-section of the E-lite Block Structure (B1 level). .	91
Figure 3-6. Horizontal cross-section of the E-lite block structure (L1 level)....	91
Figure 3-7. Horizontal cross-section of the E-lite block structure (L2 level)....	92
Figure 3-8. B2 level Crown. Note, the portion of the crown beneath the NBI region is not shown.....	93
Figure 3-9. B2 level concrete Crown. On the left, C-model without crown. On the right, E-lite with the B2 level crown integrated.	93
Figure 3-10. Horizontal cross-section of the B1 level configuration of C-model block structure (Configuration #1).....	94
Figure 3-11. B1 level configurations #2 and #3 of the E-lite block structure..	95
Figure 3-12. B1 level configuration #3 of E-lite block structure. It can be seen how the envelope cell of the triangular support was split. In addition, dedicated envelope cells were inserted for the VV PS4 penetrations.	95
Figure 3-13. L1 port envelope cell after splitting to separate the port plug from the interspace.	96
Figure 3-14. L2 port envelope cell after splitting to separate the port plug from the interspace.	97

Figure 3-15. Horizontal cross-section of the E-lite L1 port envelope next to the NBI before (left) and after (right) the modifications implemented to “close” port #7.....	97
Figure 3-16. Vertical cross-section of the E-lite L1 port envelope next to the NBI before (left) and after (right) the modifications implemented to “close” port #7.	98
Figure 3-17. NBI block structure after inserting the L2 bio-shield plug envelopes.....	98
Figure 3-18. Missing blanket in row #13. The blanket universe was not allocated to any envelope cell in the NBI model.	99
Figure 3-19. Horizontal cross-section of the NBI block structure and universes at L2 level. Two errors on the envelope cells, and their fixes, are shown. The red boxes indicate a wrong definition of the port duct envelope. The yellow boxes indicate a wrong definition of the envelopes hosting the lateral manifolds running along the sides of the upper port plug.	100
Figure 3-20. Vertical cross-section of the E-lite block structure (left) and full model (right) where I show the cut-out that was integrated below the ECH-UL ports.....	101
Figure 3-21. Horizontal planes and cylindrical surfaces by which the E-lite block structure was split. Horizontal planes at heights 1705 cm (red) and -791 cm (blue) were considered. Cylindrical surfaces with radius 1470 cm (yellow) and 1345 cm (green) were considered.....	101
Figure 3-22. CAD model of a TFC WP divided into 11 radial layers.....	102
Figure 3-23. CAD model of the TFC Casings divided into 3 layers (FRONT, SIDE, BACK).....	103
Figure 3-24. Evolution of the number of cells (blue), surfaces (orange) and materials (grey) of the ITER Tokamak reference models over the years. The number of cells, surfaces and materials of E-lite are also shown. Note there are two vertical axes.	109
Figure 4-1. Views of ECH-Upper Launcher #12.....	114
Figure 4-2. Vertical cross-section of C-model where we can see the ECH-UL #12 integrated at the top part.	115

Figure 4-3. Horizontal cross-section of E-lite with the four ULs indicated at the bottom.....	115
Figure 4-4. View of the ECH-UL #12. The two SDDR tallies representing workers in the most exposed positions of the lateral corridors are shown in red.	119
Figure 4-5. Vertical cross-section of a neutron flux ($n \cdot s^{-1} \cdot cm^{-2}$) map in E-lite. The UL#12 is on the upper right region.....	123
Figure 4-6. Horizontal cross-section of a neutron flux ($n \cdot s^{-1} \cdot cm^{-2}$) map in E-lite. The four ULs are located at the bottom (south) region (see Figure 4-3).	123
Figure 4-7. Neutron flux impinging on the inner face of the bio-shield. a) Neutron flux at a radius of 1350 cm for B2 level and a radius of 1470 cm for the rest, obtained as a mosaic with SRC-UNED as indicated in [137] b) Neutron flux at the same locations as in a), but obtained with E-lite. Taken from [176].	127
Figure 4-8. Picture of the DNFM modules. Taken from [141].....	130
Figure 4-9. The circular trajectory along which the calibration source is deployed at 3° intervals inside the tokamak is shown in red. The region with direct view of the source by the detector is shaded in blue. Taken from [176].	131
Figure 4-10. a) This image was already shown in Figure 4-9. b) The divertor cassette below which the detector is hosted and the adjacent cassettes are shown in yellow. The blue regions are those of a) and the corresponding angular positions of the source, from -55° to -20° and from 20° to 55°, are marked over the source trajectory. c,d) Fission counts, as a fraction of the total counts, in the DNFM #14 for the ^{238}U fission chamber (c) and the ^{235}U fission chamber (d) as a function of the angle between the calibration source and the detector, obtained with C-model and E-lite models. The blue regions and corresponding angles are those of b). Error bars correspond to the statistical error of the tally in the simulation. Taken from [176].	133
Figure 5-1. Thank you letter to UNED's rector from the Director General (DG) of the ITER Organization.....	143
Figure 0-1. Relative error map of the neutron flux map shown in Figure 4-5.	173
Figure 0-2. Relative error map of the neutron flux map shown in Figure 4-6.	173

Figure 0-3. Relative error maps of the neutron flux maps shown in Figure 4-7.
..... 174

LIST OF TABLES

Table 2-1. Computational loads of the EP#16 MCNP model integrated in C-model. Taken from [97].	53
Table 2-2. Evolution of the number of cells, surfaces and materials of the ITER Tokamak reference models over the years.	62
Table 2-3. Horizontal cross-sections of the inboard region of several reference models of the ITER Tokamak. The pictures show the Toroidal Field Coils (TFC), Vacuum Vessel (VV) and Blanket Shield Modules (BSM).	63
Table 2-4. Reductions in the initializing time and memory used by relevant fusion-related MCNP models when running with unmodified and modified versions of MCNP5 [151].	83
Table 2-5. Computational loads of the EP#16 MCNP model integrated in C-model when considering MCNP5 and D1SUNED.	83
Table 3-1. Rotation angles around the Z-axis (positive sense is the anti-clockwise sense) of the TGCS applied to each of one of the original block structures with respect to their original position.	90
Table 3-2. B1 level configurations considered in the E-lite block structure per sector.	96
Table 3-3. B1 level ITER ports considered in E-lite. Those ports that are included by default in C-model or the NBI model are highlighted in grey.	105
Table 3-4. L1 level ITER ports considered in E-lite. Those ports that are included by default in C-model or the NBI model are highlighted in grey.	105
Table 3-5. L2 level ITER ports considered in E-lite. Those ports that are included by default in C-model or the NBI model are highlighted in grey.	106
Table 3-6. Evolution of the number of cells, surfaces and materials of the ITER Tokamak reference models over the years. The number of cells, surfaces and materials of E-lite are also shown.	110
Table 3-7. Computational performance of the E-lite model.	110
Table 4-1. Parent isotopes, pathways and radioisotopes considered in the simulation.	116
Table 4-2. Time correction factors considered in the calculations.	118

Table 4-3. SA-2 Irradiation scenario [173].	118
Table 4-4. SDDR ($\mu\text{Sv/h}$), and relative error, in the port interspace of UL#12 for both tallies (i.e. left and right corridors) and for both C-model and E-lite. ...	119
Table 4-5. SDDR ($\mu\text{Sv/h}$), and relative error, in the port interspace of UL#12 for both tallies (i.e. left and right corridors) due to each of the different lower ports at B1 level.....	120
Table 4-6. SDDR ($\mu\text{Sv/h}$), and relative error, in the port interspace of UL#12 for both tallies (i.e. left and right corridors) due to each of the different equatorial ports at L1 level.	121
Table 4-7. SDDR ($\mu\text{Sv/h}$), and relative error, in the port interspace of UL#12 for both tallies (i.e. left and right corridors) due to each of the different upper ports at L2 level. The Upper Launchers (ULs) are highlighted in grey.	121
Table 4-8. NPS and HIST card values of the 9 statistically independent simulations run to reach NPS 10^{11}	126
Table 4-9. Fission counts per source neutron in the ^{238}U and ^{235}U fission chambers of DNFM #14 with statistical error (in brackets). Taken from [176].	132

ABBREVIATIONS

ACAB	ACTivation ABacus Inventory Code for Nuclear Applications
ACP	Activation Corrosion Products
ALARA	As Low As Reasonably Achievable
ASN	Autorité de Sûreté Nucléaire – The French Nuclear Safety Authority
BM	Blanket Module
BSM	Blanket Shield Module
CAD	Computer-Aided Design
CCFE	Culham Centre for Fusion Energy
CCP	Cryostat Cryopump
CF	MCNP Cell Flagging card
CMM	Configuration Management Model
CSG	Constructive Solid Geometry
D	Deuterium
D1S	Direct 1-Step
D1SUNED	Direct-1-Step-UNED computational system for the estimation of decay photon fields
DA	Domestic Agency
DAG-MCNP	Direct Accelerated Geometry Monte Carlo Toolkit
DEMO	DEMONstration Power Plant
DG	Directo General
DGEPP	Diagnostics Generic Equatorial Port Plug
DGUPP	Diagnostics Generic Upper Port Plug
DM	Design Model
DNB	Diagnostic Neutral Beam
DNFM	Divertor Neutron Flux Monitor

DPA	Displacements-Per-Atom
DT	Deuterium-Tritium
EAF	The European Activation File
ECH	Electron Cyclotron Heating
ELM	Edge Localized Mode
ENDF	Evaluated Nuclear Data File
EP	Equatorial Port
ERID	Electrostatic Residual Ion Dump
F4E	Fusion for Energy
FDR	Final Design Review
FENDL	Fusion Evaluated Nuclear Data Library
GEOUNED	GEOUNED CAD-to-MCNP geometry converter/inverter
GVR	Global Variance Reduction
HNB	Heating Neutral Beam
HPC	High Performance Computing
HV	High Voltage
IBED	Integrated Blanket, Edge localized mode coils and Divertor
ICRH	Ion Cyclotron Resonance Heating
ICRP	International Commission on Radiological Protection
ICH	Ion Cyclotron Heating
INB	Installation Nucléaire de Base
IO	ITER Organization
ISS	Interspace Support Structure
IVVS	In-vessel Viewing System
JCR	Journal Citation Reports
JET	Joint European Torus
LANL	Los Alamos National Laboratory
LP	Lower Port

LPR	Lost Particle Rate
MC	Monte Carlo
MCAM	Monte Carlo Automatic Modelling system
McCad	McCad geometry conversion tool
MCNP	Monte Carlo N-Particle
MCPLIB84	Monte Carlo Photoatomic Data Library
MD	Manufacturing Design
MPI	Message Passing Interface
NB	Neutral Beam
NBI	Neutral Beam Injection
NIF	National Ignition Facility
NPS	MCNP history cut-off card
ORE	Occupational Radiation Exposure
ORNL	Oak Ridge National Laboratory
PCR	Project Change Request
PF	Poloidal Field
PFC	Poloidal Field Coil
PHTS	Primary Heating Transfer System
R2S	Rigorous 2-Step
RAM	Random-access memory
RF	Radio-frequency
RH	Remote Handling
RPrS	Rapport préliminaire de sûreté identifiée – Preliminary Safety Report
SDDR	Shutdown dose rate
SDEF	MCNP general source card
SSC	Systems, Structures and components
SuperMC	Monte Carlo simulation software
TBM	Test Blanket Module

TCP	Torus Cryopump
TCWS	Tokamak Cooling Water System
TECF3IR	Tecnologías de Fisión, Fusión y Fuentes de Irradiación
TENDL-2015	TALYS-based evaluated nuclear data library
TF	Toroidal Field
TFC	Toroidal Field Coil
TGCS	Tokamak Global Coordinate System
TR	MCNP Coordination Transformation Card
UL	Upper Launcher
UM	Unstructured Mesh
UNED	Universidad Nacional de Educación a Distancia
UP	Upper Port
V&V	Verification and Validation
VR	Variance Reduction
VV	Vacuum Vessel
WP	Winding Package

ABSTRACT

ITER is the largest and most complex tokamak ever conceived and one of the most ambitious and cutting-edge engineering and energy projects in the world today. In construction in southern France, and funded by 35 nations, the purpose of this experimental reactor is to demonstrate the scientific and technological feasibility of fusion as a large-scale and carbon-free source of energy. One of the many aspects that make ITER such a technically complex and challenging machine is that it will be subjected to a variety of radiation fields; the most relevant and intense ones being due to the 14.1 MeV neutrons that are emitted in every DT plasma fusion reaction. Nuclear (or neutronics) analysis is therefore a core discipline in support of the design, commissioning and operation of the machine.

In this thesis, I have focused on the neutronics models of the ITER Tokamak, which are used in the majority of ITER nuclear analyses. They are the so-called ITER Tokamak reference models. Due to the high accuracy constraints imposed on ITER nuclear analyses, reference models have become very detailed over the years. Indeed, they represent the many penetrations and the highly heterogeneous material arrangements that this facility features with an impressive degree of realism. Reference models have successfully satisfied the ITER neutronics needs for the last two decades.

For computational reasons, reference models have almost always been partial. That is, they explicitly represent a toroidal segment of the machine and the rest is implicitly represented by means of either reflective or periodic boundary conditions. The current reference models, C-model and the NBI model, represent 40° and 80° of the machine, respectively. However, despite the high degree of realism of reference models, their partial nature could present a serious concern regarding the accuracy and feasibility of certain ITER nuclear analyses. Yet, the repercussions of their partial nature have not been evaluated to date.

In this thesis, I have identified the limitations of partial models. On the one hand, partial models introduce unquantified uncertainties in the estimation of nuclear responses due to the fact that they represent as symmetric a machine that is actually asymmetric. Particularly, current reference models obviate the

asymmetric distribution of ITER ports. On the other hand, partial models are not prepared to be directly used in applications which, by definition, require a broader (or complete) toroidal representation of the machine geometry and/or the radiation sources.

These limitations can severely affect certain ITER nuclear analyses. Particularly, I identified and focused on three: (i) the estimation of shutdown dose rates in the port interspaces, (ii) the radiation mapping in the Tokamak Complex, and beyond, and (iii) the calibration of neutron detectors. These analyses are key to demonstrate the successful and safe operation of ITER. However, these are just few examples. In general, the partial nature of reference models affects the prediction of any non-local quantities and/or local quantities influenced by a long-range environment. Considering the tight design margins of the machine and the approach of ITER nuclear operation, scheduled in 2035, the limitations of partial models constitute a growing risk.

Thanks to the recent computational advances developed at my research group, a solution to overcome the limitations of partial models in a general and robust way was found. I produced a detailed 360° neutronics model of the ITER Tokamak: the E-lite model. It constitutes the most complex and realistic model of the ITER Tokamak to date; and it does not rely on any boundary conditions. Its computational performance was evaluated, showing that the model is completely usable for ITER nuclear analysis with the currently available HPC resources.

The effectivity of E-lite in overcoming the limitations of partial models was also demonstrated. Specifically, I used E-lite in the three applications and compared its performance with that of partial models or methodological approaches based on partial models. In all cases it was shown that E-lite represents a significant step forward regarding the accuracy of the nuclear responses estimated. Furthermore, it was demonstrated that E-lite triggers the development of a set of studies that were not feasible within reasonable uncertainty margins until now. Finally, the applicability of E-lite to validate partial and/or simplified models of the tokamak for specific applications was also highlighted.

Definitely, the E-lite model constitutes an important milestone in the field of ITER nuclear analysis. And its contribution to successfully tackle the challenges posed by radiation will not only be beneficial for ITER, but also for the future

DEMO and commercial fusion reactors. The value of E-lite has been highly recognized by the ITER neutronics research community. Together with C-model and the NBI model, it has become another ITER reference model. And it has already been (and it is planned to be) used in ITER nuclear analyses of great relevance for the ITER project. In fact, such has been the success of E-lite that part of the content of this thesis was published in January 2021 in the prestigious Nature Energy journal:

- R. Juarez, G. Pedroche, M.J. Loughlin et al, “A full and heterogeneous model of the ITER tokamak for comprehensive nuclear analyses”, Nature Energy 6, 150–157 (2021).

Finally, apart from E-lite, the work performed during this thesis has also led to other relevant contributions in the context of ITER nuclear analysis. Specifically, I participated in the verification and validation (V&V) of D1SUNED, which is the ITER reference code for SDDR calculations. In addition, I produced the official nuclear data package of D1SUNED, which covers the radioisotopes and pathways of concern for ITER planned in-situ maintenance scenarios. I also was the technical responsible at TECF3IR-UNED for all the activities required to perform the latest release (2020) of ITER Radiation Maps. The importance of these maps and the quality of the work performed by TECF3IR-UNED were such that the ITER Organization Director General himself, Bernard Bigot, expressly thanked our research group for our work in this task. Finally, in addition to all these works, I have also participated in several other nuclear analyses of relevance for the project. Overall, the work from these contributions has been reflected, for the moment, in 8 publications in JCR journals.

CHAPTER 1

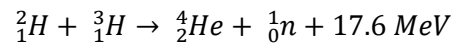
INTRODUCTION

1.1 Nuclear fusion as a power source

Nuclear fusion is a nuclear reaction by which two atomic nuclei merge to form a heavier atomic nucleus, generally emitting other particles in the process. Particularly, the nuclear fusion of light nuclei (e.g. hydrogen isotopes) leads to the release of a tremendous amount of energy. Indeed, this type of reactions are the ones that fuel the Sun and all the stars in the Universe. The energy released during the nuclear fusion process can be harnessed in a nuclear reactor. In fact, the development of nuclear fusion as a power source has been investigated since the 1950s [1] and is nowadays one of the most important research efforts worldwide. The main reason for this is that nuclear fusion has significant advantages with respect to other energy sources. Among them, we can count [2] its high-energy density, which is dramatically higher than that of coal, oil or gas; the wide availability of its fuels, which are virtually limitless; the zero emission of greenhouse gases; or, compared to fission reactors, the lower activity and half-life of the radioactive waste produced as well as the significantly safer nature of fusion reactors. These advantages make nuclear fusion a very attractive power source; one that can be able to face, in a sustainable and reliable manner, the expected increase of the global energy demand of the coming decades.

For nuclear fusion to consistently take place in a reactor, it is necessary to, first, transfer a large amount of energy to the fuel. In this way, the fuel is turned into a very hot plasma, one that can reach more than one hundred million degrees Celsius. Then, the plasma needs to be confined for sufficiently large amounts of time and at a sufficient density. In that environment, the fuel nuclei have very high kinetic energy and are so concentrated that they can come very close to each other. If the distance between the nuclei is sufficiently small for the strong nuclear force to overcome the electrostatic repulsion of the nuclei's positive charges, the nuclei fuse. The goal is to obtain more energy from the nuclear fusion reactions than the one needed for them to happen.

Among the different types of nuclear fusion reactions, the fusion of deuterium and tritium (DT) is identified to be the most efficient, as it yields the highest energy gains at the lowest temperatures [2]. This reaction is expressed as follows,



As a result of the DT fusion, an alpha particle and a neutron are produced, and 17.6 MeV of energy are released. In accordance with the conservation of linear momentum, 80% of that energy is carried by the neutron, that is, 14.1 MeV. Since neutrons do not have electrical charge, they will escape the plasma confinement and interact with the surrounding walls of the tokamak, where their kinetic energy will be transferred as heat. That heat will be the one used in future fusion reactors to produce steam and, ultimately, electricity. Thus, the DT neutrons play a fundamental role in the process of harnessing the fusion energy. However, we will see in section 1.3 that there are more reasons why neutrons, being a form of radiation, are so relevant in the context of fusion.

Due to the high temperatures of the plasma, it cannot be in contact with any material. Thus, the plasma cannot be confined in conventional vessels, like those of fission reactors. Considering this fact, two fusion technologies have been mainly developed over the years: inertial and magnetic. Inertial fusion relies on the heating and compression of small targets containing deuterium and tritium mixtures. The targets are compressed up to extreme densities for relatively short periods of time. On the other hand, magnetic fusion relies on magnetic fields to confine relatively low-density deuterium-tritium plasmas during relatively larger periods of time. Depending on the shape of the magnetic

fields, we can identify two concepts of magnetic fusion reactors: stellerators and tokamaks.

Magnetic fusion in tokamaks is the most funded and advanced approach of all; the most remarkable projects being the Joint European Torus (JET) [3], in the United Kingdom, and ITER [2], in construction in France. In addition, there are other fusion facilities of relevance, like the Wendenstein 7-X magnetic fusion stellarator [4], in Germany, or the National Ignition Facility (NIF) [5], in the USA, and the Laser MegaJoule [6], in France; the latter two being inertial fusion projects.

All the work covered in this thesis was performed in the frame of the ITER project, which is now described.

1.2 ITER

1.2.1 General description and objectives

ITER is the largest and most complex tokamak ever conceived and one of the most ambitious and cutting-edge engineering and energy projects in the world today. The idea of this international project was first proposed in 1985. Today, ITER construction in southern France is funded by 35 nations¹ and successfully advances towards the first plasma milestone [7], scheduled in December 2025. Ten years from then, the start of the deuterium-tritium operations is foreseen. In Figure 1-1, a picture of the ITER site is shown.

ITER is an experimental reactor that has been designed with the purpose of demonstrating the scientific and technological feasibility of fusion as a large-scale and carbon-free source of energy. Specifically, the main objectives of ITER are [2][8]:

- Produce 500 MW of output fusion power with a gain factor of $Q \geq 10$ during pulses of 400-600 seconds. The gain factor, Q , is the ratio between the output fusion power and the input power needed to heat the plasma. ITER will also be the first fusion device to obtain net energy gain ($Q > 1$).

¹ The 35 nations participating in ITER are: the 27 European Union countries + (through Euratom) Switzerland and the United Kingdom + China, India, Japan, Korea, the Russian Federation, and the United States.

- Demonstrate the availability and integration of technologies essential for the fusion power plants of tomorrow, such as superconducting magnets, heating systems or remote maintenance.
- Achieve a deuterium-tritium plasma in which the reaction is sustained through internal heating. In ITER, scientists want to explore a burning plasma, that is, a plasma in which the heating through self-heating reactions exceeds any external heating. Furthermore, the possibility of reaching a controlled ignition, that is, the point in which the plasma becomes self-sustainable, is not discarded.
- Test tritium breeding. Although deuterium is abundant in the sea water, tritium is rarely present in nature. That is why in future reactors the tritium will have to be produced by means of neutron interactions with lithium. Technologies aimed at guaranteeing tritium self-sufficiency will be studied in ITER.
- Demonstrate the safety characteristics of a fusion device. In 2012, after a rigorous and impartial process of examination of its safety files, ITER obtained licensing as a nuclear facility INB-174 (Installation Nucléaire de Base). The operation of ITER will serve to demonstrate how to control the plasma and fusion reactions in such a machine with negligible consequences to the environment, the workers and the public.



Figure 1-1. Picture of the ITER site (2020). Courtesy of ITER Organization.

After JET [3], which is ITER's predecessor, and the current largest operating tokamak, ITER will constitute the next step in the roadmap towards the development of nuclear fusion as a power source. Although it will not produce electricity, it will be an extraordinary test bench that will allow to select and develop the technologies necessary for the first demonstration power plant, DEMO [9]. DEMO will produce electricity based on fusion and will open the door to the commercial fusion reactors of tomorrow.

1.2.2 The facility

This thesis is about a neutronics model of the ITER Tokamak. Therefore, it is suitable at this point to have a brief overview of the tokamak. I will briefly describe its main components and their functions. This will help understand the specific problem I am addressing in this thesis. In addition, for the same purpose, I will also very briefly describe the Tokamak Complex; i.e. the building that hosts the tokamak and the most important plant systems.

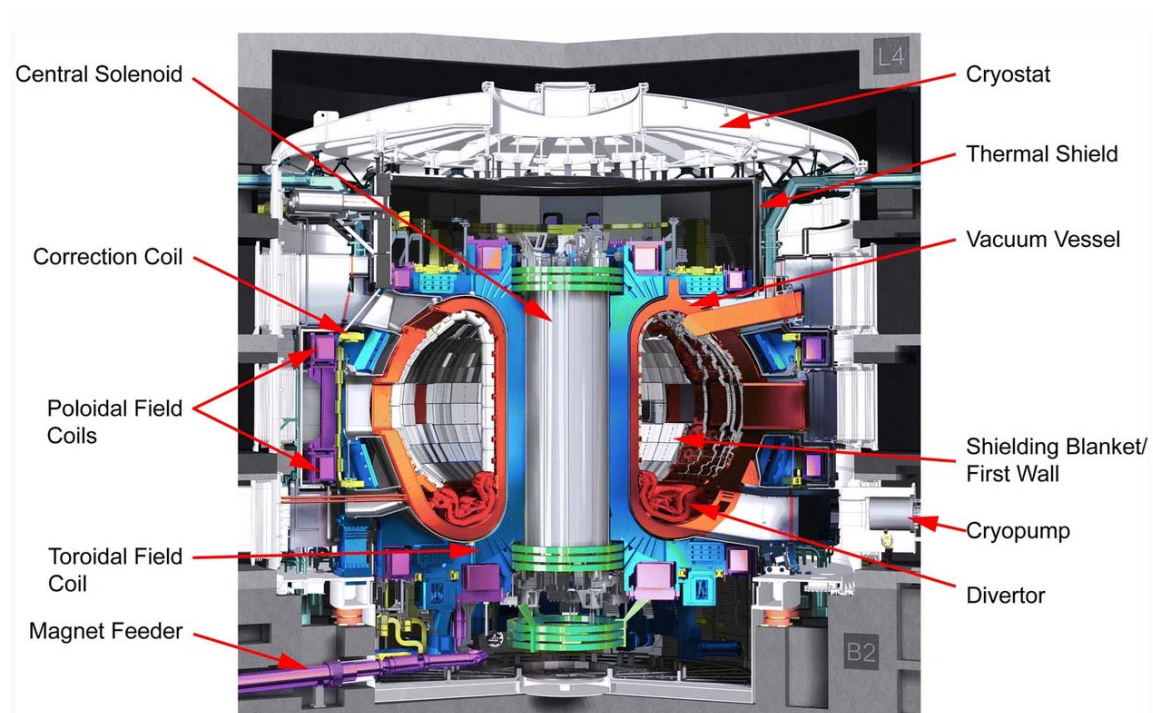


Figure 1-2. Vertical cut-view of the ITER Tokamak with the major components indicated. Courtesy of ITER Organization.

ITER Tokamak

The ITER Tokamak (Figure 1-2) will confine the burning plasma and the fusion reactions taking place within it inside a doughnut-shape vessel. To do so,

massive superconducting magnets will produce intense magnetic fields that will control the plasma and will keep it away from the vessel walls. Although many tokamaks have been built around the world, none of them resembles the ITER Tokamak in terms of scale and complexity. Indeed, it will have a plasma volume of 830 m³ [2], which is more than 8 times the 100 m³ plasma volumes of the current largest operating tokamaks, JET [3] and JT-60 [10].

The ITER machine will host a wide range of high-tech systems, elaborately interconnected, which will be deployed along five storeys inside the bio-shield. B2 and B1 storeys are underground, and L1, L2 and L3 storeys are above ground level. Radially from the plasma chamber, and in general terms, the ITER Tokamak comprises [2]:

-Blanket modules (Figure 1-3): Covering the inner wall of the vacuum vessel, 440 blanket modules will protect the steel vacuum vessel and external machine components, such as the toroidal field magnets, from the heat and high-energy neutrons produced by the fusion reactions.



Figure 1-3. Blanket modules. Courtesy of ITER Organization.

-Divertor (Figure 1-4): Situated at the bottom of the vacuum vessel, 54 divertor cassettes will control the exhaust of waste gas and impurities from the reactor to minimize the plasma contamination. In addition, like the blankets, it will also protect the surroundings from the thermal and neutronics loads. Particularly, the divertor will withstand the highest surface heat loads of the machine. That is why it will feature an armour made of tungsten, which has the highest melting point of all metals.



Figure 1-4. Divertor. Courtesy of ITER Organization.

-Vacuum vessel (Figure 1-5): It will provide a high-vacuum environment for the plasma, improve radiation shielding and plasma stability, act as the primary safety confinement barrier, and provide support for in-vessel components such as the blanket modules and the divertor.

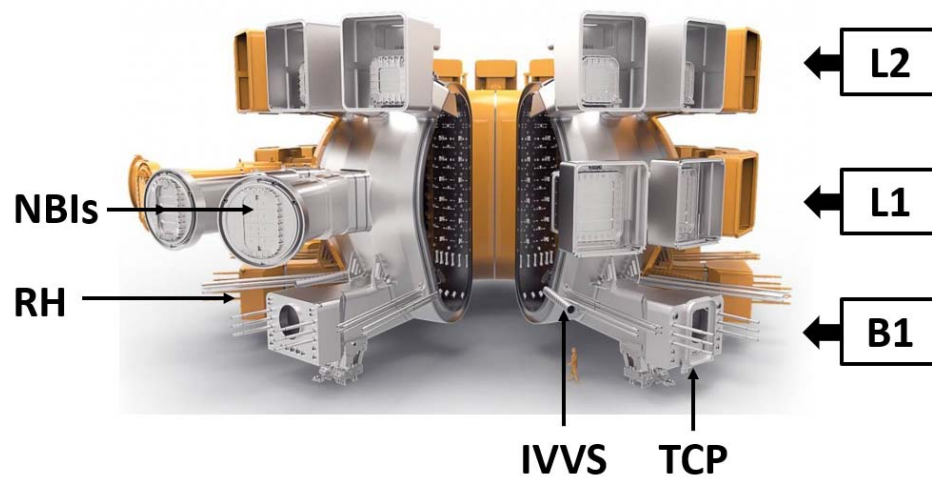


Figure 1-5. Vacuum Vessel. Courtesy of ITER Organization.

-Thermal shields (Figure 1-6): Two layers of thermal shielding will be interposed between the vacuum vessel and the cryostat to minimize heat loads transferred by thermal radiation and conduction from warm components to the components and structures that operate at 4.5K (such as the magnets).

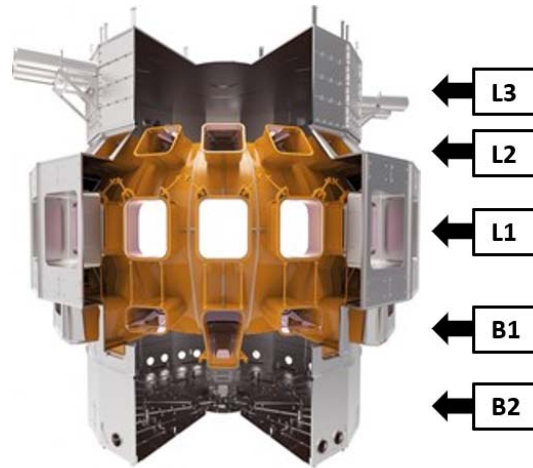


Figure 1-6. Thermal shields. Courtesy of ITER Organization.

-Magnets (Figure 1-7): They will produce the magnetic fields that will initiate, confine, shape and control the ITER plasma.

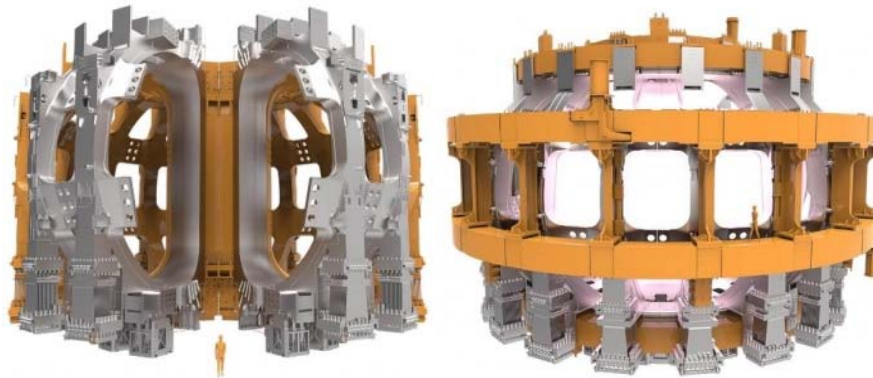


Figure 1-7. Toroidal (left) and poloidal (right) field systems. These are two of the six magnet systems. Courtesy of ITER Organization.

-Cryostat (Figure 1-8): It is a vacuum pressure chamber that will provide the high vacuum and ultra-cool environment for the vacuum vessel and the superconducting magnets.

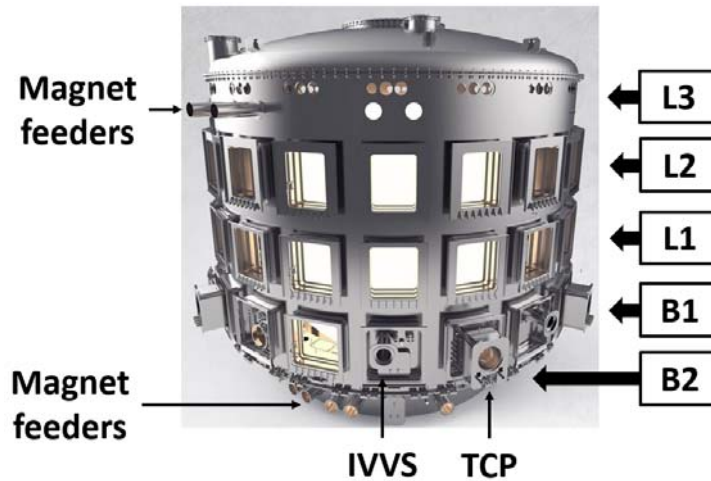


Figure 1-8. Cryostat. Courtesy of ITER Organization.

-Bio-shield: It is the concrete barrier that surrounds the ITER machine and separates it from the rest of the building, protecting the workers and the environment from the radiation generated by fusion reactions.

Access ports

Throughout the 360° of the torus, the vacuum vessel, thermal shield, cryostat and bio-shield will feature access ports (approximately, every 20°) at levels B1 (divertor ports), L1 (equatorial ports) and L2 (upper ports), which will be displayed throughout the machine as shown in Figure 1-9.

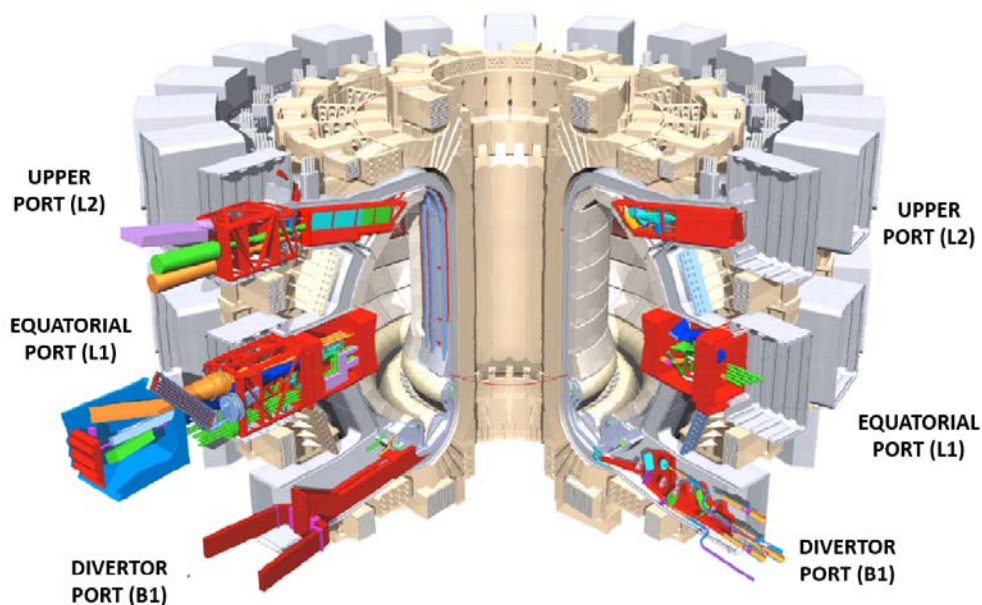


Figure 1-9. Access ports in the ITER Tokamak.

The majority of the access ports have three different regions, as shown in Figure 1-10. The first region goes from the plasma chamber up to the primary vacuum boundary, which is normally sealed by a closure plate or similar. In this region, the upper (L2) ports and all the regular equatorial (L1) ports feature a port plug. Port plugs host systems and penetrations for different purposes and as much shield as possible to protect the regions beyond from the radiation coming from the plasma. In the case of the divertor (B1) ports, there are no port plugs and each port has its own particularities (e.g. a diagnostics rack, a cryopump, etc).

In the second place, the region that goes from the back of the closure plate (or similar) up to the bio-shield is the Port Interspace. Depending on the port, this area features waveguides, mirror assemblies, valves and different types of vacuum extensions. These components are in some cases supported by the so-called Interspace Support Structure (ISS). As I will explain again later, during machine shutdown, this area is accessed in many ports by operators to perform manual and/or remotely assisted inspection and maintenance operations. In some cases, the whole ISS may be disconnected and removed to inspect the closure plate.

Finally, the region that goes from the bio-shield up to the port cell door is the Port Cell. This area can be considered as the continuation of the Port Interspace outside the bio-shield, within the so-called Tokamak Building.

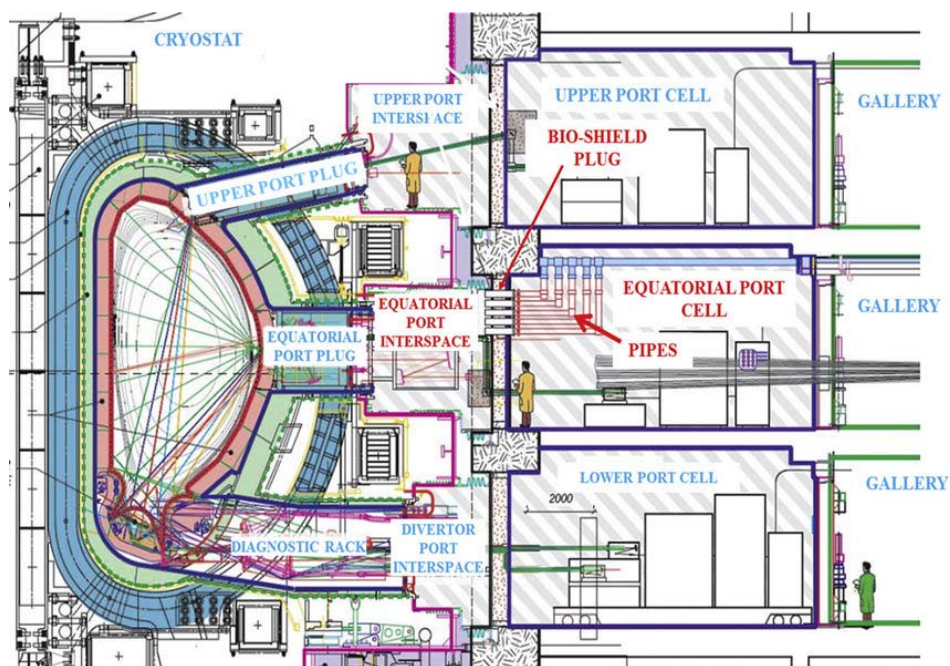


Figure 1-10. Vertical cross-section of the ITER tokamak and the out-bio-shield region. Taken from [11].

The access ports will have different functions (heating, diagnostics, tritium breeding, vacuum, etc) and shapes; each port being different from the rest. The distribution of the different types of ports is summarized in Figure 1-11.

ITER Ports Allocation

	1	2	3	4	5	6	7	8	9	10	11	12	13	14	15	16	17	18
L2	Diag	Diag	Diag	dum	dum	dum	dum	Diag	Diag	Diag	Diag	UL	UL	Diag	UL	UL	Diag	Diag
L1	Diag	Diag	Diag	2 x NBI	NBI	NBI	-	Diag	Diag	Diag	Diag	Diag	ICH	ECH	ICH	TBM	Diag	TBM
B1	-	RH	←IVVS	TCP	→IVVS	TCP	CCP	RH	←IVVS	TCP	→IVVS	TCP	CCP	RH	←IVVS	TCP	→IVVS	TCP

RH: Remote Handling Lower Port **TBM:** Test Blanket Module Port **Diag:** Diagnostics Port
IVVS: In-Vessel Viewing System Port **NBI:** Neutral Beam Injector **UL:** Electron Cyclotron Heating antenna Upper Launchers
TCP: Torus Cryopump Port **ICH:** Ion Cyclotron Heating antenna Port **dum:** Dummy Upper Port
CCP: Cryostat Cryopump Port **ECH:** Electron Cyclotron Heating antenna Port

Figure 1-11. ITER ports allocation.

At B1 level, six ports will be used for vacuum pumping with Torus Cryopumps (TCP ports) [12], six ports will host In-vessel Viewing systems (IVVS ports) [13] and three ports will host diagnostics systems mounted on racks, which can be removed to allocate equipment for remote handling operations (RH lower ports) [14]. Note the IVVS are not vertically aligned with the ports immediately above them in the same toroidal segment, but slightly tilted towards the next (→) or previous (←) port alternately. Three 20° toroidal segments of the vacuum vessel will have no access port at B1 level, as those will be used for either two cryostat cryopumps (CCP ports) [12] mounted in the cryostat, or in-cryostat inspection entries. In Figure 1-12, I show a vertical cross-section of the TCP port #4 [15]. The reader can appreciate the large empty space that needs to be left for vacuum pumping from the divertor up to the bio-shield. This large space will represent an important path for radiation to leak.

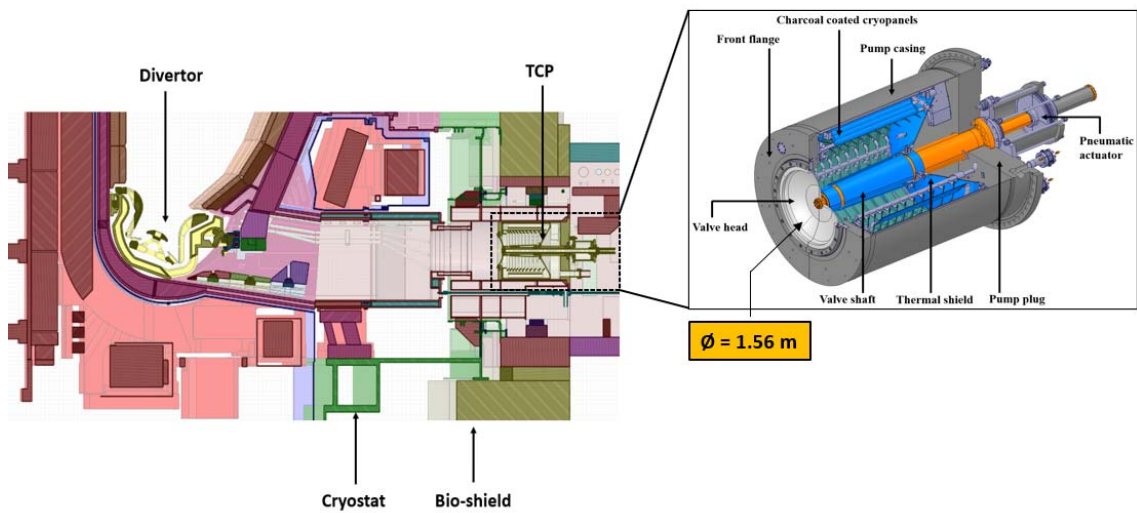


Figure 1-12. Vertical cross-section of the lower part of the tokamak, featuring the TCP port #4.

At L1 level, the regular ports will host port plugs, designed to address different tasks. Nine L1 level ports will deploy diagnostics systems to control, evaluate and optimise the plasma performance and to study burning plasma physics [16], each of them with its own particular systems and configurations. In Figure 1-13, views of the Diagnostics Equatorial Port #11 are shown [17]. It can be seen that considerably large penetrations are required to be able to receive information (i.e. electromagnetic radiation, particles) from the plasma.

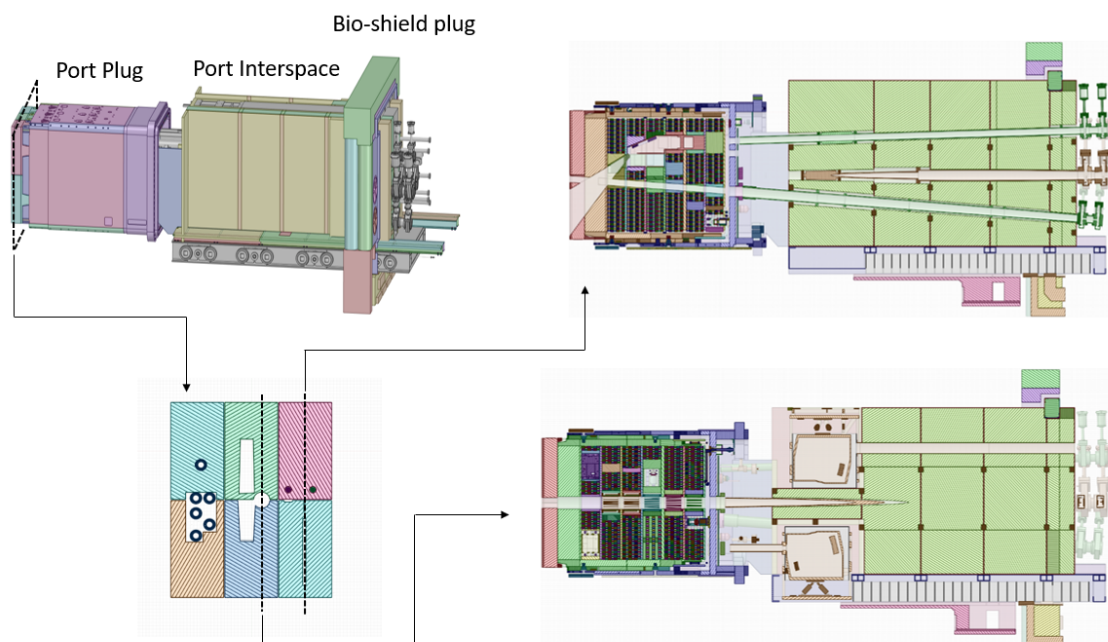


Figure 1-13. Views of the Diagnostics Equatorial Port #11.

Two ports will contain two Test Blanket Modules (TBM ports) each, which are experiments to study the tritium breeding technologies for the future commercial fusion reactors [18]. In Figure 1-14, views of an obsolete concept of TBM#16 are shown [19]. Compared to the diagnostics ports, TBM ports have significantly less penetrations.

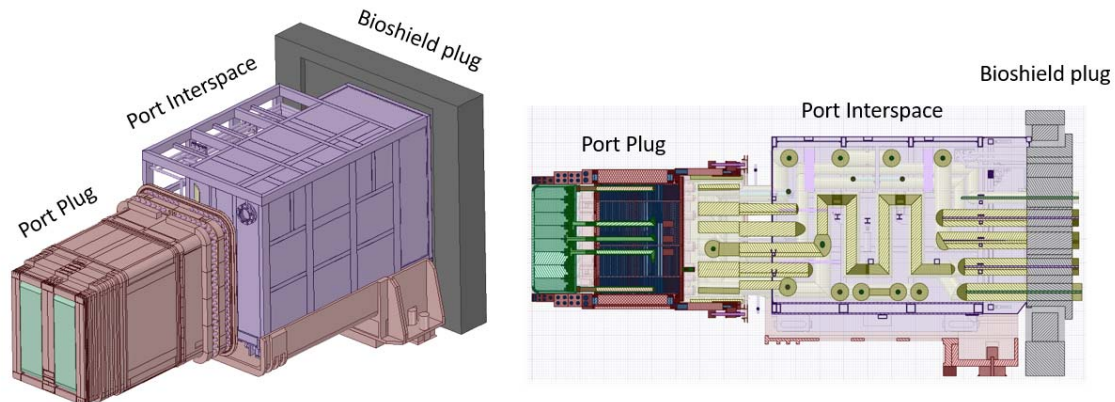


Figure 1-14. Views of an obsolete concept of TBM port #16.

Three L1 ports will be used to heat the plasma with cyclotron resonance antennas, two based on ion resonance (ICH ports) [20], and one on electron resonance (ECH port) [21]. At this level we also find the four Neutral Beam Injectors (NBI) [22] (see Figure 1-15). Three of these, the Heating Neutral Beams (HNB), will be used to heat the plasma with deuteron beams. The fourth, the Diagnostic Neutral Beam (DNB), will be used for plasma diagnosis. All of them require large empty spaces to operate. The HNBs are inclined with respect to the radial direction, while the DNB is radially aligned. Note, the NBIs are not regular ports, so they are not mounted in port plugs, but they give rise to uniquely shaped toroidal segments. Because of the inclination of the HNBs, the toroidal segment #7 of the machine is missing one equatorial port aperture in the vacuum vessel.

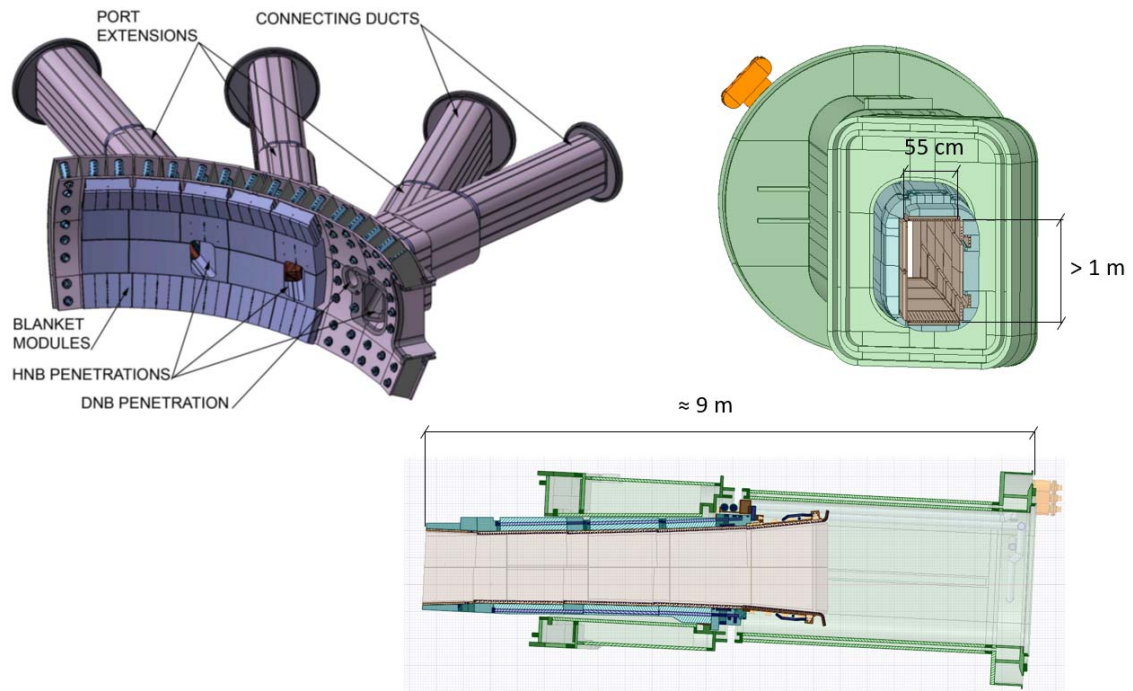


Figure 1-15. Views of the Neutral Beams.

At L2 level, the port plugs disposition is simpler. Four dummy plugs are placed above the NBIs, with the main function of shielding the radiation from the plasma. Another four port plugs will host electron cyclotron heating antennas, the so-called Upper Launchers (ECH-UL ports) [21] (see Figure 1-16). The remaining ten port plugs will host diagnostics systems, similar to those at L1 level [16].

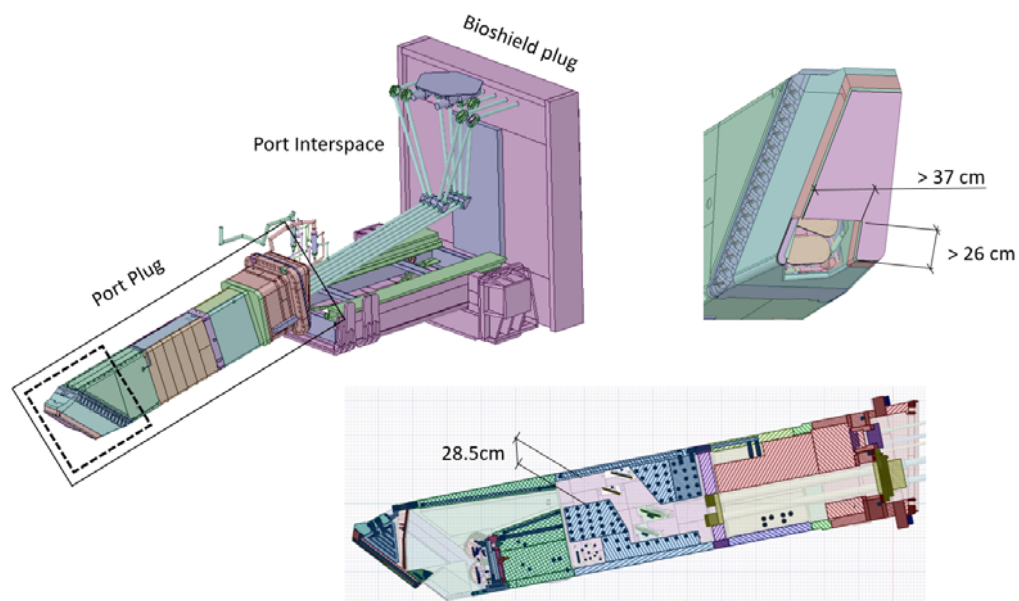


Figure 1-16. Views of an ECH-Upper Launcher.

Tokamak Complex

From all the buildings that will form part of the ITER site, the Tokamak Complex is the most relevant. At the heart of the site, the Tokamak Complex is the civil structure that will accommodate the ITER Tokamak and the more than thirty plant systems needed for the machine operation. As shown in Figure 1-17, the Tokamak Complex comprises the Tokamak Building (B11), Tritium Building (B14) and Diagnostic Building (B74). The B11 building will host the ITER Tokamak, while the B14 and B74 buildings will host tritium processing and confinement systems, on the one hand, and diagnostic equipment, cubicles for diagnostics, test laboratories, etc, on the other hand.

The Tokamak Complex is a seven-storey edifice, with two storeys underground (B2 & B1) and the other five above the ground (L1 to L5). It is mainly made of ordinary concrete, heavy concrete and borated heavy concrete and its dimensions are 120 m x 80 m x 60 m (L x W x H).

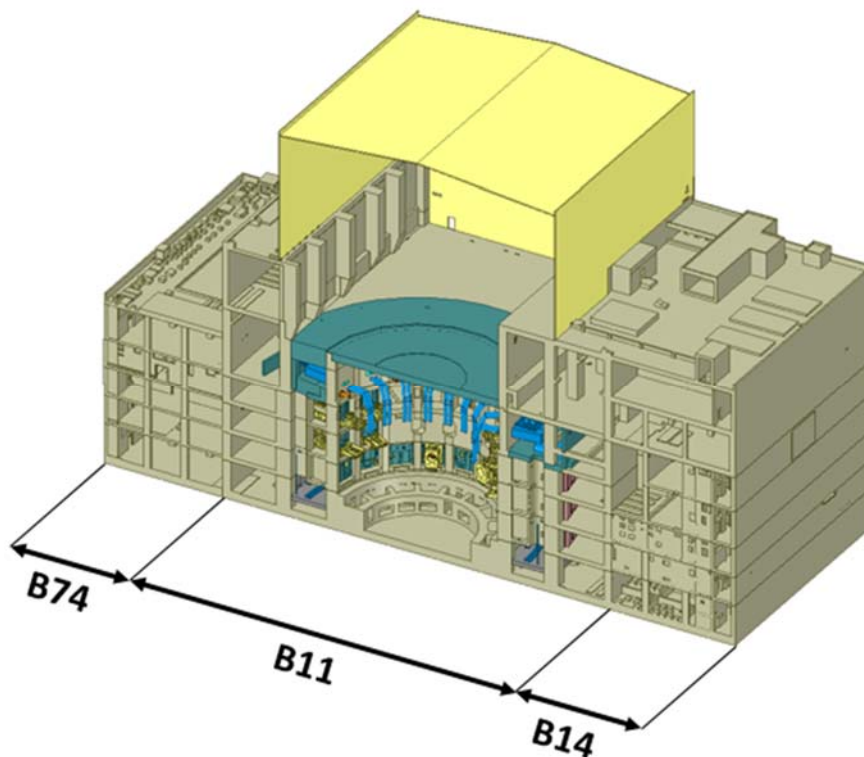


Figure 1-17. Vertical cross-section of a simplified representation of the Tokamak Complex. The Tokamak Building (B11), Diagnostics Building (B74) and Tritium Building (B14) are indicated. The ITER Tokamak would be located at the centre, inside the B11 building. Taken from [23].

All the buildings will be crowded with many systems, many of them being prolongations of the ones present inside the bio-shield. The systems will run along the different rooms and cross the walls and slabs through many penetrations (>4000). Specially concerning are the penetrations through the bio-shield plugs, as they represent an important mechanism for radiation leakage.

Summary of the main features

I now want to highlight the following main features of the ITER facility. These highlights will help understand the relevance and the motivation of this thesis as the reader continues reading it:

- ITER is a very complex and challenging engineering project. It comprises many high-tech systems and components, which are at the forefront of research and industry. Many of the components in ITER are “one of a kind”.
- It has very large dimensions in comparison to other fusion facilities. Specifically, the plasma chamber is around 8-10 times larger than that of its predecessor, JET.
- The ITER systems and components are made of many different materials (stainless steels, water, copper alloys, beryllium, concretes, etc), which are distributed heterogeneously in intricate arrangements.
- ITER has many gaps and penetrations (diagnostics, waveguides, gaps for tolerances, empty spaces for vacuum pumping, etc) and these spread throughout the entire facility. The bio-shield features many penetrations.
- ITER ports are very different from each other. Even the ones serving the same purpose, have different configurations. Many of the ports feature many and significantly large penetrations.

1.3 Radiation fields in ITER

Now that we have an idea of the ITER project and the main features of the facility, I am going to dedicate this subsection to one of the many aspects that make ITER such a technically complex and challenging machine: the presence of radiation. This section will help us understand the importance of ITER nuclear analysis (section 1.4), which is the knowledge field within which the thematic of this thesis falls.

ITER will be subjected to a variety of radiation fields. The most relevant and intense ones are due to the already presented 14.1 MeV neutrons that are emitted in every DT plasma fusion reaction. In addition, neutrons and other forms of radiation, such as photons, will also be emitted by several other mechanisms. All these forms of radiation will spread throughout the entire facility, interacting with the medium and leading to a series of alterations and processes with different implications. Many of such implications, regardless of their positive or negative nature, pose challenges that make fusion reactors even more complicated than they already are. Indeed, radiation impacts the design, licensing, construction and decommission of fusion reactors.

In this section I am going to, first, describe the most relevant mechanisms by which neutrons and photons are emitted in ITER. Then, I will explain the implications and challenges derived from the presence of neutrons and photons fields.

1.3.1 Neutron and photon sources

The most relevant sources of neutrons and photons in ITER are four. The main one, as I have already mentioned, is the DT plasma, which will lead to the most intense (neutron) radiation fields. Particularly, a total of $\approx 1.77 \cdot 10^{20}$ neutrons per second will be emitted during the 500 MW DT-plasma pulses of ITER. This means that throughout the 20 years of ITER's lifetime, with 4700h of nominal operation, a total of approximately $3 \cdot 10^{27}$ neutrons will be emitted. This neutron budget is $1.5 \cdot 10^6$ times larger than that of the two DT campaigns of JET together [24][25]. That is, ITER will be exposed to much more intense radiation fields than JET.

The other three sources, or emission mechanisms, are briefly explained below. They result from the interaction of neutrons with the medium. These four sources lead to the most significant implications and challenges.

Prompt-photons

Neutrons, as they interact with matter through all kinds of nuclear reactions, transfer their energy and lead to the excitation of the nuclei of the medium. One way in which the excited nuclei release the excess of energy is by emitting the so-called prompt photons. This mechanism of photon emission is very relevant in ITER during plasma operation. Particularly, the most relevant prompt-photon

fields are those resulting from the interaction of the DT plasma neutrons with the medium.

Activated cooling water

The water that flows through the cooling circuits of the blankets, vacuum vessel, divertor, neutral beams and other ITER components (e.g. diagnostics), will be exposed to intense DT-plasma neutron fluxes. Consequently, it will become highly activated; the most relevant activation reactions being: (i) $^{16}\text{O}(n,p)^{16}\text{N}$, (ii) $^{17}\text{O}(n,p)^{17}\text{N}$ and (iii) $^{18}\text{O}(n,\gamma)^{19}\text{O}$. The first two are threshold reactions with energy thresholds of 10 MeV and 8 MeV, respectively, while the third one already takes place with thermal neutrons [26]. Consequently, the activation of water is of most significance in regions that have a relatively direct exposition to the 14.1 MeV DT-plasma neutrons, before they have lost their energy through interactions with the medium.

The three resulting isotopes are radioactive. ^{16}N and ^{19}O emit decay photons and ^{17}N , decay neutrons. ^{16}N is the most relevant radioisotope in the activated water in ITER due to its high activity and the relatively high energy photons that it emits [26][27].

Considering the relatively short half-lives of ^{16}N (7.13 s), ^{17}N (4.14 s) and ^{19}O (26.9 s), the activated water will only emit radiation during plasma operation, as it soon decays once the exposition to neutrons ceases. However, its decay is sufficiently slow to allow highly activated water to travel through the cooling circuits and reach remote regions of the facility. These regions are beyond the bio-shield, significantly far away from the tokamak regions exposed to high energy neutrons. This feature leads to the generation of intense radiation fields in regions of the facility where the radiation coming from other sources (i.e. DT plasma) has already been significantly attenuated (by equipment, shields and/or concrete walls and slabs). This is the most characteristic aspect of this radiation source and the reason why it is so relevant in ITER. In Figure 1-18 and Figure 1-19, I show the concentration of ^{16}N throughout the ITER activated water source [28].

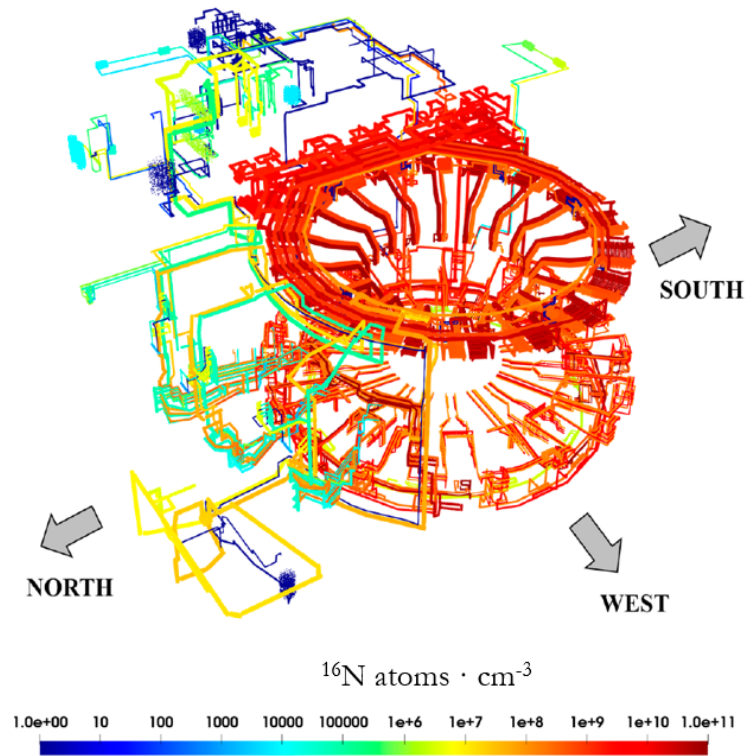


Figure 1-18. ITER activated water source. The spatial distribution of the ¹⁶N concentration (atoms · cm⁻³) is shown.

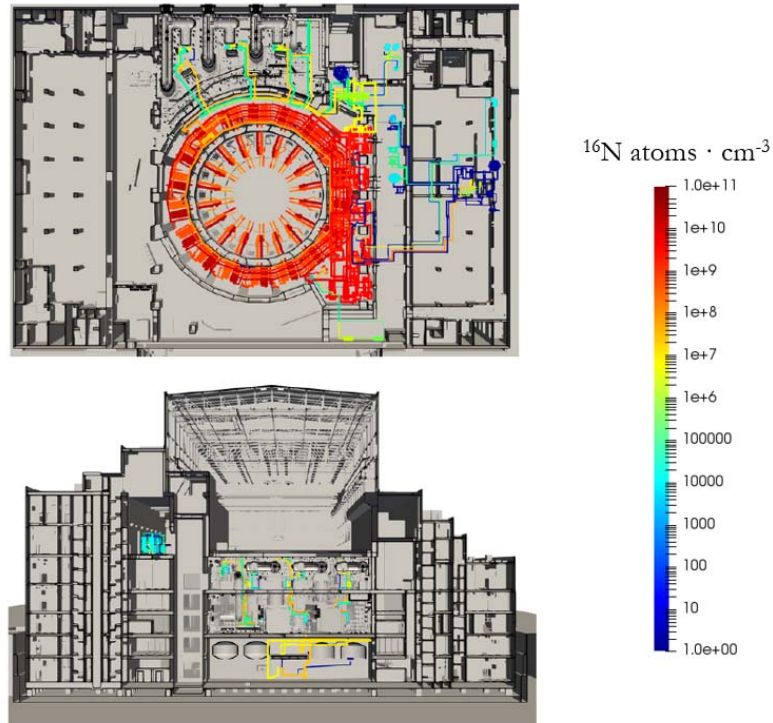


Figure 1-19. ITER activated water source inside the Tokamak Complex. The spatial distribution of the ¹⁶N concentration (atoms · cm⁻³) is shown.

It is worth noting that the activity of the water in ITER is considerably higher than in conventional fission reactors [26][29]. This is because the energy of the DT fusion neutrons (14.1 MeV) is higher than that of the average fission neutron (~2 MeV). Thus, the production of ^{16}N through the (n,p) threshold reaction is greater.

Activated materials

In addition to the cooling water, as the systems, structures and components of the facility are irradiated with neutrons (DT neutrons, activated water ^{17}N -neutrons, etc), they will as well become activated. As the activated materials decay, intense decay photon fields will arise, which may persist long after the machine shutdown. In fact, although present during plasma operation, these fields will be particularly relevant during maintenance operations and cask transfer activities, once the neutron irradiation has ceased and other radiation sources are no longer present.

Among the different activated materials of relevance, we count copper alloys, stainless steels, and concretes, which will give birth to important decay photon emitters such as ^{64}Cu , ^{58}Co , ^{60}Co , ^{54}Mn , ^{182}Ta , ^{24}Na or ^{152}Eu , through reactions like (n,p), (n, γ), (n,2n), (n,d), (n, α), etc [30]. The relevance of each radioisotope varies in time according to their decay rate. That is, a particular radioisotope can be quite relevant at a certain cooling time after machine shutdown but not at others.

As it happens with the activated cooling water, activated materials can also lead to intense radiation fields in regions far away from the original position where the activation took place. This happens, for instance, when activated components, like blanket modules, are transported from the plasma chamber to the Hot Cell Complex, during the cask transfer activities. This also happens with the formation of Activation Corrosion Products (ACPs) [31][32]. Indeed, the corrosion products formed in highly activated cooling pipes (e.g. cooling pipes of the blankets or the divertor) dissolve in the cooling water and are later propagated and deposited in remote parts of the cooling circuits.

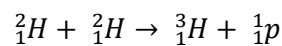
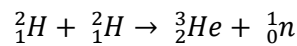
Apart from these four mechanisms of neutron and photon emission, there are many others which, although not as studied and challenging as the previous

four, have their own features and particular consequences. Here I do not pretend to cover all of them, but to briefly explain the most significant ones.

NBI ERID

As already mentioned, the Neutral Beam Injectors are one of the three different auxiliary systems that will heat the plasma up to the required temperatures. One way in which the NBI will do so is by accelerating negative deuterium ions up to 1 MeV, then neutralizing them (in the neutralizer) and finally injecting them into the plasma [22][33].

However, a significant number of deuterium ions will go through the neutralizer without getting neutralized. The function of the so called ERID (Electrostatic Residual Ion Dump) is to deflect such residual ions from the main beam and collect them before the injection. Now, as deuterium ions accumulate on the ERID plates, they can undergo fusion reactions with the new coming deuterium ions [33][34], according to



The first fusion reaction leads to the emission of neutrons. However, compared to the DT fusion, the DD fusion leads to less energetic neutrons, of 2.45 MeV. The second fusion reaction leads to the formation of tritium, which also builds up on the ERID plates and can eventually undergo DT fusions with the coming deuterium, resulting in the emission of 14.1 MeV neutrons. Thus, the NBI ERID is a source of both DD and DT neutrons. Although of significantly lower intensity than the D and DT plasma neutron sources (see below for D plasma), this source leads to neutron fields in the regions close to it that are as relevant as the radiation fields from these plasmas.

Photoneutrons from First Wall Beryllium

Neutrons (or photoneutrons) will also be emitted by the so-called photonuclear reactions, which are nuclear reactions induced by highly energetic photons. Particularly meaningful is the photonuclear reaction ${}^9\text{Be}(\gamma, \text{n}){}^8\text{Be}$ that takes place in the beryllium that forms part of the blanket modules first wall [35]. This reaction has an energy threshold of 1.665 MeV and it is mainly induced by: (i) the prompt photons that are emitted from the interaction of DT plasma neutrons

with the first wall materials, (ii) the photons from the activated water that goes through the blanket cooling channels and (iii) the decay photons from the in-vessel activated material.

The intensity of this neutron source is relatively low when compared to the intensity of the DT plasma (and all its derived sources). However, this neutron source has the particularity of being present during both machine operation and shutdown [35], being the only neutron source, from all the ones considered here, that will be present at shutdown. Furthermore, during the cask transfer activities, the blanket modules that are to be replaced will be transferred from the tokamak up to the Hot Cell Complex. Therefore, photoneutrons will be emitted in regions located far away from the original location of the blanket modules.

D plasmas

Before the DT plasmas, deuterium (D) plasmas will be studied [36]. They will be considered to assess the behaviour of the eventual DT plasmas, while avoiding the problematic of having tritium in the facility, which is a radioactive isotope. As I have mentioned above, DD fusions can also lead to the emission of neutrons, therefore, D plasmas represent another neutron source of relevance in ITER. It is true that DD neutrons are less energetic than DT neutrons (2.45 MeV vs 14.1 MeV), that the neutron emission rate during the D pulses is around two orders of magnitude lower than the DT neutron yield [37] and that the total D operation is much shorter than the DT operation [36]. Still, D plasmas will represent one of the most important neutron sources before the DT phase.

H and He plasmas

At the early phases of operation of the machine, before the D and DT plasmas, H (and possibly He) plasmas will be studied for different purposes [36]. Although with far less intensity than the D and DT plasmas, these plasmas will also lead to the emission of neutrons through different mechanisms [38][39]. On the one hand, due to the presence of residual amounts of deuterium in hydrogen, DD fusion reactions will take place in the H plasmas. In addition, these reactions will lead to the formation of tritium, which will also undergo DT fusion reactions with the residual deuterium. Of course, the number of DD and DT fusion reactions in the H plasmas is negligible when compared to the number of these reactions that will take place in the D and DT plasmas. On the other hand,

neutrons will also be emitted in both H and He plasmas due to the nuclear reactions that take place between the beryllium impurities (originated by the erosion of the first wall) and the fast H and ^3He ions that are accelerated through the different plasma heating mechanisms (i.e. NBI and ICRH) [40][41]. These neutron emission mechanisms, together with the runaway electrons (see below), will be the most important during the early phases of operation of ITER.

Runaway electrons

Runaway electrons are emitted during plasma disruptions and can reach energies of the order of tens of MeV [42]. These electrons will interact with the first wall materials (beryllium, copper, stainless steel or tungsten). As they do so, they will lead to the emission of very high energy bremsstrahlung photons, which will be capable of inducing photonuclear reactions, leading to the subsequent emission of photoneutrons [43].

Again, this neutron source is not relatively intense when compared to others, specially the DT plasma. However, it will be one of the most intense sources during the early phases of operation, with the H and He plasmas [39][44].

In conclusion, ITER will be exposed to neutron and photon fields with many different origins, intensities and energy spectra. In addition, due to the nature of the sources and the many penetrations of the facility, these radiation fields will spread throughout many different regions of the facility (many beyond the bio-shield) and will be present at different phases of the machine operation (i.e. plasma operation, maintenance activities and cask transfer activities). Consequently, neutron and photon fields lead to a variety of implications in ITER.

1.3.2 Implications of neutron and photon fields

The presence of neutron and photon fields in ITER will have a variety of implications. Some of the implications are positive and intended, while many others are not. The important thing is that, regardless of their positive or negative nature, radiation fields will lead to challenges in the design, license, operation and decommissioning of ITER. In this section, I will go through some of these implications. The goal is not to cover all of them, but to provide an

overview of implications that makes clear that nuclear analysis is an essential discipline in ITER.

I will start with those effects of radiation, particularly neutron radiation, that have positive implications.

As I mentioned before, future reactors will have to produce their own tritium to be self-sufficient. That is why one of the goals of ITER is to assess the performance of different tritium breeding technologies. As I explained before, such breeding technologies will be hosted in the TBM ports. Regardless of the specific approach, all breeding technologies will rely on the production of tritium through the irradiation of lithium with the DT plasma neutrons. Therefore, in this sense, neutrons clearly have a very important and positive role.

In addition, neutrons will be very useful in providing information regarding several essential plasma parameters [45]. Many neutron detectors will be located throughout the tokamak and count the number of neutrons that interact with them. Since the number of neutrons emitted by the plasma is linearly proportional to the number of DT fusion reactions taking place, counting the neutrons provides direct information about the fusion power or the tritium burn-up, among other parameters. Knowing the fusion power is essential to evaluate if the Q gain factor meets the ITER goals (i.e. $Q \geq 10$).

Finally, it is worth remarking again that, although ITER will not produce electricity, the energy carried by the DT plasma neutrons will be used in future fusion reactors to produce steam and, ultimately, electricity.

However, both neutrons and photons will have as well to the following negative implications, which will lead to problems that have to be tackled.

As they spread throughout the facility, neutrons and photons will modify the internal structure of the materials with which they interact, damaging them [46]. The main radiation damage mechanisms are ionization, atom displacement and impurity production (e.g. production of He or tritium gases); the latter two mechanisms being mainly due to neutron interaction. Radiation damage may significantly degrade the materials properties (physical and mechanical properties, thermal and electrical conductivity, etc), severely impacting the materials performance/purpose. In other words, radiation damage can lead to the deterioration and, ultimately, malfunction of ITER systems, structures and components.

For example, radiation damage affects diagnostics systems and components, such as mirrors, windows, bolometers or optic fibers [47], which are essential to control and analyze the plasma, in some cases for safety purposes. Electronics in general are also very sensitive to radiation [48]. Indeed, even when the electronics are exposed to relatively low levels of radiation, like those expected in remote regions of the Tokamak Complex, radiation can still lead to malfunction, false responses, failure, coloring or simply deterioration of the electronics. Again, some of the electronics are considered to be critical, as they are directly involved with safety aspects of the facility.

Therefore, radiation damage challenges both the successful and safe operation of ITER. Many efforts are put to mitigate its consequences, which rely on: (i) R&D activities to select and test materials that can withstand harsh radiation environments [47], (ii) planning periodical maintenance or replacement of components, (iii) relocation of the components in regions with lower levels of radiation and (iv) design of radiation shields.

Apart from the material damage that neutrons and photons will cause, they will also heat up the different ITER systems, structures and components. This is known as nuclear heat. In order to maintain the structural integrity of ITER SSCs, it is necessary to evacuate such nuclear heat. Thus, apart from designing the SSCs so that they efficiently evacuate the heat, in many cases cooling systems have to be designed and integrated.

Specially concerning is the nuclear heat in the superconducting magnets, and particularly in the Toroidal Field Coils [49]. Indeed, these components have to be cooled down to temperatures as low as $-269\text{ }^{\circ}\text{C}$ to correctly operate. The cryogenic system, which will circulate liquid helium through the magnets, has to be dimensioned to evacuate the nuclear heat generated in them. On the other hand, the blankets and vacuum vessel have to be designed to shield the magnets as much as possible from the radiation to minimize the nuclear heating in the magnets.

Another one of the most important negative implications of neutron and photon radiation is that it is a biological hazard. In order to guarantee a safe working environment in all areas where personnel will be present, ITER must achieve a design that is compliant with strict limits on the biological doses to be received by workers. Furthermore, it is mandatory to implement an ALARA program (As Low As Reasonably Achievable) to further reduce the exposure of workers below

those limits [50]. These are milestones in support of ITER licensing and commissioning and will be of high relevance for the future fusion reactors.

Workers will be exposed to radiation fields of different intensities during plasma operation, maintenance activities and cask transfer activities. During operation, the DT plasma and the activated water are specially concerning [51]. Indeed, until recently, the resulting radiation fields violated the radiological zoning of the Tokamak Complex and the radiation limits outside of it [52][53].

However, the highest and most concerning exposition takes place during the hands-on maintenance activities, after machine shutdown (i.e. no plasma). This is because, during these activities, workers get very close to regions of the machine that have been highly activated by neutron irradiation during machine operation. Thus, they get exposed to relatively intense decay photon fields. Not to mention that, in many cases, the maintenance areas are badly lighted, crowded with many systems, hence very difficult to access, and that operators have to wear special suits (e.g. bubble-suits) to avoid contamination (tritium, beryllium, activated dust), which reduce their mobility.

Reducing the intensity of the decay photon fields in these maintenance areas is very challenging. What is worst, it is even challenging to just fulfill the limits in these areas. The port interspaces are an example of these regions. They are subjected to a dose rate limit of $100 \mu\text{Sv/h}$ at 10^6 seconds (~ 12 days) after machine shutdown for planned hands-on maintenance activities [50]. However, currently many of them do not fulfill it [54].

Many efforts are put into limiting the exposition of workers to radiation during the different phases of operation. During plasma operation these efforts rely on designing and implementing shields, limiting access to certain rooms, relocating the position of penetrations through which radiation may escape, etc. During maintenance and cask transfer activities, apart from the previous measures, the efforts also rely on: considering low-activation materials, eliminating systems to avoid their maintenance, using temporary shields, planning and rehearsing the maintenance activities, etc. In some cases, like the NB Cell area, the radiation fields during maintenance are so intense and the area is so crowded with systems that the maintenance operations are fully carried out by remote-handling. This approach, however, is very sophisticated and expensive.

Finally, the last negative implication that I want to include here is the generation of radioactive waste as a consequence of the intense neutron irradiation. This radwaste will have to be adequately managed and stored to guarantee the safety of the workers and the public. For this, adequate planning and strategies have to be conceived [55].

Taking advantage of or mitigating, respectively, the positive and negative implications that I have just indicated is a very challenging design task in ITER. This is because ITER is a machine of unparalleled complexity, with very tight design margins. This means that adding any extra complexity, even if it is just a little, is already quite challenging. However, the complexity added in ITER due to the presence of radiation is quite meaningful. Indeed, radiation fields and sources, as well as their implications, extend all over the facility, beyond the bio-shield, and are present during all phases of operation (plasma operation, maintenance activities and cask transfer activities). We also have to keep in mind that the closest facility to ITER is JET, and JET is far simpler and has a neutron budget $1.5 \cdot 10^6$ times lower. Therefore, although many radiation problems are common to other facilities, ITER radiation problems are quite unique in many ways. Not to forget that some radiation sources, like the activated water, are more problematic in ITER than in conventional fission reactors [26][29].

1.4 ITER nuclear analysis

To face the design challenges derived from the presence of radiation in ITER it is necessary to rely on the engineering discipline of nuclear analysis [56]. Nuclear analysis allows to characterize the radiation fields, as well as the processes they lead to. Thanks to this discipline it is possible to: estimate the amount of tritium produced by a certain TBM concept (see Figure 1-20), support the calibration of neutron detectors with the required accuracy, calculate the nuclear heating in the superconducting magnets, evaluate the radiation damage in the diagnostics components, foresee the amount of dose received by workers while maintaining a port interspace, etc. Thus, nuclear analysis provides very valuable information that is key to guarantee the successful and safe operation of ITER. In the context of this thesis, ITER nuclear analysis is the field of knowledge within which the thematic of this thesis falls.

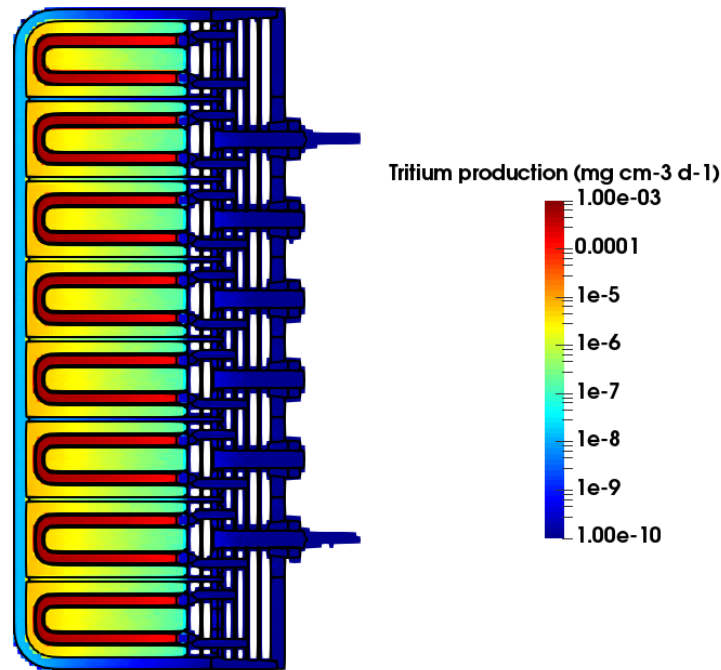


Figure 1-20. Example of tritium production ($\text{mg}\cdot\text{cm}^{-3}\cdot\text{d}^{-1}$) map in a TBM concept.

1.4.1 Activation and radiation transport calculations

ITER nuclear analysis is essentially based on the performance of activation and radiation transport (or neutronics) calculations with the goal of computing diverse nuclear responses (flux, nuclear heat, dpa, gas production, specific activity, damage, doses, etc). There are many codes that have been developed for these purposes, primarily for the fission industry, but also for fusion facilities.

With regards to the activation, ACAB [57] (which was developed by my codirector Javier Sanz) and FISPACT-II [58] are two of the reference fusion inventory codes to be used in ITER [59]. With respect to the radiation transport, Denovo [60], Attila [61], Serpent [62] and MCNP [63] are examples of codes used in ITER. The first two radiation transport codes mentioned use deterministic methods to solve the Boltzmann transport equation while the last two rely on Monte Carlo methods. MCNP is the ITER reference code for radiation transport simulations [59].

Both activation and radiation transport codes have to be provided with nuclear data to be able to simulate the physical process of the interaction of radiation with matter. Dedicated libraries have been developed for this purpose, being

EAF2007 [64] and FENDL-3.1d [65] two of the ITER reference nuclear data libraries for activation and radiation transport simulations, respectively [59].

I will now present MCNP and the nature of Monte Carlo codes in a bit more detail due to their relevance in the context of this thesis.

Monte Carlo N-Particle (MCNP)

MCNP code has been extensively validated and used for many years to assist the nuclear design of many fission and fusion facilities worldwide. It is in continuous development at Los Alamos National Laboratory since before 1977.

MCNP allows to simulate the kind of radiation transport problems required in ITER, which: involve neutral particles (i.e. neutrons and photons), are time-independent and require complex 3D geometry and source models. Furthermore, being a Monte Carlo code, it allows to perform such simulations with a higher degree of accuracy than deterministic codes. Indeed, it allows for a point-wise resolution in both space and energy.

MCNP, and all Monte Carlo codes, rely on the simulation of individual particles to record some aspects (tallies) of their average behaviour. The average behavior of particles in the physical system is then inferred (using the central limit theorem) from the average behavior of the simulated particles [66]. Provided that the computational models (sources, geometry, nuclear data, etc) are 100% accurate, the quality of the inference (that is, the quality of the result of interest) only depends on the number of histories simulated. In other words, the larger the number of particles simulated, the lower the statistical uncertainty. However, the statistical error is inversely proportional to the square root of the number of histories. That is, many histories have to be simulated to achieve a significant reduction of the error. Therefore, Monte Carlo calculations can be very computationally demanding. This is the main drawback of MCNP and all Monte Carlo codes.

1.4.2 Complexity of ITER nuclear analysis

Activation and radiation transport calculations have been carried out in the fission industry for many years. Thus, many codes and methodologies have been developed and used for that end. However, the performance of this kind of computational simulations in fusion facilities is relatively recent. Therefore, although specific codes and methods have been developed to address the

particular needs of these facilities, still many of the codes originally developed for fission, like MCNP, are applied in fusion facilities. This has caused the appearance of many new challenges in the field, hence making nuclear analysis of fusion facilities, and particularly of ITER, significantly complex.

In essence, the complexity of ITER nuclear analyses derives from the need of producing, and running simulations with, very detailed 3D neutronics models of intricate geometries and radiation sources.

The reasons for such need of detailed models are the following.

The first reason is that ITER nuclear analyses are subjected to very high quality and accuracy requirements. That is, the uncertainties in the nuclear responses need to be minimal. This is because ITER is a very complex machine, with very tight design margins, and nuclear analyses are the basis of many decisions that affect technical, economical and safety aspects.

We have to keep in mind that, as I mentioned before, there are many cases in which the nuclear responses of concern are very close or above the imposed requirements. This is the case of the doses in the port interspaces. Having reliable information to decide which are the optimal measures (e.g. shields) to fulfil the requirements is crucial to minimize the impact on the ITER design. Not to mention that ITER has to demonstrate to the French Nuclear Safety Authority (Autorité de Sûreté Nucléaire, ASN) that it will fulfil all safety requirements. This demonstration has to be justified on the basis of sound and reliable nuclear analyses.

The second reason is that ITER geometries and sources are full features that highly impact the nuclear responses. Geometries are full of gaps and penetrations (i.e. streaming paths) and have a highly heterogeneous configuration of materials with different absorbing/moderating properties. On the other hand, ITER radiation sources have very intricate geometrical configurations and (intensity/angular/energy) emission distributions, like I showed in the case of the activated water. Therefore, ITER geometries and radiation sources need to be modelled in very high detail to be able to capture all these features. Otherwise, unquantified uncertainties due to modelling approximations are introduced in the final responses.

Producing models of ITER geometries and radiation sources is very costly. It requires a lot of human time as well as the development of dedicated

computational methodologies and tools [67]. Furthermore, once produced, these models are very heavy computationally speaking, what makes them very difficult to handle. In some cases they are so heavy that it is impossible to run simulations with them.

On the other hand, even when they are light enough to be used, running radiation transport calculations with such models is as well a very complex and computationally demanding task. This is because, given the nature of ITER geometries, ITER radiation transport problems combine intense shielding with a rich profusion of streaming paths. Thus, these problems require the simulation of many histories to adequately penetrate the shields and sample the streaming paths. Furthermore, as happens in many ITER problems, it is normally necessary to achieve low statistical uncertainties in a broad region of the problem phase-space (e.g. neutron flux with energy resolution in a large area). This requires the simulation of even more histories. As a result, ITER radiation transport problems are very computationally demanding in terms of computational time.

In order to be able to solve this kind of problems in a feasible amount of computational time, it is necessary to rely on the parallelization of calculations in High Performance Computing (HPC) facilities and on the use of variance reduction (VR) techniques. The latter are techniques that are aimed at favouring the simulation of those particles that contribute more to the response of interest, while disregarding the simulation of those particles that are not as contributing. In this way, lower statistical uncertainties are obtained with the simulation of less histories. However, VR techniques are not infallible and are problem dependent, what requires user experience. Furthermore, some of the techniques, like those based on weight windows, may lead to the exacerbated production of tracks (i.e. long history problem), which may significantly detriment the efficiency of the calculations, or even make them impractical. Thus, although sophisticated VR algorithms have been developed, special care must be taken when using them.

To face the continuous demand of the ITER project of nuclear analyses of such complexity, the ITER nuclear analysis division has developed, over the years, a strategy [68][69]. One of the main pillars of such strategy is allowing many international institutions to efficiently participate, in a coordinated manner, in the ITER global neutronics effort. In other words, this strategy has gathered an

ITER neutronics community. This community has managed to make continuous joint efforts to face the complexity of ITER nuclear analyses over the years. Computational methodologies, codes and models (geometry models, nuclear data libraries, radiation source models, etc) have been improved to be able to perform faster and/or more accurate nuclear analyses [67]. In this way, the challenges posed by ITER nuclear analyses have been progressively tackled and, as a result, this field has been taken to the next level in terms of realism and accuracy. However, still, there are and there will be many more challenges to be faced.

1.5 Motivation and objectives of this thesis

There are several aspects involved in an ITER nuclear analysis, the most relevant being: codes, methodologies and computational models (geometry models, nuclear data libraries, radiation source models, etc). As I have just said in the previous section, each of these aspects is in constant evolution and improvement with the goal of making ITER nuclear analyses faster and/or more accurate. That is why the Instructions for Nuclear Analysis [59] has been updated several times over the last years. These instructions are the ITER official document that indicates the specific codes, methodologies and computational models to be considered for ITER nuclear analyses.

In this thesis, I have focused my interest on one of the aspects of ITER nuclear analysis: the geometry models of the ITER Tokamak, the so-called ITER Tokamak reference neutronics models. These reference models are the result of many joint efforts from the neutronics community and they have efficiently allowed to address many of the project's neutronics needs over the years. Thus, they have played an essential role in the ITER neutronics strategy. Their evolution goes from the very first and simple 3D models (BRAND model [70][71], 2000), to the current detailed 3D C-model [72] and NBI [73] MCNP models, which are made of thousands of bodies and material definitions.

In that process, reference models have reached an unprecedented level of detail. Indeed, current reference models represent the high degree of material heterogeneity of the machine as well as the majority of gaps and penetrations with a high degree of realism. This level of detail is necessary to minimize as much as possible the uncertainties introduced in the nuclear responses due to modelling approximations.

The approach followed in ITER when producing reference models has always been, except few exceptions [74], to represent a portion of the machine instead of the complete tokamak. In other words, the majority of reference models have always been partial models. Specifically, partial models represent explicitly a toroidal section of the machine and the rest is implicitly represented by means of either periodic or reflective boundary conditions. The current C-model and NBI models are partial. They represent 40° and 80° toroidal sectors of the machine, respectively.

The reasons for producing partial models instead of full models are basically three.

First of all, given that the size of a partial model is smaller than the size of a full model, a lower number of histories is needed to flood the geometry with particles. This means that if we want to reach the same statistical uncertainties in a nuclear response with a 40° and 360° model, the partial model would require 9 times less histories. This is an important advantage since, as we have seen, ITER radiation transport problems are very demanding computationally.

To understand the second reason why reference models are partial we have to understand, first, that as models are more detailed, they become heavier computationally speaking. That is, they demand more RAM memory and more, loading-, plotting- and simulation-time. Consequently, models become very difficult to manage, review and update. Not to mention that calculations take even more time with them. Thus, partial models are comparatively easier to handle than full models. This allows to reduce the time spent performing a nuclear analysis.

Having said this, the truth is that current reference models are so detailed that they have pushed to the limit the capacities of currently available codes and computational resources. This does not only mean that current partial models are already very difficult to handle, but that producing a full model with the same degree of detail is simply unfeasible. In fact, certain nuclear analyses are already unfeasible with current reference partial models.

Finally, the third reason is that partial models require less modelling efforts to be produced than a full model.

Now, the interesting question here is: Does using partial models to represent the ITER Tokamak come at any cost? With partial models, the full machine is

represented by means of reflective or periodic boundary conditions. Thus, the assumption is made that the machine has a toroidal symmetry. However, as can be inferred from section 1.2.2, it is clear that this is not the case. Indeed, ITER ports are very different from each other, hence, not symmetrical at all. This means that with partial models we are not capturing the machine asymmetry beyond the area explicitly represented. However, it is not possible to predict whether the asymmetry of the machine can have an impact or not on the nuclear responses. Thus, partial models introduce unquantified uncertainties in the nuclear responses estimated.

Given the high constraints on the quality of ITER nuclear analyses, the uncertainties introduced by partial models may be intolerable. Yet, although specific approaches have been implemented to reduce these uncertainties, not much research has been done to fully understand their potential repercussions. There are surely many reasons for that to be the case. Probably, however, one of the most plausible reasons is that, given the already high complexity of partial models, there has not been much more (computational) room for improvement. However, recent computational advances developed at different institutions, including the TECF3IR research group at UNED, changed the paradigm regarding the limits of the geometry modelling. Motivated by these advances, me and my directors wanted to analyze, understand and solve, if possible, the abovementioned implication, as well as others, derived from the partial nature of ITER reference models. Specifically, in this thesis I have pursued three main objectives:

- Objective #1: Review the geometry modelling methodologies of the ITER Tokamak and identify limitations of partial models.
- Objective #2: Taking advantage of recent computational advances, propose and develop a solution to mitigate the limitations identified.
- Objective #3: Analyze and test the solution proposed in order to evaluate its effectivity in overcoming the limitations identified.

I would like to proudly advance here that the outcome of this thesis has been very successful. Indeed, it has opened the door to a new way of modelling the ITER tokamak, with an unprecedented degree of realism. Not only that, thanks to the work presented here it is now possible to perform ITER nuclear analyses that were not feasible before. In fact, such has been the success that part of the

content of this thesis was published in January 2021 in the prestigious Nature Energy journal:

- R. Juarez, G. Pedroche, M.J. Loughlin et al, “A full and heterogeneous model of the ITER tokamak for comprehensive nuclear analyses”, Nature Energy 6, 150–157 (2021).

1.6 Structure of this thesis

The remaining part of this thesis comprises five more chapters.

Chapter 2, titled “State of the art”, is dedicated to the Objective #1 of this thesis. I review the geometry modelling methodology in ITER, with special focus on the geometry models of the ITER Tokamak, the so-called reference models. I also identify limitations of the current partial models, focusing on specific ITER-relevant applications. Finally, I also go through the recent computational advances that motivated this thesis and provided us with a pathway to overcome the limitations identified. In short, this chapter contextualizes this thesis and further motivates its purpose.

Chapter 3, titled “E-lite”, is dedicated to the Objective #2 of this thesis. It describes the proposal of this thesis to solve the limitations identified, namely, the development of a 360° model, called E-lite. In this chapter I go through the main features of E-lite and the methodology to produce it. I also demonstrate that the model is a feasible and usable solution for ITER nuclear analyses.

Chapter 4, titled “Calculations and evaluation”, is dedicated to Objective #3 of this thesis. Therein, I evaluate the effectiveness of the solution proposed in overcoming the limitations identified. I apply E-lite in three different applications identified in Chapter 2 and I compare its performance with respect to other approaches relying on partial models. The goal of this chapter is to demonstrate that E-lite is not only feasible and usable, but also useful, and in some cases completely necessary, to tackle the challenges associated to specific ITER nuclear analyses.

Chapter 5, titled “Impact of this thesis”, reviews the impact of this thesis. On the one hand, and most importantly, I focus on the impact of E-lite on the ITER project. Specifically, I indicate specific nuclear analysis of relevance for the ITER project in which E-lite has been (or is going to be) applied. These applications show that E-lite’s repercussion extends beyond the context of this thesis and

that, indeed, the model represents a research product well-received by the ITER neutronics community. On the other hand, I take the chance to briefly indicate other contributions in the context of ITER nuclear analysis to which this thesis has led. These contributions are not directly related to E-lite, but they have indirectly contributed to the objectives of this thesis. In addition, some of these contributions have also been considerably important for the ITER project. Particularly, I put special emphasis on those works in which I have participated and that were highly recognized and/or published in journal articles.

Chapter 6 is the last one and is dedicated to the “Conclusions and future work”.

CHAPTER 2

STATE OF THE ART

In this chapter, I am going to finish contextualizing and motivating the purpose of this thesis. Specifically, in the coming sections I am going to:

- Section 2.1. I will review the general features of the neutronics modelling of ITER geometries, with special focus on the geometries of the ITER Tokamak. This section will be useful to understand why ITER Tokamak reference models exist and why they have been partial so far.
- Section 2.2. I will describe the main features of the ITER Tokamak reference models that are used in current ITER nuclear analyses. In addition, I will briefly describe how they have evolved over the years until reaching an unprecedented level of realism.
- Section 2.3. I will explain which are the limitations of the current ITER Tokamak reference models that have been identified in this thesis. Furthermore, I will identify ITER relevant applications which may be severely affected by these limitations.
- Section 2.4. I will go through the recent computational advances that motivated this thesis and provided us with a pathway to overcome the limitations identified.

2.1 On the neutronics modelling of ITER geometries

In this section I am going to review the current status and general features of the neutronics modelling of ITER geometries. Particularly, I am going to cover in a bit more depth the reasons why ITER models have to be so detailed (section 2.1.1). Then, I will describe the general methodology followed currently in ITER

to produce such detailed models (section 2.1.2). Finally, I will explain the problematics of producing such detailed models (section 2.1.3).

This section will be useful to understand why ITER Tokamak reference models exist and why they have been partial so far.

2.1.1 The importance of producing detailed geometry models

Producing a neutronics model of a geometry requires specifying: its shape, the materials from which is made of and the mass of the different materials. All these aspects impact the number and type of interactions between the radiation and the matter. That is, these aspects determine how radiation is going to propagate through the medium and the effect of radiation on it.

This means that any deviation from the reality in the shape, materials or masses of the model leads to deviations in the nuclear responses that are computed with the model. Of course, the degree of deviation in the responses depends on many factors: the nature (shape, material, mass) and amount of deviation from the reality and the features of the problem under study (i.e. neutron/photon source, nuclear response of interest, etc).

For example, the content of Co impurities in a stainless-steel shield is irrelevant regarding its neutron shielding performance. However, the Co content is crucial if we are interested in knowing the doses received by a worker due to the activation and decay of that same shield.

However, it is very difficult to predict the impact on nuclear responses of the deviations introduced in the geometry models. And when geometries are as complex as those of ITER, these predictions are simply impossible. As a result, deviations in the geometry models introduce uncertainties in the nuclear responses, which cannot be quantified.

ITER geometries are full of gaps and features that lead to streaming paths. They are also characterized for presenting intricate material arrangements, which combine materials with different moderating/absorbing properties (i.e. components made of steel that contain cooling water channels). As I will show below, these are aspects that highly affect the nuclear responses. That is, if they are not accurately represented in a neutronics model, they can lead to significant deviations in the nuclear responses, which cannot be predicted. Therefore, to minimize the uncertainties due to geometry modelling

approximations, which is a requirement in ITER nuclear analyses, neutronics models have to be as faithful to the reality as possible.

Particularly, in this subsection I want to give evidence of the impact that streaming paths (i.e. gaps, penetrations), as well as the accurate representation of the material heterogeneity, can have on ITER nuclear responses. There is a significant amount of literature on this topic [75]–[82]. We will have a look now at the main conclusions of some of these studies. These will serve as examples to better understand the importance of producing very realistic and detailed models in ITER. All this discussion applies to ITER geometries in general, but it is especially oriented towards the geometries of the ITER Tokamak.

In [75], they highlight the importance of streaming paths regarding the shutdown dose rates (SDDR) in the port interspaces of diagnostics ports. Particularly, they identify four main contributors to this quantity: streaming through the port plug gaps and systems, streaming through the gaps between the port plugs and the vacuum vessel port extension, cross-talk from neighbouring ports and streaming through areas of reduced shielding in the blankets and vacuum vessel. Three of these contributors involve the streaming through gaps or low shielding regions. In addition, they also report the differences between considering only one labyrinth (i.e. dog-leg) or two in the space between the port plugs and the blankets and vacuum vessel port extension [76] (see Figure 2-1). Considering just one labyrinth led to around 400 $\mu\text{Sv/h}$ at the front of the interspace of the analyzed port; considering a double-labyrinth led to 140 $\mu\text{Sv/h}$. Finally, in that same study, already 65 $\mu\text{Sv/h}$ on the interspace (that is, 65% of the SDDR requirement on the interspaces at 10^6 s of cooling time) are attributed to the streaming effects through areas of low shielding in the blankets.

On the other hand, the study conducted in [77] analyzes the impact of the size of the vertical and horizontal gaps between the blanket modules. These gaps are necessary for the assembly of the blankets and other technical constraints, but they lead to a radiation streaming towards the inboard legs of the toroidal field coils, which are located behind the vacuum vessel. Consequently, a significant amount of nuclear heat is deposited on the toroidal field coils, which must be known and limited to guarantee its adequate removal and the maintenance of the magnets's superconductivity. Varying the size of the horizontal and vertical gaps between the blankets from 2cm to 1cm led to a decrease of 30% on the

total integral nuclear heat deposited on the inboard legs and of 40% on the peak values.

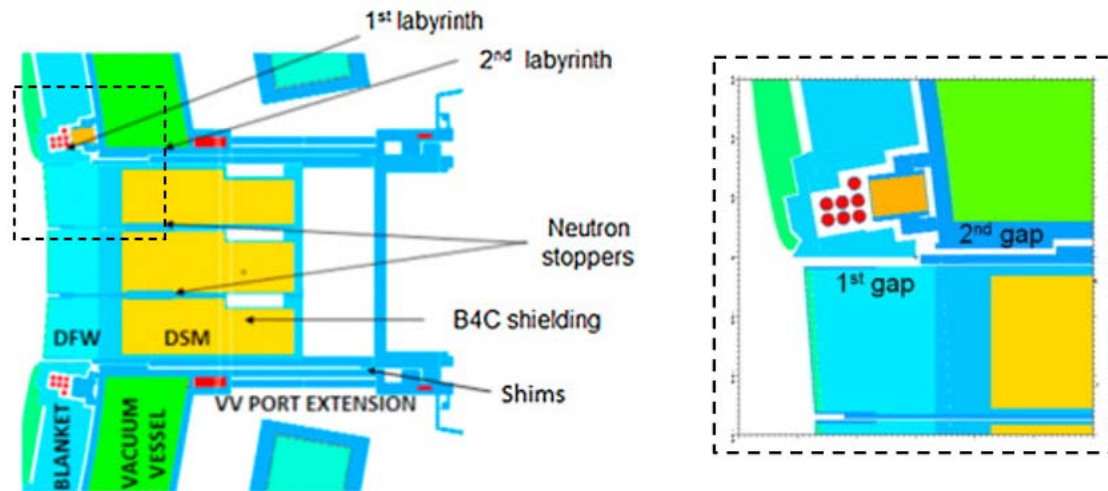


Figure 2-1. Schematic view of the double-labyrinth in the space between the port plugs and the blanket and vacuum vessel port extension [75][76].

The two previous studies mainly underline the importance of gaps and penetrations in ITER. Since they are obvious streaming paths, it is clear that changes in their sizes and/or configuration can lead to important variations in the nuclear responses. The following two studies highlight the importance of explicitly representing the heterogeneous material configurations of ITER. To do so, they assess the impact of the modelling approximation known as material homogenization.

Specifically, material homogenization is used in many occasions to simplify the level of detail of geometries. When using this modelling approximation, the bodies of different materials are combined to form a homogeneous volume, normally with a simple geometrical shape, made of a material mixture. The total mass within the homogeneous volume is preserved. To do so, the density and chemical composition of the material mixture is derived as a combination of the densities and chemical compositions of the independent materials, which are weighed by their corresponding volume fractions within the total homogeneous volume. In Figure 2-2, I show an example of homogenization of a blanket module. In that example, all the different bodies of a blanket module are simplified and reduced to two simple geometrical bodies made of two material mixtures.

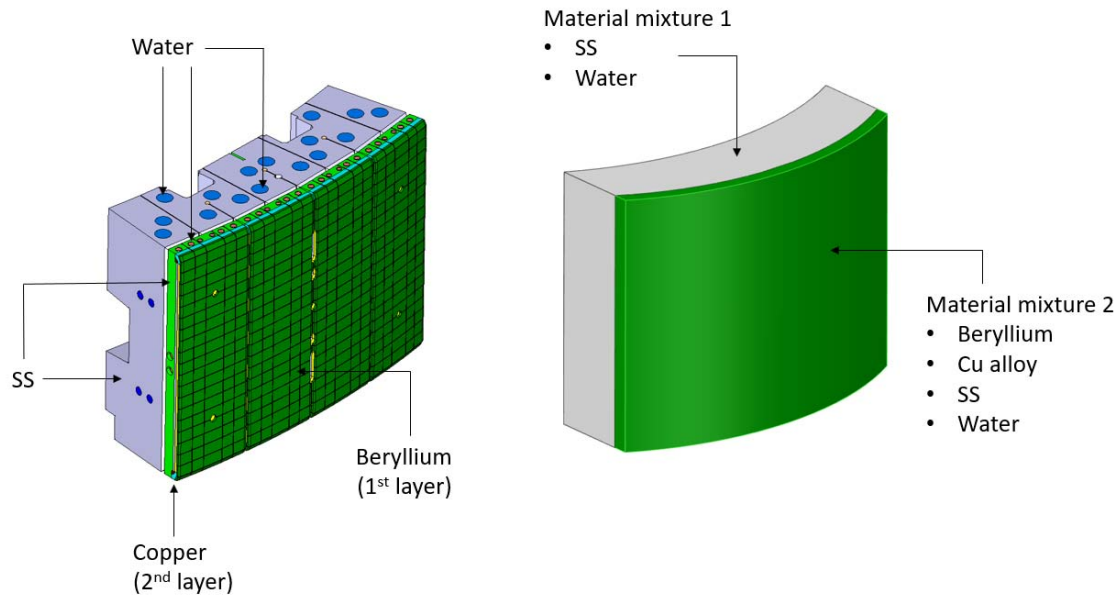


Figure 2-2. Example of homogenization. Detailed (left) and homogenized (right) models of a blanket module.

In [78], they analyze the effect of material homogenization of a blanket module (i.e. BM#04) on the nuclear heating deposited on the blanket components and the portion of the vacuum vessel behind it. The nuclear heating on the blanket components was reported to be 11-70% higher, depending on the component, when a homogenized blanket model was considered instead of an heterogeneous one. On the other hand, the average nuclear heating deposited on the vacuum vessel right behind the central region of the BM#04 was reported to be 76% lower when a homogenized blanket was considered. Furthermore, the peak nuclear heat values that were observed on the vacuum vessel when the detailed blanket model was considered were not observed when the homogenized blanket was considered. At those peak locations the nuclear heat is, therefore, underestimated by 86% when the homogenized blanket model is considered.

Of great interest is as well the shielding analysis reported in [79], which makes an exhaustive investigation on the effect of homogenizing steel and water when considering different simple configurations of water-steel layers and pipes (see Figure 2-3). The analysis concludes that, in all the cases studied, heterogeneous configurations show poorer shielding performance than the equivalent homogeneous ones. It is also observed that the ratio between the shielding performances (i.e. attenuation at the back of the steel-water shield) of the homogeneous and heterogeneous cases decreases and tends to an asymptotic value as the size of the layers/pipes decreases (and the number of layers/pipes

increases). The critical size of the layers/pipes below which the asymptotic behaviour of the ratio is observed coincides more or less with the average mean free path of the neutrons through the medium.

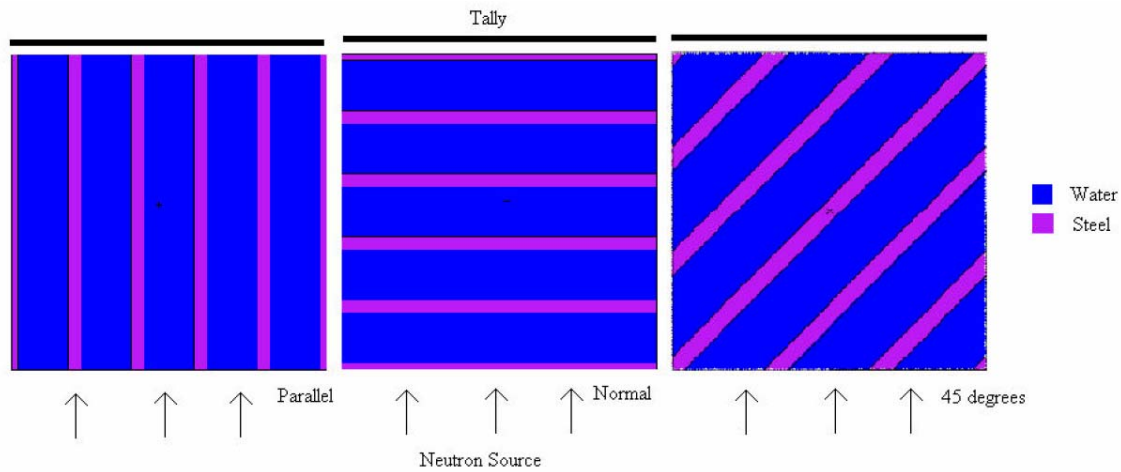


Figure 2-3. Cross-sections showing the orientations of the pipes/layers studied in [79]: parallel (left), normal (centre) and at 45° to the flux (right, pipes only).

The asymptotic value of the ratio, however, depends on the orientation of the pipes/layers with the respect to the incident flux. When the pipes/layers are normal with respect to the incident flux, the asymptotic value of the ratio is approximately 1, that is, the heterogeneous shield has almost the same shielding performance as the homogeneous one. On the other hand, when the pipes/layers are parallel to the incident flux, the asymptotic value is approximately 4, that is, the heterogeneous shield has a shielding performance 4 times lower than the homogeneous one. This is attributed to the streaming effects through the water channels, which are less absorbent than the steel.

Of course, the impact of material homogenization depends on how different (from a neutronics point of view) the homogenized materials are, the size of the homogenized region and its location in the problem under study, etc. Nonetheless, since it is not possible to accurately predict the impact of homogenization on the nuclear responses of interest, this modelling approximation always introduces uncertainties in the results, which cannot be quantified.

Hopefully, it is now a bit clearer why ITER geometries are modelled in as much detail as possible, that is, considering all gaps and penetrations and preserving the material heterogeneity.

In the next subsection I will explain how ITER geometries are modelled.

2.1.2 Current methodology to model ITER geometries

In this subsection I will explain the current methodology that is followed in ITER nuclear analyses to model an ITER geometry (e.g. a blanket, a port plug, a divertor cassette, etc) with as much detail as possible. This methodology has been consolidated in ITER for the last two decades. It allows to produce very realistic neutronics models by working directly with the CAD models of the components.

Before describing the methodology, I will indicate how geometries are modelled in MCNP format and then present the agents that make the current modelling methodology viable, i.e. CAD-to-MCNP tools, CAD programs and HPC facilities.

MCNP geometries

In MCNP, the geometries are traditionally modelled using the Constructive Solid Geometry (CSG) technique. In this approach, the bodies of the geometry, called cells, are defined as combinations of regions bounded by first- and second-degree surfaces and fourth-degree elliptical tori. Specifically, cells are defined by unions, intersections and complements of the regions bounded by the surfaces. Then, the corresponding materials (or void) and densities are assigned to the cells.

In addition, since the release of MCNP6, it is also possible to define geometries by means of unstructured meshes (UM), generated with programs like Abaqus [83]. However, although investigated [84], the production of geometries following this approach is not yet consolidated in ITER.

The geometry definition, together with the rest of parameters of the radiation transport problem, are provided in an input text file that is later read by the code.

CAD-to-MCNP tools

In the last two decades, CAD-to-MCNP conversion tools such as SuperMC [85][86] (former MCAM [87]) or McCad [88] have been developed. These tools opened the door to a new paradigm of 3D geometry modelling in ITER. They allow to automatically convert CAD models of ITER systems, structures and components (SSCs) into MCNP input files, in CSG format.

These CAD models embody the latest approved and available geometrical description of the SSCs design. Thus, the level of realism and fidelity that can be achieved in the machine representation thanks to these tools is outstanding (see Figure 2-4).

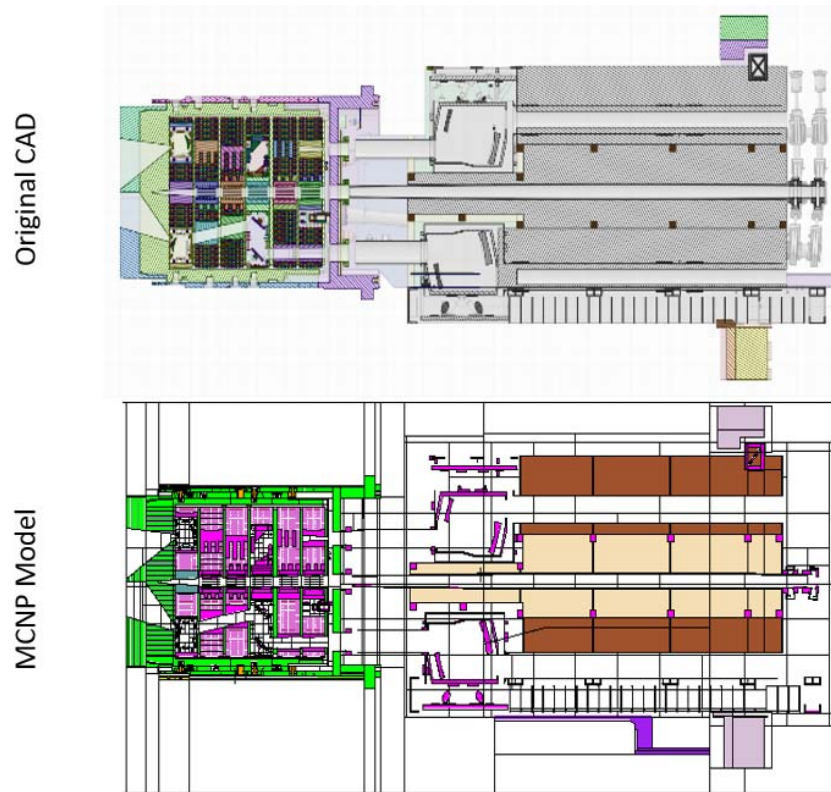


Figure 2-4. Vertical cross-sections of the original CAD (top) and MCNP (bottom) models of EP#11.

Before this kind of tools existed, ITER geometries, including the first reference models of the tokamak [70][71], were modelled by hand directly in MCNP format. This was a very hard task, which required lots of human efforts and time. By reading [69], one can infer that producing a model of around 2800 cells was considered as a singular feat at that time. Nowadays, however, 3D models are routinely made of tens of thousands of cells and surfaces and hundreds of materials. Reaching that same level of complexity by hand modelling would require an unfeasible amount of time and human resources.

Consequently, these tools, specially SuperMC [85][86], have been of great utility for the ITER neutronics community and they are currently used to model almost all the ITER geometries of relevance [72][89].

CAD programs

CAD programs such as Spaceclaim [90] are essential to manipulate the CAD models before their conversion into MCNP. They essentially allow to perform the preprocessing activities that I will describe below.

HPC facilities

The increased accessibility to High Performance Computing (HPC) infrastructures has also been crucial to be able to produce very detailed neutronics models. Indeed, detailed models are very computationally demanding. Thus, HPC infrastructures, such as Marenstrum [91] or Marconi [92], have allowed to run huge parallel Monte Carlo simulations with such computationally demanding models and in dramatically shorter times than desk or smaller-scale clusters.

The methodology

Despite the many computational advances of recent years, producing a neutronics model of an ITER geometry is not a trivial task. There are several activities that have to be carried out prior to and after conversion of a CAD model into MCNP format. These activities, as I will indicate in the next subsection, still require many human resources.

Specifically, the methodology to produce a neutronics models of an SSC comprises the following steps:

Reception and clarification of information

Firstly, CAD files, material information (i.e. chemical compositions and densities) and any other additional indications are sent by IO to the institution in charge of producing the neutronics model.

After reception, IO and the institution clarify all the input data (missing data, inconsistencies, etc) and any modifications and decisions are recorded.

Preparation of 3D CAD models for translation into MCNP

The CAD models have to undergo a process of preparation-for-translation in which:

- Unnecessary details for nuclear analysis are removed. For example, fillet edges, small holes for the screws, etc (see Figure 2-5). Leaving these details leads to a significant increase in the complexity of models.

However, the impact on the nuclear responses of removing them can be advanced to be negligible due to the relatively small deviation from the real geometry. Of course, experience and good judgment is required for this task.

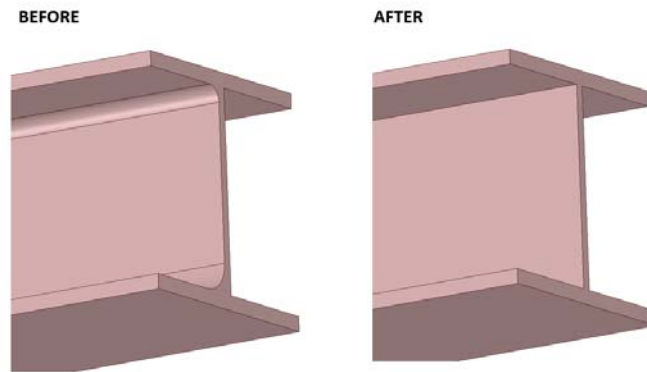


Figure 2-5. Example of the kind of unnecessary details for the nuclear analysis that are removed.

- Complex bodies are split into simpler ones (see Figure 2-6). This facilitates the conversion of the bodies into MCNP format and makes the transport process more efficient.

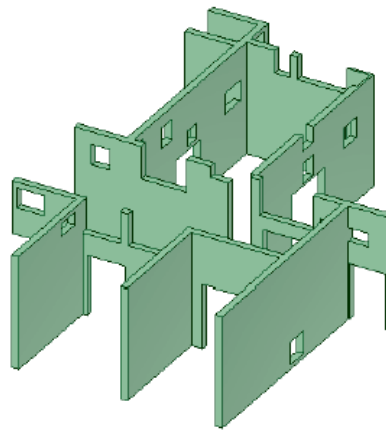


Figure 2-6. Example of a complex body that has to be split prior to its translation to MCNP format.

- Surfaces that cannot be handled by MCNP are replaced by others. For example, SP-lines like those shown in Figure 2-7 have to be replaced by other types of surfaces (e.g. planes).

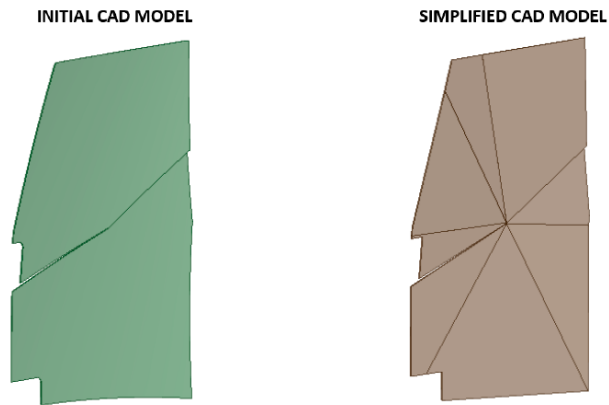


Figure 2-7. Example of a body (mirror) that is mainly made of *sp*-lines, which are approximated by planes.

- Interferences/clashes in the geometry are resolved (see Figure 2-8). Otherwise, they lead to errors in the geometry definition of the MCNP models that can cause the so-called lost particles. That is, particle histories whose simulation is interrupted because the particle reaches a region of the space that is occupied by two cells at the same time. This kind of errors do not allow to correctly sample the complete geometry, therefore, they affect the quality of the responses.

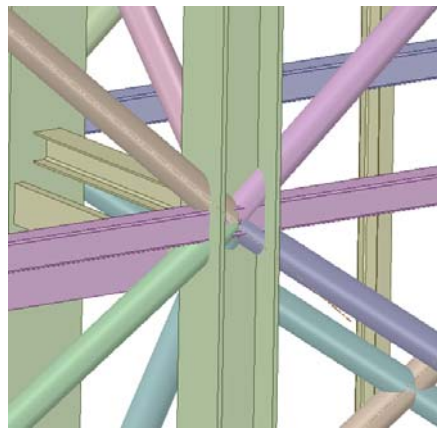


Figure 2-8. Example of the kind of clashes that may be present in the original CAD models.

- The different CAD bodies are grouped/colored for different purposes. Normally, bodies made of the same material are grouped together. This facilitates the later tasks of assigning materials to the cells in the MCNP input or identifying specific components.

In this process is where the CAD tools, like SpaceClaim [90], are used. The above are general steps for the CAD preparation. Each case may present its own particularities.

Once this process is finished, visual inspection of all the modifications is required for Quality Assurance purposes. In addition, any changes in the volume of the bodies must be recorded as well. This information is necessary to derive density correction factors which are later applied to the MCNP cells to preserve the total mass of the original bodies.

Conversion into MCNP

Once the CAD model is prepared, the CAD-to-MCNP tool is then used to convert the CAD model into MCNP format. At this stage, comments are generally assigned to the groups of CAD components using the CAD-to-MCNP tool. In this way, the different components can be easily identified in the MCNP input.

The conversion is normally performed using the “automatic void generation” option of the CAD-to-MCNP tools. This option creates void cells (i.e. cells with no material) that cover all the regions of the model domain that do not have CAD bodies. In other words, these cells fill in all the empty space up to the graveyard (i.e. the region of the models where the particle tracks are intentionally killed). Defining all regions of the model univocally is necessary to perform the transport with MCNP. Otherwise, undefined regions lead to lost particles.

Verification

Once the MCNP input of the geometry of interest is generated, several inspections are carried out to guarantee that it correctly represents the original SSC. This includes:

- Making 2D MCNP plots of the geometry and comparing them with the same 2D cross-sections of the prepared CAD model (see Figure 2-4).
- Running calculations in void mode to detect geometry errors that lead to lost particles. As I explained above, these errors may be the result of interferences/clashes that were not identified in the CAD-preparation phase or that arise due to the conversion process. In addition, the conversion process can also lead to the appearance of small undefined regions of the geometry that are not covered by any cell. The interferences/clashes are solved by subtracting one cell from another. On the other hand, specific cells have to be produced to fill in the regions that were not covered by any cell.
- Performing volume checks to verify the conversion process. Particularly, the volumes of the cells of the MCNP input are measured (stochastically)

and compared with the volumes of the CAD bodies as measured by the CAD-to-MCNP tool (see Figure 2-9). This kind of checks allows to identify conversion errors that lead to significant deviations in the shape of the original bodies.

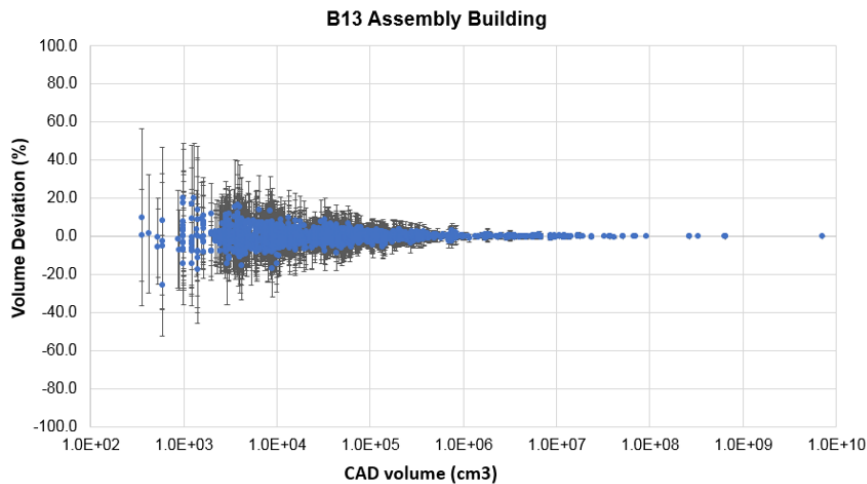


Figure 2-9. MCNP/CAD cell volume deviation (%) per cell as a function of the CAD volume (cm³).

Material and density allocation

Once the MCNP input is ready, materials and densities are allocated to the cells by means of verified automated scripts. If needed, any necessary density correction factors are applied to reflect the correct volume/mass of the components. The assignment of the materials and density correction factors is done on the basis of the comments that the cells have.

On the other hand, the chemical compositions of the materials are defined in MCNP format.

Again, 2D MCNP plots are performed to verify that the material allocation was carried out correctly. In addition, independent verifications of the material chemical compositions are carried by an independent analyst.

Integration

If necessary, the MCNP model of the SSC of concern is integrated in a bigger MCNP model. This normally happens with the SSCs that belong to the tokamak. Specifically, the MCNP models are integrated in already existing MCNP models of the tokamak, the so-called reference models, subject of section 2.2.

This general methodology applies to all ITER geometries, including the geometries of the tokamak's SSCs. Of course, there are variations of it whenever is required. More information on the ITER geometry modelling methodology can be found in the PhD. thesis of my colleague Antonio Jesús López-Revelles [23].

2.1.3 The problematics of modelling ITER geometries

The previous modelling methodology has been consolidated in ITER nuclear analyses for the last two decades. Despite this fact, the production of ITER neutronics models is still one of the main reasons why ITER nuclear analyses are so complex. This is because modelling ITER geometries is a very demanding task in terms of human resources. Furthermore, ITER neutronics models are very computationally demanding. We will now have a look at both of these aspects and their implications.

High demand of human resources

Carrying out all the steps of the above methodology to produce an ITER neutronics model requires a lot of human time. The following are some of the most demanding steps.

I will start with input data clarification. In many cases, this process is not straightforward and requires several interactions between IO and the institution in charge of the modelling. Sometimes, this is because the design of the components modelled is not mature enough. Therefore, assumptions and decisions have to be reached when the material information, the mass or even the shape of the components is not clear. In other cases, the shape of the model is clear, but it is not reflected in the CAD models provided. Consequently, modifications on the input CAD models have to be implemented to reflect the actual design.

The preparation of the CAD models for conversion into MCNP format is also a very demanding step. This is because geometries comprise many bodies which are full of details to be removed, splines to be replaced, interferences to be resolved, etc. Bodies like the one shown in Figure 2-7, which are full of splines, are specially demanding. Indeed, the spline faces have to be normally approximated by planes using the SpaceClaim program. In some cases, the prepared CAD models resemble the result of an sculptural process.

It is true that the Spaceclaim program has tools that allow to do many of these tasks simultaneously (i.e. remove every instance of a particular detail at the same time). It even allows the user to program geometry processing scripts to automate some of the tasks [93]. However, still, the preparation of CAD models is a very repetitive and tedious activity. In fact, it is normally one of the most time-consuming steps of all the modelling process.

Finally, it is worth mentioning here that the verification and debugging activities are as well a very time-consuming part of the modelling process. Specially demanding is the task of fixing lost particles. This task requires carrying out an iterative process until no (or a relatively low amount of) lost particles are observed. The process consists of: running void-mode simulations, registering lost particles, making 2D plots at the locations where the particles are lost, inspecting the geometry to identify the geometry error and fixing the geometry errors in the MCNP input.

On top of all this, we have to take into account the changing nature of the ITER project. With this I mean that some aspects of the original data may change during the modelling process, what requires further interaction with IO or, even worse, repeating some of the modelling steps.

It is not surprising then that producing neutronics models of ITER geometries can represent, approximately, 70% of the total time required to perform an ITER nuclear analysis. Sometimes even more. For example, the nuclear analysis for EP#11 reported in [94] took more than 4 months. Producing the model for that analysis and reporting its preparation took around 3 months of a full-time dedicated nuclear analyst at TECF3IR-UNED. When the models are larger (i.e. a full tokamak reference model), several analysts from several institutions are required to produce sub-models of it in an amount of time that can fit in with the tight calendars of ITER.

Important efforts are being made by the ITER neutronics community to optimize the modelling process, making it less tedious and time-consuming. For example, the tool DAG-MCNP [95] has been developed, which allows to perform radiation transport calculations directly on the CAD models. That is, without the need to convert the CAD models into MCNP format and, therefore, reducing the time needed in their preparation. The UM capabilities incorporated in MCNP6 are also the subject of investigation [84], as they could also simplify the preparation

of the neutronics models. In addition, the community is making use of the scripting possibilities offered by SpaceClaim to automate modelling tasks.

The results of these efforts are already being used when modelling ITER geometries [93][96]. Still, however, more time and research are needed to reach the point in which the production of ITER models becomes straightforward, automatic and simple.

All this discussion is very enriching to understand why the reference models of the ITER Tokamak exist on the first place and why they have played such an important role in ITER neutronics. Indeed, as we will see in the next section, they are particularly useful with regards to the economization of geometry modelling efforts.

High demand of computational resources

To be able to produce realistic models, these need to represent the many bodies and materials that form part of the ITER geometries. Thus, they have to be made of many cells, surfaces and materials. However, as models become more detailed and are made of more cells, surfaces and materials, they become as well more computationally demanding. That is, they consume more RAM memory and demand more loading, simulation and plotting time. As I have just mentioned before, having access to HPC facilities has allowed to produce and run simulations with very computationally demanding models. However, current ITER models, specially the ITER Tokamak reference models, are so detailed that they have pushed to the limit the computational capacities of MCNP and of the current HPC facilities. Certainly, they are made of more than one hundred thousand cells and surfaces and hundreds of materials.

This has several implications. To see them, let us consider an extreme case: the MCNP model of the TBM port #16, from [19], integrated in the tokamak reference model C-model. In Table 2-1, I provide the values of the RAM memory consumption and the loading and plotting times of the model, which are extracted from [97].

Table 2-1. Computational loads of the EP#16 MCNP model integrated in C-model. Taken from [97].

Quantity	Value
RAM memory	10.2 GB/cpu
Loading time	304 min
Plotting time	Impractical

On the one hand, the RAM memory consumption of this model is 10.2 GB. When the MPI libraries are used to run a simulation in parallel, which is the standard approach in ITER nuclear analyses, this means that the 10.2 GB are allocated to each of the processes (i.e. cpu) of a node. However, this large RAM memory demand per process normally exceeds the total memory available on the computational node. Consequently, less processes per node must be allocated to reduce the total RAM memory request of the simulation. This is a relevant source of inefficiency and implies wasting computational resources. Node loads (i.e. processes allocated divided by the total node processors available) as low as 25% have been observed for instance in ITER applications on Marconi HPC. This corresponds to a waste of 75% of the computational resources (normally measured in node·hours) used for the simulation.

On the other hand, plotting this model with lines is completely impractical as the time taken to plot it is virtually infinite. This aspect has consequences in the debugging process of the MCNP models. Indeed, as I mentioned before, plotting the geometries is a useful method to inspect geometrical errors that can lead to lost particles. In addition, plotting is useful to check whether the integration of a particular model into a bigger one was done correctly. Consequently, the debugging and check processes have to rely on indirect approaches, what makes them even more tedious and time-consuming for the analyst.

Finally, the high loading time makes the model even more complicated to handle. Analysts have to wait many hours for the geometry to load every time a debugging/check process has to be carried out. Or before launching every simulation.

It is true that not all ITER models are as computationally demanding as the model from [19]. This model is almost impractical to use with MCNP and the current HPC computational capacities. But generally, and specially the tokamak

reference models, ITER models lead to considerable wastes of computational resources and are very difficult to handle.

This is a very important aspect in the context of this thesis. As I mentioned in the Introduction, it explains one of the reasons why the ITER Tokamak reference models are and have (almost always) been partial so far.

2.2 ITER Tokamak reference models

It is now the moment of talking about the central focus of this thesis: the ITER Tokamak reference neutronics models. As their name indicates, these are the models that represent the systems, structures and components of the ITER Tokamak. That includes the blankets, vacuum vessel, magnets, cryostat, etc. These models are developed, updated and distributed within the ITER neutronics community, which is coordinated by the IO central team. They are meant to be used as the standard models to perform nuclear analyses in the tokamak.

The ITER Tokamak reference models have played a very important role in the ITER neutronics strategy [68]. This is because they have allowed to efficiently face the continuous demand of nuclear analysis of the project. Indeed, all of them have been employed to compute a broad range of nuclear responses (neutron flux, nuclear heating, helium production, dpa, shutdown dose rates during maintenance, etc) for many SSCs (blankets, vacuum vessel, magnets, port systems, etc) and at different design stages (conceptual, preliminary and final design review, scoping shielding studies, etc). The following are just a few examples of nuclear analyses in which they have been used [98]–[103].

The key to the success of the ITER Tokamak reference models is that they provide a common framework that allows to carry out nuclear analyses in a consistent manner and with a significant save of geometry modelling resources. Since these models represent the main systems, structures and components of the ITER machine, analysts do not need to re-do from scratch a complete ITER machine model every time they do an analysis. As I explained in the previous section, this would cost an incredible amount of human resources. Instead, analysts simply have to adapt (if needed) specific SSCs of the reference models that are of interest for their application. The rest of SSCs of the machine, which will be important to take into account the effect of the environment in the radiation fields, can be left intact.

As a result, many experts, coordinated by the IO central team, can efficiently participate in the neutronics global effort, hence increasing the overall productivity. At the same time, the use of reference models facilitates the control and standardization of the analyses, which guarantees their quality. This is something crucial to be able to compare studies with different design proposals or to demonstrate to the French authorities that ITER will operate safely.

Finally, another important advantage of the reference models is that they are based on a modular concept. This allows to share and parallelize the efforts of developing and updating the models of components between the members of the neutronics community. In turn, it allows reaching a much higher level of detail in the modelling of the different components.

I will now describe the main features of the ITER Tokamak reference models (section 2.2.1). Then I will briefly go through the different reference models that have been produced over the years (section 2.2.2). Finally, we will see the effect on some nuclear responses of updating and detailing the reference models (section 2.2.3).

2.2.1 General description of the reference models

The approach followed in ITER when producing reference models has always been, except few exceptions [74], to represent a portion of the machine instead of the complete tokamak. In other words, the majority of reference models have always been partial models. Specifically, partial models explicitly represent a toroidal section of the machine (see Figure 2-10) and they rely on the use of either periodic or reflective boundary conditions to implicitly represent the rest of the tokamak (see Figure 2-11 to Figure 2-13). This approach assumes that a fraction of the tokamak is representative of the rest. That is, that the tokamak has a toroidal symmetry.

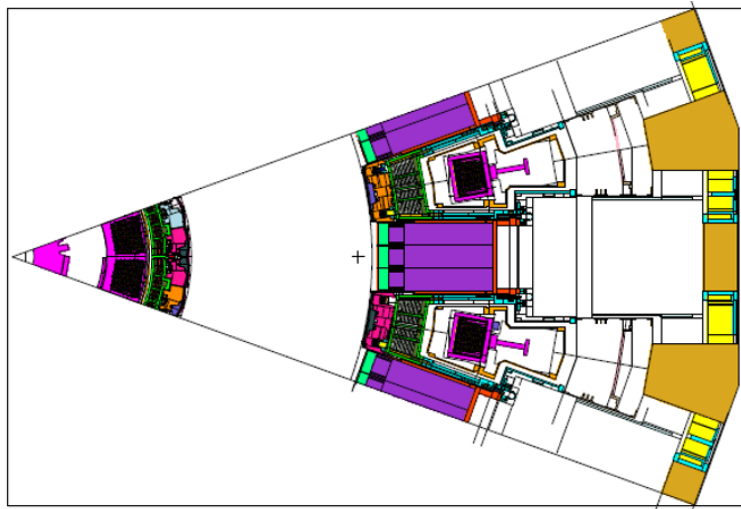


Figure 2-10. Horizontal cross-section of the ITER Tokamak reference model C-model. The model represents 40° of the machine.

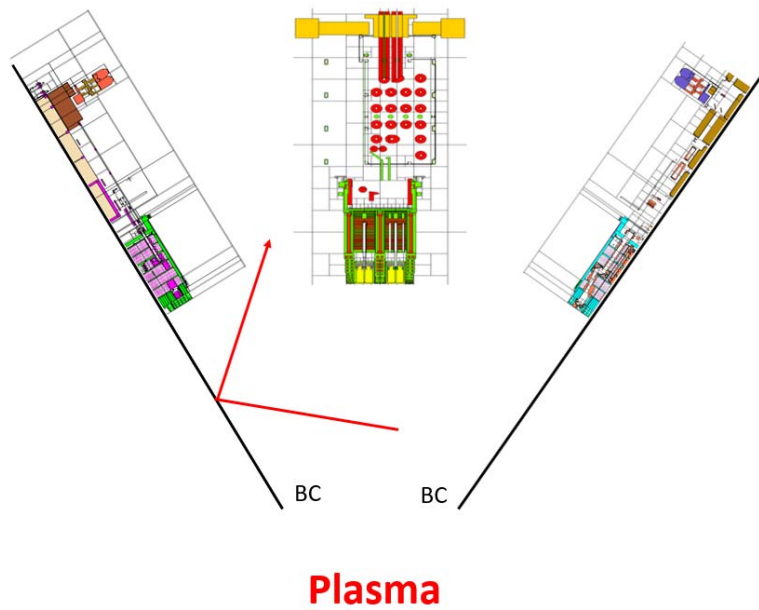


Figure 2-11. Schematic representation of a horizontal cross-section of a partial model that has reflective boundary conditions (BC). The model features one complete port at the centre and two halves on the laterals. The illustration represents how a radiation particle (in red) is reflected at the boundary.

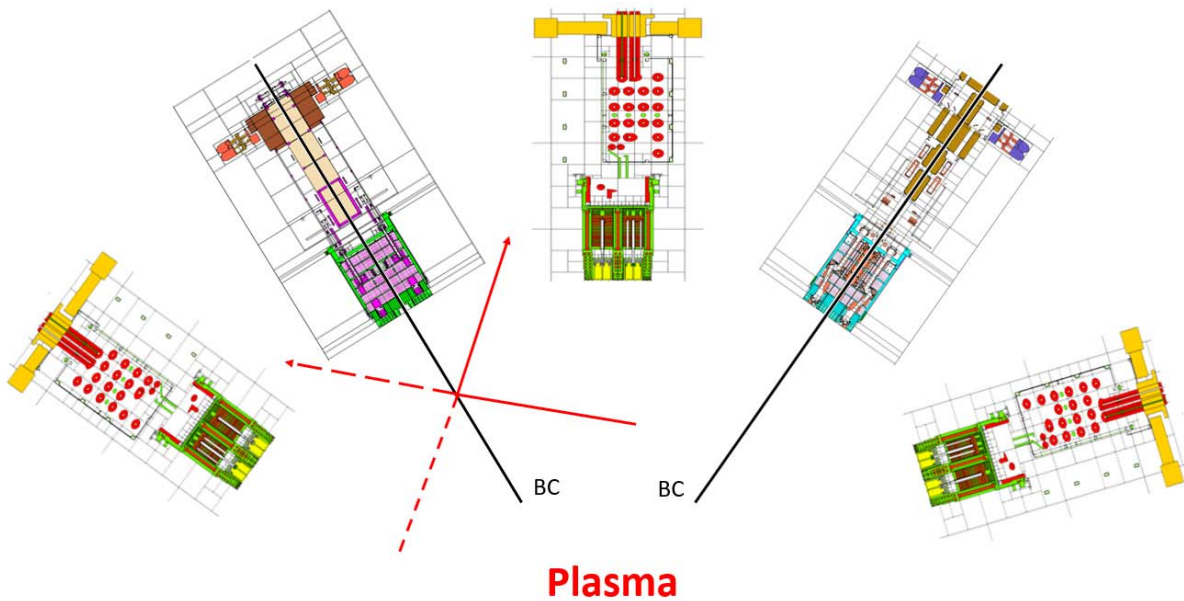


Figure 2-12. This picture is based on that of Figure 2-11. It illustrates the machine (although here I only included the neighbourhood) that is actually being represented when reflective boundary conditions (BC) are considered. Note how the additional ports and the dashed trajectory are mirrored with respect to the BCs.

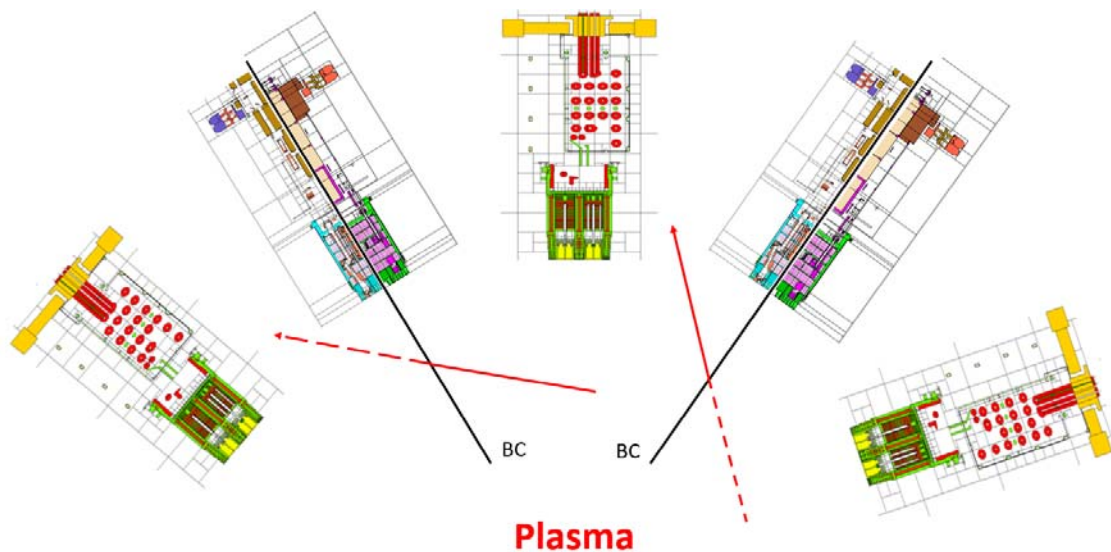


Figure 2-13. This picture is similar to that of Figure 2-12. However, here I illustrate the machine that is actually being represented when periodic (instead of reflective) boundary conditions (BC) are considered.

The first reference models represented a 20° [70][71] toroidal section of the machine. However, for more than a decade, the majority of reference models represent a 40° toroidal section, although two 80° models have also been made. The current reference models, C-model [72] and the NBI model [73], represent 40° and 80° toroidal sectors of the machine, respectively.

As I mentioned in the Introduction, the reasons for producing partial models instead of full models are basically three.

First of all, because partial models require less Monte Carlo histories to flood the geometry of the model. Thus, for a given nuclear response, they require less histories to reach sufficiently low statistical uncertainties. That is, the simulations with partial models take less computational time.

The second reason is that partial models are less computationally demanding in terms of RAM memory and loading and plotting times. Therefore, as we saw in the previous section, they are easier to manage, review and update. That is, partial models are comparatively easier to handle than full models, what reduces the time spent performing a nuclear analysis. However, in the case of the current reference models, these are so detailed that they have pushed to the limit the computational capacities of MCNP and the current HPC infrastructures. Thus, producing a full model with the same degree of detail is simply unfeasible computationally speaking.

The third reason is simply that producing a full model requires larger modelling efforts than producing a partial model.

Reference models represent the tokamak up to the bio-shield. The 40° reference models represent, on the middle, one set of complete upper, equatorial and lower ports that are vertically aligned (i.e. even port configuration) and, close to the boundaries, two sets of half ports in upper, central and lower positions (see Figure 2-14). On the other hand, the 80° models represent the complete NBI region at the equatorial level (see Figure 2-15). These models also include sets of complete upper and lower ports above and beneath the NBI region, respectively, and two sets of half ports close to the boundaries.

In addition, reference models also represent all the main SSCs of the machine, that is, blankets, divertor, vacuum vessel, thermal shields, magnet systems, cryostat and bio-shield. Apart from the geometrical description, reference models also include the material cards for the material definitions of all the represented components. Furthermore, the models are prepared to be used with a definition of the plasma neutron radiation source, which over the years has been provided either as an external Fortran subroutine [68] or as an SDEF card [104][105].

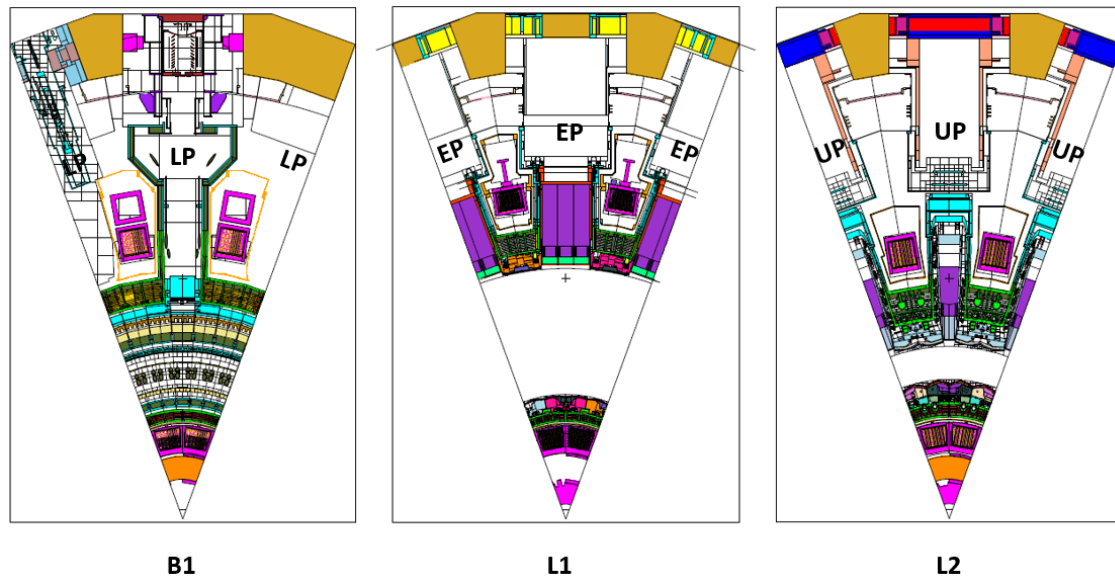


Figure 2-14. Horizontal cross-sections of C-model (40°) at B1, L1 and L2 levels. The lower (LP), equatorial (EP) and upper (UP) ports are indicated. The bio-shield is coloured in orange-brown.

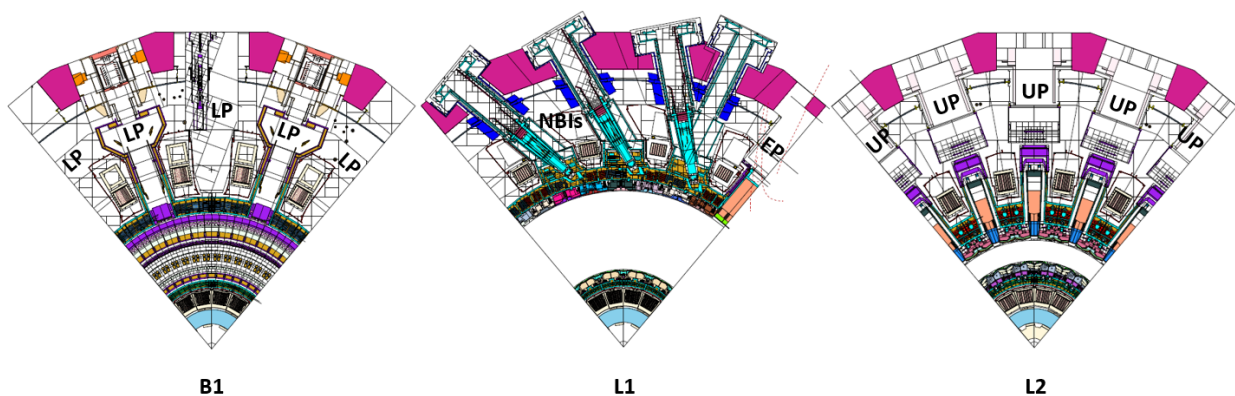


Figure 2-15. Horizontal cross-sections of an NBI model (80°) at B1, L1 and L2 levels. The lower (LP), equatorial (EP) and upper (UP) ports are indicated. The bio-shield is coloured in pink-purple.

Since almost the beginning, reference models have been based on a modular concept, as follows. On a first level, they are made of the so-called envelope cells, which fill the entire space of the toroidal section with a reduced number of relatively simple geometrical bodies. The envelope cells conform what is known as the block structure. Then, on the following level(s), the envelope cells of the block structure are filled in with the cells representing the different tokamak systems, structures and components (SSCs) in detail; these are the so-called universes. This modularity can be achieved thanks to MCNP universes (i.e. “FILL” and “U” cards).

Modularity is quite useful as it facilitates the manipulation, adaptation and update the reference partial models. This is because only single standalone

models (i.e. universes) have to be updated/adapted, which can later be directly replaced in the model assembly.

Modularity is particularly beneficial for the radiation shielding analysis of port systems [54][72] as the port models included by default in the reference models can be easily replaced with the ports of concern for the specific analysis. Furthermore, if a specific SSC is repeated several instances on different locations and with different orientations, as it is the case of the divertor cassettes, there is no need to replicate and re-orientate the SSC that same number of times; the same standalone model can be integrated and re-oriented in several envelope cells straightforwardly. This last aspect is also beneficial from the point of view of computational performance, since avoiding the replication of cells and surfaces reduces the computational load of the reference models.

Finally, as I said at the beginning of the section, the last main advantage of modularity is that it allows many institutions to collaborate at the same time in the production of the tokamak SSCs neutronics models (i.e. universes) to be integrated in the reference partial models. As we saw in the previous section, modelling tasks require a great investment in manpower. Particularly, producing a complete reference model represents a gargantuan modelling effort. Thus, this collaboration is essential.

2.2.2 Evolution of the reference models

In the last two decades, successive reference models have been produced and updated.

The first reference model of relevance was the BRAND model [70][71]. It was produced by hand in 2000 and it represented a 20° regular sector of the tokamak. In Figure 2-16 I show vertical and horizontal cross-sections of this model. It was made of more than 2800 cells, what was considered as a feat at that time [69]. Then, from 2006 to 2008 it was updated [106] by means of MCAM [87], predecessor of SuperMC [85][86], and it was toroidally extended up to 40°.

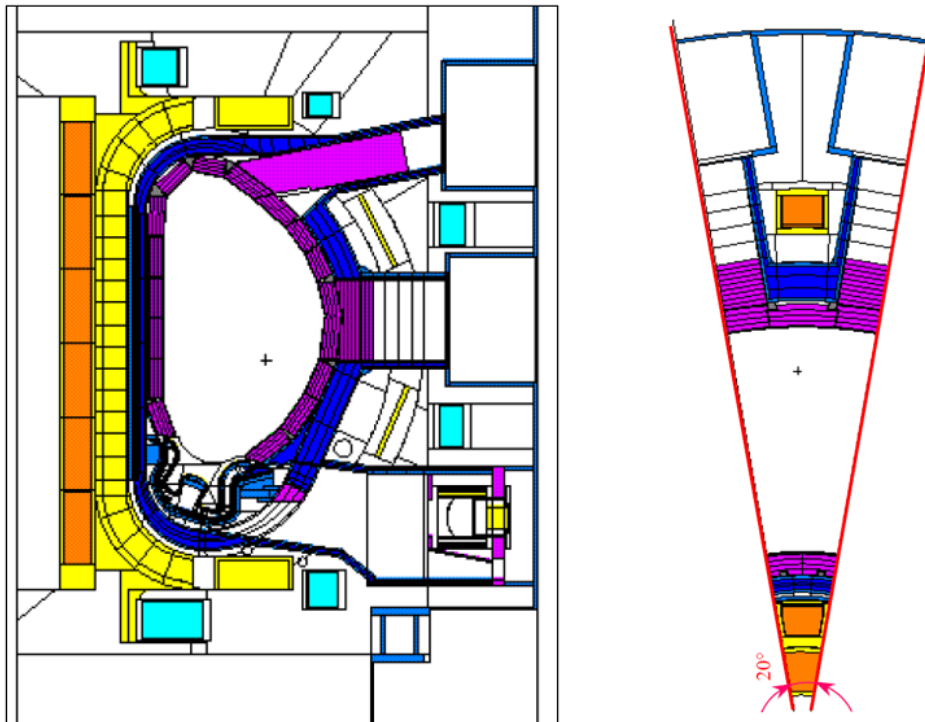


Figure 2-16. Vertical and horizontal cross-sections of the BRAND model (2000) of the ITER Tokamak.

Afterwards, from 2008 up to 2016, the next generation of reference models formed part of the so-called “-lite” series: A-lite [68][100], B-lite [107] and C-lite [108]. These models, and their respective intermediate versions, were regularly updated and improved by a collaborative effort. In the process, not only the latest available configuration of the machine design at the time was considered, but the SSCs were progressively modelled with a higher degree of detail. The level of simplification of the universes was reduced and progressively homogenized regions were substituted with heterogenous specifications and material definitions. In turn, the tokamak models have been growing in complexity over the years. This is something that can be observed in Figure 2-17 and Table 2-2, where the number of cells, surfaces and materials used for each of them, and other models that I will present below, are shown. In addition, in Table 2-3, I show horizontal cross-sections of the inboard region of some of the models to which I have, or I will refer, in this section. In these cross-sections, the increase in detail in the representation of the toroidal field coils, vacuum vessel and blankets can be appreciated.

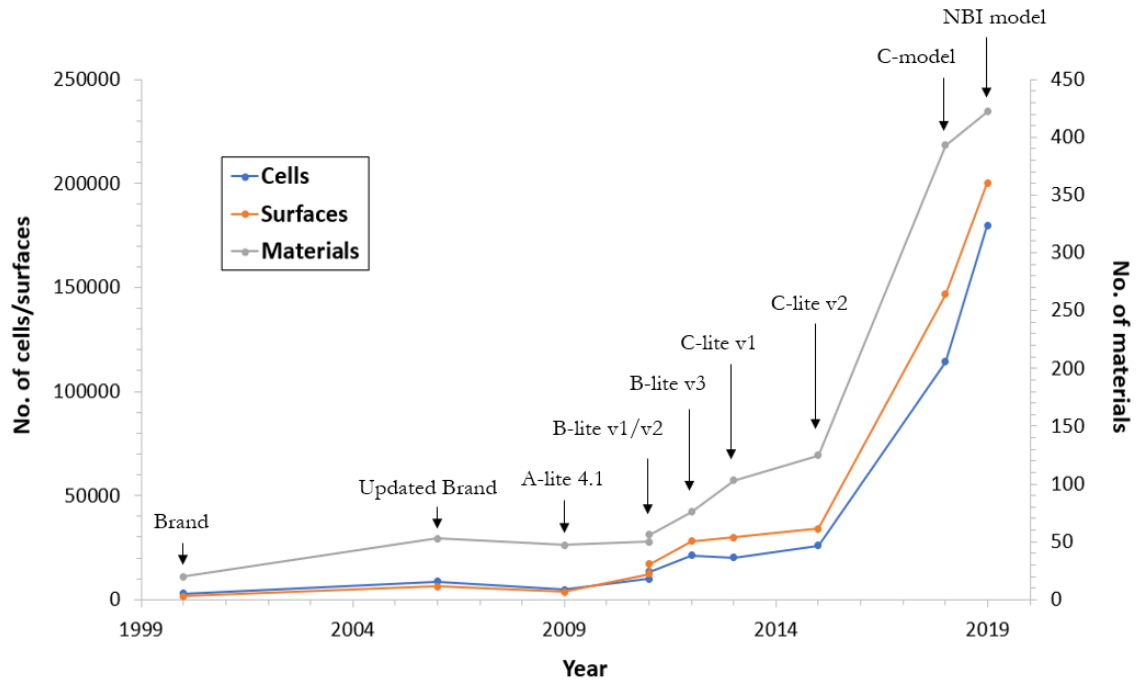
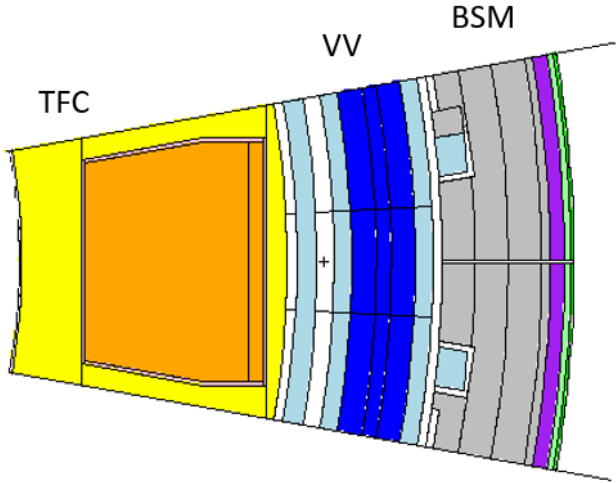
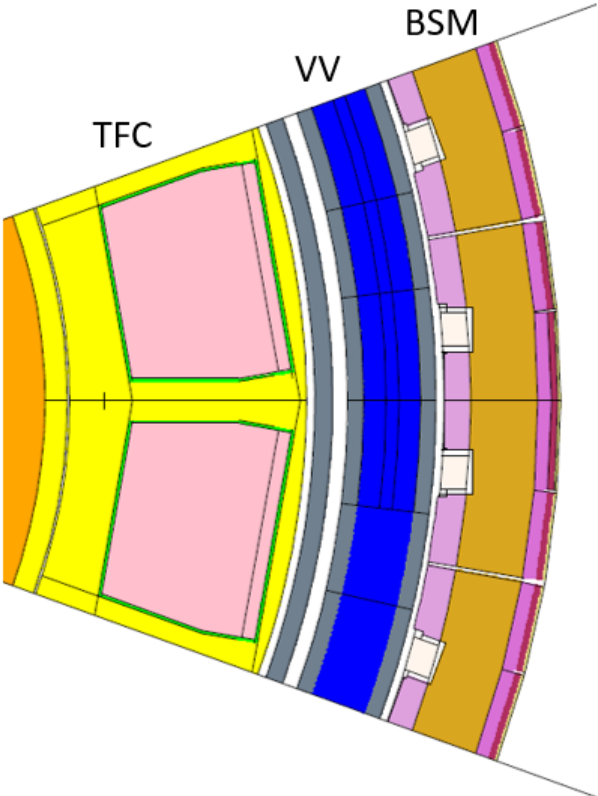


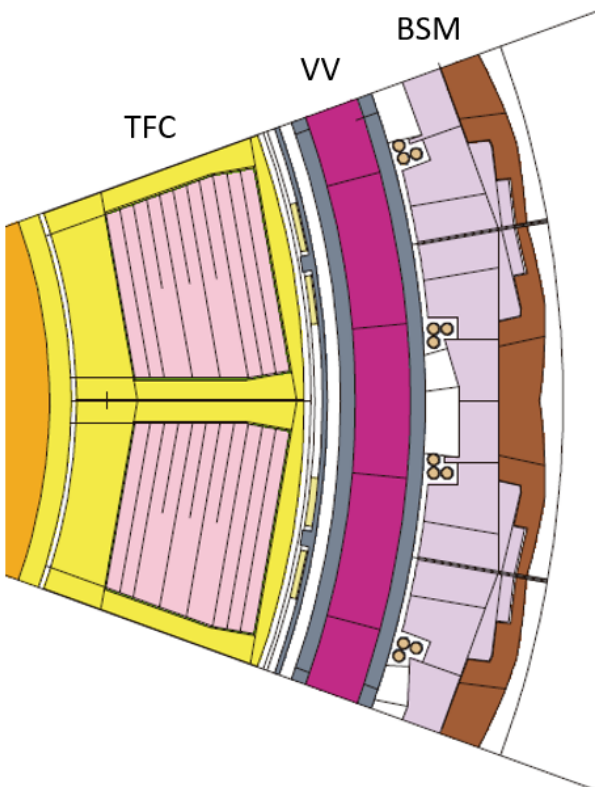
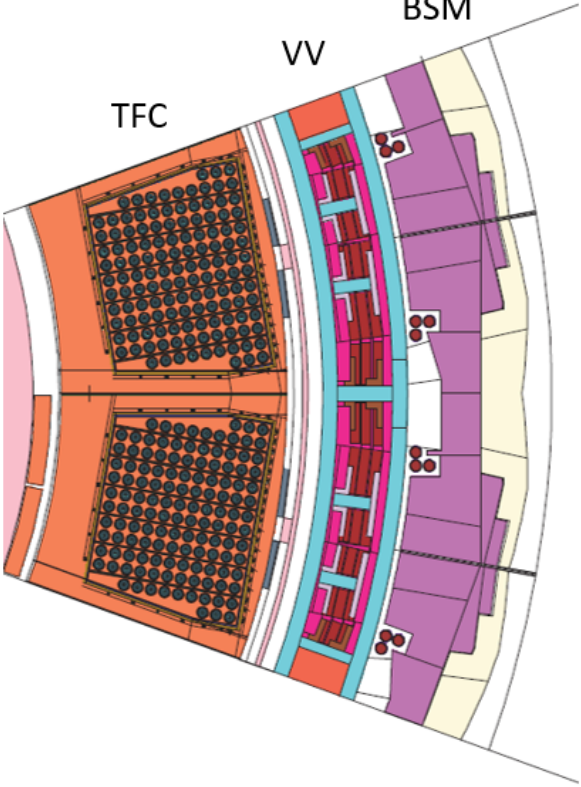
Figure 2-17. Evolution of the number of cells (blue), surfaces (orange) and materials (grey) of the ITER Tokamak reference models over the years. Note there are two vertical axes.

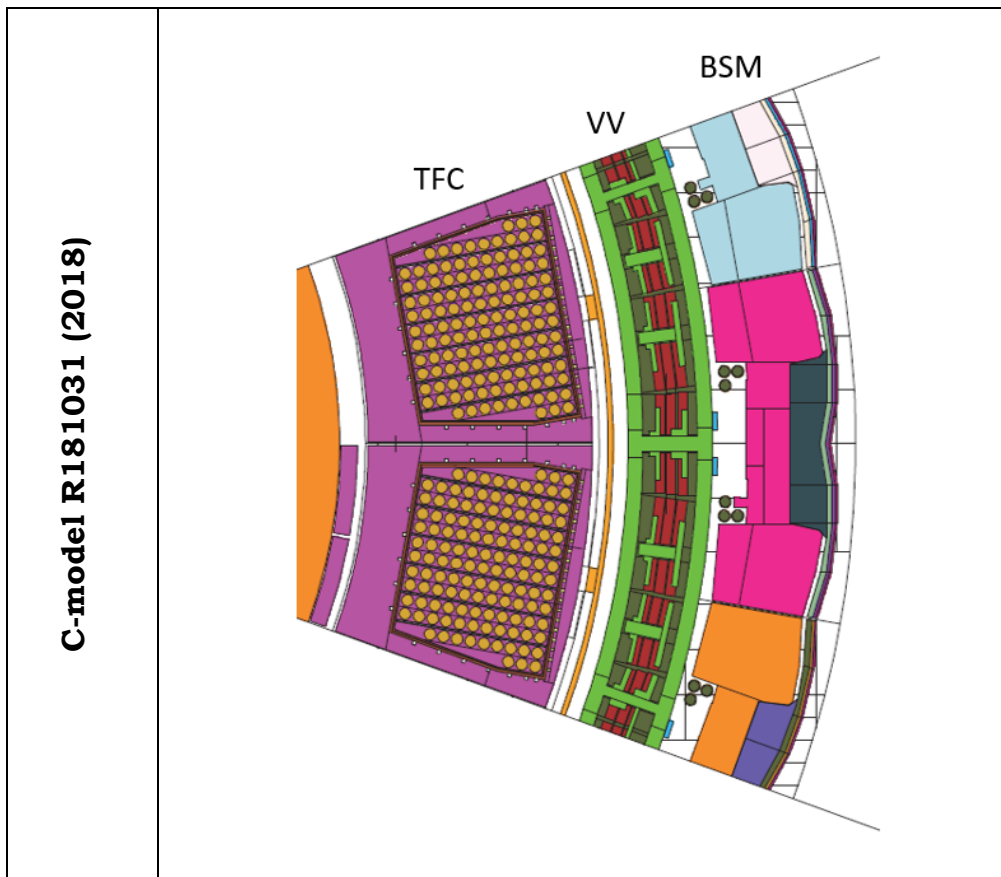
Table 2-2. Evolution of the number of cells, surfaces and materials of the ITER Tokamak reference models over the years.

Model	Year of release	No. of cells	No. of surfaces	No. of materials
Brand	2000	2936	1586	20
Updated Brand	2006	8760	6275	53
A-lite 4.1	2009	4679	3632	47
B-lite v1	2011	10084	12319	50
B-lite v2	2011	13287	17029	56
B-lite v3	2012	21216	27920	76
C-lite v1	2013	20259	29988	103
C-lite v2	2015	26045	34107	125
C-model (R181031)	2018	114285	146802	393
NBI model	2019	179832	200372	422

Table 2-3. Horizontal cross-sections of the inboard region of several reference models of the ITER Tokamak. The pictures show the Toroidal Field Coils (TFC), Vacuum Vessel (VV) and Blanket Shield Modules (BSM).

<p>Updated Brand (2006-2008), prior to the 40° extension</p>	
<p>A-lite 9.1 (2009)</p>	

<p>B-lite v3 (2012)</p>	 <p>A cross-sectional diagram of a curved structure. From left to right, it shows a yellow outer layer, a pink inner layer with horizontal lines, a thin grey layer, a thick magenta layer, a thin grey layer, and a brown outermost layer. Small circular features are visible within the brown layer. Labels 'TFC', 'VV', and 'BSM' are positioned above the corresponding layers.</p>
<p>C-lite v2 (2015)</p>	 <p>A cross-sectional diagram of a curved structure. From left to right, it shows a pink outer layer, an orange inner layer with a grid of dark blue circles, a thin light blue layer, a thick red layer, a thin light blue layer, a purple layer, and a yellow outermost layer. Small circular features are visible within the purple layer. Labels 'TFC', 'VV', and 'BSM' are positioned above the corresponding layers.</p>



In Figure 2-18, cross-section of the B-lite v2 model are shown. Note, A-lite, B-lite and C-lite models represent a 40° toroidal sector of the ITER Tokamak. In Figure 2-19, I show a horizontal cross-section view of the only 80° -lite model [109] that was produced to represent the NBI region. It was based on A-lite.

Since 2016, the 40° ITER Tokamak reference model is C-model [72][110]. This model, and its successive versions, have reached an unprecedented level of realism. This is mainly due to an increased detailed modelling of in-vessel and vessel components, such as the blanket modules, in-vessel coils, divertor cassettes or the vacuum vessel. Particularly, the vacuum vessel model is fully heterogeneous, i.e. no material mixtures were applied at all. Even the cooling water is modelled explicitly. Furthermore, the latest Diagnostics Generic Equatorial [111] and Upper Port [112] models, together with the Final Design Review (FDR) neutronics model of the Torus Cryopump [113], were integrated in C-model.

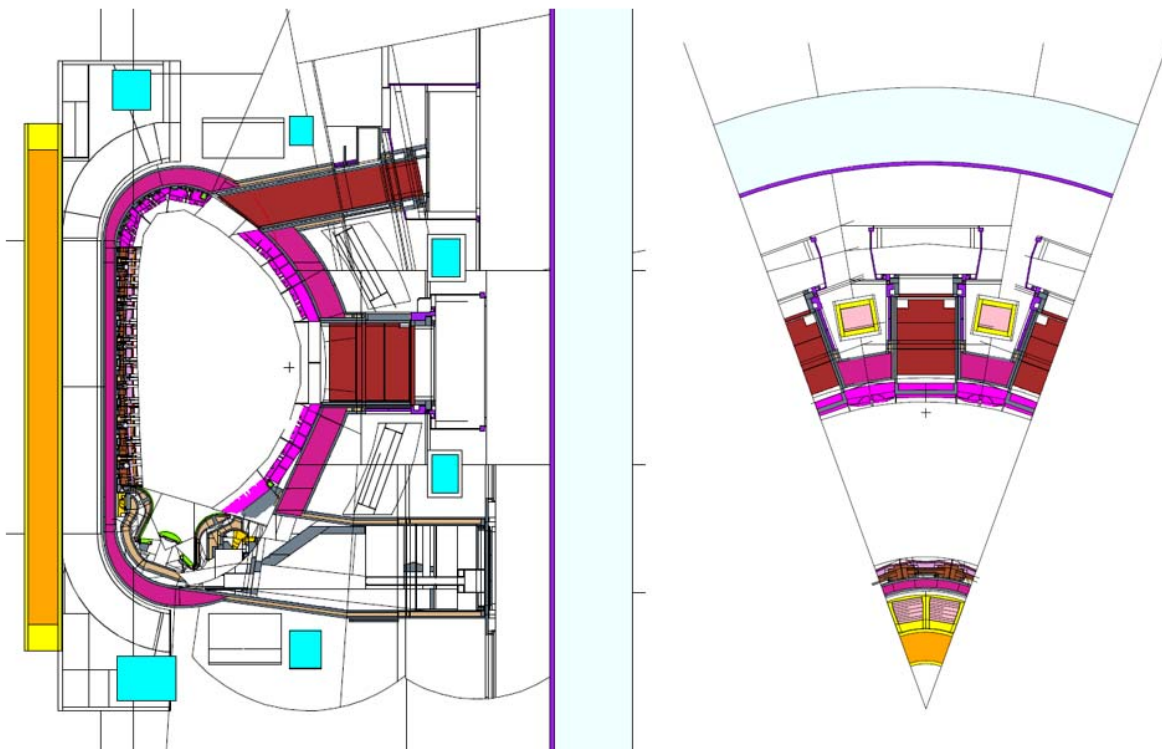


Figure 2-18. Vertical and horizontal cross-sections of the B-lite v2 model (2011) of the ITER Tokamak.

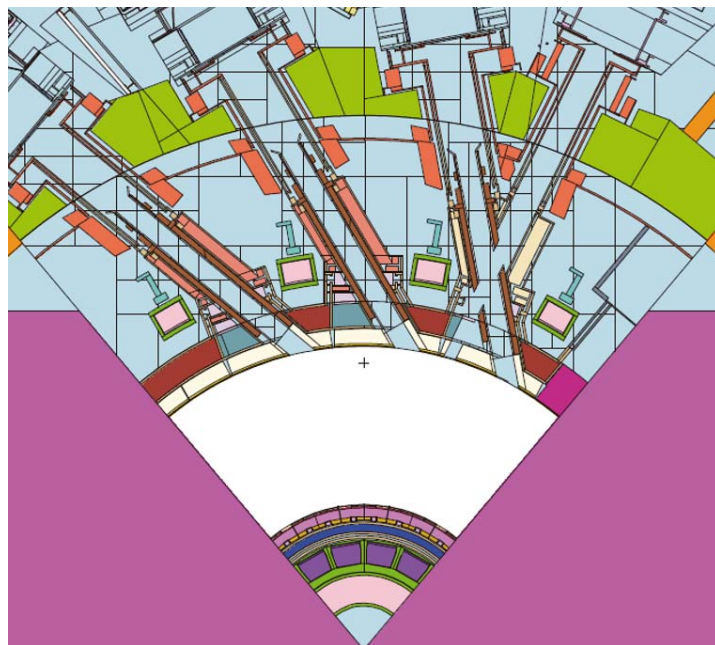


Figure 2-19. Horizontal cross-section of the tokamak model representing the NBI region. The model is based on A-lite.

In addition to the updated neutronics models of specific SSCs, the latest Project Change Requests (PCR) to the baseline, that affected the neutronics performance, were also included. For instance, materials compositions and

impurities levels were updated according to PCR-722 [114] and the gap configuration at the interface between the ports and the vacuum vessel and blankets was changed in line with PCR-439 [115] and PCR-644 [116].

It is important to note that C-model achievements are so valuable not only due to the increased detail and representativity, but because, for the first time, a proper quality assurance procedure was followed in the modelling process itself [72]. Guidelines were followed in order to ensure the reliability of the neutronics models in terms of geometry and mass accuracy or reduced material mixing. Furthermore, the methodology followed in the production of many of the models was standardized, documented and validated and the models themselves were documented and independently verified.

The human efforts employed in the first release of C-model are estimated to be roughly 5 person-year [72]. This is a significant amount of human resources that required the collaboration of a total of 11 institutions. Indeed, compared to previous “-lite” models, C-model is significantly much more complex, as can be seen in Figure 2-17, Table 2-2 and Table 2-3. In Figure 2-20, vertical and horizontal cross-sections of C-model are shown.

The last reference model developed was released in 2019. It is an 80° reference model produced by CCFE and the ITER Organization to represent the NBI region [73]. Note, a new model for this region had not been done/updated since the first 80° A-lite-based model. This new model inherits many of the features of C-model block structure and many of its universes. Additionally, new SSCs were modelled, such as the neutral beams duct liners and vacuum vessel port extensions and connecting duct, or re-modelled, such as the thermal shield, cryostat or the Toroidal Field Coils (TFC). Thus, this model is even more complex than C-model, as shown in Figure 2-17 and Table 2-2. Horizontal cross-sections of this model can be found in Figure 2-15.

As stated in the previous section, C-model and the NBI model are so complex and computationally demanding that they have pushed to the limit the capacities of MCNP and the current HPC facilities.

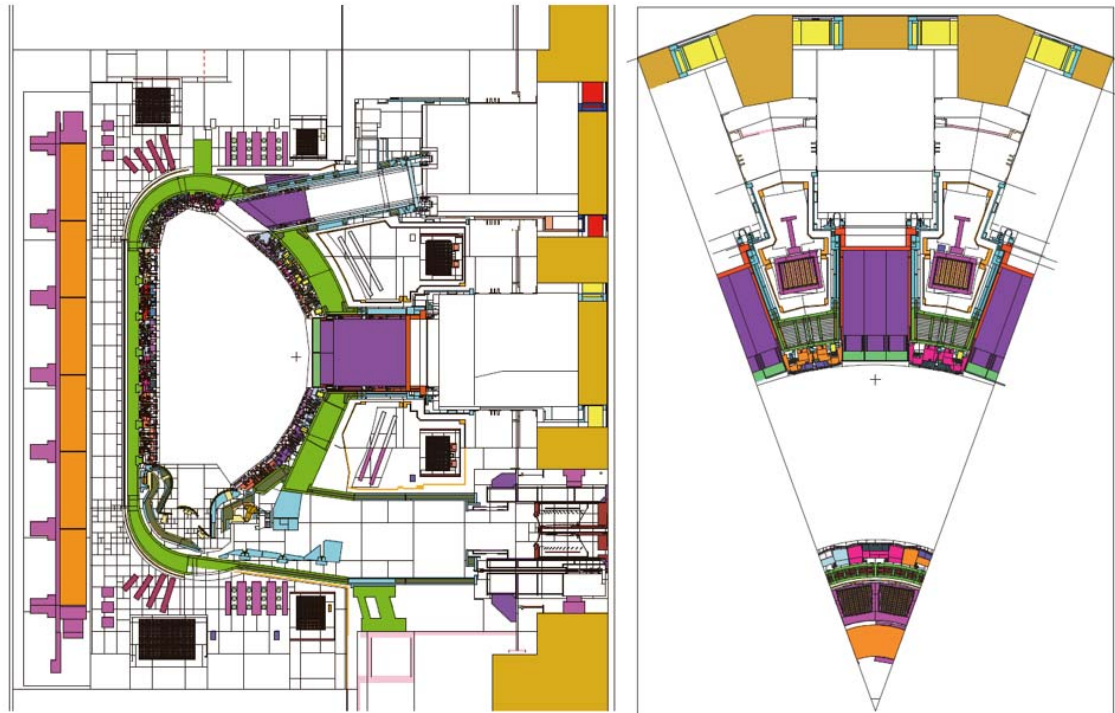


Figure 2-20. Vertical and horizontal cross-sections of C-model R181031 (2018) of the ITER Tokamak.

2.2.3 Impact on nuclear responses

Particularly interesting is to see the impact on the nuclear responses of the updates in the design of the SSCs and the higher levels of detail that are reflected in the successive reference models [102][117]–[119].

For example, in [117], a comparison is shown of the nuclear heat values in the vacuum vessel components as computed with B-lite and C-lite. The total heat in all the vacuum vessel components is reported to be 16.69 MW in C-lite, a 35% higher than in B-lite (12.35 MW). Specifically, the nuclear heat in the triangular support and the equatorial outboard part of the vacuum vessel are, respectively, 2.4 and 2.3 times higher in C-lite than in B-lite. The reasons for these changes were attributed to updates on the masses of blanket modules located in the vicinity of the vacuum vessel components. Similarly, in [118] the same nuclear heat results in the vacuum vessel components are reported for C-model. In that case, results in the total heating only differed by 8.3% between C-model (18.08 MW) and C-lite (16.69 MW) and the differences observed for specific components were within 20-30%. Again, these changes were attributed to the use of more detailed models and changes in the design of the nearby in-vessel components.

Another example is the study [119], where they report shutdown dose rate (SDDR) results at 10^6 seconds of cooling time in the upper port interspace, considering both C-lite and C-model. In the study, a dedicated and detailed environment of the upper port plug was integrated in C-model. Nonetheless, it was observed that the SDDR values in the interspace maintenance corridors did not change significantly. Indeed, the SDDR in C-model ($274 \mu\text{Sv/h}$) was only 8% higher than in C-lite ($254 \mu\text{Sv/h}$). A priori, a higher increase in the SDDR was expected as the changes in the upper port environment considered in C-model led, in principle, to a higher radiation streaming. However, further analysis of all the differences between C-lite and C-model indicated that the similarity in the results could be attributed to additional compensatory modifications included in C-model. For example, the presence of shielding blocks in the C-model lower port, which led to a reduction in the SDDR in the above ports [120], could compensate the mentioned streaming.

Certainly, the above examples give an idea of how difficult is to predict the impact that the changes introduced in the successive reference models (i.e. updates in the design, increase detail of models, etc) may have. There is an intricate dependency between the changes introduced, the nuclear response of interest and the components/area under study. Some changes only have a local effect, while others affect globally and so on and so forth. This is the reason why the reference models are continuously updated to represent the latest tokamak design and the different SSCs in as much detail as possible. In this way, the uncertainties in the nuclear responses associated to the geometry modelling can be reduced as much as possible. This strategy has culminated in the current C-model and NBI model, which have allowed reaching an unprecedented degree of detail and realism.

2.3 Limitations of partial models

It is clear that the ITER Tokamak reference models have achieved an unprecedented level of realism and that they have played a very relevant role in the ITER neutronics strategy. However, their partial nature leads to limitations that, given the high accuracy requirements of ITER nuclear analyses, may have intolerable implications. In this section, I am going to identify the limitations of partial models, together with ITER-relevant applications that may be severely affected by them.

The first limitation comes from assuming that a fraction of the machine faithfully represents the complete machine by means of periodic or reflective boundary conditions. In other words, the assumption that the machine has a toroidal symmetry. However, as can be inferred from section 1.2.2, it is clear that this is not the case. Indeed, ITER ports are very different from each other, hence, not symmetrical at all. This means that partial models, regardless of how detailed and realistic they become, always deviate from the reality as they are incapable of capturing the machine asymmetry beyond the area explicitly represented by them.

However, when performing an analysis, it is not possible to predict whether the asymmetry of the machine can have an impact or not on the nuclear responses. Thus, partial models introduce uncertainties in the nuclear responses estimated. Even worse, these uncertainties cannot be quantified and have remained unquantified to date.

In summary, one of the main limitations of partial models is that they introduce unquantified uncertainties in the estimation of nuclear responses (more or less severe depending on the nuclear response) due to the fact that they represent as symmetric a machine that is actually asymmetric.

The second limitation of partial models is that they are not prepared to be directly used in applications which, by definition, require a broader (or complete) toroidal representation of the machine geometry and/or the radiation sources. For example, reference models cannot be used to tally responses due to a point-wise source (e.g. calibration source) that is located outside the toroidal extension covered by the model. To do so, the reflective/periodic boundary conditions would have to be removed. However, this would mean that the rest of the machine is no longer taken into account in the calculation.

As simple as they may seem, these two limitations have important consequences for ITER applications. I am now going to identify three relevant applications of ITER affected by them.

2.3.1 Shutdown dose rates in port interspaces

The Project Requirements [50] dictate that the shutdown dose rates (SDDR) in the port interspaces have to be below 100 $\mu\text{Sv/h}$ at 10^6 s of cooling time (about 12 days) after machine shutdown for planned hands-on maintenance activities. As I have already mentioned, fulfilling such requirement is very challenging and

concerning for the ITER project. Indeed, many of the port interspaces do not fulfil the required limits currently [54]. This is because ITER port interspaces get highly activated by the plasma neutrons, and the resulting decay photon fields are very intense. On the other hand, the margin to reduce the intensity of such fields is very tight. For example, the implementation of shields is subjected to many technical (weight, accessibility, flammability, manufacturability, toxicity, etc) and economical constraints.

To fulfil the SDDR requirements in the ITER port interspaces, it is essential to accurately characterize the decay photon fields resulting from the neutron activation. In this way, it is possible to evaluate which are the optimal measures (e.g. shields, reduction of impurities) that can fulfil the SDDR requirement while minimizing the impact on the ITER design. In fact, such is the importance of this kind of analyses that, in recent years, an intense research activity has taken place to develop more reliable, robust and faster computational methods and tools for ITER SDDR analysis [97][121]–[128].

However, the first limitation of partial models can have an important impact on the accuracy of the SDDR estimations in the port interspaces. Specifically, this limitation affects the estimation of the radiation cross-talk, which is a phenomenon that has been intensely investigated in recent years [75][120][129]. It basically consists in the propagation of radiation from one poloidal/toroidal location to another. In the case of the shutdown doses, an example of cross-talk is the activation of material at one port interspace due to neutrons exiting the plasma chamber through a neighboring lateral or vertical port (see Figure 2-21). The propagation of decay photons from one port to another is also considered as another form of cross-talk.

Radiation cross-talk is one of the main drivers of the SDDR levels in the port interspaces [75]. In fact, in some cases, it may be the most relevant driver, more than the streaming through the ports themselves [130]. Furthermore, cross-talk may lead to SDDR values that are already very close to or above the requirements [130]–[132].

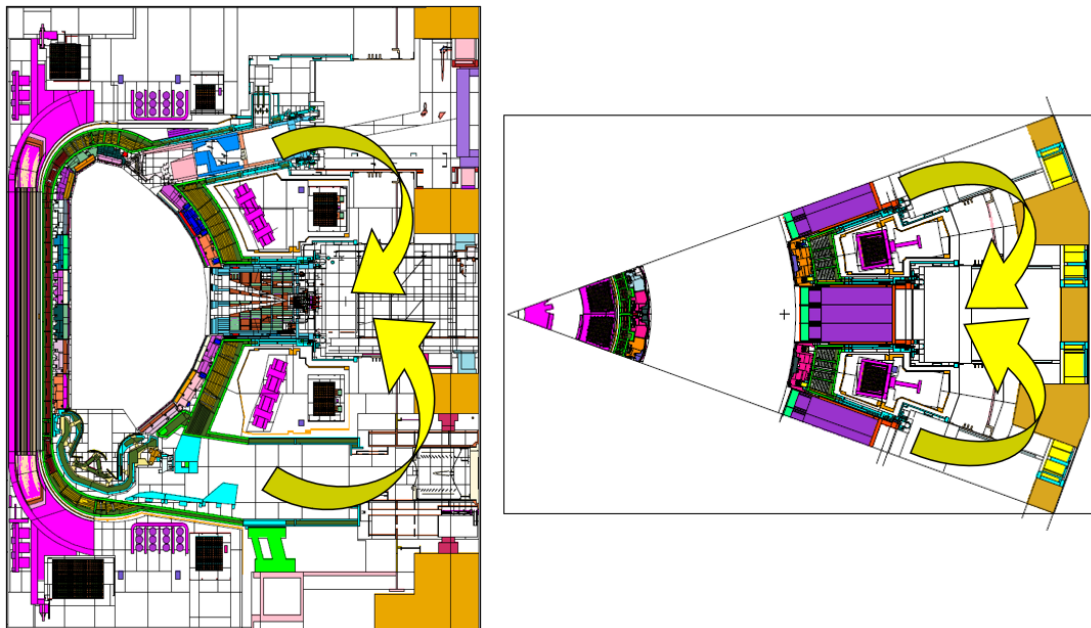


Figure 2-21. Examples of radiation cross-talk. On the left-hand side, the vertical cross-talk towards the equatorial port is represented. On the right-hand side, the lateral cross-talk towards the central port is represented.

Due to the symmetry assumption of partial models, the radiation cross-talk, specially the lateral one, remains partially or completely unassessed at most of the port interspaces. Certainly, partial models do not take into account the variability in the features (i.e. streaming paths) of each port, which are determinant regarding the cross-talk they induce in their neighbor ports. This aspect introduces considerable uncertainties in the estimations of the SDDR in the port interspaces. Considering that many port interspaces present shutdown dose levels beyond or very close to the requirement [54], and that many design efforts have to be performed to meet such requirement, these uncertainties are particularly problematic.

Certainly, attempts have been made to improve the SDDR cross-talk treatment with partial models, such as the flipping of partial models to model the short-range cross-talk in odd-numbered ports [133][134] (see Figure 2-22). These attempts, however, only improve the representation of the cross-talk coming from the B1 level towards other poloidal positions. Still, they are not sufficient to fully represent all the cross-talk, specially the cross-talk from other toroidal positions, i.e. lateral cross-talk.

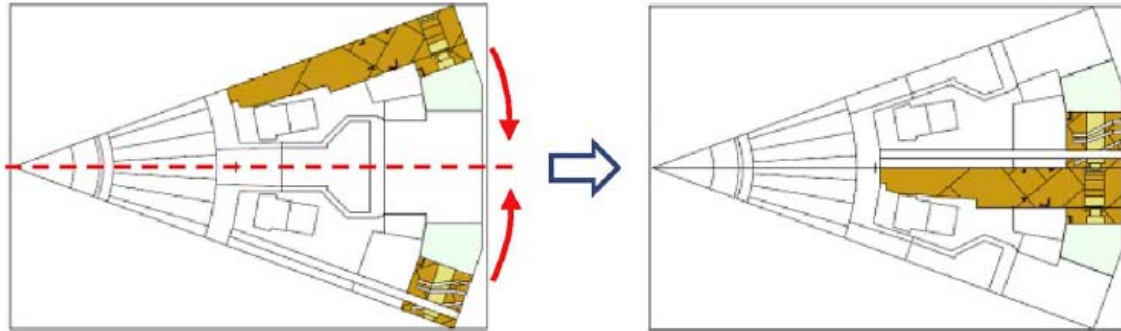


Figure 2-22. Illustration showing the flipping of partial models to relocate the IVVS port as the central port. Taken from [134].

2.3.2 Radiation mapping in the Tokamak Complex

As we have already seen, during plasma operation, the Tokamak Complex will be subjected to intense radiation fields due to the plasma and the activated water sources. Thus, the characterization of the radiation conditions in the Tokamak Complex, and beyond it, is of high importance. Specifically, for two main reasons. On the one hand, to validate the design of the Tokamak Complex with respect to the compliance of the radiological zoning and safety limits, which guarantee that dose limits are respected for workers and the public. On the other hand, to determine the correct disposition of electronic equipment, which can be seriously damaged by radiation, and to define equipment qualification programmes (if needed).

Both aspects are fundamental for ITER design and operation. In fact, in recent years the ITER project has devoted many efforts to develop, optimize and qualify a series of shields, the so-called PIM-466 [135], to guarantee that the radiation levels in the Tokamak Complex do not violate the stipulated requirements [53].

However, the reliability of the radiation maps due to the plasma source is affected by both limitations of partial models. This is quite problematic; not only because the radiation maps are a very important input for the ITER design, but because they undergo a severe process of scrutiny by ASN, who needs to be convinced that these maps are a reliable proof to claim the safe operation of ITER [68][136].

To indicate the reason why the reliability of the radiation maps is affected by the limitations of partial models I have to, first, briefly explain how radiation maps have been computed until now.

To compute the ITER radiation maps, dedicated MCNP models of the Tokamak Complex have to be used, like the one from [89], which was used in the radiation maps from 2016 [137]. This model represents the civil structures of the B11, B14 and B74 buildings. As shown in Figure 2-23 and Figure 2-24, this MCNP model, as well as all existing MCNP models of the Tokamak Complex, are defined from the bio-shield onwards. However, as we have just seen in section 2.2, the ITER Tokamak reference models are defined up to the bio-shield. Therefore, this means that both current tokamak and Tokamak Complex reference models are bounded by the bio-shield (see Figure 2-25).

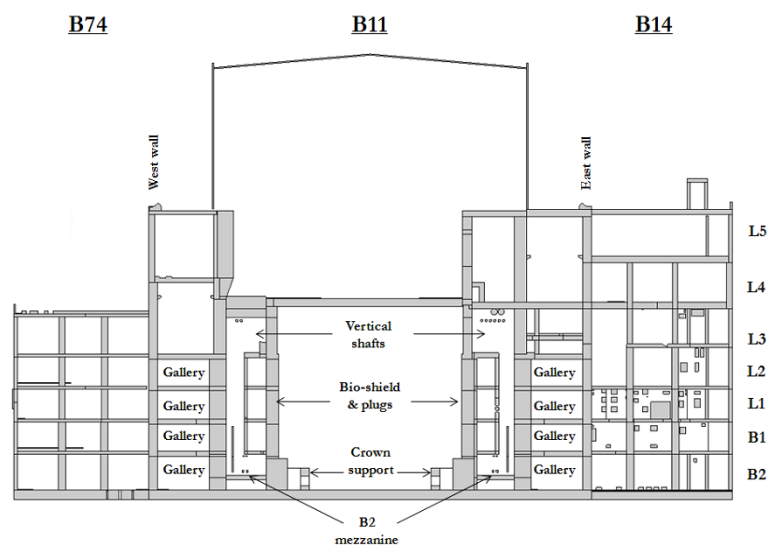


Figure 2-23. Vertical cross-section of the Tokamak Complex MCNP model [89]. Taken from [137].

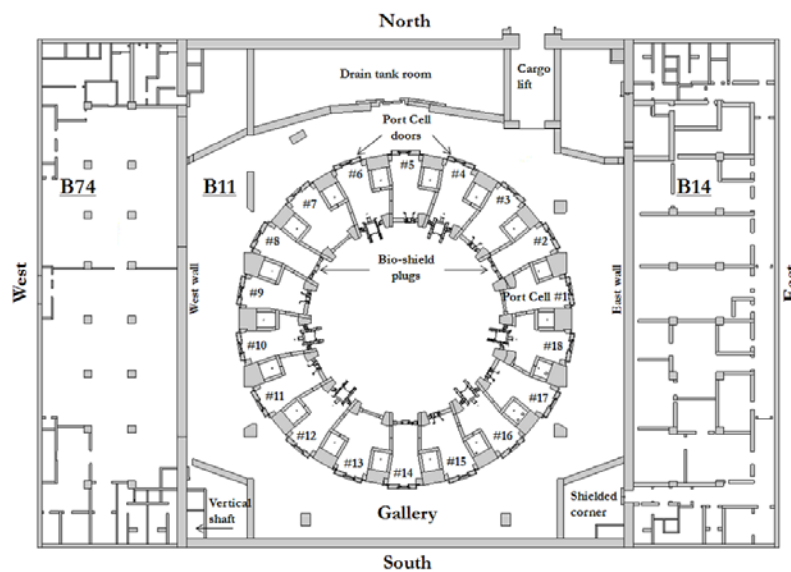


Figure 2-24. Horizontal cross-section of the Tokamak Complex MCNP model [89]. Taken from [137].

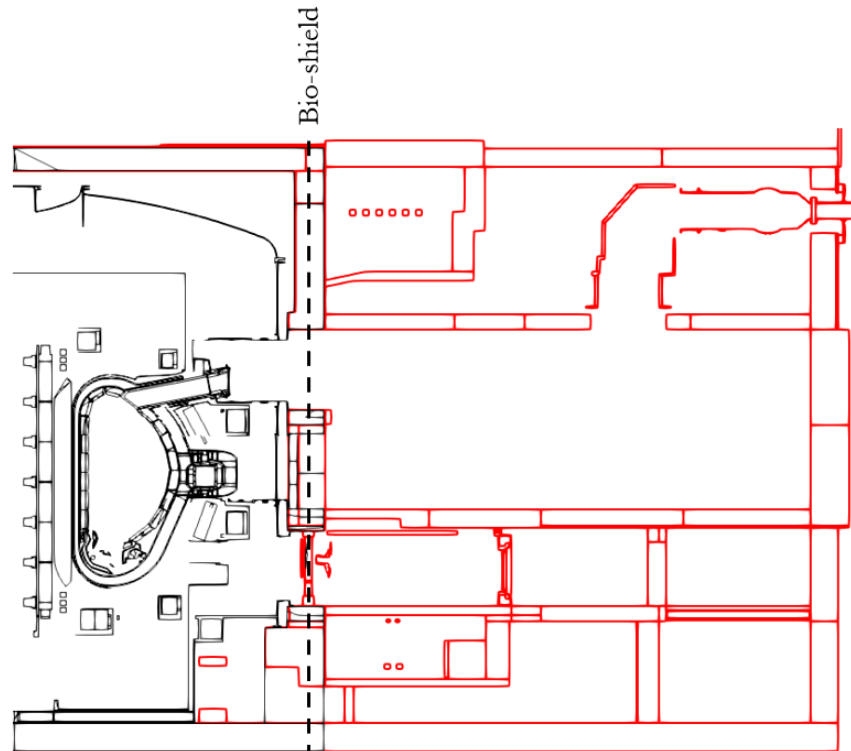


Figure 2-25. Vertical cross-section of tokamak (black) and Tokamak Complex (red) models where it can be seen that the bio-shield is the boundary of both models.

Among other things, this situation affects the computation of radiation maps due to the plasma source. Indeed, the tokamak models contain the plasma, whereas the Tokamak Complex models represent the region of interest for the radiation maps. Consequently, the radiation transmission through the bio-shield has to be coupled somehow between both models.

This coupling has been achieved in previous ITER radiation maps by modelling an intermediate plasma source right in front of the bio-shield [138][139]. To do so, it is necessary to first characterize the plasma radiation impinging on the bio-shield by running simulations with the tokamak models. Then, this information is used to model the intermediate source, which can eventually be used to run simulations in the Tokamak Complex models. In Figure 2-26, I show an schematic representation of this process for one single port (e.g. TCP port) [15].

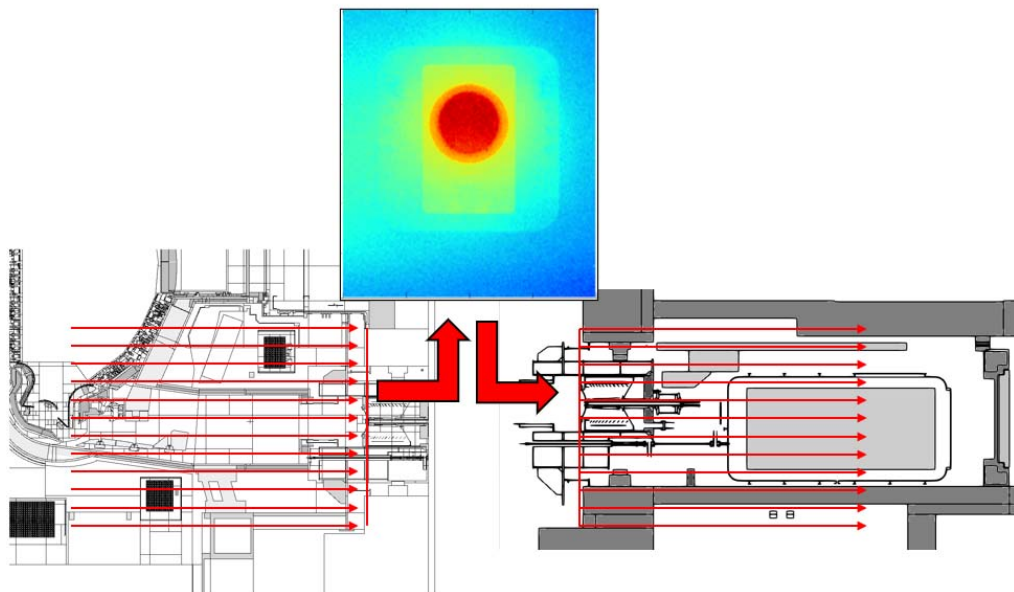


Figure 2-26. Schematic representation of how the radiation transmission is coupled between the tokamak and Tokamak Complex models by means of an intermediate source. Taken from [15].

It is in the modelling of this intermediate plasma source where the partial nature of the reference models has consequences. Indeed, the intermediate plasma source needs to cover the 360° of the bio-shield, while the partial models only cover 40° or 80° . Thus, to produce a 360° intermediate source, it is necessary to somehow combine together different sources, which are independently modelled by means of partial models.

This was done in a very sophisticated way in the Radiation Maps from 2016 [51][137], where the SRC-UNED [139][140] approach was developed and followed. As can be seen in Figure 2-27, a mosaic source was built by combining together individual tesserae.

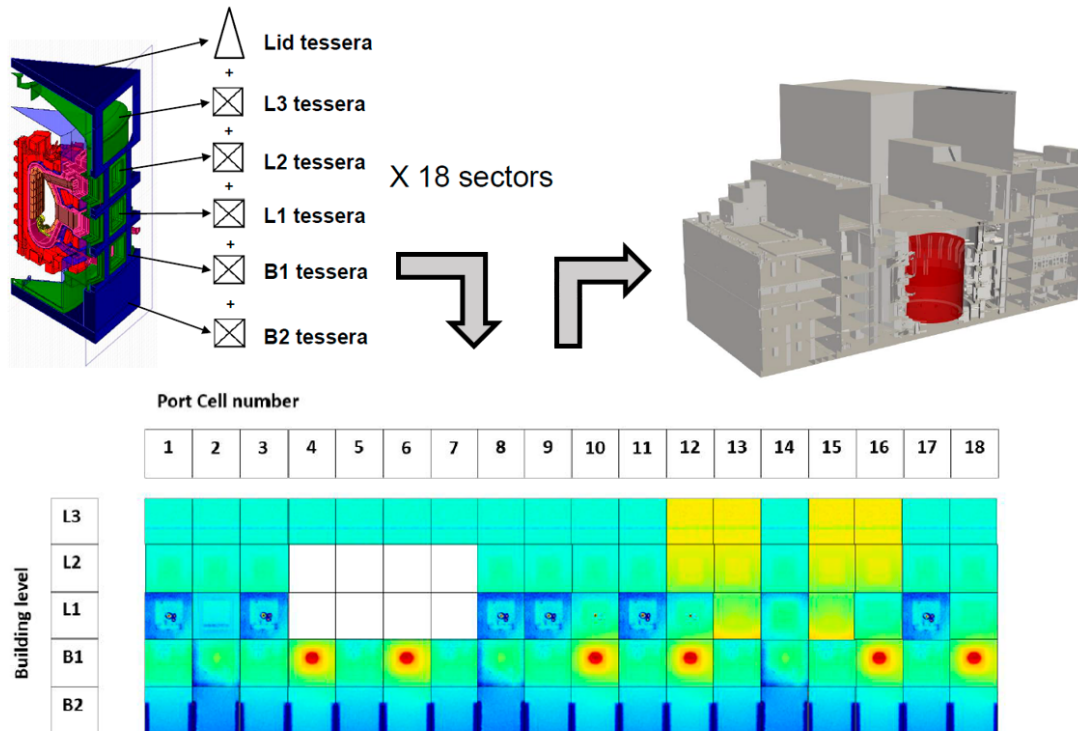


Figure 2-27. Mosaic source approach to produce an intermediate plasma source for radiation mapping in the Tokamak Complex [137][139][140].

However, regardless of the approach, building a 360° source with partial models has the following drawbacks.

First, as we have seen in the previous section, partial models do not accurately capture the lateral radiation cross-talk between the ports. Consequently, the resulting intermediate source features, unavoidably, non-physical discontinuities between ports. This can be clearly seen in the mosaic from Figure 2-27.

Particularly, in [137], the majority of tesserae of the mosaic source were computed in the so-called local approach to save computational resources. That is, pretty much all the cross-talk from the neighbor ports was neglected. That is why, in this case, the discontinuities are so obvious. On the other hand, note the L1 and L2 levels corresponding to the NB sector are not represented, however, this is not due to a technical limitation of the approach [139][140], but rather due to a decision regarding the scope of that study [137].

It could be argued that the impact of the in-bio-shield cross-talk on the radiation levels beyond the bio-shield is not significant. Certainly, the cross-talk radiation has suffered more interactions and has a lower energy and a greater angle of

incidence in the bio-shield than the radiation that travels through direct streaming paths. In other words, the cross-talk radiation is not as penetrating as the radiation streaming and it may not impact far away regions.

However, it is not possible to predict the impact of the in-bio-shield cross-talk on the radiation levels beyond the bio-shield. Therefore, the use of partial models to model intermediate radiation sources, leads to unquantified uncertainties in the radiation fields beyond the bio-shield. Not to mention the fact that the kind of non-physical discontinuities observed in Figure 2-27, with or without impact, do not give confidence on the robustness of the modelling of the intermediate radiation source. This last aspect is not trivial as, ultimately, the French authorities need to be convinced of the quality of the nuclear analysis [68][136].

The second drawback of using partial models in the modelling of an intermediate radiation source is the need to perform many independent calculations. In [137], 34 simulations were needed to model the source. This leads to a significant consumption of computational resources. Furthermore, the independent review of the intermediate source modelling is challenging as it requires the review of all the simulations and the traceability of all the partial models (one for each simulation). Ultimately, this situation also affects the reliability of the calculations.

2.3.3 Calibration of neutron detectors

The neutron detectors in fusion reactors provide measurements of the neutron emission, which indicates the fusion power, the tritium burnup and other plasma parameters [45]. Therefore, the detectors are central to the monitoring of the performance and safety of such devices. For ITER, the neutron emission rate is essential to guarantee the occupational radiation safety and to maintain a proper tritium accountancy. This rate is also one of the most important measured parameters because it will confirm the gain factor, $Q \geq 10$. Consequently, the absolute calibration of these detectors is of major relevance for ITER. Since the plasma power and the tritium burnup are considered by the French authorities as safety measurements, the neutron emission must be determined with a 10% accuracy [141], what requires a very accurate calibration process.

Multiple detectors will be deployed in ITER at different toroidal and poloidal locations, both in-vessel and ex-vessel, to measure the neutron emission in different diagnostics systems [141] (see Figure 2-28). Only the most sensitive detectors will be calibrated in experimental campaigns. The rest will be calibrated during ITER D and DT phases, using plasma reference shots and previously calibrated systems as a reference for cross-calibration.

The design of the calibration of such a comprehensive set of detectors with the required accuracy, and the calibration itself, are challenges that still require years of work. Fortunately, substantial experience in neutron detector calibration in fusion devices exists, for example, from the campaigns on JET [142]–[145], TFTR (Tokamak Fusion Test Reactor) [146], MAST (Mega Ampere Spherical Tokamak) [147], JT-60 (Japan Torus-60) [148] and LHD (Large Helical Device) [149].

As the machines and the calibration of neutron detectors have grown in complexity, neutronics simulations that support the experimental calibration campaigns play a crucial role [150]. Among other things, the simulations are used to predict and correct the distortion in the detector measurements due to aspects of the machine geometrical configuration that are different during the calibration and during the D/DT experiments (e.g. the presence of the remote-handling device that holds the calibration source); to take into account the differences in the properties of the calibration and the plasma neutron sources (i.e. spatial distributions of the neutron emission intensity, direction and energy spectrum); or to support the direct calibration of specific detectors (i.e. neutron activation system), which, at the same time, will be useful to cross-calibrate other detectors that are too far from the calibration source in the experimental campaigns. Thus, the quality and accuracy of the neutronics calculations directly affect the accuracy of the calibration of the neutron detectors.

A key aspect that determines the quality of the neutronics calculations are the geometrical models used. Geometry models have to be validated against experimental data prior to their use in support of the calibration process. This validation is normally done by comparing the measurements in the neutron detectors that are obtained experimentally during the calibration campaign with those obtained with the neutronics simulations, which should represent the exact calibration configuration.

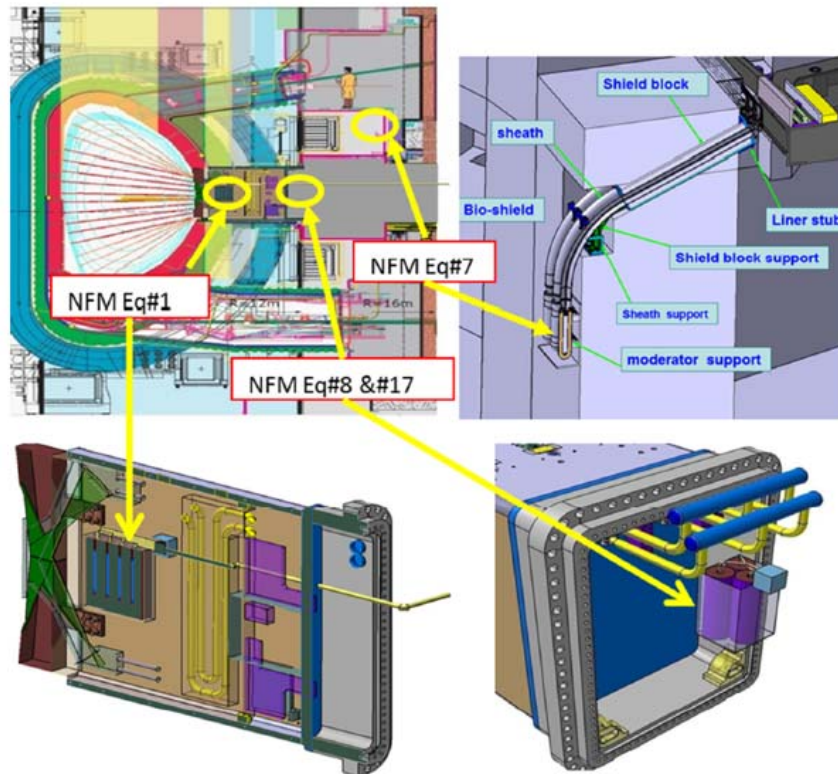


Figure 2-28. Locations where one of the most relevant types of neutron detectors, the neutron flux monitors (NFM), will be placed. Taken from [141].

Nonetheless, note that even if the models are validated for a specific application (e.g. specific calibration configuration), that does not mean that they are validated for all experimental configurations or for the conditions during the plasma campaigns. Consequently, uncertainties in the final calibration due to the neutronics modelling of the tokamaks always exist. The geometry models used in the simulations that supported the last JET calibration campaigns [142]–[145] were considered validated for the calibration configurations, however, the uncertainty in the final calibration due to the geometry models remained unevaluated, although probably with limited impact [145].

Such limited impact should not be expected in the case of the calibration at ITER, given the targeted accuracy (10%) and the increased complexity of the tokamak. Models used in the neutronics calculations to calibrate the ITER neutron detectors should be as detailed as possible to minimize the modelling uncertainties.

However, regardless of how detailed they are, using partial models to support the calibration of the ITER neutron detectors may represent a significant risk

regarding the accuracy of the calibration. This is because the calibration experiments require knowing the specific contribution to a particular detector of neutron sources that are located beyond the $40^\circ/80^\circ$ toroidal region covered by current partial models. Specifically, to be able to recreate such experiments with partial models, it would not be possible to use their boundary conditions. This means that partial models would not be able to represent the influence of the rest of the machine beyond their geometrical definition. Consequently, partial models would lead to unquantifiable uncertainties in the estimated results that could severely affect the accuracy of the calibration.

The cases exposed in 2.3.1, 2.3.2 and 2.3.3 are just few examples of very relevant applications that are affected by the partial nature of the ITER Tokamak reference models. However, there are more, like the estimation of the nuclear heating in the poloidal field superconducting magnets or the estimation of radiation fields in the tokamak due to the runaway electrons. In general, the partial nature of reference models affects the prediction of any non-local quantities and/or local quantities influenced by a long-range environment. In addition, calculations involving asymmetric sources (i.e. runaway electrons) are also affected.

As we have seen, there have been attempts, some of them quite sophisticated, to reduce the impact of the limitations of partial models for specific situations. Some of these solutions, like the mosaic approach for the intermediate plasma source, are complex approaches that are prone to errors and difficult and tedious to review independently. In addition, they cover, one by one, dedicated solutions for specific problems, that is, they are not general. But the main difficulty for all of them is that, despite their attempts to reduce the uncertainties (due to the symmetry assumption, the methodological approach used, etc) at a high price, the uncertainties themselves remain unquantified. Furthermore, the profusion of ad hoc prepared models and approaches that present unquantified uncertainties is undesirable from a safety perspective, as such a profusion increases the chances for errors and the effort spent in independent reviews.

Considering the relevance of the quantities affected by the limitations of partial models, the current level of sophistication of ITER nuclear analysis that is required to demonstrate ITER safety and the approach of ITER nuclear

operation, scheduled in 2035, the limitations of partial models represent a growing risk. It is therefore not only desirable, but mandatory to overcome them in a general and robust way.

We have seen in the previous sections, however, that the current reference models have already pushed the existing computational capabilities to the limit. Therefore, one would think that there is not much (computational) room left to solve the limitations associated to the partiality of reference models. Fortunately, in the next section we will see how recent computational developments have opened a way to find a solution.

2.4 Recent computational developments

Models like C-model, the NBI model, or combinations of these with port models like the TBM model [19], have pushed the computational capacities of MCNP and the current HPC facilities to the limit. These models do not only lead to a waste of computational resources (sometimes prohibitively) due to their high RAM memory load, but they are very difficult to manage, adapt and debug due to their loading and plotting times. As a result, performing ITER nuclear analysis with them becomes an even more challenging task.

This situation motivated my co-director, Rafael Juárez, and my colleagues, Javier Alguacil and Patrick Sauvan, at TECF3IR research group of UNED, to look into the MCNP code to inspect if there were ways to optimize its computational performance. In parallel, Oak Ridge National Laboratory was carrying out its own insights. The outcome of these examinations was very fruitful. Indeed, in [151] the main mechanisms driving the RAM memory consumption of the MCNP models were identified by Javier Alguacil and Patrick Sauvan. Furthermore, improvements on the original MCNP5 code were implemented to significantly reduce the memory consumption and loading time of the MCNP models.

In [151], they considered several fusion-related models with an increasing level of complexity to evaluate the effectivity of the improvements. They evaluated three parameters: the simulation initializing time, the memory used to store the geometry and the total memory used. These quantities were evaluated running the models considered with the modified and unmodified versions of MCNP5. The reductions observed on each quantity are presented in Table 2-4.

Table 2-4. Reductions in the initializing time and memory used by relevant fusion-related MCNP models when running with unmodified and modified versions of MCNP5 [151].

MCNP Input	Initializing time	Memory used by the geometry	Total memory used
FNG-Dose*	3.22%	89.0%	0.3%
JET*	55.54%	98.5%	5.1%
C-lite*	30.75%	94.7%	11.3%
C-lite DSM*	27.31%	96.3%	37.0%
C-lite EP12*	61.14%	98.9%	69.4%
C-lite EP11*	53.33%	97.9%	59.4%
C-Model*	17.12%	96.6%	71.9%

*: Dedicated references for these models can be found in [151].

Significant reductions were achieved in the memory taken by the geometry. Furthermore, when the geometry was the main driver of the RAM memory consumption (in comparison with the nuclear data and other aspects), significant reductions were also observed in the total memory. With respect to the loading-time, different degrees of reduction were observed, but overall they were as well remarkable.

Since [151], Patrick Sauvan has continued investigating the MCNP code and has further improved the subroutines related with the memory consumption and with the loading, plotting and simulation of the models. These further improvements have been implemented in the tool D1SUNED [97]. This tool is the ITER reference tool for SDDR calculations, but can also be used to compute the same standard nuclear responses that are calculated with MCNP. In Table 2-5, I show the RAM memory consumption and the plotting and loading times of the TBM model, integrated in C-model, that was mentioned in section 2.1.3. The figures were calculated considering both the original MCNP5 and D1SUNED.

Table 2-5. Computational loads of the EP#16 MCNP model integrated in C-model when considering MCNP5 and D1SUNED.

Quantity	Value (MCNP5)	Value (D1SUNED)	Reduction
RAM memory	10.2 GB/cpu	2.2 GB/cpu	79%
Loading time	304 min	6.5 min	98%
Plotting time	Impractical	50 min	Feasible

As can be seen, the reductions that are achieved with D1SUNED are outstanding and they have had very relevant implications for the ITER

neutronics. This is because they have opened the door to the possibility of producing neutronics models with a considerably higher degree of complexity than current ones. This is something that was unimaginable a few years ago. Indeed, since the access to HPC facilities and the development of CAD-to-MCNP tools, these developments clearly represent the next milestone in the geometry modelling of ITER geometries. In the context of this thesis, these developments have been crucial to respond to the problems posed in the previous section. Without them, the solution proposed, namely the E-lite 360° model, would not have been possible.

CHAPTER 3

E-LITE

This chapter is devoted to describing the solution proposed and developed in this thesis, namely the E-lite 360° model, to face the limitations of partial models indicated in section 2.3. I will briefly introduce E-lite in section 3.1. Then, in section 3.2, I will describe the model and the methodology followed to produce it. Finally, in section 3.3, I will provide a summary of the main aspects of the computational performance of E-lite, which proof its usability for ITER nuclear analysis.

3.1 E-lite: a 360° model of the ITER Tokamak

As we have seen, the main limitations of the ITER Tokamak reference models that I have identified in this thesis are inherent to their partial nature. It is obvious then to think that a full 360° model would be able to overcome them. Certainly, a 360° model would not have to rely on any boundary conditions. Therefore, it would be capable of representing all asymmetric features of the machine, specially the asymmetric ports distribution. In this way, it would leave behind the uncertainties derived from the symmetry assumption that is made with partial models. Furthermore, such a model could be directly used in any application requiring a full 360° definition of the geometry or the radiation sources.

As obvious as it sounds, the solution proposed in this thesis to solve the limitations of partial models was producing a 360° model of the ITER Tokamak. The key here is how to produce such a model.

Being aware of the high computational demands of the latest reference models, C-model and NBI model, a plausible approach to develop a 360° model could be by producing a simple 360° model, like that from [74]. That is, a model that represented the full tokamak, but that had a lower degree of detail and a higher level of homogenization than the current reference models.

It could be argued that such a 360° model could be sufficient to tackle the limitations of partial models identified in the previous chapter, or at least sufficient to help quantify their impact. However, as we have seen, it is very difficult, or impossible, to quantify the uncertainties in the nuclear responses introduced by any approximation in the geometry modelling. Therefore, it could be that the uncertainties and problems that are reduced by having a 360° model do not compensate the level of uncertainties introduced by its simplistic representation. This, in any case, cannot be checked.

In view of the strict quality demands of current ITER nuclear analysis, a 360° model that is as detailed and heterogeneous as possible is desirable. At least, as detailed as the current C-model and NBI model. The problem with this option is that it is unfeasible to conceive with the original MCNP capabilities and the current HPC infrastructures. However, the recent computational developments that I have just described in section 2.4 and that are included in D1SUNED, suggest that such an option is not impossible anymore.

And that is what my directors and myself have demonstrated in this thesis. We have made use of the potential of the recent computational advances to produce a 360° model of unprecedented complexity: the E-lite 360° model.

The E-lite model is based on the latest versions of C-model and the NBI model, consequently, it is the most complex model of the ITER Tokamak ever built and the first 360° model with such a degree of detail and heterogeneity. Thus, it is the most realistic representation of the ITER Tokamak ever conceived.

In Figure 3-1 - Figure 3-3, I show horizontal cross-sections of the model at B1, L1 and L2 levels, respectively. In Figure 3-4, I show a vertical cross-section. As can be seen, it represents the full tokamak up to the bio-shield and, thus, it does not need to make use of any kind of boundary conditions. Representations of all the main SSCs of the tokamak, especially of the different access ports, are included in the model.

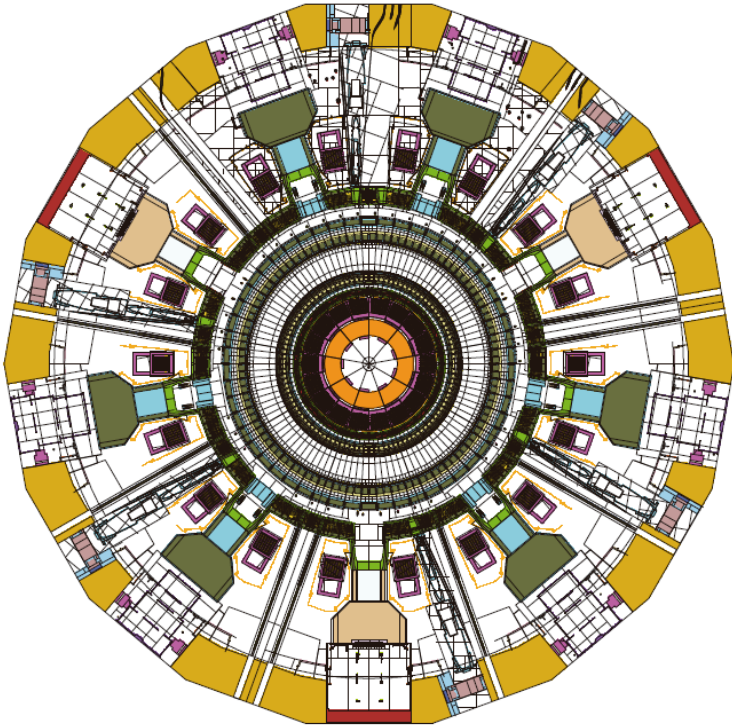


Figure 3-1. Horizontal cross-section of the E-lite model at B1 level.

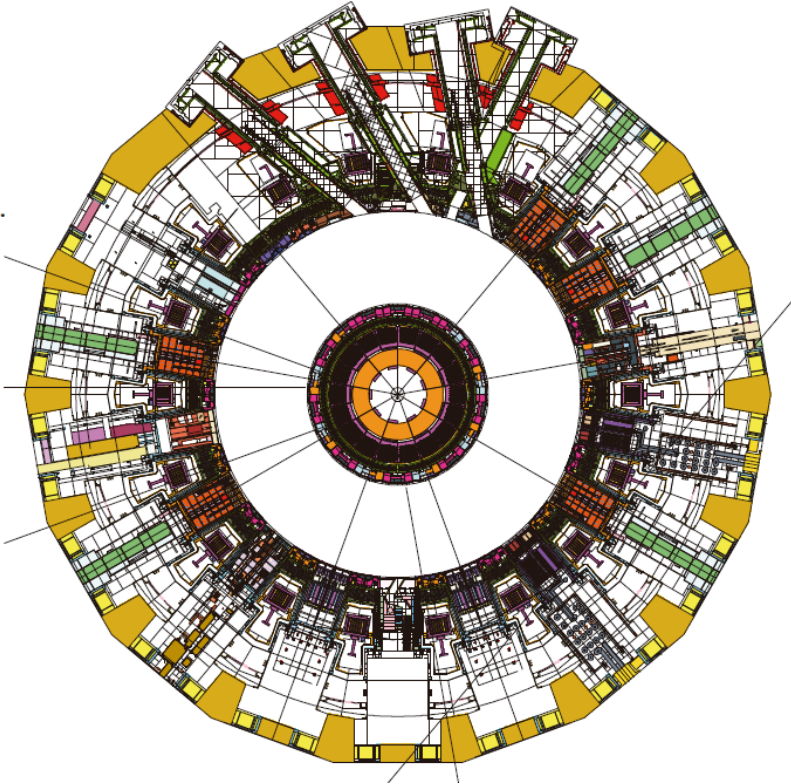


Figure 3-2. Horizontal cross-section of the E-lite model at L1 level.

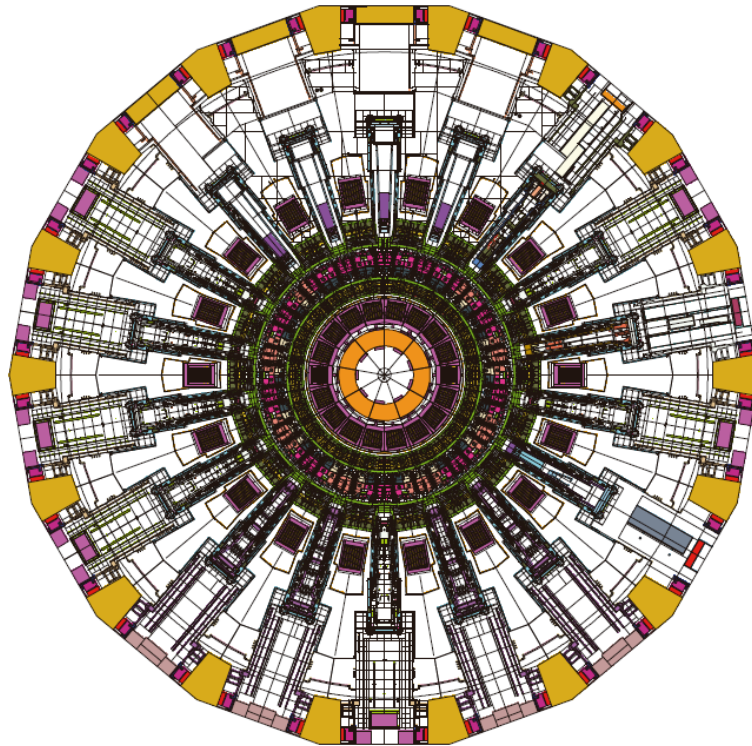


Figure 3-3. Horizontal cross-section of the E-lite model at L2 level.

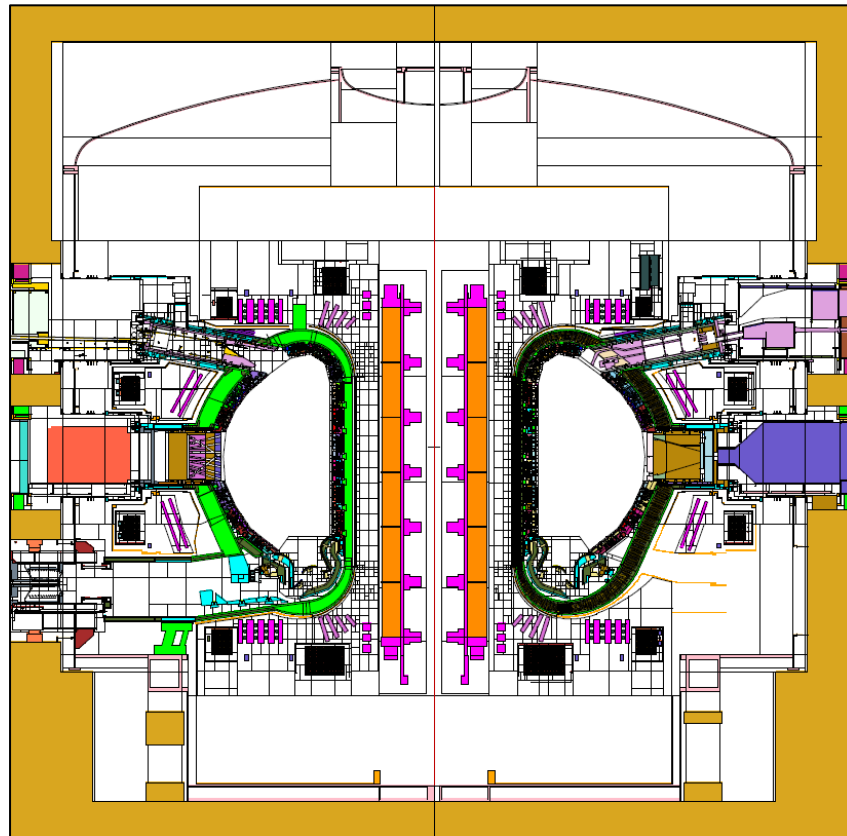


Figure 3-4. Vertical cross-section of the E-lite model.

3.2 Methodology

To produce E-lite, I took advantage of the great efforts and work already made by the ITER neutronics community. Indeed, E-lite was mainly built by recycling and re-assembling the best available representations of the tokamak existing to date, C-model (40°) and the NBI model (80°).

The general methodology followed to build E-lite comprised the following steps:

1. Production of a 360° universe block structure. This was done by repeating seven times the universe block structure of C-model and including the block structure of the latest NBI model (section 3.2.1).
2. Modification of the block structure. This was done for different purposes: to include asymmetries of the machine and/or improve its representation, to prepare the model for specific applications, etc, (section 3.2.2).
3. Population of the definitive block structure with MCNP models of the SSCs of the tokamak (blankets, vacuum vessel, thermal shield, neutral beam injectors, etc) that were taken either from C-model or the NBI model. Regarding the port plugs, which represent one of the main sources of asymmetry of the tokamak from a neutronics point of view, all the available MCNP models were included by following a strategy of ‘representative ports’ (section 3.2.3).
4. Assignment of the material cards (section 3.2.4).
5. Lost particles debugging (section 3.2.5).
6. Adaptation of the plasma source definition (section 3.2.6).
7. Definition of standard tallies to compute certain responses of interest (section 3.2.7).

These operations are now described in more detail in the following subsections.

3.2.1 Assembly of the block structure

The block structure is the group of envelope cells inside which, the detailed MCNP models of the SSCs are integrated by means of MCNP universes. The E-lite 360° block structure is the result of joining seven replicated instances of the C-model block structure ($7 \cdot 40 = 280^\circ$) and one instance of the NBI 80° model block structure. The cells and surfaces of the final block structure were

renumbered with the numjuggler² tool [152] to avoid having several cells or surfaces with the same identification number, as this situation leads to a fatal error in MCNP.

The individual block structures were positioned according to the ITER standard coordinate system, known as the Tokamak Global Coordinate System (TGCS). To do so, each one of the replicated C-model block structures was rotated by applying transformations (TR cards) to its surfaces. The block structure of the NBI model, on the other hand, was already correctly oriented. In Table 3-1, I summarize the rotation angles around the Z-axis of the TGCS (positive sense is the anti-clockwise sense) that were applied to each block structure with respect to their original position. These rotations were applied as well to the corresponding transformations of the FILL cards, which are the cell parameters that indicate which is the universe to be integrated within the envelope cell. In this way, the universes are as well rotated and located in the correct position.

Table 3-1. Rotation angles around the Z-axis (positive sense is the anti-clockwise sense) of the TGCS applied to each of one of the original block structures with respect to their original position.

Sector*	Block Structure	Rotation angle (°)
1	C-model	30
2 & 3	NBI	-
4	C-model	150
5	C-model	-170
6	C-model	-130
7	C-model	-90
8	C-model	-50
9	C-model	-10

In Figure 3-5 to Figure 3-7, horizontal cross-sections of the E-lite block structure are shown at B1, L1 and L2 level.

² Numjuggler is a software package used to automatically renumber the cell, surface and universe identification numbers in an MCNP input file while preserving the syntax and definitions.

B1 level

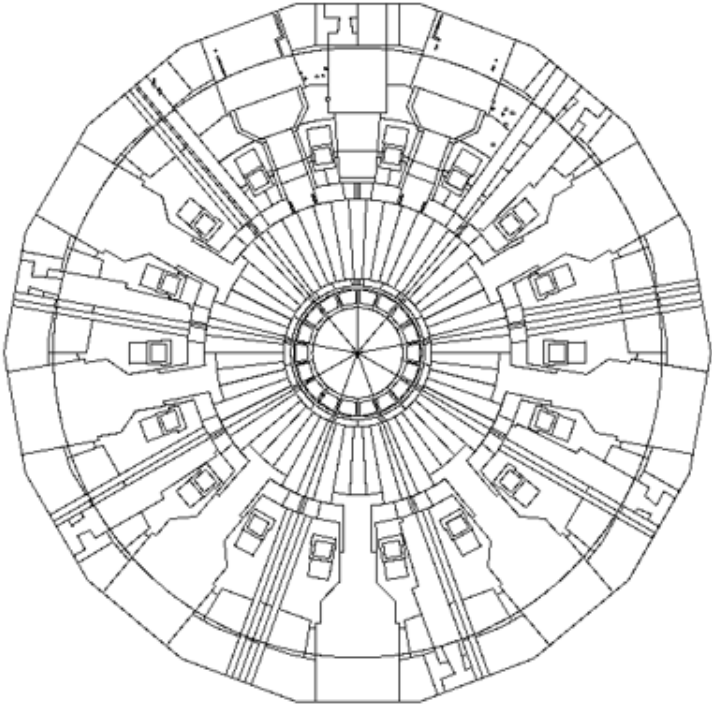


Figure 3-5. Horizontal cross-section of the E-lite Block Structure (B1 level).

L1 level

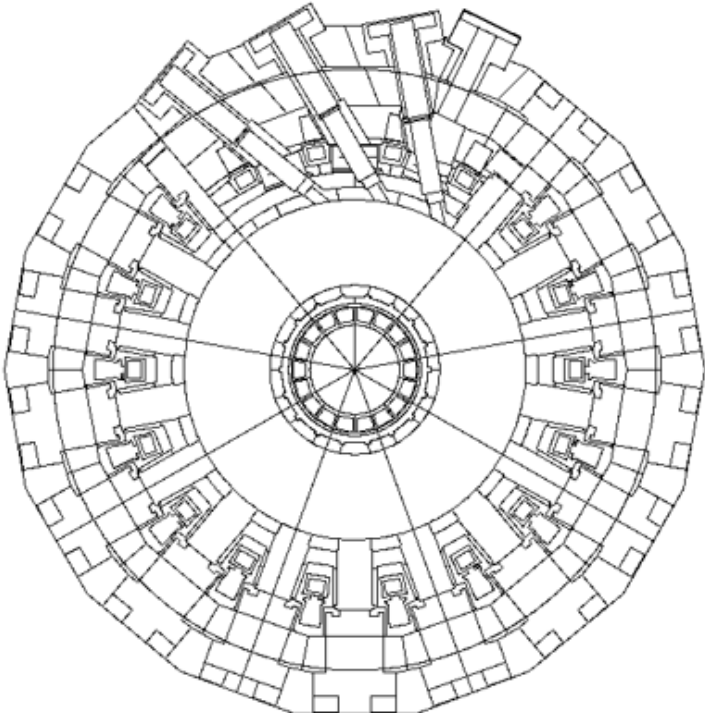


Figure 3-6. Horizontal cross-section of the E-lite block structure (L1 level).

L2 level

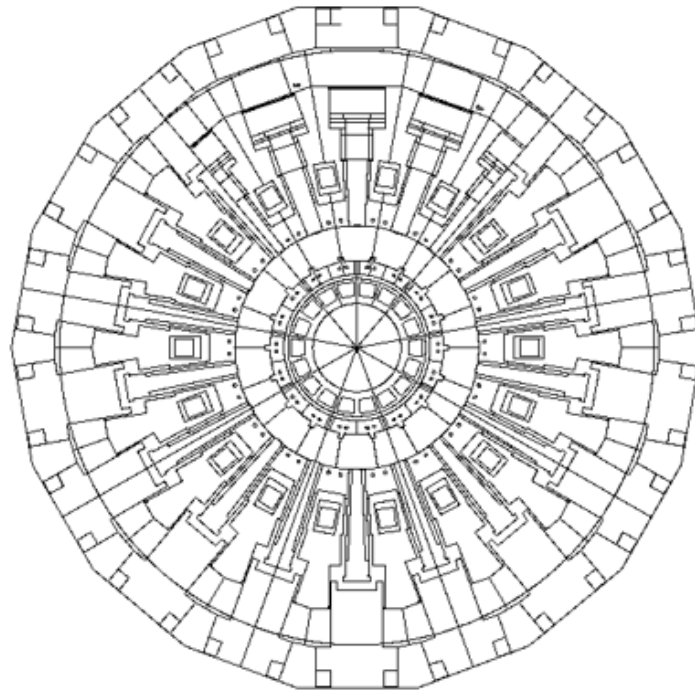


Figure 3-7. Horizontal cross-section of the E-lite block structure (L2 level).

3.2.2 Further modifications of the block structure

Once assembled, the E-lite 360° block structure was further modified. The main modifications were aimed at improving the representation of the actual tokamak baseline configuration (e.g. including asymmetric features of the machine) and facilitating, or simply making possible, the computation of specific nuclear responses. Other modifications were also made regarding the subsequent integration of universes and to correct errors in the original NBI model.

All the modifications are fully reported in [153]. I now briefly describe the most relevant ones.

B2 concrete crown

At B2 level there is a concrete structure, the so-called concrete crown, aimed at supporting the weight loads of the machine. While the NBI model did include the B2 level concrete crown, C-model did not. As shown in Figure 3-8, this is a voluminous structure. It is located below the vacuum vessel and had to be included to take into account its shielding effect at B2 level and to be consistent with the NBI sector. Therefore, a model of the crown, extracted from the latest

available CMM of the Tokamak Complex civil structures, was converted into MCNP and introduced in the E-lite block structure, as shown in Figure 3-9.

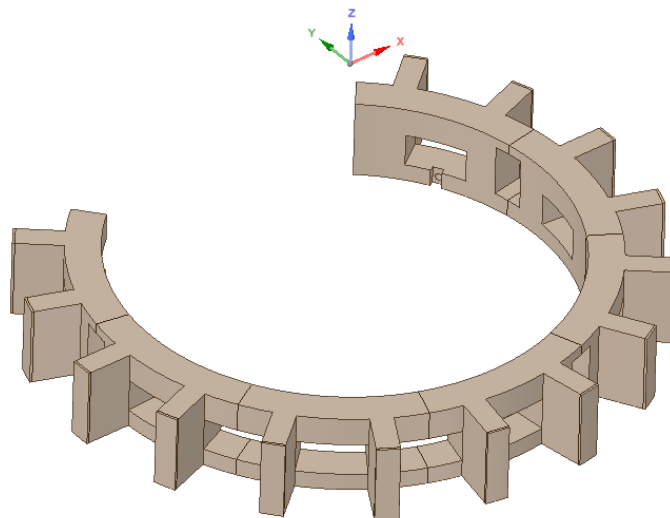


Figure 3-8. B2 level Crown. Note, the portion of the crown beneath the NBI region is not shown.

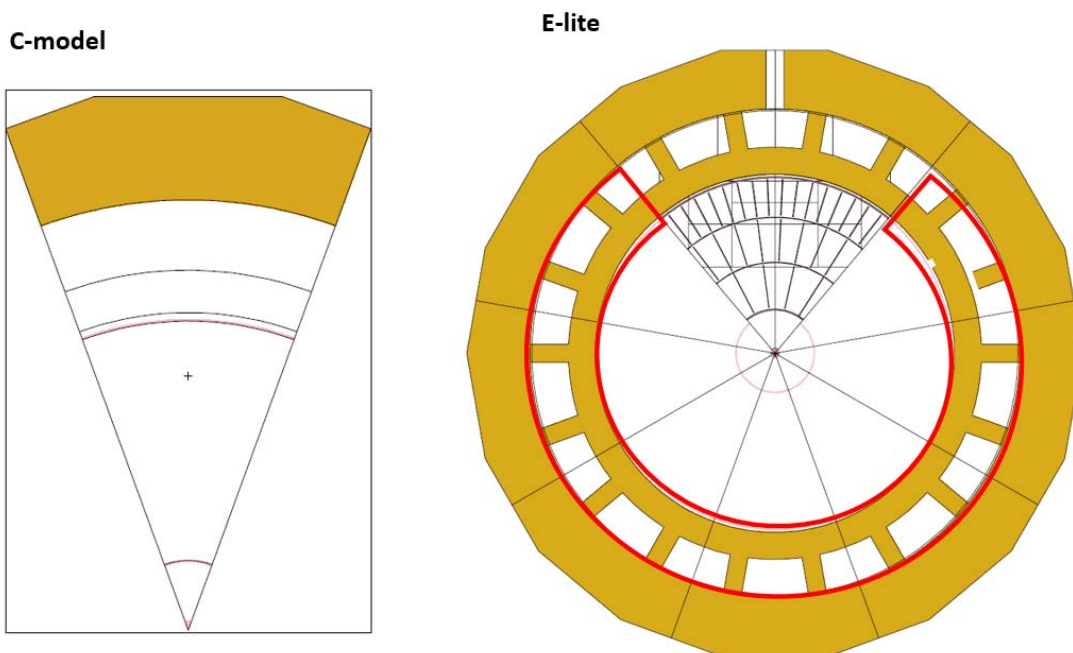


Figure 3-9. B2 level concrete Crown. On the left, C-model without crown. On the right, E-lite with the B2 level crown integrated.

B1 port configuration

The C-model block structure has the following configuration of ports/apertures at the B1 level, in order of increasing angle: divertor pipes (Y- position), an even central port (that is, a torus cryopump or a remote-handling port) and an in-

vessel viewing system port tilted towards the central port (Y+ position). This configuration (referred to as Configuration #1) is shown in Figure 3-10.

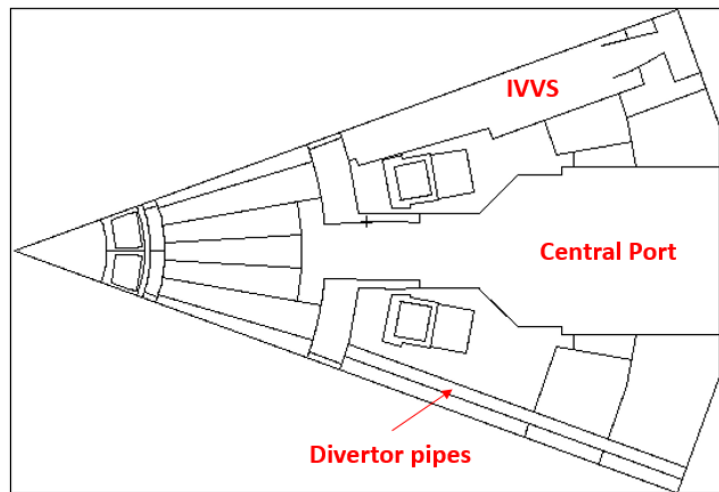


Figure 3-10. Horizontal cross-section of the B1 level configuration of C-model block structure (Configuration #1).

In line with the description of the B1 level layout provided in section 1.2.2, two further B1 configurations have been produced in order to represent:

- a) IVVS ports at B1 ports #3, #5, #9, #11, #15 and #17 alternately tilted to the previous or next port.
- b) Divertor pipes next to each IVVS port and in the ports #1, #7 and #13, which in reality have no vacuum vessel penetrations. Specifically, port #1 is closed and ports #7 and #13 feature a Cryostat Cryopump.

These two configurations, configurations #2 and #3, are shown in Figure 3-11, where individual sectors extracted from the E-lite block structure are displayed. As can be seen, configuration #2 has no IVVS envelopes and instead it has got two divertor pipes envelopes on the (Y-) and (Y+) locations, the latter being a mirrored version of the former. On the other hand, configuration #3 features one IVVS envelope and one divertor pipe envelope, just like the original C-model block structure. However, in this configuration, these envelopes are mirrored, (Y+) \leftrightarrow (Y-), with respect to the central plane.

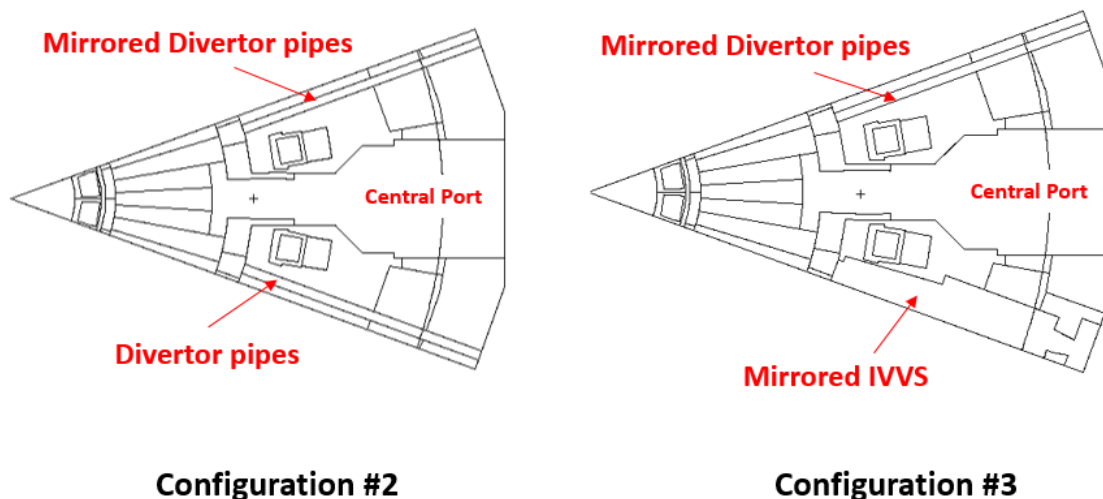


Figure 3-11. B1 level configurations #2 and #3 of the E-lite block structure.

In addition to the modifications of the IVVS and divertor pipes envelope cells, the cells hosting the VV triangular support and the VV PS4 penetrations were as well modified to adequately represent the penetrations of the IVVS and the divertor pipes through the VV. In Figure 3-12, I show cross-section of one of the sectors of the E-lite block structure (Configuration #3) showing how the VV triangular support envelope was split in three.

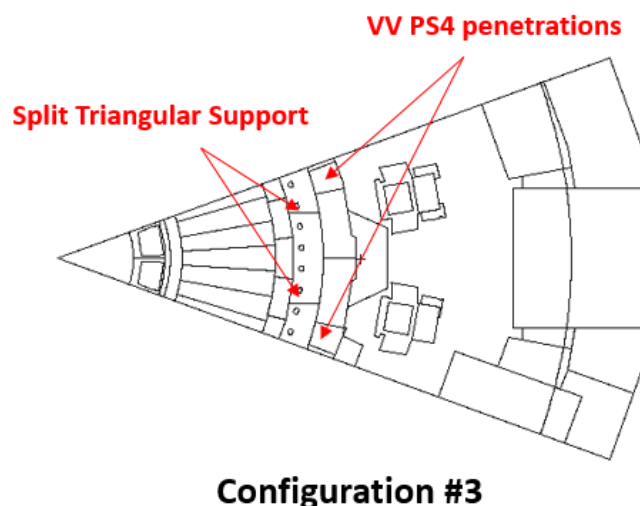


Figure 3-12. B1 level configuration #3 of E-lite block structure. It can be seen how the envelope cell of the triangular support was split. In addition, dedicated envelope cells were inserted for the VV PS4 penetrations.

In Table 3-2, I indicate which B1 level configuration was considered per tokamak sector.

Table 3-2. B1 level configurations considered in the E-lite block structure per sector.

Sector	B1 level configuration
1	1
2	2*
3	3*
4	1
5	2
6	3
7	1
8	2
9	3

“*”: these configurations were already present in the NBI model for these sectors.

Splitting of L1 and L2 port envelopes

On Figure 3-13 and Figure 3-14 I show vertical cross-sections of the C-model envelope cells that host the L1 and L2 access ports universes, respectively. These envelopes were split to be able to correctly integrate MCNP port models that were produced for previous reference models (that is, C-lite) and, therefore, were thought to be integrated in several envelope cells, not just one. Basically, the port plug region was separated from the interspace region. In case of the L1 level, the interspace region was further split. In Figure 3-13 and Figure 3-14, I show examples of how the L1 and L2 port envelopes were split, respectively.

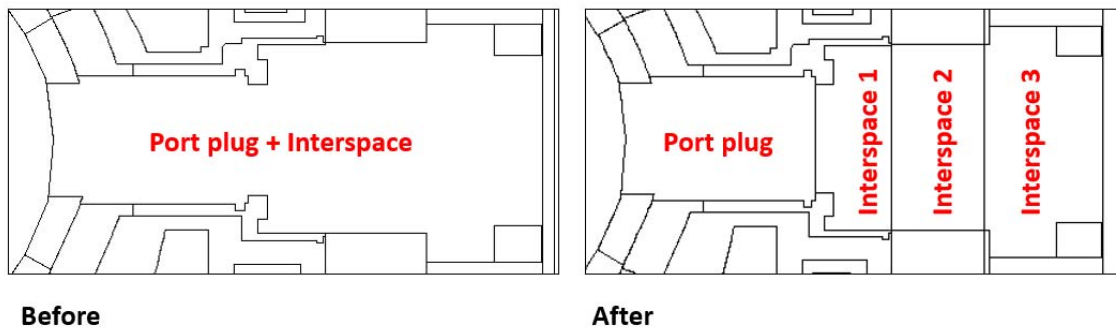


Figure 3-13. L1 port envelope cell after splitting to separate the port plug from the interspace.

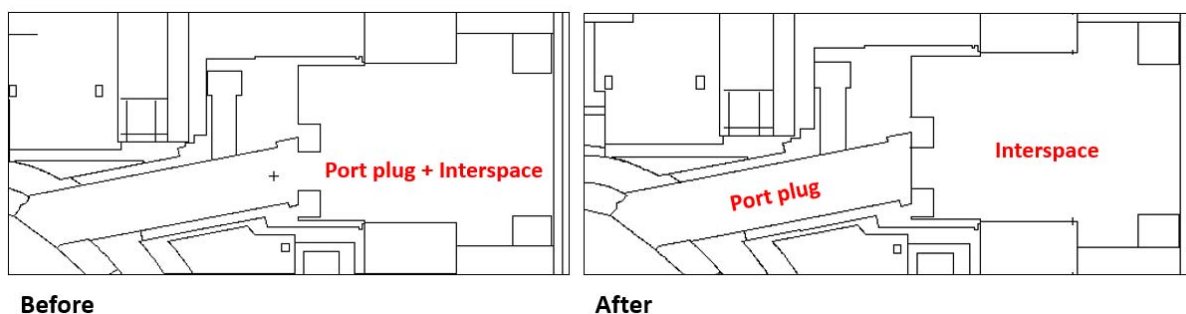


Figure 3-14. L2 port envelope cell after splitting to separate the port plug from the interspace.

Closure of equatorial port #7

Due to the Neutral Beams inclination, the L1 port #7 does not feature an aperture in the vacuum vessel. To close port #7, the L1 port envelope cells beside the NBI sector were modified and split into several envelope cells in which the bio-shield, cryostat, vacuum vessel and the blankets could be integrated. This is shown in Figure 3-15 and Figure 3-16, where horizontal and vertical cross-sections are shown, respectively.

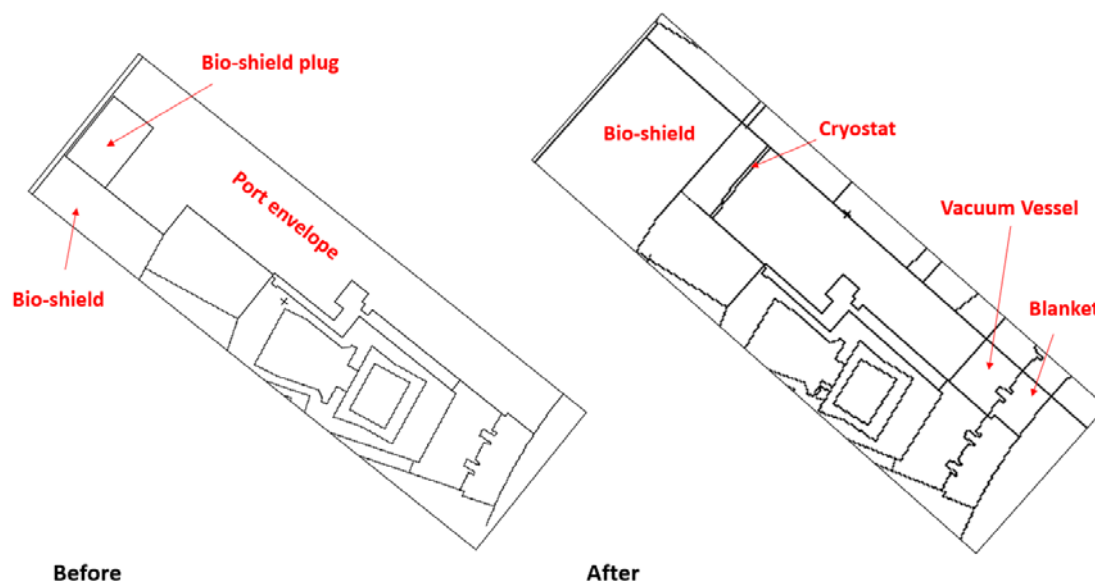


Figure 3-15. Horizontal cross-section of the E-lite L1 port envelope next to the NBI before (left) and after (right) the modifications implemented to “close” port #7.

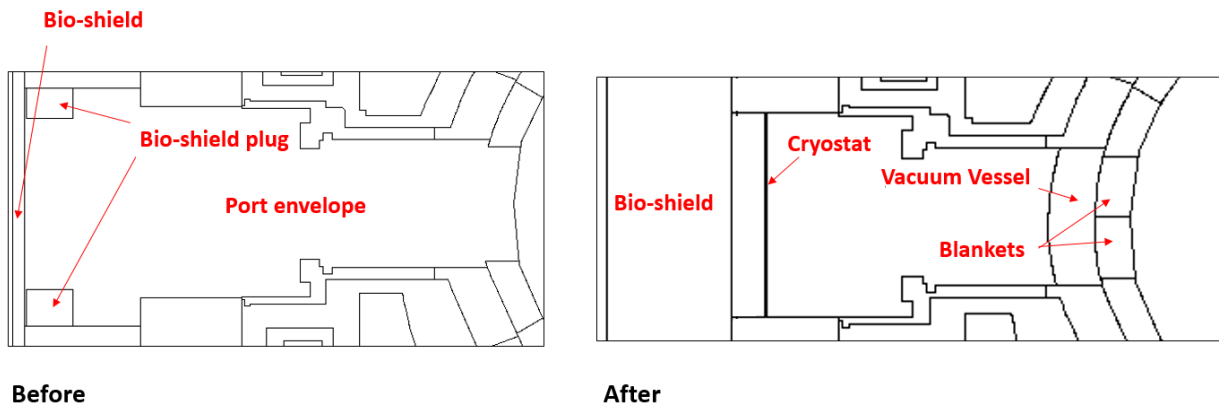


Figure 3-16. Vertical cross-section of the E-lite L1 port envelope next to the NBI before (left) and after (right) the modifications implemented to “close” port #7.

Bio-shield plugs in the NBI sectors

The NBI model did not include a representation of the B1, L1 and L2 bio-shield plugs. Thus, dedicated envelope cells were introduced in the E-lite block structure to be able to integrate the corresponding universes. In Figure 3-17, I show an example of the result of this operation for the L2 bio-shield plugs.

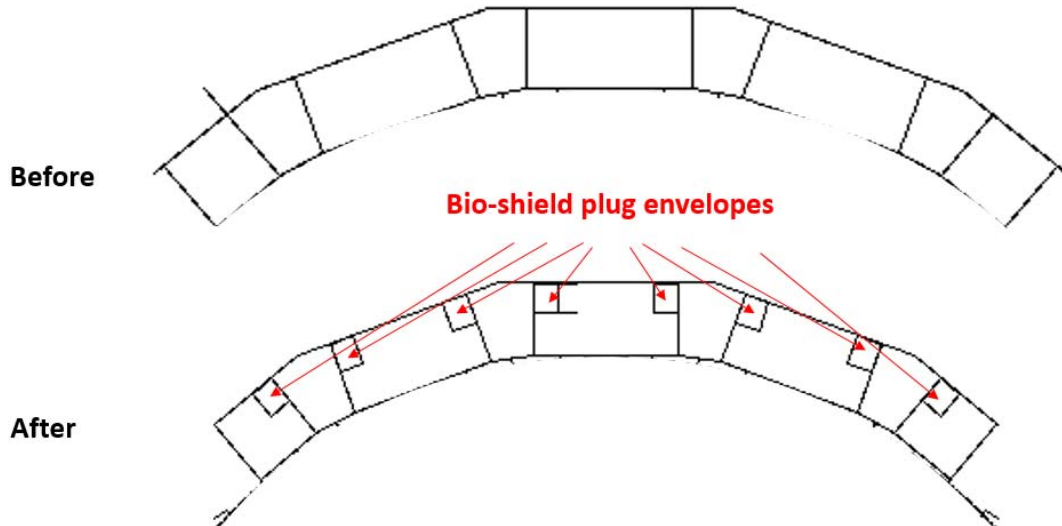


Figure 3-17. NBI block structure after inserting the L2 bio-shield plug envelopes.

Correction of allocation of universes in the NBI sectors

The original NBI model had some errors regarding the allocation of the universes of certain SSCs, such as the Torus Cryopumps ports, the toroidal field coils casings or the poloidal field coils struts. The universes were either allocated in

wrong envelope cells or directly missing. In Figure 3-18, an example is shown of a missing blanket. To solve these problems, appropriate “FILL” cards were assigned to the envelope cells hosting these universes.



Figure 3-18. Missing blanket in row #13. The blanket universe was not allocated to any envelope cell in the NBI model.

Correction of envelopes of the NBI sectors

Some of the envelopes of the NBI model block structure were wrongly defined. Consequently, the universes of the SSCs hosted inside of them were misrepresented. Furthermore, in some cases, universes could not be allocated because dedicated envelope cells did not exist. As an example, in Figure 3-19 I show a horizontal cross-section of the NBI block structure and universes at L2 level where two errors can be seen. On the one hand, the envelope of the port duct is wrongly defined as it is smaller than the port duct itself, consequently, the front cover of the port duct is missing. On the other hand, the envelope is not prepared to host the blanket manifolds that run along the upper port plugs, so these are not included. On the right-hand side of the figure, the corrected versions of the envelopes and universes are shown.

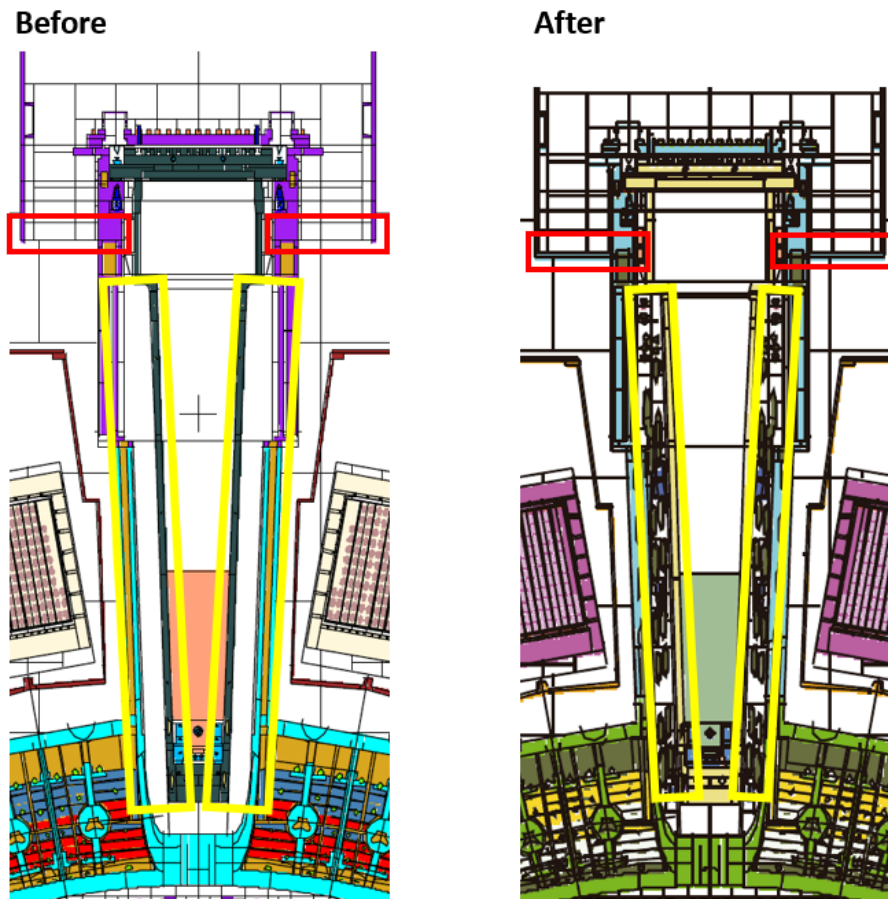


Figure 3-19. Horizontal cross-section of the NBI block structure and universes at L2 level. Two errors on the envelope cells, and their fixes, are shown. The red boxes indicate a wrong definition of the port duct envelope. The yellow boxes indicate a wrong definition of the envelopes hosting the lateral manifolds running along the sides of the upper port plug.

Blanket cut-outs

Some of the blanket modules of the tokamak feature cut-outs to host diagnostics systems or to allow radiofrequency to leave the antennas at L2 level and reach the plasma. These constitute relevant radiation streaming paths as relevant portions of the blankets, which have a shielding function, are removed. In Figure 3-20, I show one of the cut-outs that was integrated beneath the L2 ECH antennas (ports #12, #13, #15 and #16).

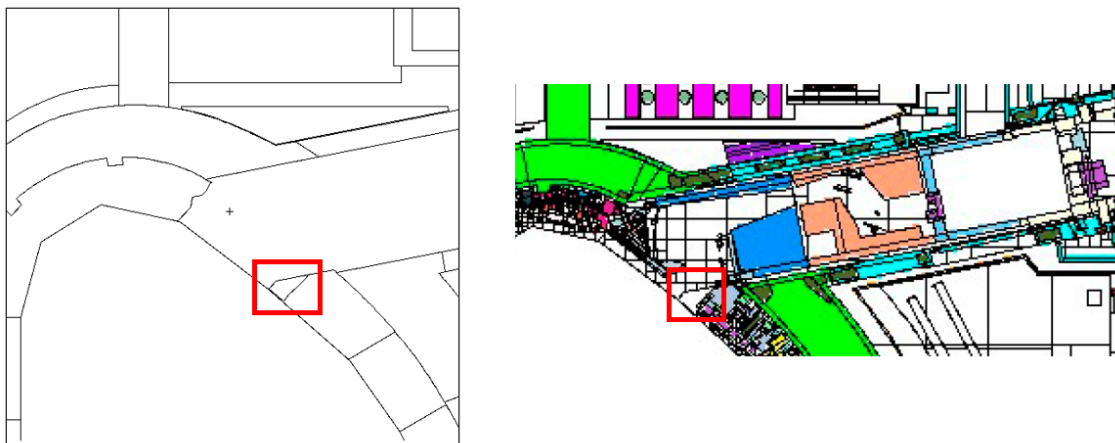


Figure 3-20. Vertical cross-section of the E-lite block structure (left) and full model (right) where I show the cut-out that was integrated below the ECH-UL ports.

Surfaces to couple the radiation transmission outside the bio-shield

One of the main applications for which E-lite was conceived is the coupling of the radiation transmission from the tokamak to the out-bio-shield regions of the Tokamak Complex (i.e. building an intermediate source). To this end, the block structure was split by several surfaces (i.e. planes and cylinders), which are meant to record information on the radiation impinging on the inner face of the bio-shield. This information can later be used to model a radiation source to predict the radiation levels beyond the bio-shield.

In Figure 3-21, I show the surfaces by which the block structure was split.

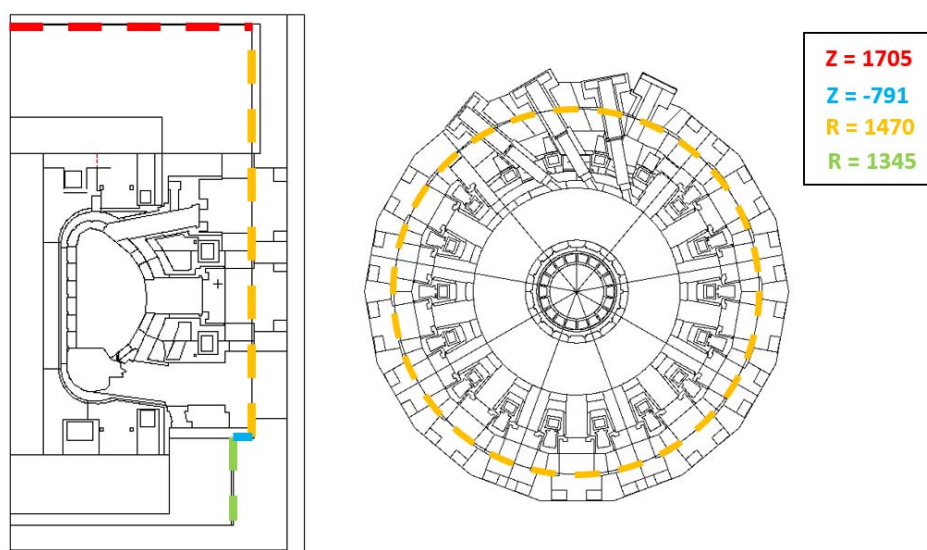


Figure 3-21. Horizontal planes and cylindrical surfaces by which the E-lite block structure was split. Horizontal planes at heights 1705 cm (red) and -791 cm (blue) were considered. Cylindrical surfaces with radius 1470 cm (yellow) and 1345 cm (green) were considered.

Splitting of the toroidal field coils to tally nuclear heating

Another useful application of the E-lite model is the computation of the nuclear heat in the magnet systems, especially in the poloidal and toroidal field coils. With respect to the toroidal field coils (TFC), it is relevant for design engineers to have an idea of where, within the magnets, the nuclear heat is being deposited. This information is essential to design the cooling system that will maintain the magnets at the required temperature. For this reason, the envelope cells of the TFC Winding Package (WP) and the TFC Casing were split into several layers and regions, respectively [154].

In Figure 3-22, I show a CAD model of the envelope cell of one of the TFC WP (there are 18 in total). The envelope cell is divided in 11 radial layers. On the other hand, on Figure 3-23 I show a CAD model of the one of the envelope cells of the TFC Casing. The envelope cell is divided in three regions, FRONT, BACK, SIDE. The division of the envelope cells in such way allows to define specific tallies to estimate the nuclear heating in a specific layer or region.

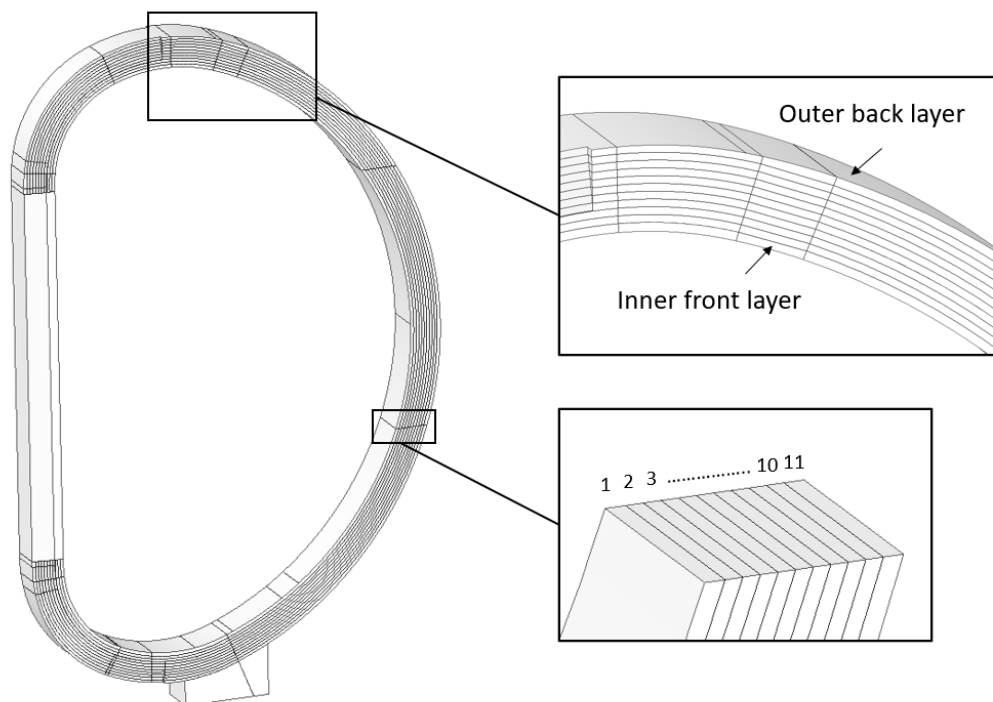


Figure 3-22. CAD model of a TFC WP divided into 11 radial layers.

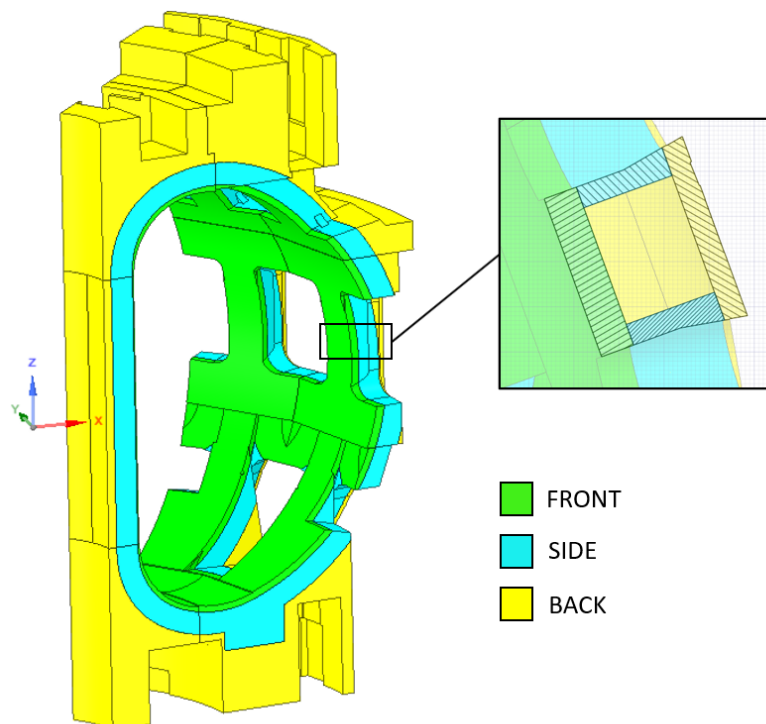


Figure 3-23. CAD model of the TFC Casings divided into 3 layers (FRONT, SIDE, BACK).

3.2.3 Allocation of universes

All the universes of the tokamak SSCs present in C-model and the NBI model were integrated in E-lite. The integration of these universes was done trying to preserve, to the extent possible, all the original cell, surface, material and universe identification numbers. However, in some cases, some renumbering was necessary (using numjuggler tool). With respect to the universes that are common to both C-model and the NBI model, it was decided to integrate in E-lite those universes that are present in the NBI model. This is because these universes contain modifications to reduce the lost particle rate (that is, geometry errors) that their homologous C-model versions do not contain.

Regarding the ITER ports, which represent one of the main sources of asymmetry of the machine from a neutronics point of view, the latest available and approved MCNP models were integrated into the E-lite model. However, since many ITER ports still do not have a dedicated representation in MCNP, a *strategy of representative ports* was followed [139][137].

This strategy was followed in 2016 in the construction of the mosaic source [139] to compute ITER Radiation Maps inside the Tokamak Complex due to the plasma radiation (excepting the NBI region) [137]. Its philosophy is to use all

available MCNP models to provide, to the extent possible, the most realistic yet conservative representation of the full machine. Specifically, available MCNP models are used to represent either the actual port or other ports that perform similar functions. For example, the MCNP model of EP#11, which is a diagnostics port, is used to represent EP#09, which is another diagnostic port for which there is no MCNP model currently available. Note that the representative ports are selected seeking a higher neutron flux streaming than that of the represented port as designed today, to be conservative. In this way, all the ports are represented either realistically or conservatively.

In some cases, the ports incorporated were modified with different purposes prior to their insertion in E-lite. Particularly, the Generic RH-LP MCNP model was modified to incorporate the optical path of the Divertor Thompson Scattering (DTS) system, which represents a large aperture in the radial direction. This system is only located in the RH-LP #8, but its optical path was integrated in all the RH-LPs (#2, #8 and #14) in line with the strategy of representative ports. Otherwise, the RH-LPs would have featured a fully shielded rack, which would have been optimistic. On the other hand, the Diagnostics Generic Upper Port Plugs incorporated in the upper ports #4-#7 were also modified. Specifically, the mass of B₄C of their Drawer Shield Modules was lowered from 624 kg to 356 kg to better represent the actual B₄C content. This modification was made according to ITER specifications. More information can be found in [153].

In Table 3-3, Table 3-4 and Table 3-5, information on the ports integrated in E-lite is summarized for B1, L1, and L2 levels, respectively. Those ports that are included by default in C-model or the NBI model are highlighted in grey.

The strategy of representative ports is rather accurate in terms of shielding for the torus cryopump and in-vessel viewing system ports at the B1 level, the test blanket module and ion cyclotron heating ports at the L1 level, and the electron cyclotron heating upper launcher ports at the L2 level, as radiation transmission through each one of these types of port is relatively similar in all its occurrences. However, the situation for diagnostics port plugs is different at the three levels of B1, L1 and L2. Each port will accommodate different systems with diverse aperture shapes and dimensions. Consequently, these are the ports most affected by the proposed approach and bring substantial levels of conservatism. Nonetheless, as new MCNP models of ports become available in the future, these

will be integrated in the same manner in future versions of E-lite and, therefore, this strategy will be gradually abandoned.

Table 3-3. B1 level ITER ports considered in E-lite. Those ports that are included by default in C-model or the NBI model are highlighted in grey.

B1 level ITER ports			
#	Actual ITER port	Representation in E-lite	Reference of MCNP report
01	Closed Port	Divertor Pipes	[110]
02	RH-LP #02	Generic RH-LP + DTS	[155] [156]
03	IVVS #03	IVVS #3	[110]
04	TCP #04	TCP #4	[113]
05	IVVS #05	IVVS #3	[110]
06	TCP #06	TCP #4	[113]
07	CCP #07	Divertor Pipes	[110]
08	RH-LP #08	Generic RH-LP + DTS	[155] [156]
09	IVVS #09	IVVS #3	[110]
10	TCP #10	TCP #4	[113]
11	IVVS #11	IVVS #3	[110]
12	TCP #12	TCP #4	[113]
13	CCP #13	Divertor Pipes	[110]
14	RH-LP #14	Generic RH-LP + DTS	[155] [156]
15	IVVS #15	IVVS #3	[110]
16	TCP #16	TCP #4	[113]
17	IVVS #17	IVVS #3	[110]
18	TCP #18	TCP #4	[113]

Table 3-4. L1 level ITER ports considered in E-lite. Those ports that are included by default in C-model or the NBI model are highlighted in grey.

L1 level ITER ports			
#	Actual ITER port	Representation in E-lite	Reference of MCNP model
01	Diagnostics EP#01	Diagnostics EP#01	[157]
02	Diagnostics EP#02	Diagnostics EP#11	[17]
03	Diagnostics EP#03	Diagnostics EP#11	[17]
04	NBI	NBI	[73]
05	NBI	NBI	[73]
06	NBI	NBI	[73]
07	NBI	NBI	[73]
08	Diagnostics EP#08	Diagnostics EP#08	[158]
09	Diagnostics EP#09	Diagnostics EP#11	[17]
10	Diagnostics EP#10	Diagnostics EP#10	[159]
11	Diagnostics EP#11	Diagnostics EP#11	[17]
12	Diagnostics EP#12	Diagnostics EP#12	[160]
13	ICH #13	ICH #15	[161]
14	ECH #14	ECH #14	[162]
15	ICH #15	ICH #15	[161]
16	TBM #16	TBM #16	[163]
17	Diagnostics EP#17	Diagnostics EP#11	[17]
18	TBM #18	TBM #16	[163]

Table 3-5. L2 level ITER ports considered in E-lite. Those ports that are included by default in C-model or the NBI model are highlighted in grey.

L2 level ITER ports			
#	Actual ITER port	Representation in E-lite	Reference of MCNP model
01	Diagnostics UP#01	Diagnostics UP#01	[164]
02	Diagnostics UP#02	Diagnostics UP#18	[165]
03	Diagnostics UP#03	Diagnostics UP#03	[166]
04	Dummy UP#04	Diagnostics Generic Equatorial Port Plug	[110]
05	Dummy UP#05	Diagnostics Generic Equatorial Port Plug	[110]
06	Dummy UP#06	Diagnostics Generic Equatorial Port Plug	[110]
07	Dummy UP#07	Diagnostics Generic Equatorial Port Plug	[110]
08	Diagnostics UP#08	Diagnostics UP#18	[165]
09	Diagnostics UP#09	Diagnostics UP#18	[165]
10	Diagnostics UP#10	Diagnostics UP#18	[165]
11	Diagnostics UP#11	Diagnostics UP#18	[165]
12	ECH-UL #12	ECH-UL #12	[167]
13	ECH-UL #13	ECH-UL #12	[167]
14	Diagnostics UP#14	Diagnostics UP#18	[165]
15	ECH-UL #15	ECH-UL #12	[167]
16	ECH-UL #16	ECH-UL #12	[167]
17	Diagnostics UP#17	Diagnostics UP#17	[168]
18	Diagnostics UP#18	Diagnostics UP#18	[165]

The general procedure to integrate the MCNP models of the ITER ports in E-lite consisted of the following steps:

- Isolation of the port MCNP model: When necessary, the ports (cell, surfaces, and materials) were isolated from the original MCNP model in which they were integrated. Due to the nature of the isolation process, unfortunately, some comment lines (i.e. not affecting the model geometry) included in the original input file to provide information were lost (e.g. comments indicating the materials used).
- Removal/Insertion/Modification of cell cards: Certain cell cards were removed (e.g. specific cards used in D1SUNED calculations) from the original MCNP model. Universe (U) cards were inserted and/or renumbered. The importance (IMP) cards of the outer cells of the models were switched from IMP=0 to IMP=1 to avoid any undesired particle killing.
- Renumbering of cell, surface and material identification numbers: The models (cells, surfaces and materials) were renumbered using

numjuggler tool to avoid overlapping of cell, surface or material identification numbers. Firstly, the models were renumbered incrementally. Then, the cells, surfaces and materials identification numbers were incremented by specific integer values.

- Lost particles debugging: When necessary, lost particles due to the overlapping of regions or the presence of coincident surfaces between the envelope and the universe were corrected.
- Adjustment of neutron cross-section libraries: The neutron cross-section libraries were adjusted as per section 3.2.4.

3.2.4 Materials

The chemical compositions of the material cards of the original universes (C-model, NBI model and ITER ports) have been preserved, except in very particular cases (see section 7.2.4 of [153]).

With respect to the neutron cross-section libraries:

- For the universes of the C-model and the NBI model, the libraries originally present have been preserved. These are FENDL-3.1d [65] and ENDF/B-VII.1 [169] or TENDL-2015 [170].
- For the MCNP models of the ITER ports, libraries have been changed to FENDL-3.1d [65] to the extent possible. This was done by using the script “FENDL.-exe” [171]. In those cases where an isotope/element is not included in this library, ENDF/B-VII.1 [169] or TENDL-2015 [170] libraries were used instead (in this order of preference).

3.2.5 Lost particles debugging

The E-lite model was debugged in an iterative process by fixing geometry errors that lead to lost particles. Many of the lost particles were inherited from the native models, and some others resulted from the integration process. The kind of errors fixed were: overlapping of cells, coincident surfaces between the universe and the envelope and absence of universe outer cells extending beyond the confinement boundaries of the envelope. The great majority of the fixes implemented consisted in either one of the following: subtracting one cell from another, slightly changing the definition of surfaces or applying slight translations to the FILL cards.

Each time, the lost particle rate (LPR) was checked by running the model in void mode with D1SUNED v3.1.4 [97] with an inward-directed biased cosine source on a spherical surface (Radius = 20 m) centered at the origin of coordinates. A final LPR of $1.3 \cdot 10^{-6}$, after running 10^8 histories, was achieved.

3.2.6 Plasma source definition

C-model and the NBI model include a definition of the standard ITER DT neutron source (Inductive operation II with 500MW of fusion power) in the form of an SDEF card [104][105]. This SDEF card was originally prepared to be run in any partial model, regardless of the toroidal section covered. Thus, just few parameters of the “CEL” distribution needed to be adapted to run in the complete 360° .

3.2.7 Standard Tallies

Various sets of standard tallies were defined for the E-lite model to compute several quantities in the ITER Tokamak during plasma operation activities [154]. The tallies were defined based on the standard tallies originally included in C-model. The groups of tallies defined were the following:

- Mesh tallies (FMESH) covering the entire geometry to compute:
 - Neutron flux in 5 energy (MeV) groups ($[E_{\min}, 10^{-6}]$, $[10^{-6}, 0.1]$, $[0.1, 1]$, $[1, 10]$, $[10, 20]$) + Total.
 - Photon flux in 4 energy (MeV) groups ($[E_{\min}, 0.01]$, $[0.01, 1]$, $[1, 5]$, $[5, 100]$) + Total.
 - DPA in SS316L(N)-IG after 4700h of full 500 MW operation.
 - Tritium, He³ and He⁴ (ppm) in B₄C after 4700h of full 500 MW operation.
 - Absorbed Dose (Gy) in silicon and polyethylene after 4700h of full 500 MW operation due to neutrons and photons.
 - Nuclear Heating (W/cm³) in SS316L(N)-IG, water and polyethylene due to neutrons and photons.
- Tallies to compute the neutron surface current density (F1) and the neutron flux (F2) on the plasma boundary.
- Tallies to compute the integral nuclear heating (F6:N,P) in the:
 - Blanket & Divertor.
 - Vacuum Vessel, Port Extensions, and Port Ducts.
 - Thermal Shields.
 - Cryostat.
 - Port plugs.
 - PF coils.

- TF coils.
- Correction coils.
- Central Solenoid.
- Duct Liners and Connecting Duct Liners (Only in sectors 2&3)
- Tallies to compute the neutron/photon flux (F4:N and F4:P) and integral nuclear heating (F6:N and F6:P) in all the TFC WP, TFC Casing and TFC Ground insulation. These tallies have radial (see end of section 3.2.2) and poloidal distributions.

3.3 Computational performance

E-lite is the most complex model of the ITER Tokamak ever conceived. This can be clearly seen in the significant increase in the number of cells, surfaces and materials of E-lite with respect to previous models (see Figure 3-24 and Table 3-6). To be honest, it was not clear from the beginning whether producing E-lite was going to be a success or not. To our knowledge, this was the first time that an attempt to produce such a complex model was made. Therefore, even with the confidence in the potential of D1SUNED capabilities, my directors and I did not know a priori what the outcome of this venture was going to be. Fortunately, in this section I demonstrate that E-lite is completely feasible and usable for ITER neutronics analyses.

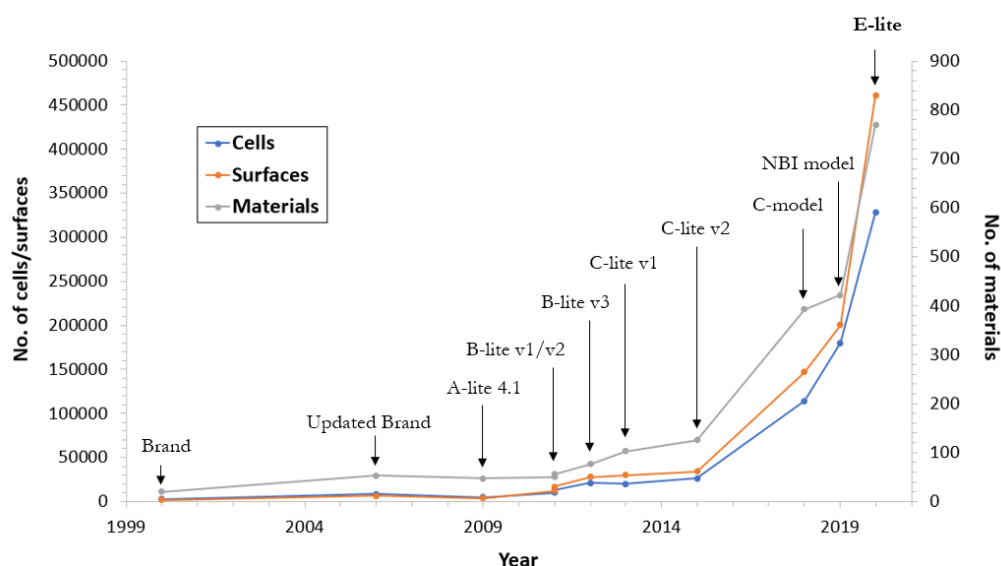


Figure 3-24. Evolution of the number of cells (blue), surfaces (orange) and materials (grey) of the ITER Tokamak reference models over the years. The number of cells, surfaces and materials of E-lite are also shown. Note there are two vertical axes.

Table 3-6. Evolution of the number of cells, surfaces and materials of the ITER Tokamak reference models over the years. The number of cells, surfaces and materials of E-lite are also shown.

Model	Year of release	No. of cells	No. of surfaces	No. of materials
Brand	2000	2936	1586	20
Updated Brand	2006	8760	6275	53
A-lite 4.1	2009	4679	3632	47
B-lite v1	2011	10084	12319	50
B-lite v2	2011	13287	17029	56
B-lite v3	2012	21216	27920	76
C-lite v1	2013	20259	29988	103
C-lite v2	2015	26045	34107	125
C-model	2018	114285	146802	393
NBI model	2019	179832	200372	422
E-lite	2020	328521	461038	770

To demonstrate that the model is usable for ITER nuclear analyses it is necessary to characterize its computational performance. This is done in Table 3-7.

Table 3-7. Computational performance of the E-lite model.

Quantity	Value
RAM (master)	20.2 GB
RAM (slave)	2.4 GB
Loading time	41.8 min
Lost-particle rate	1.3×10^{-6}
Running time	$1.8 \cdot 10^5$ cpu·h

The computational features presented here were evaluated with D1SUNED v.3.1.4 [97]. These were obtained with an Intel i7 4790 K processor and DDR3-1600 RAM (random-access memory) running in parallel with an Intel MPI (message-passing interface). Intel Fortran 2018 was used with default compilation options. RAM consumption was computed as the maximum resident set size of each process during the lifetime of an MPI parallelized simulation. Loading time was computed as the duration of a simulation of one history (number of particle histories, NPS = 1). Finally, the running time refers to a neutron-only run up to NPS = 10^{11} with the plasma neutron source and using a weight windows variance reduction produced with a global variance reduction (GVR) approach [172] with a softening power of 0.5. This simulation was the one performed for the application explained in 4.2.

All the values for computational performance are manageable in the currently available HPC infrastructures, thus, the E-lite model is perfectly usable for ITER nuclear analyses.

However, it is important to remark again that all this is possible thanks to the computational improvements incorporated in D1SUNED. Without them, E-lite would not have been feasible.

CHAPTER 4

CALCULATIONS AND EVALUATION

In this chapter I evaluate the effectiveness of E-lite in overcoming the limitations of current ITER Tokamak reference models. Specifically, I have used E-lite in the three ITER-relevant applications already identified in Chapter 2: the estimation of shutdown dose rates in port interspaces (section 4.1), the radiation mapping in the Tokamak Complex (section 4.2) and the calibration of neutron detectors (section 4.3). In all the cases, I have compared the performance of E-lite with the performance of either current partial models or methodological approaches relying on partial models.

This chapter demonstrates that E-lite is not only feasible and usable, but also highly useful and beneficial, and in some cases completely necessary, to tackle the challenges associated to specific ITER nuclear analyses.

4.1 Shutdown dose rates in port interspaces

4.1.1 Introduction

As I mentioned in section 2.3.1, partial models fail to accurately capture the radiation cross-talk. Among other things, this introduces uncertainties in the estimation of the SDDR in the port interspaces, which is subjected to the requirement of being lower than 100 $\mu\text{Sv/h}$ at 10^6 s of cooling time (about 12 days) after machine shutdown for planned hands-on maintenance activities.

In this section, I demonstrate how E-lite represents a significant improvement in terms of the cross-talk treatment with respect to partial models. To do so, I performed a nuclear analysis in which I used both C-model (40°) and E-lite

(360°) to compute and compare the SDDR in the port interspace of the Electron Cyclotron Heating (ECH) Launcher #12.

This and all the Upper Launcher (UL) ports (#12, #13, #15 and #16) have been intensely studied at TECF3IR-UNED in recent years. In fact, some of my colleagues, specially Antonio Jesús López-Revelles, performed the SDDR analysis for the Final Design Review (FDR) of the Upper Launchers [167].

The analysis of these ports is very illustrative to show the impact of the radiation cross-talk on the SDDR. Although the study was focused on UL#12, similar conclusions to the ones reached here can be expected for the rest of ULs.

4.1.2 Methodology

To represent the UL#12, I considered the MCNP model from [167], which corresponded to the baseline configuration of the UL#12 at the time of the study. A picture of the UL#12 was shown in Figure 1-16 and it is shown again in Figure 4-1.

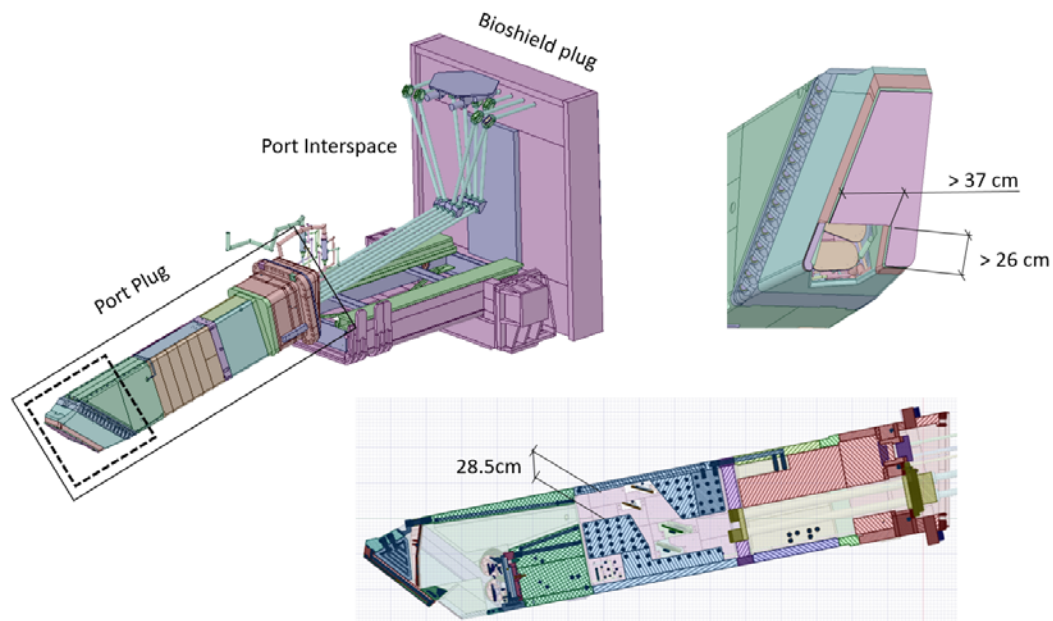


Figure 4-1. Views of ECH-Upper Launcher #12.

Since all the ULs are similar to each other, I considered the same UL MCNP model for the rest of them. The MCNP model of the UL was integrated in both C-model and E-lite (see Figure 4-2 and Figure 4-3). To recreate the environment of UL#12, I considered the same MCNP models of the neighbour ports in both C-model and E-lite.

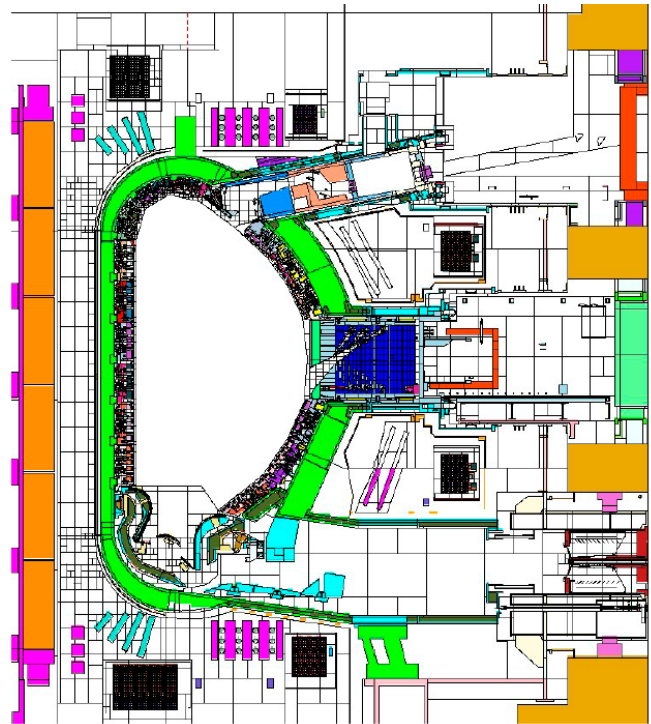


Figure 4-2. Vertical cross-section of C-model where we can see the ECH-UL #12 integrated at the top part.

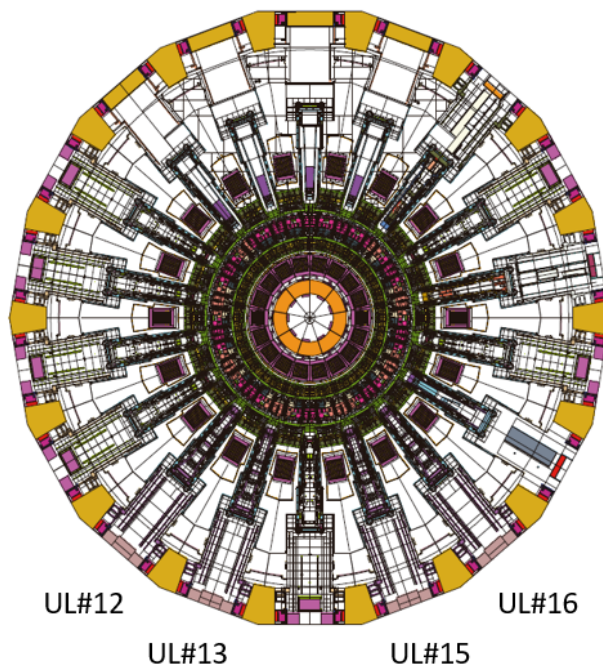


Figure 4-3. Horizontal cross-section of E-lite with the four ULs indicated at the bottom.

The calculations were run with D1SUNED v3.1.4 [97], which is the ITER reference code for SDDR calculations [59]. The code is a modification of MCNP [63], in which the Direct 1-Step (D1S) [126] methodology to compute SDDR was implemented.

In D1SUNED, the parent isotopes, pathways and daughter radioisotopes to be considered in a calculation have to be indicated in an external file, i.e. the reactions file. In Table 4-1, I indicate the pathways considered for this calculation. The time correction factors are provided in Table 4-2. The latter are normalized according to the source term value considered, 1.773E+20 n/s, which represents the neutron production rate at 500 MW of operation.

Table 4-1. Parent isotopes, pathways and radioisotopes considered in the simulation.

Isotope	Pathway	Reaction File		
²² Na	²³ Na (n, 2n) ²² Na	11023.99c	16	11022
³⁷ Ar	⁴⁰ Ca (n, α) ³⁷ Ar	20040.99c	107	18037
⁴⁷ Ca	⁴⁶ Ca (n, γ) ⁴⁷ Ca	20046.99c	102	20047
	⁴⁸ Ca (n, 2n) ⁴⁷ Ca	20048.99c	16	20047
⁴⁶ Sc	⁴⁵ Sc (n, γ) ⁴⁶ Sc	21045.99c	102	21046
	⁴⁵ Sc (n, γ) ^{46m} Sc (IT →) ⁴⁶ Sc			
	⁴⁶ Ti (n, p) ⁴⁶ Sc	22046.99c	103	21046
	⁴⁶ Ti (n, p) ^{46m} Sc (IT →) ⁴⁶ Sc			
	⁴⁷ Ti (n, np) ⁴⁶ Sc	22047.99c	28	21046
	⁴⁷ Ti (n, np) ^{46m} Sc (IT →) ⁴⁶ Sc			
	⁴⁷ Ti (n, d) ⁴⁶ Sc	22047.99c	104	21046
⁴⁷ Ti (n, d) ^{46m} Sc (IT →) ⁴⁶ Sc				
⁴⁷ Sc	⁴⁷ Ti (n, p) ⁴⁷ Sc	22047.99c	103	21047
	⁴⁸ Ti (n, np) ⁴⁷ Sc	22048.99c	28	21047
	⁴⁸ Ti (n, d) ⁴⁷ Sc	22048.99c	104	21047
⁵¹ Cr	⁵⁰ Cr (n, γ) ⁵¹ Cr	24050.99c	102	24051
	⁵² Cr (n, 2n) ⁵¹ Cr	24052.99c	16	24051
	⁵⁴ Fe (n, α) ⁵¹ Cr	26054.99c	107	24051
⁵⁴ Mn	⁵⁵ Mn (n, 2n) ⁵⁴ Mn	25055.99c	16	25054
	⁵⁴ Fe (n, p) ⁵⁴ Mn	26054.99c	103	25054
	⁵⁶ Fe (n, t) ⁵⁴ Mn	26056.99c	105	25054
	⁵⁸ Ni (n, pa) ⁵⁴ Mn	28058.99c	112	25054
⁵⁵ Fe	⁵⁴ Fe (n, γ) ⁵⁵ Fe	26054.99c	102	26055
	⁵⁶ Fe (n, 2n) ⁵⁵ Fe	26056.99c	16	26055
⁵⁹ Fe	⁵⁸ Fe (n, γ) ⁵⁹ Fe	26058.99c	102	26059
	⁵⁹ Co (n, p) ⁵⁹ Fe	27059.99c	103	26059
	⁶² Ni (n, α) ⁵⁹ Fe	28062.99c	107	26059
⁵⁷ Co	⁵⁸ Ni (n, np) ⁵⁷ Co	28058.99c	28	27057
	⁵⁸ Ni (n, d) ⁵⁷ Co	28058.99c	104	27057
⁵⁸ Co	⁵⁹ Co (n, 2n) ⁵⁸ Co	27059.99c	16	27058
	⁵⁹ Co (n, 2n) ^{58m} Co (IT →) ⁵⁸ Co			
	⁵⁸ Ni (n, p) ⁵⁸ Co	28058.99c	103	27058
	⁵⁸ Ni (n, p) ^{58m} Co (IT →) ⁵⁸ Co			
⁶⁰ Co	⁵⁹ Co (n, γ) ⁶⁰ Co	27059.99c	102	27060
	⁵⁹ Co (n, γ) ^{60m} Co (IT →) ⁶⁰ Co			
	⁶⁰ Ni (n, p) ⁶⁰ Co	28060.99c	103	27060
	⁶⁰ Ni (n, p) ^{60m} Co (IT →) ⁶⁰ Co			
	⁶¹ Ni (n, np) ⁶⁰ Co	28061.99c	28	27060
	⁶¹ Ni (n, np) ^{60m} Co (IT →) ⁶⁰ Co			
	⁶¹ Ni (n, d) ⁶⁰ Co	28061.99c	104	27060
	⁶¹ Ni (n, d) ^{60m} Co (IT →) ⁶⁰ Co			
	⁶³ Cu (n, α) ⁶⁰ Co	29063.99c	107	27060
⁶³ Cu (n, α) ^{60m} Co (IT →) ⁶⁰ Co				

^{65}Zn	$^{64}\text{Zn} (n, \gamma) ^{65}\text{Zn}$	30064.99c	102	30065
	$^{66}\text{Zn} (n, 2n) ^{65}\text{Zn}$	30066.99c	16	30065
^{84}Rb	$^{85}\text{Rb} (n, 2n) ^{84}\text{Rb}$	37085.99c	16	37084
	$^{85}\text{Rb} (n, 2n) ^{84\text{m}}\text{Rb} (IT \rightarrow) ^{84}\text{Rb}$			
	$^{84}\text{Sr} (n, p) ^{84}\text{Rb}$	38084.99c	103	37084
	$^{84}\text{Sr} (n, p) ^{84\text{m}}\text{Rb} (IT \rightarrow) ^{84}\text{Rb}$			
^{86}Rb	$^{85}\text{Rb} (n, \gamma) ^{86}\text{Rb}$	37085.99c	102	37086
	$^{85}\text{Rb} (n, \gamma) ^{86\text{m}}\text{Rb} (IT \rightarrow) ^{86}\text{Rb}$			
	$^{87}\text{Rb} (n, 2n) ^{86}\text{Rb}$	37087.99c	16	37086
	$^{87}\text{Rb} (n, 2n) ^{86\text{m}}\text{Rb} (IT \rightarrow) ^{86}\text{Rb}$			
	$^{86}\text{Sr} (n, p) ^{86}\text{Rb}$	38086.99c	103	37086
	$^{86}\text{Sr} (n, p) ^{86\text{m}}\text{Rb} (IT \rightarrow) ^{86}\text{Rb}$			
^{85}Sr	$^{84}\text{Sr} (n, \gamma) ^{85}\text{Sr}$	38084.99c	102	38085
	$^{84}\text{Sr} (n, \gamma) ^{85\text{m}}\text{Sr} (IT \rightarrow) ^{85}\text{Sr}$			
	$^{86}\text{Sr} (n, 2n) ^{85}\text{Sr}$	38086.99c	16	38085
	$^{86}\text{Sr} (n, 2n) ^{85\text{m}}\text{Sr} (IT \rightarrow) ^{85}\text{Sr}$			
^{88}Y	$^{89}\text{Y} (n, 2n) ^{88}\text{Y}$	39089.99c	16	39088
$^{92\text{m}}\text{Nb}$	$^{93}\text{Nb} (n, 2n) ^{92\text{m}}\text{Nb}$	41093.99c	316	41092
	$^{92}\text{Mo} (n, p) ^{92\text{m}}\text{Nb}$	42092.99c	403	41092
^{124}Sb	$^{123}\text{Sb} (n, \gamma) ^{124}\text{Sb}$	51123.99c	102	51124
	$^{123}\text{Sb} (n, \gamma) ^{124\text{m}}\text{Sb} (IT \rightarrow) ^{124}\text{Sb}$			
	$^{123}\text{Sb} (n, \gamma) ^{124\text{n}}\text{Sb} (IT \rightarrow) ^{124\text{m}}\text{Sb} (IT \rightarrow) ^{124}\text{Sb}$			
^{134}Cs	$^{133}\text{Cs} (n, \gamma) ^{134}\text{Cs}$	55133.99c	102	55134
	$^{133}\text{Cs} (n, \gamma) ^{134\text{m}}\text{Cs} (IT \rightarrow) ^{134}\text{Cs}$			
^{152}Eu	$^{151}\text{Eu} (n, \gamma) ^{152}\text{Eu}$	63151.99c	102	63152
	$^{153}\text{Eu} (n, 2n) ^{152}\text{Eu}$	63153.99c	16	63152
^{154}Eu	$^{153}\text{Eu} (n, \gamma) ^{154}\text{Eu}$	63153.99c	102	63154
	$^{153}\text{Eu} (n, \gamma) ^{154\text{m}}\text{Eu} (IT \rightarrow) ^{154}\text{Eu}$			
^{160}Tb	$^{159}\text{Tb} (n, \gamma) ^{160}\text{Tb}$	65159.99c	102	65160
^{181}Hf	$^{184}\text{W} (n, \alpha) ^{181}\text{Hf}$	74184.99c	107	72181
^{182}Ta	$^{181}\text{Ta} (n, \gamma) ^{182}\text{Ta}$	73181.99c	102	73182
	$^{181}\text{Ta} (n, \gamma) ^{182\text{m}}\text{Ta} (IT \rightarrow) ^{182}\text{Ta}$			
	$^{181}\text{Ta} (n, \gamma) ^{182\text{n}}\text{Ta} (IT \rightarrow) ^{182\text{m}}\text{Ta} (IT \rightarrow) ^{182}\text{Ta}$			
	$^{182}\text{W} (n, p) ^{182}\text{Ta}$	74182.99c	103	73182
	$^{182}\text{W} (n, p) ^{182\text{m}}\text{Ta} (IT \rightarrow) ^{182}\text{Ta}$			
	$^{182}\text{W} (n, p) ^{182\text{n}}\text{Ta} (IT \rightarrow) ^{182\text{m}}\text{Ta} (IT \rightarrow) ^{182}\text{Ta}$			
	$^{183}\text{W} (n, np) ^{182}\text{Ta}$	74183.99c	28	73182
	$^{183}\text{W} (n, np) ^{182\text{m}}\text{Ta} (IT \rightarrow) ^{182}\text{Ta}$			
	$^{183}\text{W} (n, np) ^{182\text{n}}\text{Ta} (IT \rightarrow) ^{182\text{m}}\text{Ta} (IT \rightarrow) ^{182}\text{Ta}$			
	$^{183}\text{W} (n, d) ^{182}\text{Ta}$	74183.99c	104	73182
	$^{183}\text{W} (n, d) ^{182\text{m}}\text{Ta} (IT \rightarrow) ^{182}\text{Ta}$			
	$^{183}\text{W} (n, d) ^{182\text{n}}\text{Ta} (IT \rightarrow) ^{182\text{m}}\text{Ta} (IT \rightarrow) ^{182}\text{Ta}$			
^{181}W	$^{180}\text{W} (n, \gamma) ^{181}\text{W}$	74180.99c	102	74181
	$^{182}\text{W} (n, 2n) ^{181}\text{W}$	74182.99c	16	74181
^{187}W	$^{186}\text{W} (n, \gamma) ^{187}\text{W}$	74186.99c	102	74187
^{233}Pa	$^{232}\text{Th} (n, \gamma) ^{233}\text{Th} (\beta^- \rightarrow) ^{233}\text{Pa}$	90232.99c	102	91233

Table 4-2. Time correction factors considered in the calculations.

Radioisotope	Time correction factor	Radioisotope	Time correction factor
Na22	$4.737 \cdot 10^{-2}$	Rb86	$8.403 \cdot 10^{-2}$
Ar37	$8.355 \cdot 10^{-2}$	Sr85	$8.286 \cdot 10^{-2}$
Ca47	$8.701 \cdot 10^{-2}$	Y88	$8.001 \cdot 10^{-2}$
Sc46	$8.184 \cdot 10^{-2}$	Nb92m	$8.485 \cdot 10^{-2}$
Sc47	$8.834 \cdot 10^{-2}$	Sb124	$8.303 \cdot 10^{-2}$
Cr51	$8.370 \cdot 10^{-2}$	Cs134	$5.028 \cdot 10^{-2}$
Mn54	$6.296 \cdot 10^{-2}$	Eu152	$2.066 \cdot 10^{-2}$
Fe55	$4.672 \cdot 10^{-2}$	Eu154	$2.816 \cdot 10^{-2}$
Fe59	$8.340 \cdot 10^{-2}$	Tb160	$8.253 \cdot 10^{-2}$
Co57	$6.541 \cdot 10^{-2}$	Hf181	$8.344 \cdot 10^{-2}$
Co58	$8.260 \cdot 10^{-2}$	Ta182	$7.926 \cdot 10^{-2}$
Co60	$3.675 \cdot 10^{-2}$	W181	$7.865 \cdot 10^{-2}$
Zn65	$6.735 \cdot 10^{-2}$	W187	$9.882 \cdot 10^{-2}$
Rb84	$8.358 \cdot 10^{-2}$	Pa233	$8.372 \cdot 10^{-2}$

The irradiation scenario considered was the full ITER SA-2 [173], shown in Table 4-3. The SDDR was computed at 10^6 seconds of cooling time after the complete scenario.

Table 4-3. SA-2 Irradiation scenario [173].

Duration	Fusion power (MW)	Repetition
2 yr	2.68	Once
10 yr	20.6	
0.667 yr	0	
1.325 yr	41.5	
3920 s	0	17 times
400 s	500	
3920 s	0	3 times
400 s	700	

The official D1SUNED cross-section data were considered [30] for the parent isotopes tabulated in Table 4-1. These data were made by combining FENDL3.1d [65] library for neutron transport, and EAF2007 [64] library for activation. For the rest of isotopes, the original data included in C-model and E-lite were considered. MCPLIB84 cross-sections library [174] was considered for the decay photon transport.

The C-model and E-lite calculations were run to an NPS of $1 \cdot 10^9$ and $6 \cdot 10^9$, respectively. The Global Variance Reduction (GVR) [172] technique was used to be able to speed up the calculations. A softening power of 0.5 was considered.

The SDDR was computed in the tallies shown in Figure 4-4. These tallies represent workers (dimensions $60 \times 44 \times 190 \text{ cm}^3$) standing at the front of the

UL interspace, on the right and left maintenance corridors, respectively. These are the tallies where the highest SDDRs are expected. The ICRP-74 fluence-to-dose conversion factors recommended by ITER were considered [175].

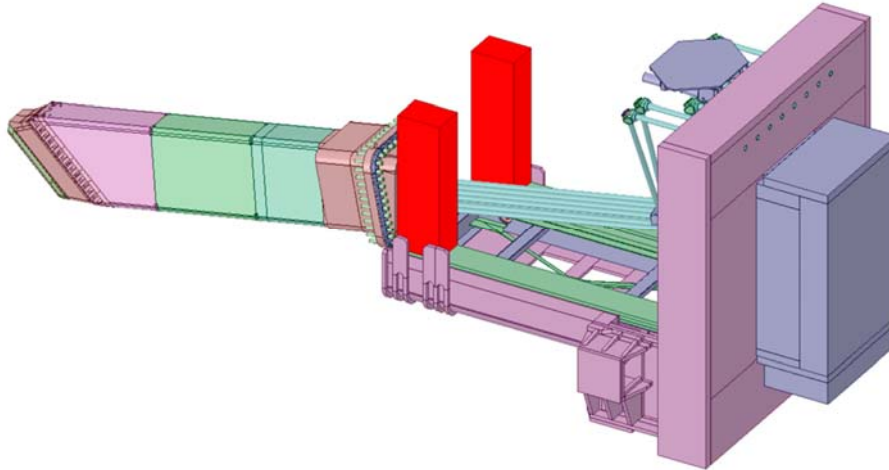


Figure 4-4. View of the ECH-UL #12. The two SDDR tallies representing workers in the most exposed positions of the lateral corridors are shown in red.

Finally, to be able to quantify the cross-talk from the neighbour ports towards the port interspace of UL#12, in the E-lite calculation I applied the CF (Cell Flagging) MCNP card to all the envelope cells hosting the port plugs of the tokamak. The CF cards allow to discern the contribution to a specific tally of: (i) the decay photons that are produced by neutrons that first travelled through a specific (flagged) cell and (ii) decay photons that travelled through a specific (flagged) cell.

4.1.3 Results and discussion

In Table 4-4, I show the results of the SDDR in the port interspace of UL#12 for both tallies and for both C-model and E-lite.

Table 4-4. SDDR ($\mu\text{Sv/h}$), and relative error, in the port interspace of UL#12 for both tallies (i.e. left and right corridors) and for both C-model and E-lite.

	Left corridor		Right corridor	
	SDDR ($\mu\text{Sv/h}$)	Relative error	SDDR ($\mu\text{Sv/h}$)	Relative error
C-model	654	0.007	672	0.006
E-lite	485	0.03	518	0.03

In both cases, it is clear that the SDDR limit of 100 $\mu\text{Sv/h}$ at 10^6 seconds of cooling time is not met by far. Shielding measures were developed in a collaboration between TECF3IR-UNED and IO to reduce the SDDR levels below the limit, however, these measures exceed the scope of this section.

Regardless of this fact, the most striking aspect of these results is that C-model SDDR values are 169 $\mu\text{Sv/h}$ (34.8%) and 154 $\mu\text{Sv/h}$ (29.7%) higher for the left and right corridor tallies, respectively, than those of E-lite. Note these differences already represent SDDR values that are larger than the 100 $\mu\text{Sv/h}$ limit that has to be fulfilled, what makes them specially concerning.

To understand the reason for these differences we have to, first, analyze the values from Table 4-5 - Table 4-7, where I tabulate the contribution (i.e. cross-talk) from the different Lower, Equatorial and Upper ports, respectively, to the SDDR in the port interspace of the UL#12. These values were calculated with E-lite.

Table 4-5. SDDR ($\mu\text{Sv/h}$), and relative error, in the port interspace of UL#12 for both tallies (i.e. left and right corridors) due to each of the different lower ports at B1 level.

	Left corridor		Right corridor	
	SDDR ($\mu\text{Sv/h}$)	Relative error	SDDR ($\mu\text{Sv/h}$)	Relative error
LP#01	0.0	0.0	0.0	0.0
LP#02	0.0	1.0	0.0	0.0
LP#03	0.0	0.7	0.0	1.0
LP#04	0.0	1.0	0.0	0.8
LP#05	0.0	1.0	0.0	1.0
LP#06	0.0	0.7	0.0	1.0
LP#07	0.0	1.0	0.0	0.0
LP#08	0.1	0.7	0.1	0.6
LP#09	0.0	0.9	0.0	0.5
LP#10	0.2	0.3	0.2	0.3
LP#11	0.5	0.3	0.4	0.3
LP#12	1.2	0.3	2.1	0.3
LP#13	0.0	0.6	0.0	0.4
LP#14	0.2	0.5	0.7	0.3
LP#15	0.0	0.7	0.0	0.6
LP#16	0.0	0.7	0.1	0.8
LP#17	0.0	0.7	0.0	0.7
LP#18	0.0	0.8	0.0	1.0
Total	2.2		3.6	

Table 4-6. SDDR ($\mu\text{Sv/h}$), and relative error, in the port interspace of UL#12 for both tallies (i.e. left and right corridors) due to each of the different equatorial ports at L1 level.

	Left corridor		Right corridor	
	SDDR ($\mu\text{Sv/h}$)	Relative error	SDDR ($\mu\text{Sv/h}$)	Relative error
EP#01	0.0	0.5	0.1	0.6
EP#02	0.2	0.8	0.1	0.7
EP#03	0.1	0.8	0.1	1.0
NB	2.2	0.2	1.9	0.2
EP#08	1.1	0.4	0.7	0.3
EP#09	0.4	0.3	0.4	0.3
EP#10	2.4	0.2	1.2	0.2
EP#11	3.5	0.1	2.3	0.2
EP#12	8.1	0.1	8.2	0.1
EP#13	1.5	0.3	1.7	0.3
EP#14	1.6	0.4	1.9	0.2
EP#15	0.4	0.6	0.3	0.3
EP#16	0.5	0.5	1.0	0.3
EP#17	0.4	0.4	0.2	0.4
EP#18	0.2	0.3	0.1	0.3
Total	22.6		20.2	

Table 4-7. SDDR ($\mu\text{Sv/h}$), and relative error, in the port interspace of UL#12 for both tallies (i.e. left and right corridors) due to each of the different upper ports at L2 level. The Upper Launchers (ULs) are highlighted in grey.

	Left corridor		Right corridor	
	SDDR ($\mu\text{Sv/h}$)	Relative error	SDDR ($\mu\text{Sv/h}$)	Relative error
UP#01	1.7	0.2	1.2	0.2
UP#02	1.3	0.2	1.7	0.2
UP#03	1.7	0.2	1.9	0.2
UP#04	1.9	0.3	1.5	0.2
UP#05	1.5	0.2	1.6	0.2
UP#06	2.3	0.2	3.3	0.2
UP#07	2.8	0.2	3.0	0.2
UP#08	4.4	0.2	4.7	0.2
UP#09	4.3	0.1	4.8	0.1
UP#10	6.3	0.1	6.6	0.1
UP#11	24.5	0.1	17.7	0.1
UP#12	-	-	-	-
UP#13	78.9	0.1	100.9	0.0
UP#14	7.2	0.1	7.4	0.1
UP#15	27.7	0.1	32.5	0.1
UP#16	23.4	0.1	21.9	0.1
UP#17	3.4	0.2	4.7	0.2
UP#18	3.2	0.3	2.2	0.2
Total	196.5		217.6	

From these Tables, it can be seen that the total cross-talk from all ports (B1, L1 and L2) is equal to 221.3 $\mu\text{Sv/h}$ and 241.4 $\mu\text{Sv/h}$ for the left and right corridor tallies, respectively. These values are already 2.2 and 2.4 times higher, respectively, than the required 100 $\mu\text{Sv/h}$ limit and they represent 45.6% and 46.6% of the total SDDR in each of the corridor tallies, respectively. Certainly, the cross-talk from neighbour ports is a key driver of the SDDR in the port interspace of UL#12. Thus, it is clear that significant changes in the cross-talk representation could lead to significant changes in the total SDDR values.

Looking into more detail, we can see that the most relevant cross-talk is that coming from the L2 level ports. Indeed, the cross-talk from the L2 level neighbour ports represents 88.8% and 90.1% of the total cross-talk in each tally, respectively. But, particularly, the most remarkable contribution by far is that from the neighbour Upper Launchers (ULs #13, #15 & #16). They represent 58.7% and 64.3% of the total cross-talk, respectively, in each tally.

Particularly, the contribution from UL#13 is 3.2 and 5.7 higher, respectively, than the contribution of the UP#11, which is the other direct neighbour port of UL#12. Furthermore, the contributions from the UL#15 and #UL#16, which are separated from UL#12 by two and three ports, respectively, are of the same order or even up to 1.8 times higher than the contribution of UP#11. These observations indicate that the ULs have a significant impact on the SDDR levels of neighbour port interspaces and that this impact has a long range of influence. The latter observation is quite remarkable and, until the existence of E-lite, it could not be confirmed with current partial models.

The large impact of the ULs is due to the fact that they feature a significant opening at the front of each port plug. In addition, the blanket modules from row #11 that are below the ULs feature as well a cut-out. This opening and the cut-out exist to allow the injection of the electron-cyclotron microwave into the plasma. However, as shown in Figure 4-5, they represent a significant streaming path for the neutrons to travel towards the upper region of the UL and activate components (e.g. port duct) that lead to high SDDRs in its port interspace. In addition, since the region above the upper ports is relatively empty, neutrons can easily spread towards other neighbour ports and activate their port interspaces (see Figure 4-6). Note the scales of Figure 4-5 and Figure 4-6 are different; one is logarithmic while the other is linear. Relative error maps of these neutron flux maps are provided in Appendix I.

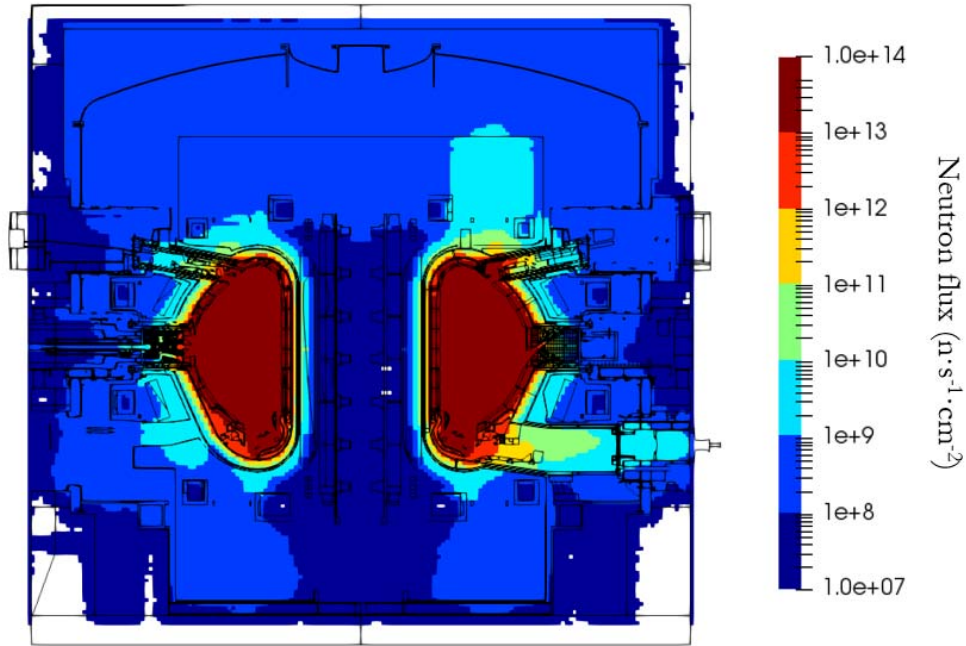


Figure 4-5. Vertical cross-section of a neutron flux ($n \cdot s^{-1} \cdot cm^{-2}$) map in E-lite. The UL#12 is on the upper right region.

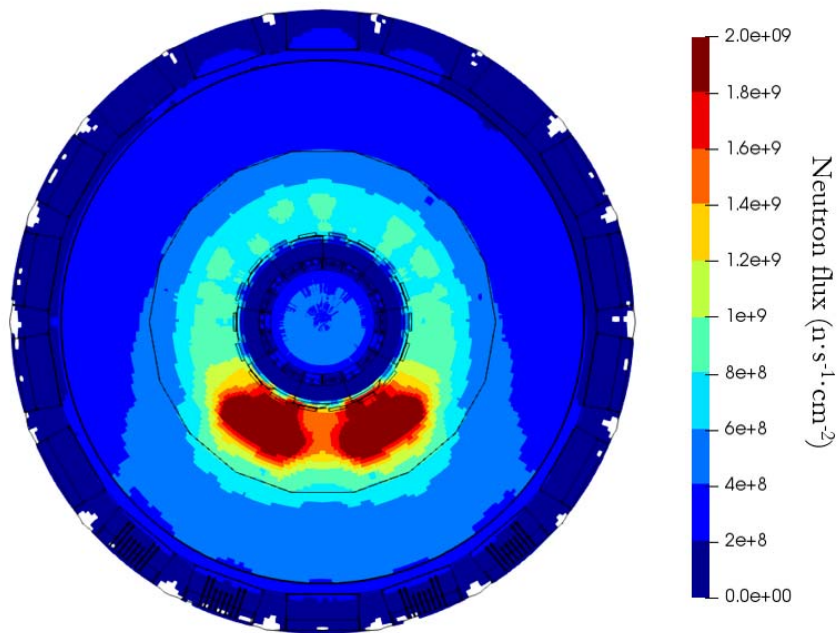


Figure 4-6. Horizontal cross-section of a neutron flux ($n \cdot s^{-1} \cdot cm^{-2}$) map in E-lite. The four ULs are located at the bottom (south) region (see Figure 4-3).

Once these features of the ULs are clear, to finish understanding the reason for the differences between C-model's and E-lite's results, we have to make the following realization. C-model features one UL (i.e. UL#12) at the center of the L2 level and half UL on the right-hand side (i.e. UL#13). That is, it explicitly

represents 1.5 ULs. However, due to the use of reflective boundary conditions, C-model is implicitly representing a machine with a total of (9×1.5) 13.5 ULs. This is a considerably higher number of ULs compared with the 4 that are present in the actual machine and represented in E-lite.

Therefore, considering the large impact and long range of influence of the ULs, the cross-talk towards the UL#12 is significantly overestimated with C-model, what explains the difference between the results obtained with it and those obtained with E-lite.

4.1.4 Conclusion

This example manifests how E-lite represents a considerable improvement with regards to the treatment of the cross-talk. In this particular case, it brings to light the fact that not only the cross-talk from the directly adjacent ports may be relevant for the SDDR. Indeed, ports relatively far away from the one of interest can impact the SDDR in its port interspace.

In this case, compared to C-model, E-lite led to a considerable reduction of the SDDR levels in the port interspace, of around $160 \mu\text{Sv/h}$, which is already 1.6 times more than the SDDR value imposed by the requirement. However, this will not always be the case. For instance, the cross-talk from the NBI towards the upper, equatorial and lower ports #2 and #8 (or further ports) cannot be captured currently with C-model or the NBI model. In that case, the use of E-lite would lead to a significant increase in the SDDR levels of these port interspaces compared to using current partial models. Of course, there would be many other cases in which the amount of reduction or increase in the SDDR due to the use of E-lite may not be so dramatic.

In any case, the important point here is that the uncertainties in the SDDR derived from the symmetry assumption can now be avoided. This is an achievement of major relevance. On the one hand, it allows to better select optimal measures (e.g. shields) to fulfil the SDDR requirement in the port interspaces, while minimizing the impact on the ITER design. On the other hand, it makes the demonstration of the safe operation of ITER more robust.

Furthermore, partial models will still be recurrently used for SDDR applications, as they have important benefits with respect to full models. However, now they will be able to benefit from E-lite to assess their uncertainties, derived from the symmetry assumption. In other words, E-lite can be used to validate them. E-

lite makes such an strategy viable because it provides a reference for comparison.

4.2 Radiation mapping in the Tokamak Complex

4.2.1 Introduction

As I mentioned in section 2.3.2, it is necessary to model an intermediate source right in front of the bio-shield to simulate the radiation fields due to the plasma source in the Tokamak Complex. However, modelling such sources with partial models has relevant limitations.

On the one hand, given that the cross-talk is not accurately captured by partial models, the source models feature unavoidable non-physical discontinuities. The impact of such discontinuities on the radiation levels beyond the bio-shield cannot be predicted. In other words, the source models introduce uncertainties in the nuclear responses of interest. On the other hand, the intermediate source models require many individual simulations. This leads to a considerably high consumption of computational resources and makes the review of the source models very tedious and time-consuming. These limitations affect the quality of nuclear responses which are very relevant for radiological protection and safety matters and the correct disposition of electronics equipment.

In this section, I illustrate how E-lite effectively overcomes such limitations when modelling an intermediate source for the radiation mapping in the Tokamak Complex. To do so, I am going to compare the radiation conditions (i.e. neutron flux) right in front of the bio-shield when considering E-lite and the intermediate plasma source from [137], which was modelled with partial models of the tokamak.

4.2.2 Methodology

Two different radiation transport calculations were performed. One with E-lite and the other one with the plasma source model from [137]. In both cases the neutron flux was computed right in front of the bio-shield. D1SUNED v.3.1.4. [97] was used to run the calculations. Apart from being the ITER reference code for SDDR analysis, this tool can also be used to compute the same standard nuclear responses that are calculated with MCNP. For that, the PRMPT card has to be considered.

With respect to the E-lite calculation, the simulation was run up to an NPS of 10^{11} histories. The Global Variance Reduction (GVR) [172] technique was used to be able to obtain sufficiently low relative errors with a reasonable amount of computational resources. A softening power of 0.5 was considered.

For computational reasons, the simulation was split into nine statistically independent runs each with lower NPS and different seeds (that is, HIST card values) (See Table 4-8). The results were merged with MCNP merger software.

On the other hand, the plasma source model from [137] was run in void mode and up to 10^9 histories (NPS= 10^9). There was no need to use any Variance Reduction technique.

Table 4-8. NPS and HIST card values of the 9 statistically independent simulations run to reach NPS 10^{11} .

Case #	NPS	HIST
1	$3.0 \cdot 10^{10}$	1
2	$1.0 \cdot 10^9$	40000000001
3	$1.5 \cdot 10^{10}$	60000000001
4	$1.5 \cdot 10^{10}$	80000000001
5	$1.0 \cdot 10^{10}$	100000000001
6	$5.0 \cdot 10^9$	120000000001
7	$1.0 \cdot 10^9$	180000000001
8	$1.5 \cdot 10^{10}$	200000000001
9	$1.5 \cdot 10^{10}$	220000000001

4.2.3 Results and discussion

In Figure 4-7, I provide neutron flux maps for both E-lite and the mosaic source from [137]. The maps show the neutron flux right in front of the bio-shield.

The relative errors of the neutron flux maps shown in Figure 4-7 are provided in the Annex I. The resulting errors are in general well below 10%, as recommended by the MCNP manual [66].

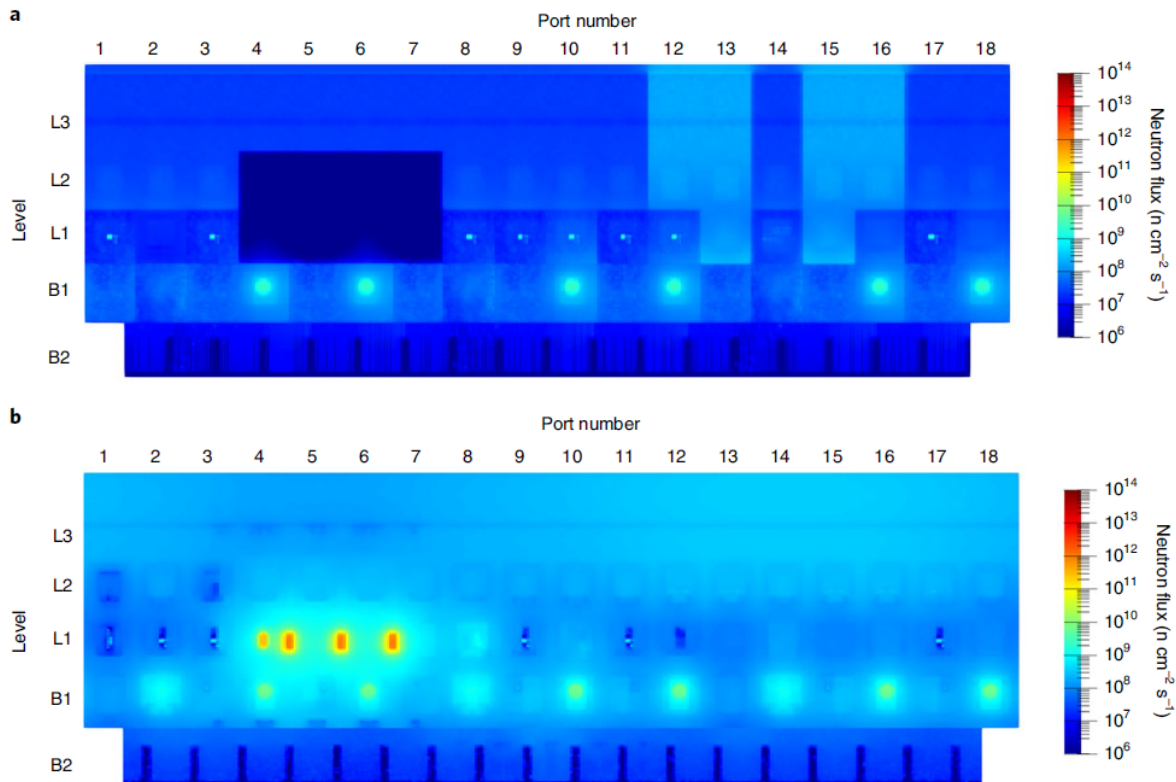


Figure 4-7. Neutron flux impinging on the inner face of the bio-shield. **a)** Neutron flux at a radius of 1350 cm for B2 level and a radius of 1470 cm for the rest, obtained as a mosaic with SRC-UNED as indicated in [137] **b)** Neutron flux at the same locations as in a), but obtained with E-lite. Taken from [176].

By inspecting Figure 4-7, many differences between both maps can be spotted. I will discuss now the origin of such differences.

Firstly, there is a difference due to the fact that the L1 and L2 levels corresponding to the NB sector are not represented in the mosaic source. However, this is not due to a technical limitation of the mosaic source approach [140], but rather due to a decision regarding the scope of the study in which it was used [51].

Secondly, there are differences due to the use of more up-to-date representations of ports. This leads to situations like that of the RH-LPs (#2, #8 and #14) at B1 level. In this case, the MCNP model of the RH-LPs was updated in E-lite and now these ports lead to a higher radiation transmission than the version that was included in [137] (for reasons out of the scope of this thesis). In addition, many MCNP models of the representative ports (see strategy of representative ports in 3.2.3) used in [137] have been substituted by the models of the actual ports. For example, in [137] there were EP#11 ports at the L1 ports #01, #03, #08, #09, #10, #12 and #17, apart from port #11 itself. In E-lite, the

equatorial ports #01, #08, #10 and #12 have been replaced with MCNP models of the actual ports.

Thirdly, there are other differences that are due to the fact that the mosaic from [137] was modelled in local approach. That is, it was modelled neglecting pretty much all the cross-talk between ports. This is one of the main reasons why the background radiation in Figure 4-7-a is generally lower compared to Figure 4-7-b. Another reason for this could be the fact that the map produced with E-lite includes the contribution of the neutron backscattering in the bio-shield, while the map from [137] does not (i.e. the source was run in void mode). However, the impact of this last aspect is expected to be minor.

Up to this point, the differences spotted are not due to the use of a 360° model. For the sake of the comparison, I could have tried to minimize these differences by modelling a mosaic source in global approach, including the L1 and L2 levels of the NB sector and with the exact same ports as E-lite. However, I have not done so for two reasons.

On the one hand, because it would have implied wasting too many computational hours on modelling a mosaic source that would not have served any purpose other than just being compared with E-lite. Note the mosaic source from [137] was used in the release of radiation maps from 2016. The other reason I have not done so is because, for the purpose of this comparison, the mosaic source from [137] is completely suitable.

Indeed, the most relevant difference that I want to highlight here is the disappearance of the non-physical discontinuities that are observed in Figure 4-7-a. This difference is only due to the use of a continuous 360° model, like E-lite. Specifically, the discontinuities disappear because E-lite allows to fully capture the cross-talk between ports in a realistic manner. This is very important in the case of the cross-talk from the NB sector, which is quite intense. Note that, even if the NB sector had been included in the mosaic source, its influence beyond its 80° geometrical definition could not have been captured with current partial models.

As a result, the map produced with E-lite (Figure 4-7-b) is a smooth and more reliable representation of the radiation impinging on the bio-shield. Ultimately, this means that modelling an intermediate source for radiation mapping with E-lite avoids the uncertainties introduced with mosaic sources.

The other great difference between the two approaches, which cannot be observed in Figure 4-7, is the fact that, with E-lite, just one single calculation is needed to characterize the radiation right in front of the bio-shield. In the case of the mosaic source, 34 simulations and models were needed. Thus, with E-lite, the traceability and review of the source modelling is considerably simplified in terms of human efforts. Not to mention the save in computational resources derived from the increased efficiency of running just one simulation.

4.2.4 Conclusion

In conclusion, E-lite represents a major improvement regarding the modelling of intermediate radiation sources for the computation of radiation maps in the ITER Tokamak Complex and beyond it. Relevant unassessed uncertainties that follow from the construction of sophisticated intermediate sources with partial models can now be avoided. E-lite allows for a more robust and a far more easily reviewable approach in support of the ITER safety case towards nuclear operations.

Intermediate sources modelled with partial models will still be of interest to conduct local studies, which require fewer computational resources. However, these intermediate sources could be now be validated using intermediate sources produced with E-lite. The uncertainties due to the toroidal symmetry assumption and/or the methodological approach used to produce the intermediate source with partial models could be quantified case by case. As I mentioned in the previous section, note that E-lite makes such an strategy viable because it provides a reference for comparison.

4.3 Calibration of neutron detectors

4.3.1 Introduction

As I mentioned in section 2.3.3, in principle, partial models are not suitable to support the calibration of ITER neutron detectors with the required level of uncertainty (<10%). This is because in many calibration experiments it is necessary to know the exact contribution of neutron sources that are located beyond the 40°/80° toroidal region covered by the partial models. In those situations, the boundary conditions of partial models have to be removed. However, without the boundary conditions, partial models are not able to represent the influence of the rest of the machine beyond their explicit

geometrical definition. Consequently, if partial models were used to recreate a calibration experiment of this kind, they would introduce unquantifiable uncertainties in the results.

In this section, I illustrate how E-lite represents a valuable and necessary step towards the accurate calibration of ITER neutron detectors. I do not do so by validating E-lite against experimental data. Basically, because the calibration of neutron detectors will take place several years from now. Instead, I have simulated a calibration experiment using both E-lite (360°) and C-model (40°) with the objective of demonstrating the unsuitability of current partial models to support the calibration of neutron detectors.

Specifically, I reproduced a hypothetical neutronics calculation that would be needed in the process of calibrating, for DT operation, one of the most exposed and important type of detectors in ITER, the Divertor Neutron Flux Monitors (DNFMs). These will be located below the divertor dome (see Figure 4-8) and will be one of the closest detectors to the calibration source, hence easier to calibrate. For convenience, I selected the DNFM detector below the port #14 divertor central cassette that will measure fission counts in two fission chambers containing ^{238}U and ^{235}U , respectively.

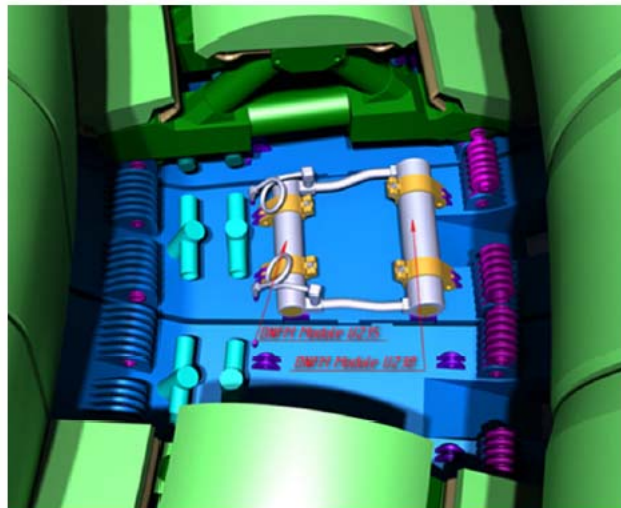
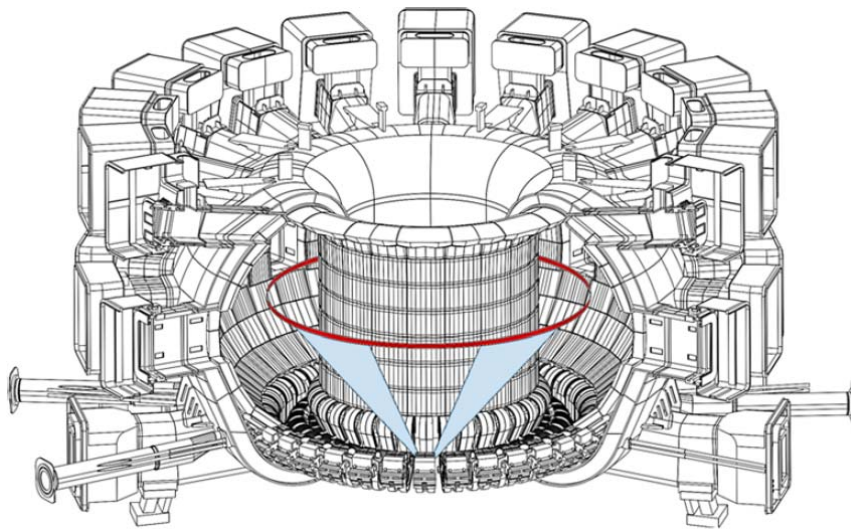


Figure 4-8. Picture of the DNFM modules. Taken from [141].

4.3.2 Methodology

For the DT calibration, a deuterium–tritium neutron generator with known intensity will be deployed inside the vessel at different radial, poloidal and toroidal locations. To simplify the exercise, I modelled the source as a group of

point-wise isotropic monoenergetic 14.1 MeV neutron sources using an SDEF card. It was assumed that the source device did not distort the resulting neutron flux. The sources were located at 3° intervals around a circumference in the central plane of the tokamak (see Figure 4-9). Position 0° corresponds to the location of the source directly above the detector. The circle was centred in the tokamak at a radius of $r = 600$ cm and a height of $Z = 60$ cm with respect to the Tokamak Global Coordinate System (TGCS).



*Figure 4-9. The circular trajectory along which the calibration source is deployed at 3° intervals inside the tokamak is shown in red. The region with direct view of the source by the detector is shaded in blue.
Taken from [176].*

Radiation transport calculations were performed with the D1SUNED v3.1.4 code [97] to calculate fission counts in the fission chambers of the DNFM#14. The independent contribution of each of the point-wise sources was filtered.

Both C-model and E-lite were considered. Note that to be able to discern the independent contribution of each source, no boundary conditions were considered in C-model. This is because many of the point-wise sources are located beyond the 40° toroidal region represented by this model. In other words, when simulating this exercise with C-model, the remaining 320° of the machine were not represented at all by any means.

The same port models for the toroidal segments #13, #14 and #15 were used in E-lite and C-model to represent the environment of the divertor port #14.

To calculate the total counts (fission events) recorded by the DNFM #14 fission chambers, the detector was modelled as a single-voxel mesh tally of 10×10×10

cm³ centred at (0, -470, -435) cm. Multiplier cards to obtain fission events in ²³⁸U and ²³⁵U were applied with MT reaction type number 18.

In addition, a cylindrical mesh was imposed over the circular distribution of sources, and the 'srcimp' option of D1SUNED v.3.1.4 was used to filter the contribution of each of the point-wise sources.

Weight windows maps were produced with the Global Variance Reduction (GVR) technique [172]. The 360° simulation was run up to NPS = 10¹⁰, and the simulation with only a 40° sector was run up to NPS = 10¹¹.

4.3.3 Results and discussion

The total counts (fission events) per source neutron recorded by the DNFM #14 ²³⁸U and ²³⁵U fission chambers are tabulated in Table 4-9 for C-model and E-lite, respectively. In Figure 4-10, I show, for both chambers and both models, the relative counts, as a fraction of the total counts, and as a function of the angle between the calibration source and the detector.

Table 4-9. Fission counts per source neutron in the ²³⁸U and ²³⁵U fission chambers of DNFM #14 with statistical error (in brackets). Taken from [176].

Model	²³⁸U fission chamber (counts/source neutron)	²³⁵U fission chamber (counts/source neutron)
C-model	1.25·10 ⁻⁹ (<0.01)	1.98·10 ⁻⁷ (<0.01)
E-lite	1.29·10 ⁻⁹ (<0.01)	3.20·10 ⁻⁷ (<0.01)

The total counts per source neutron and the angular dependence obtained for the ²³⁸U fission chamber using E-lite are very similar to those obtained using C-model. The fission events in ²³⁸U are dominated by high-energy neutrons, and the measurement will largely depend only on the material between the source and the detector. This material scatters the neutrons away from the detector. Lower-energy neutrons, scattered from other parts of the machine, have lost enough energy that they do not induce fission in the ²³⁸U fission chamber.

Three regions are observed that are delimited by the angles ±20° and ±55° (see Figure 4-10). The first (central) region corresponds to the shadow of the divertor dome above the detector. The second (blue) region corresponds to a relatively direct view of the detector from the source, and therefore the signal decays more

slowly with angle. The third (outer) region is the shadow of the neighbouring divertor cassette and farther components.

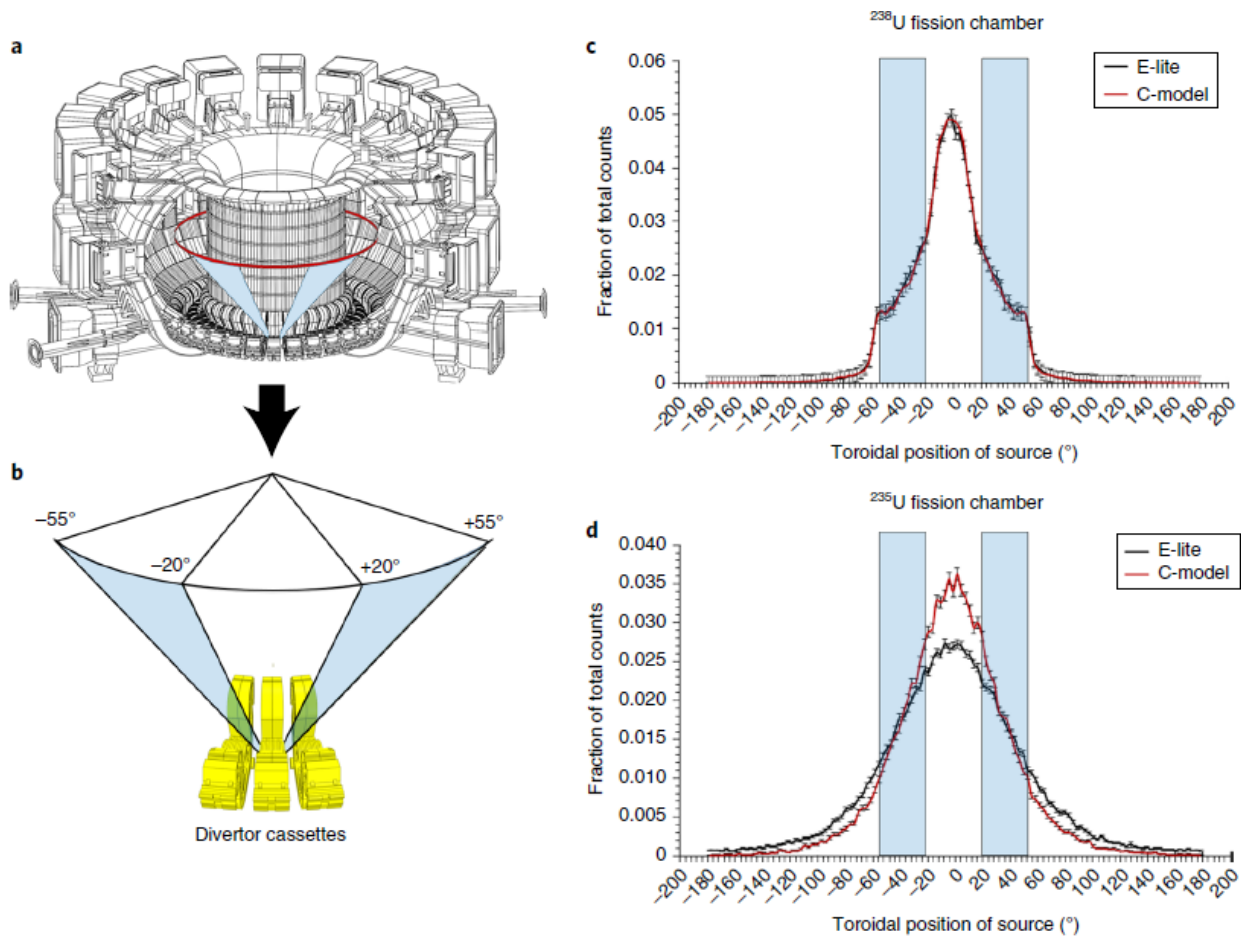


Figure 4-10. **a)** This image was already shown in Figure 4-9. **b)** The divertor cassette below which the detector is hosted and the adjacent cassettes are shown in yellow. The blue regions are those of **a)** and the corresponding angular positions of the source, from -55° to -20° and from 20° to 55° , are marked over the source trajectory. **c,d)** Fission counts, as a fraction of the total counts, in the DNFM #14 for the ^{238}U fission chamber (**c)** and the ^{235}U fission chamber (**d)** as a function of the angle between the calibration source and the detector, obtained with C-model and E-lite models. The blue regions and corresponding angles are those of **b)**. Error bars correspond to the statistical error of the tally in the simulation. Taken from [176].

As the central and the two adjacent divertor cassettes are included in both E-lite and C-model, the predicted responses are similar. This is an example of how a partial model, like C-model, yields similar results to those yielded by a 360° model for a particular application, which, in principle, required a 360° model by definition. This is due to the fact that the nuclear response of interest is local and influenced by a short-range environment, within the 40° that C-model comprises.

Of course, to validate both models for calibration purposes it would be necessary to compare the responses obtained here with those obtained experimentally, however, beyond the scope of calibration, this example makes clear the following point. The results of C-model for this particular application can only be trusted because we have the results from E-lite as a reference, which is considered to be the best existing representation of the tokamak. Otherwise, even if accurate, the fact that 320° of the machine were missing, would have challenged the reliability on C-model results. In other words, this exercise is also an example of how E-lite could be used to validate C-model for a specific application and to quantify an uncertainty in the 40° representation of the ITER tokamak.

On the other hand, the ^{235}U fission chambers are more sensitive than the ^{238}U fission chambers and are sensitive to lower-energy scattered neutrons. The total counts per source neutron obtained for the ^{235}U fission chamber using E-lite are 63% higher than when using C-model. Even the measurement at 0° is a 33% higher with E-lite. As the fission events in ^{235}U are much more sensitive to the low-energy neutrons, the simulation results depend strongly on proper modelling of the detector environment that scatters and moderates the neutrons. In the absence of 320° of the machine in C-model, a noticeable part of the scattered flux is lost. This is an example of how a 40° representation of the ITER tokamak fails to represent a local quantity influenced by a long-range environment, beyond 40°.

Again, it would be necessary to compare the results obtained here with those obtained experimentally to validate both models regarding their use for calibration purposes. However, by simply comparing with the E-lite results, which by definition have to be more accurate, it is clear that C-model could not be used to conduct the calibration of the ^{235}U fission chambers respecting a 10% accuracy requirement.

Note that the DNFMs are one of the detectors that present the most symmetric environment; indeed, the NBI, which leads to a considerable amount of cross-talk, is located right on the opposite side of the tokamak. Therefore, for other detectors, this exercise, if at all possible, may result in larger differences between E-lite and C-model.

4.3.4 Conclusion

In conclusion, this exercise demonstrates that E-lite has two main advantages. On the one hand, the case of the ^{235}U fission chambers demonstrates that E-lite constitutes an essential step towards the accurate calibration of ITER neutron detectors. Indeed, it demonstrates that partial models can introduce uncertainties beyond the requirement (<10%) of the neutron detectors, what makes them unsuitable to support the calibration experiments. On the other hand, the case of the ^{238}U fission chambers demonstrates that E-lite is a robust reference that can be used to validate the results from partial models. This last conclusion was already reached in 4.1.4 and 4.2.4.

CHAPTER 5

IMPACT OF THIS THESIS

In this chapter I review the impact of this thesis. On the one hand, and most importantly, I focus on the impact of E-lite (section 5.1). Specifically, I indicate nuclear analyses of relevance for the ITER project in which E-lite has been (or is going to be) applied. These applications show that E-lite's repercussion extends beyond the context of this thesis and that, indeed, the model represents a research product well-received by the ITER neutronics community. On the other hand, I take the chance to briefly indicate other contributions in the context of ITER nuclear analysis to which this thesis has led (section 5.2). These contributions are not directly related to E-lite, but they have indirectly contributed to the objectives of this thesis. In addition, some of these contributions have also been considerably important for the ITER project. Particularly, I put special emphasis on those works in which I have participated and that were highly recognized and/or published in journal articles.

5.1 Impact of E-lite on the ITER project

The benefits from using E-lite for certain applications have been recognized and valued by the whole ITER neutronics community. In fact, together with C-model and the NBI model, E-lite has become a reference model of the ITER Tokamak for neutronics analysis. Consequently, it has already been (and it is foreseen to be) applied in nuclear analysis of great relevance for the project.

The most remarkable application of E-lite is associated to the latest release of ITER official radiation maps in the Tokamak Complex during machine operation [177][178]. Particularly, I used E-lite to model the intermediate plasma source

that was later considered in the performance of the plasma maps. The calculations described in section 4.2 were the ones considered to model such plasma source [179].

This release of radiation maps provides information on the radiation conditions not only within the Tokamak Complex, but also outside. Among other things, these maps have been key for the ITER project to demonstrate to the French regulator that there are no violations of the radiation safety limits outside the building. In addition, these maps have been very useful to evaluate a series of shields, known as PIM-466 [135], which were developed and approved by IO after many design efforts. The shields resulted to be effective in solving violations of the radiological zoning previously identified in 2016 [53] and in guaranteeing acceptable radiation conditions for electronics. In section 5.2.2, I will also indicate other contributions of this thesis to this release of radiation maps.

E-lite has also been used in the production of several radiation maps after machine shutdown.

An initial version of E-lite was used by TECF3IR-UNED in the SDDR analysis for the FDR of the ECH-ULs [167]. The FDR is a very important milestone within the design process of ITER SSCs as it is a necessary step towards its fabrication. Particularly, the ECH-UL #14 is a First Plasma port, so it has to be built and assembled in the machine by 2025. The SDDR analysis performed with E-lite served to confirm the effectivity of a shielding concept in fulfilling the 100 $\mu\text{Sv/h}$ requirement in the ULs port interspaces at 10^6 seconds after machine shutdown for planned hands-on maintenance activities. Such shielding concept was developed by colleagues of TECF3IR-UNED research group, specially by Antonio Jesús López-Revelles and Rafael Juárez, in collaboration with IO.

E-lite has also been extensively applied by TECF3IR-UNED in the SDDR calculations within the recent ALARA programme that was launched by IO in 2019 [180][181]. This activity aims at analyzing several locations of the machine with the purpose of investigating ALARA measures in an integrated manner (SDDR maps, Contamination Maps, Human and Organizational Factor, etc). SDDR maps are a vital input for this activity in order to be able to evaluate the effectiveness of the different measures (e.g. reduction of the maintenance time of a component, implementation of permanent/temporary shields, use of specific suits by operators, etc) in terms of the reduction of the final Occupational Radiation Exposure (ORE). It is important to remark the Project

Requirements [50] state that “the collective annual worker dose, averaged over the operational lifetime of ITER, shall be ALARA and in any case shall not exceed an annual target of 0.5 person·Sv”.

Finally, E-lite was recently used by F4E in the performance of the ITER radiation maps after machine shutdown outside the vacuum vessel and inside the bio-shield [182]. The aim of this task was to provide a global picture of the SDDR in all the ITER ports within the bio-shield. For this particular analysis, E-lite was improved to represent missing components which could potentially contribute to the SDDR fields, such as the magnet feeders or the Tokamak Cooling Water System [183].

In the short term, E-lite is foreseen to be used by F4E to compute the nuclear heating in the in-vessel components, vacuum vessel and the superconducting coils. For this task, the standard tallies defined in this thesis will be considered ([154] and section 3.2.7). This task is needed to validate the design of these components from the standpoints of thermo-mechanics and thermal computational fluid dynamics. In addition, E-lite will also be used by TECF3IR-UNED to compute the maps during operation and after machine shutdown inside the vacuum vessel. These maps will be particularly useful to evaluate radiation conditions during the operation of the IVVS and the Divertor Remote Handling System. In the mid-term, E-lite will be used again to update the radiation maps during machine operation within the Tokamak Complex as part of the update of the Preliminary Safety Report (RPrS) [136], which is the document that presents all the safety analyses performed for ITER and that was sent to ASN in 2010 for its examination.

Apart from these applications, several others are expected. We can expect the use of E-lite in all those applications involving non-local nuclear responses and/or local responses affected by a long-range environment. This kind of applications include the simulation of the pre-deuterium-tritium asymmetric neutron sources, like those produced by runaway electrons, to address their relevance for safety and machine protection. In addition, E-lite could be used to perform the extensive nuclear analyses that will be needed to support the calibration of all the ITER neutron detectors.

However, having said all this, E-lite is not intended to be used on a general basis for every ITER nuclear analysis. There are many cases in which doing so would be impractical. This is because E-lite demands approximately 9 times more

Monte Carlo histories (i.e. simulation time) than C-model to compute nuclear responses with the same statistical error. Furthermore, it is computationally heavier and harder to handle. Therefore, the reality is that partial models will still be used to perform many of ITER nuclear analyses, even when these analyses do not involve the computation of local nuclear responses influenced by a short-range environment.

However, the important point is that the nuclear analyses performed with partial models can now benefit from the existence of E-lite. Indeed, another application of E-lite is to validate partial and/or simplified models for specific applications and to quantify their uncertainties. In other words, E-lite will allow to increase the reliability on results obtained with partial and/or simplified models.

Such has been the value and impact of E-lite that part of the content of this thesis was published in January 2021 in the prestigious Nature Energy journal:

- R. Juarez, G. Pedroche, M.J. Loughlin et al, “A full and heterogeneous model of the ITER tokamak for comprehensive nuclear analyses”, Nature Energy 6, 150–157 (2021).

5.2 Other relevant contributions

Apart from all the work that has already been presented in relation to E-lite, in the time frame of this thesis I have also made other contributions in the context of ITER nuclear analysis. These contributions are not directly linked to the development of E-lite. However, they provided me with very valuable experience, training and insights that have as well contributed to the main objectives of this thesis. In addition, some of these works constituted a very important contribution to the progress of the ITER project and the ITER Nuclear Analysis field. In the coming subsections, I want to briefly indicate the most relevant contributions, particularly those that were highly recognized and/or resulted in scientific publications.

5.2.1 D1SUNED: V&V and nuclear data package

As previously mentioned, D1SUNED [97] is the ITER reference code for SDDR calculations [59]. It was developed by Patrick Sauvan, from the TECF3IR-UNED research group. D1SUNED is an implementation of the Direct 1-Step (D1S) methodology [126] in MCNP [63] that offers many analysis capabilities that make it very powerful for SDDR analysis [15][19][184]–[186]. In addition, it

features important improvements of MCNP's performance regarding the treatment of complex neutronics models [151]. These are the improvements that have made E-lite feasible and usable. Furthermore, these improvements are also the reason why the code is used in many standard ITER analyses (i.e. to compute quantities during machine operation) instead of MCNP. Through a contract with TECF3IR-UNED, the ITER project acquired an unlimited number of licenses to use and distribute D1SUNED within the ITER neutronics community.

In this thesis I have made the following contributions to the D1SUNED tool. I have participated in the verification and validation (V&V) process of the code according to the ITER standards [187]. The V&V of D1SUNED was one of the requirements imposed by ITER prior to its acquisition. Specifically, I participated in the production of the following deliverables [188][189]. Part of that work was reflected too in the following publication about D1SUNED:

- P. Sauvan, R. Juarez, G. Pedroche *et al.*, "D1SUNED system for the determination of decay photon related quantities," *Fusion Eng. Des.*, vol. 151, p. 111399, Feb. 2020, doi: 10.1016/j.fusengdes.2019.111399.

D1SUNED, like any other D1S code, relies on special nuclear data libraries in which the prompt photon cross-sections are replaced with decay photon cross-sections. The cross-sections are produced automatically with a set of computational scripts that were also developed by Patrick Sauvan. In this thesis, I used those scripts to produce the official nuclear data package of D1SUNED for ITER planned in-situ maintenance scenarios [190]. To do so, first, I had to perform activation calculations with ACAB [57], which was developed by my director Javier Sanz, to characterize the inventory of concern for such scenarios. In other words, I identified which were the radioisotopes of concern (i.e. those contributing to the SDDR field) as well as the pathways leading to them. This work was reflected in an ITER deliverable [190] and in the following publication:

- G. Pedroche, P. Sauvan, J. Alguacil, J. Sanz, and R. Juárez, "Nuclear data for D1SUNED for the study of ITER planned in-situ maintenance dose scenarios," *Fusion Eng. Des.*, vol. 170, p. 112646, Sep. 2021, doi: 10.1016/j.fusengdes.2021.112646.

5.2.2 ITER 2020 Radiation Maps

I have already pointed out several times the relevance of ITER radiation maps for the ITER project. In addition, in section 5.1, I highlighted the special relevance of the last release of radiation maps [177][178]. These maps demonstrate that the ITER radiation levels comply with the requirements, including the onsite unregulated area at ground level. Furthermore, they also indicate that the limit for public exposure falls within the boundary of the INB perimeter.

Apart from using E-lite to model the intermediate source that was used to compute the radiation maps due to the plasma, TECF3IR-UNED also carried out all the modelling and simulation tasks required for the computation of the radiation maps. Specifically, we:

- Produced a model for the ITER site [191] that included the following sub-models:
 - Tokamak Complex civil works, comprising the B11, B14 and B74 [192].
 - Environment of the Tokamak Complex, including the B11 roof, soil and Auxiliary Buildings (Seismic slab B12-19, Assembly Hall B13, Hot Cell Complex B21, High Voltage (HV) Building B37) [193].
 - NB Cell and HV Deck systems structures and components [194].
- Produced a model for the activated water source that represented the whole TCWS (outside the bio-shield) and other relevant water circuits [28].
- Produced the model for the intermediate plasma radiation source [179].
- Performed the calculations to compute the radiation maps [177][178].

This was a gargantuan activity that required the participation of almost all the TECF3IR-UNED research group. Particularly, I was the Technical Responsible of these tasks and I participated in all of them at different levels.

In addition to the deliverables above indicated, the work on the modelling of the activated water source was also reflected in the following publication:

- M. De Pietri, J. Alguacil, A. Kolsek, G. Pedroche *et al.*, “Integral modelling of the ITER cooling water systems radiation source for applications outside of the Bio-shield,” *Fusion Eng. Des.*, vol. 171, p. 112575, Oct. 2021, doi: 10.1016/j.fusengdes.2021.112575.

We are also already working on a publication on the radiation maps themselves that reflects all the work done.



Figure 5-1. Thank you letter to UNED's rector from the Director General (DG) of the ITER Organization.

Finally, I want to high-light that the importance and the quality of the work done was such that the Director General (DG) of the ITER Organization, Bernard Bigot, wrote a thank you letter (see Figure 5-1) to the rector of UNED, Ricardo Mairal, for our work and our timely performance.

5.2.3 Other nuclear analyses of relevance

Finally, I also want to mention that I have participated in several other nuclear analyses that have been as well very important for the ITER project. These include, but are not limited to, the nuclear analyses for the Design Reviews of relevant ITER ports [15][19][94][195], the production of ITER radiation maps after machine shutdown in the Tokamak Complex [196] or the nuclear analysis for the assessment of modifications in the R1 slab of the Tokamak Complex [197]. These works have been carried out in collaboration with several other members of the TECF3IR-UNED research group, especially with Antonio Jesús López-Revelles, Aljaž Kolšek and Rafael Jaurez.

The work performed in some of the ITER nuclear analyses in which I participated has been reflected in the following journal articles:

- R. Juárez, J. Guirao, A. Kolšek, A. Lopez, G. Pedroche *et al.*, “The use of the long modular diagnostics shield module to mitigate shutdown dose rates in the ITER diagnostics equatorial ports,” *Nucl. Fusion*, vol. 58, no. 5, p. 056015, May 2018, doi: 10.1088/1741-4326/aaadce.
- R. Juárez, A. Lopez, P. Sauvan, G. Pedroche *et al.*, “Update in the nuclear responses of the European TBMs for ITER during operation and shutdown,” *Fusion Eng. Des.*, vol. 134, pp. 92–96, Sep. 2018, doi: 10.1016/j.fusengdes.2018.06.022.
- A. Kolšek, R. Juarez, A. Lopez, G. Pedroche *et al.*, “Shutdown dose rate mitigation in the ITER upper ports,” *Fusion Eng. Des.*, vol. 136, pp. 228–232, Nov. 2018, doi: 10.1016/j.fusengdes.2018.01.070.
- G. Pedroche *et al.*, “Nuclear analysis of the ITER torus cryopumps,” *Nucl. Fusion*, vol. 59, no. 10, p. 106045, 2019, doi: 10.1088/1741-4326/ab38d1.
- R. Juarez, M. Loughlin, A. Lopez, G. Pedroche *et al.*, “Improved radiation shielding analysis considering vector calculus,” *Int. J. Energy Res.*, vol. 45, no. 8, pp. 11904–11915, 2020, doi: 10.1002/er.5919.

CHAPTER 6

CONCLUSIONS AND FUTURE WORK

6.1 Conclusions

In this thesis I have successfully accomplished the three objectives posed at the beginning of it.

The first objective was to identify the limitations of the reference neutronics models of the ITER Tokamak regarding the accuracy and/or feasibility of ITER relevant applications. The limitations are essentially two and arise from their partial nature.

The first limitation is that reference models introduce unquantified uncertainties in the estimation of nuclear responses (more or less severe depending on the nuclear response) due to the fact that they represent as symmetric a machine that is actually asymmetric. Particularly, current reference models obviate the asymmetric distribution of ITER ports.

The second limitation of partial models is that they are not prepared to be directly used in applications which, by definition, require a broader (or complete) toroidal representation of the machine geometry and/or the radiation sources.

These limitations can severely affect certain ITER nuclear analyses. Particularly, I identified and focused on three of such applications: (i) the estimation of SDDR

in the port interspaces, (ii) the radiation mapping in the Tokamak Complex, and beyond, and (iii) the calibration of neutron detectors.

These are just few examples of very relevant applications that are affected by the partial nature of the ITER Tokamak reference models. However, there are more, like the estimation of the nuclear heating in the poloidal field superconducting magnets or the estimation of radiation fields in the tokamak due to the runaway electrons. In general, the partial nature of reference models affects the prediction of any non-local quantities and/or local quantities influenced by a long-range environment. In addition, calculations involving asymmetric sources (i.e. runaway electrons) are also affected.

The above applications are very relevant regarding the successful and safe operation of ITER. Considering this, the tight design margins of the machine and the approach of ITER nuclear operation, scheduled in 2035, the limitations of partial models constitute a growing risk. There have been attempts to reduce the impact of the limitations of partial models for specific situations, but none of them are satisfactory. They are not general, they cannot mitigate the uncertainties derived from the symmetry assumption and they can turn out to be very sophisticated.

That is why the second objective of this thesis was to propose and develop a solution to overcome the limitations of partial models in a general and robust way. To do so, I produced a detailed 360° neutronics model of the ITER Tokamak: the E-lite model.

E-lite does not rely on any kind of boundary conditions. Thus, it leaves behind the symmetry assumption of partial models, together with its associated uncertainties. In addition, being a 360° model, it is ready to be used in any application, regardless of the toroidal extension of the machine required by it. In general terms, E-lite is based on seven replications of the C-model (40°), the inclusion of the NBI sector (80°), the allocation of the most up-to-date models of port plugs following a strategy of representative ports, and the manipulation of the block structure for different purposes (to reflect specific asymmetries of the machine and/or improve its representation, to correct errors, to prepare the model for specific applications, etc).

E-lite is the most complex and realistic model of the ITER Tokamak to date. It could only be produced thanks to the recent computational advances

incorporated in D1SUNED, which dramatically improve the capacity of MCNP to handle very large models. The computational performance of E-lite was evaluated, showing that the model is completely usable for ITER nuclear analysis with the currently available HPC resources.

Finally, the third objective of this thesis was to analyze and test the effectivity of E-lite in overcoming the limitations identified. In other words, the objective was to demonstrate that E-lite is not only feasible and usable, but useful for ITER nuclear analysis. To accomplish this objective, I used E-lite in the three applications previously identified and compared its performance with that of partial models or methodological approaches based on partial models.

In the first application, I showed how E-lite, compared to C-model, can lead to a significant reduction in the SDDR levels in the port interspace of UL#12 after 10^6 seconds of cooling time. Particularly, the SDDR was $160 \mu\text{Sv/h}$ lower with E-lite. This difference is already 1.6 times the $100 \mu\text{Sv/h}$ limit that has to be fulfilled. The reason for this difference is due to the better representation of the cross-talk that is achieved with E-lite. Of course, it cannot be expected that all ports will show the same degree of difference. But the important point is that, regardless of their magnitude, E-lite avoids the uncertainties derived from the misrepresentation of the cross-talk by partial models.

In the second application, I showed how E-lite, compared to the approach used in previous radiation maps, represents a major improvement regarding the modelling of intermediate radiation sources for the radiation mapping in the Tokamak Complex, and beyond. Due to the better representation of the cross-talk, E-lite leads to a smoother characterization of the radiation impinging on the bio-shield, without any non-physical discontinuities. As a result, all the unquantified uncertainties in the nuclear responses computed beyond the bio-shield, derived from the misrepresentation of the cross-talk, are again avoided. Furthermore, the characterization of the radiation impinging on the bio-shield is considerably simplified with E-lite. Just one single calculation with one single model is needed, thus, the traceability and review of the source modelling is considerably simplified; not to mention the safe in computational resources derived from the increased efficiency of running just one simulation.

In the third application, I showed how E-lite is a valuable and necessary step towards the accurate calibration of ITER neutron detectors. In the case of the ^{235}U fission chambers, the total counts per source neutron obtained with E-lite

were 63% higher than those obtained with C-model. Even when the source was placed right on top of the detector, the measurement was a 33% higher with E-lite. This is because, in the absence of 320° of the machine in C-model, a noticeable part of the scattered flux was lost. Clearly, C-model cannot be used in this case to support the calibration with an uncertainty <10%. In the case of the ²³⁸U fission chambers, it is true that the results were similar between both models. However, the reality is that the results from C-model could only be trusted because we had the results from E-lite as a reference. Otherwise, even if accurate, the fact that 320° of the machine were missing, would have challenged the reliability on C-model results.

These three applications give evidence of how E-lite increases the quality of ITER nuclear analyses. They explain why, together with C-model and the NBI model, E-lite has become an ITER reference model of the tokamak.

In fact, in the course of this thesis, E-lite has been applied to several nuclear analyses of relevance for the ITER project. E-lite was used to model the intermediate plasma source used in the latest update of the ITER radiation maps in the Tokamak Complex, and beyond, during machine operation. This task constituted an important milestone for the project as it was required by ASN to respond to relevant radiological concerns during machine operation. E-lite has also been applied to compute the recent SDDR ex-vessel radiation maps inside the bio-shield, the SDDR calculations for the ECH-UL Final Design Review and many of the SDDR calculations for the ITER ALARA program.

In the short term, E-lite is foreseen to be used to compute the nuclear heating in the in-vessel components, vacuum vessel and the superconducting coils. In addition, E-lite will also be used to compute shutdown in-vessel radiation maps. In the mid-term, a future version of E-lite will be used again to update the radiation maps during machine operation within the Tokamak Complex as part of the update of the RPrS.

In general, the use of E-lite in applications involving non-local nuclear responses and/or local responses affected by a long-range environment can be expected. For instance, E-lite could be used to perform the extensive nuclear analyses that will be needed to support the calibration of all the ITER neutron detectors.

The above does not mean that E-lite will be used for all ITER nuclear analyses. There are many cases in which doing so would be very impractical in computational terms. Therefore, partial models will still be used on a regular basis. However, if needed, E-lite now makes it possible to validate partial and/or simplified models for specific applications and to quantify their uncertainties.

In conclusion, in this thesis I have produced E-lite, a detailed 360° MCNP model of the ITER Tokamak that overcomes the limitations of current partial models. It represents a tremendous step forward in terms of the realism in the determination of certain relevant radiological quantities and it triggers the development of a set of studies that were not feasible within reasonable uncertainty margins until now. In addition, it also allows to validate partial and/or simplified models of the tokamak for specific applications. Definitely, the E-lite model constitutes an important milestone in the field of ITER nuclear analysis. And its contribution to successfully tackle the challenges posed by radiation will not only be beneficial for ITER, but also for the future DEMO and commercial fusion reactors.

The value of E-lite has been highly recognized by the ITER neutronics research community. In fact, such has been the success of E-lite that part of the content of this thesis was published in January 2021 in the prestigious Nature Energy journal:

- R. Juarez, G. Pedroche, M.J. Loughlin et al, “A full and heterogeneous model of the ITER tokamak for comprehensive nuclear analyses”, Nature Energy 6, 150–157 (2021).

Finally, apart from E-lite, the work performed during this thesis has also led to other relevant contributions in the context of ITER nuclear analysis. Specifically, I participated in the verification and validation (V&V) of D1SUNED, which is the ITER reference code for SDDR calculations. In addition, I produced the official nuclear data package of D1SUNED, which covers the radioisotopes and pathways of concern for ITER planned in-situ maintenance scenarios. I also was the technical responsible at TECF3IR-UNED for all the activities required to perform the latest release (2020) of ITER Radiation Maps. The importance of these maps has already been highlighted, but I want to add that the IO Director General himself, Bernard Bigot, expressly thanked TECF3IR-UNED for our work in this task. Finally, I have also participated in several other nuclear analyses

of relevance for the project. Overall, the work from these contributions has been reflected, for the moment, in 8 publications in JCR journals.

6.2 Future work

Apart from the future applications of E-lite in the ITER projects outlined in the conclusions and in section 5.1 (shutdown in-vessel maps, nuclear heating of in-vessel and ex-vessel components, calibration of neutron detectors...), I briefly indicate here other future works.

The block structures of C-model and the NBI model, on which the E-lite model is based, were not conceived to represent the complete tokamak. That is why it was necessary to modify them to better represent aspects of the machine that are relevant from a neutronics point of view. As we have seen, in this thesis I implemented modifications to, among other things, correctly represent the B1 configuration, the blanket cut-outs, to correct errors in the NBI block structure, etc. On the other hand, missing components like the TCWS (IBED PHTS and VV PHTS) or the magnet feeders were not represented in the original version of E-lite, but were inserted by F4E [183] to compute ex-vessel radiation maps inside the bio-shield and after machine shutdown [182]. Even with that, there are still aspects of the machine that are not fully represented in E-lite or that can be further improved [198].

The problem is that all these changes were introduced by hand, working directly on the MCNP input of E-lite. By updating and improving the E-lite model in this manner (i.e. by means of successive patches) the MCNP input becomes increasingly complex and more difficult to understand, handle and update. In addition, it becomes very difficult to maintain the traceability of all the modifications. Furthermore, many of the modifications in the original block structures have been introduced by means of the complement region operator (i.e. "#"), thus, the amount of redundant surfaces increases, and with that, the inefficiency and computational time of the simulations.

Therefore, a future work of relevance would be the development, from scratch, of a 360° block structure specifically conceived to represent the complete machine. Such block structure should be conceived from the start by means of CAD programs, like Spaceclaim, and considering a CAD model of the complete machine as a basis. In that way, it would be pretty simple (far more than working directly with an MCNP input) to represent in detail and in a clean

manner all aspects of the machine, specially those representing relevant sources of asymmetry. Once produced in CAD, then the translation of the block structure into MCNP format would be straightforward with a CAD-to-MCNP software.

It is important to remark that it would be desirable that the block structure included envelope cells specifically dedicated to as many SSCs of the tokamak as possible, even if MCNP representations are not available at the time. In this way, at least, space reservations would exist in the block structure and, whenever the MCNP models of the SSC are available, the envelope cells of concern could be straightforwardly filled in by means of MCNP universes. The end result of this task would be a much cleaner, better organized, more realistic, efficient and easily updatable 360° model.

Another future work of relevance, which is complementary to the previous one, is the development of a computational tool that allows to obtain partial and/or simplified models in a straightforward and standardize manner from the same 360° fully detailed model. The idea is that the tool could, on the one hand, break down the MCNP input of a 360° model into portions that have the toroidal section and the type of boundary conditions specified by the user. On the other hand, the tool could homogenize several components of the geometry. For instance, it would be useful that the user could specify specific envelope cells of interest, containing detailed universes of a SSC, that are to be homogenized to produce cells made of material mixtures.

In this way, the need of having several tokamak reference models would be avoided. Just one fully detailed 360° model of the tokamak would be needed. And from that, the rest of partial and/or simplified models could be derived. This approach would save the many neutronics efforts that would result from maintaining and regularly updating several reference models of the tokamak. Not to mention that the proliferation of several reference models, each with its own updating process and degree of maturity, is a praxis that can end up diminishing the robustness and quality of the nuclear analysis.

This computational tool, combined with the development of a well-thought 360° block structure, would be key steps to support the transition of the future ITER neutronics efforts towards the production of detailed 360° models; without losing the benefits derived from using partial and/or simpler models when

needed. This strategy could be as well useful for other similar tokamaks, and the future DEMO and commercial reactors.

Finally, I also want to indicate, in general terms, other aspects that are worth investigating and improving to face potential future needs regarding 360° models of the ITER Tokamak, with applicability to future reactors.

It is true that a lot has been done in recent years with respect to the optimization of the performance of radiation transport codes to handle large models, however, it is still necessary to keep improving their performance since the complexity of ITER neutronics models will keep increasing over the years. The reader should be aware that the majority of the SSCs represented in E-lite are replications, by means of MCNP universes, of a given one. For instance, there is no difference in E-lite between the blanket modules that are represented in sector 6, and those that are represented in sectors 7, 8 or 9. This is not the case, however, in the actual machine. Some of the differences between components in one or other sectors may not have an impact from a neutronics point of view, but others will, like the different port configuration of each sector.

As we have seen, in the absence of neutronics models for each of the ports, a strategy of representative ports had to be followed. As a result, for example, many of the diagnostics ports at L2 (a total of seven) are represented at the moment by the latest available version of the UP#18. Although the strategy of representative ports is useful, and conservative, for many applications, it should be gradually abandoned as new MCNP models of ports are available.

However, the availability of new models of ports (and other SSCs) will lead to a considerable increase of the complexity (i.e. number of cells, surfaces and materials) of the overall 360° models. Furthermore, some of the models of ports that are already available and included in E-lite, reflect designs that are not yet mature, and which will evolve in terms of level of details. In other words, the complexity of future 360° models will come both from the progressive availability of new models of ports (and other SSCs) as well as from the increase of maturity and detail of their designs.

It is therefore necessary to keep optimizing the radiation transport codes so that, together with the improvements in the HPC infrastructures, it becomes possible to withstand and handle the future 360° models. One path to follow in this sense is to explore the potential benefits of considering the OpenMP parallelization

scheme, instead of or in combination with MPI, when compiling the MCNP radiation transport code. In this way, it may be possible to further reduce (or more efficiently manage) the RAM memory consumption, among other parameters, of large neutronics models.

On the other hand, it is important to keep in mind the fact that modelling geometries for radiation transport is still a task that is very tedious and demands many human efforts. Indeed, it is the bottleneck of many current ITER nuclear analyses. Therefore, all initiatives aimed at increasing the efficiency of the geometry modelling process are as well of great value for the development of complex 360° models and, in general, any fusion related geometries.

In this sense, as I already mentioned previously, it is desirable to keep exploring the different existing geometry modelling approaches, as well as new ones. It is necessary to investigate and fully understand the benefits, limitations and paths for improvement in the use of UM, DAG-MCNP-like tools and scripting environments of CAD software (like that of SpaceClaim).

The TECF3IR-UNED research group has at the moment a research line dedicated to this field. It is led by my colleague Juan Pablo Catalán. Him and other colleagues, like Juan García and Patrick Sauvan, have developed a CAD-to-MCNP tool, GEOUNED [199], which already features improvements with respect to other similar tools (i.e. SuperMC, McCad). Overall, the final goal of this research line is to manage to produce complex neutronics geometries in the most simple and automatic way possible.

REFERENCES

- [1] <https://www.euro-fusion.org/>.
- [2] <https://www.iter.org/>.
- [3] <https://www.euro-fusion.org/devices/jet/>.
- [4] <https://www.ipp.mpg.de/w7x>.
- [5] <https://lasers.llnl.gov/>.
- [6] <http://www-lmj.cea.fr/>.
- [7] B. Bigot, "ITER assembly phase: Progress toward first plasma," *Fusion Eng. Des.*, vol. 164, no. November 2020, p. 112207, 2021, doi: 10.1016/j.fusengdes.2020.112207.
- [8] S. Ishizaka, "Project specification," ITER Report ITER_D_2DY7NG v2.0, 2010.
- [9] <https://www.euro-fusion.org/programme/demo/>.
- [10] M. Kikuchi, "The large tokamak JT-60: a history of the fight to achieve the Japanese fusion research mission," *Eur. Phys. J. H*, vol. 43, no. 4, pp. 551–577, 2018, doi: 10.1140/epjh/e2018-90054-2.
- [11] T. Dang, D. Ying, Q. Yang, M. Loughlin, and A. Davis, "First neutronics analysis for ITER bio-shield equatorial port plug," *Fusion Eng. Des.*, vol. 87, no. 7–8, pp. 1447–1452, 2012, doi: 10.1016/j.fusengdes.2012.03.036.
- [12] C. Day and D. Murdoch, "The ITER vacuum systems," *J. Phys. Conf. Ser.*, vol. 114, p. 012013, May 2008, doi: 10.1088/1742-6596/114/1/012013.
- [13] G. Dubus *et al.*, "Conceptual design finalisation of the ITER In-Vessel Viewing and Metrology System (IVVS)," *Fusion Eng. Des.*, vol. 88, no. 9–10, pp. 1973–1977, Oct. 2013, doi: 10.1016/j.fusengdes.2013.02.125.
- [14] N. Casal *et al.*, "Design and integration of lower ports for ITER diagnostic systems," *Fusion Eng. Des.*, vol. 96–97, pp. 83–88, Oct. 2015, doi: 10.1016/j.fusengdes.2015.06.186.
- [15] G. Pedroche *et al.*, "Nuclear analysis of the ITER torus cryopumps," *Nucl. Fusion*, vol. 59, no. 10, p. 106045, 2019, doi: 10.1088/1741-

- 4326/ab38d1.
- [16] A. Costley, A. Malaquias, T. Sugie, G. Vayakis, and C. Walker, “1 CT-5 ITER Diagnostics : Design Choices and Solutions *,” 2002.
- [17] R. Juarez, A. Kolsek, M. De Pietri, “D11-1 - Description of the production of the MCNP models of EP n11 as per Section 6.3.1,” ITER Report ITER_D_Y87CJW v1.0, 2020.
- [18] L. M. Giancarli *et al.*, “Overview of the ITER TBM Program,” *Fusion Eng. Des.*, vol. 87, no. 5–6, pp. 395–402, 2012, doi: 10.1016/j.fusengdes.2011.11.005.
- [19] R. Juárez *et al.*, “Update in the nuclear responses of the European TBMs for ITER during operation and shutdown,” *Fusion Eng. Des.*, vol. 134, pp. 92–96, Sep. 2018, doi: 10.1016/j.fusengdes.2018.06.022.
- [20] P. Lamalle *et al.*, “Status of the ITER ion cyclotron heating and current drive system,” *AIP Conf. Proc.*, vol. 1689, no. December, 2015, doi: 10.1063/1.4936472.
- [21] M. Henderson *et al.*, “An overview of the ITER electron cyclotron H&CD system,” in *2009 34th International Conference on Infrared, Millimeter, and Terahertz Waves*, Sep. 2009, pp. 1–4. doi: 10.1109/ICIMW.2009.5325524.
- [22] R. S. Hemsworth *et al.*, “Overview of the design of the ITER heating neutral beam injectors,” *New J. Phys.*, vol. 19, no. 2, p. 025005, Feb. 2017, doi: 10.1088/1367-2630/19/2/025005.
- [23] A.J. López-Revelles, “Neutron analyses and design of components for ITER,” PhD. Thesis, UNED, 2018.
- [24] E. Joffrin *et al.*, “Overview of the JET preparation for deuterium-tritium operation with the ITER like-wall,” *Nucl. Fusion*, vol. 59, no. 11, 2019, doi: 10.1088/1741-4326/ab2276.
- [25] H. Weisen *et al.*, “The scientific case for a JET D-T experiment,” in *AIP Conference Proceedings*, 2014, pp. 77–86. doi: 10.1063/1.4894028.
- [26] A. Žohar and L. Snoj, “On the dose fields due to activated cooling water in nuclear facilities,” *Prog. Nucl. Energy*, vol. 117, p. 103042, Nov. 2019, doi: 10.1016/j.pnucene.2019.103042.

-
- [27] S. Jakhar, “Nuclear Analysis of N-16 and N-17 radiation fields from TCWS activated water,” ITER Report ITER_D_QZ7BEK v2.1, 2016.
- [28] R. Juarez, M. De Pietri, J. Alguacil, A. Kolsek, “Water source modelling for ITER Radiation Maps,” ITER Report ITER_D_YNWTFW v1.3, 2021.
- [29] T.N. Todd, “Radiation Effects in Fission and Fusion Power Generation,” ICTP-IAEA Workshop on Radiation Effects in Nuclear Waste Forms, 2016.
- [30] G. Pedroche, P. Sauvan, J. Alguacil, J. Sanz, and R. Juárez, “Nuclear data for D1SUNED for the study of ITER planned in-situ maintenance dose scenarios,” *Fusion Eng. Des.*, vol. 170, p. 112646, Sep. 2021, doi: 10.1016/j.fusengdes.2021.112646.
- [31] G. Cambi, D. G. Ceperaga, L. Di Pace, C. Rizzello, and M. Zucchetti, “Dust and corrosion product effluents assessment in ITER,” *Fusion Eng. Des.*, vol. 51–52, pp. 471–476, 2000, doi: 10.1016/S0920-3796(00)00268-4.
- [32] L. Di Pace, G. Cambi, D. G. Ceperaga, E. Sobrero, and M. Costa, “Activated corrosion products in ITER first wall and shielding blanket heat transfer system,” in *Proceedings of 16th International Symposium on Fusion Engineering*, 1995, vol. 1, pp. 333–336 vol.1. doi: 10.1109/FUSION.1995.534235.
- [33] T. Eade, “Deliverable 2 - NBI Dose rate optimization,” ITER Report ITER_D_LY8GDK v1.0, 2014.
- [34] M. J. Loughlin, “Neutronic analysis of ITER neutral beam test bed,” *Fusion Eng. Des.*, vol. 74, no. 1–4, pp. 461–465, 2005, doi: 10.1016/j.fusengdes.2005.06.163.
- [35] V. Khripunov, “The ITER first wall as a source of photo-neutrons,” *Fusion Eng. Des.*, vol. 56–57, pp. 899–903, 2001, doi: 10.1016/S0920-3796(01)00374-X.
- [36] ITER Organization, “ITER Research Plan within the Staged Approach (Level III - Provisional Version),” ITR-18-003, 2018, <https://www.iter.org/technical-reports?id=9>.
- [37] S. Zheng *et al.*, “Neutronics analysis for the test blanket modules proposed for EAST and ITER,” *Nucl. Fusion*, vol. 47, no. 8, pp. 1053–1056, Aug. 2007, doi: 10.1088/0029-5515/47/8/040.

- [38] A. Loarte, M. Lehnen, A. Polevoi, “Upper estimates for neutron production during FP and PFPO,” ITER Report ITER_D_WWCMD7 v2.2, 2020.
- [39] I. Raskinyté, “TR19/002 – Shutdown dose rates and radioactivity inventory calculations In early operations Deliverable D1 – Technical Report,” ITER Report ITER_D_2MML43 v2.3, 2020.
- [40] M. Gatu Johnson *et al.*, “Neutron emission from beryllium reactions in JET deuterium plasmas with 3 He minority,” *Nucl. Fusion*, vol. 50, no. 4, p. 045005, Apr. 2010, doi: 10.1088/0029-5515/50/4/045005.
- [41] A. V. Krasilnikov *et al.*, “Evidence of $9\text{ Be} + p$ nuclear reactions during 2 ω CH and hydrogen minority ICRH in JET-ILW hydrogen and deuterium plasmas,” *Nucl. Fusion*, vol. 58, no. 2, p. 026033, Feb. 2018, doi: 10.1088/1741-4326/aa90c3.
- [42] A. H. Boozer, “Runaway electrons and ITER,” *Nucl. Fusion*, vol. 57, no. 5, p. 056018, May 2017, doi: 10.1088/1741-4326/aa6355.
- [43] O. N. Jarvis, G. Sadler, and J. L. Thompson, “Photoneutron production accompanying plasma disruptions in JET,” *Nucl. Fusion*, vol. 28, no. 11, pp. 1981–1993, Nov. 1988, doi: 10.1088/0029-5515/28/11/005.
- [44] D. Flammini, “Neutron production from de-confined runaway electrons in ITER,” ITER Report ITER_D_7K7PBD v1.0, 2016.
- [45] P. Batistoni, “On the absolute calibration of neutron measurements in fusion reactors,” *Fusion Eng. Des.*, vol. 105, pp. 58–69, Apr. 2016, doi: 10.1016/j.fusengdes.2016.02.064.
- [46] J. C. Slater, “The Effects of Radiation on Materials,” *J. Appl. Phys.*, vol. 22, no. 3, pp. 237–256, Mar. 1951, doi: 10.1063/1.1699937.
- [47] N. Casal *et al.*, “Functional materials for ITER diagnostic systems – Radiation aspects,” *Fusion Eng. Des.*, vol. 125, pp. 277–282, Dec. 2017, doi: 10.1016/j.fusengdes.2017.08.017.
- [48] D. Hamilton, “ITER Policy on EEE in Tokamak Complex,” ITER Report ITER_D_6ZX6S3 v3.6, 2012.
- [49] M. J. Loughlin, E. Polunovskiy, K. Ioki, M. Merola, G. Sannazzaro, and M. Sawan, “Nuclear Shielding for the Toroidal Field Coils of ITER,” *Fusion Sci. Technol.*, vol. 60, no. 1, pp. 81–86, Jul. 2011, doi: 10.13182/FST11-

- A12331.
- [50] S. Chiochio, K. Grosset, “Project Requirements (PR),” ITER Report ITER_D_27ZRW8 v6.3, 2020.
- [51] S. Jakhar, “Radiation Maps During Plasma Operations (Mode-0),” ITER Report ITER_D_RJLLFY v2.1, 2016.
- [52] J. Wang, “Safety requirement Roombook,” ITER Report ITER_D_KF63PB v2.11, 2016.
- [53] E. Polunovskiy, “Assessment of Safety Roombook radiological zonings in and around tokamak complex during mode-0,” ITER Report ITER_D_TP9T64 v2.6, 2019.
- [54] A. Kolsek, “Methodological advances in the analysis of Shutdown Dose Rate and shielding design proposals to mitigate it in ITER Diagnostic Port Interspaces,” PhD. Thesis, UNED, 2019.
- [55] S. Rosanvallon *et al.*, “ITER waste management,” *Fusion Eng. Des.*, vol. 85, no. 10–12, pp. 1788–1791, Dec. 2010, doi: 10.1016/j.fusengdes.2010.05.040.
- [56] M. Loughlin, E. Polunovskiy, and N. Taylor, “The impact of nuclear analysis on ITER design and licensing,” *Fusion Eng. Des.*, vol. 87, no. 5–6, pp. 646–651, 2012, doi: 10.1016/j.fusengdes.2012.01.045.
- [57] J. Sanz, O. Cabellos and N. García-Herranz, “ACAB 2008: Activation Code V2008,” 2008.
- [58] J.-C. Sublet, J. W. Eastwood, J. G. Morgan, M. R. Gilbert, M. Fleming, and W. Arter, “FISPACT-II: An Advanced Simulation System for Activation, Transmutation and Material Modelling,” *Nucl. Data Sheets*, vol. 139, pp. 77–137, Jan. 2017, doi: 10.1016/j.nds.2017.01.002.
- [59] M. Loughlin, “Instructions for Nuclear Analyses,” ITER Report ITER_D_R7XRXB v5.3, 2021.
- [60] T. M. Evans, A. S. Stafford, R. N. Slaybaugh, and K. T. Clarno, “Denovo: A New Three-Dimensional Parallel Discrete Ordinates Code in SCALE,” *Nucl. Technol.*, vol. 171, no. 2, pp. 171–200, Aug. 2010, doi: 10.13182/NT171-171.
- [61] T. Wareing, J. McGhee, and J. Morel, “ATTILA: A three-dimensional,

- unstructured tetrahedral mesh discrete ordinates transport code,” *Trans. Am. Nucl. Soc.*, vol. 75, 1996.
- [62] J. Leppänen, M. Pusa, T. Viitanen, V. Valtavirta, and T. Kaltiaisenaho, “The Serpent Monte Carlo code: Status, development and applications in 2013,” *Ann. Nucl. Energy*, vol. 82, pp. 142–150, Aug. 2015, doi: 10.1016/j.anucene.2014.08.024.
- [63] X-5 Monte Carlo Team, i “MCNP - Version 5, Vol. I: Overview and Theory,” LA-UR-03-1987 (2003).
- [64] R.A. Forrest, J. Kopecky, J.-Ch. Sublet, “The European Activation File: EAF-2007 neutron-induced cross section library,” UKAEA FUS 535, 2007.
- [65] FENDL-3.1d: Fusion Evaluated Nuclear Data Library v.3.1d (International Atomic Energy Agency, 2018); <https://www-nds.iaea.org/fendl/>.
- [66] X-5 Monte Carlo Team, i “MCNP - Version 5, Vol. II: User’s Guide,” LA-CP-03-0245 (2003).
- [67] R. Pampin *et al.*, “Developments and needs in nuclear analysis of fusion technology,” *Fusion Eng. Des.*, vol. 88, no. 6–8, pp. 454–460, Oct. 2013, doi: 10.1016/j.fusengdes.2013.03.049.
- [68] M. J. Loughlin *et al.*, “Iter nuclear analysis strategy and requirements,” *Fusion Sci. Technol.*, vol. 56, no. 2, pp. 566–572, 2009, doi: 10.13182/FST56-566.
- [69] H. Iida, V. Khripunov, L. Petrizzi, G. Federici, “Nuclear Analysis Report,” ITER Report ITER_D_22F2ST v2.0, 2004.
- [70] G. Ruvutuso, H. Iida, “Three-Dimensional model of the ITER-FEAT reactor for Monte Carlo nuclear analyses with MCNP,” ITER Report ITER_D_22F8QH v1.0, 2000.
- [71] G. Ruvutuso, H. Iida, L. Petrizzi, “Updated of Basic 3-D model of ITER for Monte Carlo nuclear analyses with MCNP,” ITER Report ITER_D_22F8WC v1.0, 2000.
- [72] D. Leichtle *et al.*, “The ITER tokamak neutronics reference model C-Model,” *Fusion Eng. Des.*, vol. 136, no. April, pp. 742–746, 2018, doi: 10.1016/j.fusengdes.2018.04.002.
- [73] “A. Valentine, ‘ITER MCNP NB Sector Model Document,’ ITER Report

-
- ITER_D_YC96UU v1.0, 2019”.
- [74] B. Colling, A. Burns, A. Davis, A. Turner, “Using Serpent in nuclear fusion analysis,” 8th International Serpent User Group Meeting, Espoo, Finland, 2018, http://montecarlo.vtt.fi/mtg/2018_Espoo/Colling1.pdf.
- [75] A. Suarez *et al.*, “Neutronic analysis of the Diagnostic Equatorial Ports in ITER,” *Fusion Eng. Des.*, vol. 98–99, pp. 1427–1431, Oct. 2015, doi: 10.1016/j.fusengdes.2015.06.091.
- [76] A. Serikov *et al.*, “Shut-Down Dose Rate analysis for ITER Diagnostic Equatorial and Upper Ports,” *Fusion Eng. Des.*, vol. 89, no. 9–10, pp. 1964–1968, Oct. 2014, doi: 10.1016/j.fusengdes.2014.01.025.
- [77] H. Iida, “Fast Neutron Flux and Nuclear Heat in the TF Coil Inboard Legs vs. Gap Width among Blanket Modules,” ITER Report ITER_D_226DRK v2.0, 2003.
- [78] T. D. Bohm, M. E. Sawan, and P. P. H. Wilson, “The impact of simplifications on 3-D neutronics analysis of blanket modules in iter,” *Fusion Sci. Technol.*, vol. 64, no. 3, pp. 587–591, 2013, doi: 10.13182/FST13-A19156.
- [79] R. Pampin, A. Davis, D. James “Systematic study of neutron shielding options for ITER generic diagnostic port plug design,” W6-TPDS-DIASUP, EFDA/06-1436, 2007.
- [80] A. Serikov *et al.*, “Mitigation of radiation streaming inside the ITER ports,” *Prog. Nucl. Sci. Technol.*, vol. 4, pp. 113–117, 2014, doi: 10.15669/pnst.4.113.
- [81] S. Sato, H. Iida, “The Effect of Flexible Joint Module on Nuclear Heating in the TF Coil inboard Leg,” ITER Report ITER_D_22C44S v2.0, 2000.
- [82] E. Polunovskiy, “Systematic errors in VV Heating Estimate: Modelling of water in blanket,” ITER Report ITER_D_PRFV75 v1.1, 2015.
- [83] J. Kulesza, R. Martz, “MCNP6 Unstructured Mesh Tutorial Using Abaqus/CAE 6.12-1,” LA-UR-15-25143, 2015.
- [84] M. De Pietri, M. Fabbri, D. Laghi, and R. Pampin, “A preliminary assessment of MCNP unstructured mesh integration in the ITER neutronics model,” *Fusion Eng. Des.*, vol. 146, pp. 697–700, Sep. 2019,
-

- doi: 10.1016/j.fusengdes.2019.01.058.
- [85] Y. Wu, “Multifunctional Neutronics Calculation Methodology and Program for Nuclear Design and Radiation Safety Evaluation,” *Fusion Sci. Technol.*, vol. 74, no. 4, pp. 321–329, Nov. 2018, doi: 10.1080/15361055.2018.1475162.
- [86] Y. Wu *et al.*, “CAD-based Monte Carlo program for integrated simulation of nuclear system SuperMC,” *Ann. Nucl. Energy*, vol. 82, pp. 161–168, Aug. 2015, doi: 10.1016/j.anucene.2014.08.058.
- [87] Y. Li *et al.*, “Benchmarking of MCAM 4.0 with the ITER 3D model,” *Fusion Eng. Des.*, vol. 82, no. 15–24, pp. 2861–2866, Oct. 2007, doi: 10.1016/j.fusengdes.2007.02.022.
- [88] D. Große, U. Fischer, K. Kondo, D. Leichtle, P. Pereslavytsev, and A. Serikov, “Status of the McCad geometry conversion tool and related visualization capabilities for 3D fusion neutronics calculations,” *Fusion Eng. Des.*, vol. 88, no. 9–10, pp. 2210–2214, Oct. 2013, doi: 10.1016/j.fusengdes.2013.02.146.
- [89] A. J. López-Revelles *et al.*, “MCNP model of the ITER Tokamak Complex,” *Fusion Eng. Des.*, vol. 136, pp. 859–863, Nov. 2018, doi: 10.1016/j.fusengdes.2018.04.023.
- [90] <https://www.ansys.com/products/3d-design/ansys-spaceclaim>.
- [91] <https://www.bsc.es/marenostrum/marenostrum>.
- [92] <https://www.hpc.cineca.it/hardware/marconi>.
- [93] M. De Pietri *et al.*, “Integral modelling of the ITER cooling water systems radiation source for applications outside of the Bio-shield,” *Fusion Eng. Des.*, vol. 171, p. 112575, Oct. 2021, doi: 10.1016/j.fusengdes.2021.112575.
- [94] A. Kolsek, R. Juarez, G. Pedroche, A. Lopez, “D04 - Modelling and calculations of new modular EP#11,” ITER Report ITER_D_VDM9T8 v1.1, 2018.
- [95] P. P. H. Wilson, T. J. Tautges, J. A. Kraftcheck, B. M. Smith, and D. L. Henderson, “Acceleration techniques for the direct use of CAD-based geometry in fusion neutronics analysis,” *Fusion Eng. Des.*, vol. 85, no. 10–

-
- 12, pp. 1759–1765, Dec. 2010, doi: 10.1016/j.fusengdes.2010.05.030.
- [96] H. Chohan, M. Fabbri, R. Pampin, A. Portone, G. D’Amico, and Á. Cubí, “Application of MCNP unstructured mesh in the design process of the ITER EC-UL M3 mirror,” *Fusion Eng. Des.*, vol. 166, p. 112282, May 2021, doi: 10.1016/j.fusengdes.2021.112282.
- [97] P. Sauvan *et al.*, “D1SUNED system for the determination of decay photon related quantities,” *Fusion Eng. Des.*, vol. 151, p. 111399, Feb. 2020, doi: 10.1016/j.fusengdes.2019.111399.
- [98] “H. Iida, L. Petrizzi, E. Polunovskiy, G. Federici, ‘Assessment of effects on the nuclear heating in the TF coil inboard leg arising from the change of the shield blanket material mixture,’ ITER Report ITER_D_24V592 v1.0, 2006”.
- [99] S. Zheng, E. Polunovskiy, “Nuclear Heat of TF Inboard Legs with Fine Structures of Inboard Blanket,” ITER Report ITER_D_28MXPR v2.0, 2007.
- [100] M. Loughlin, “Nuclear Heating in Additional borated steel on Thermal Shield,” ITER Report ITER_D_2NTB7Q v1.1, 2009.
- [101] E. Polunovskiy, “Nuclear heating in blanket and vacuum vessel,” ITER Report ITER_D_6NSH37 v1.1, 2012.
- [102] E. Polunovskiy, “Nuclear responses in TFC,” ITER Report ITER_D_BP6B8V v2.1, 2015.
- [103] R. Juarez, A. Kolsek, M. De Pietri, “D12-4 - Determination of quantities in EP n12 during machine operation as per Section 6.1.3,” ITER Report ITER_D_Y87EMW v1.0, 2019.
- [104] E. Polunovskiy, “D-T neutron emission rate for standard neutron source for ITER nuclear analysis with MCNP code,” ITER Report ITER_D_2FV7QR v1.0, 2008.
- [105] E. Polunovskiy, “SDEF card for the ITER standard neutron source (inductive operation scenario with 500MW of fusion power),” ITER Report ITER_D_2KS8CN v1.4, 2010.
- [106] Q. Zeng, Y. Meng, S. Zheng, Y. Wu, “Update of the ITER 3-D Model for MCNP and the Nuclear Data Library for Dose Calculation,” ITER Report ITER_D_27YENS v1.0, 2008.
-

- [107] E. Polunovskiy, “Use of B-lite,” ITER Report ITER_D_65AV6Z v1.0, 2011.
- [108] E. Polunovskiy, “Status of C-lite,” ITER Report ITER_D_AHXTBV v1.0, 2012.
- [109] E. Polunovskiy, “Neutron current in NB ducts at intersection of NB duct axes with cryostat wall (Energy spectrum and angular distribution),” ITER Report ITER_D_6P784D v1.0, 2012.
- [110] E. Polunovskiy, “C-model_R181031 model document,” ITER Report ITER_D_XETSWC v1.5, 2019.
- [111] A. J. Lopez, “Diagnostics Generic Equatorial Port Plug,” ITER Report ITER_D_VPQ534.
- [112] A. J. Lopez, “Diagnostics Generic Upper Port Plug,” ITER Report ITER_D_VPQ4V9.
- [113] “R. Juárez, A. Lopez, A. Kolsek, G. Pedroche, J. Sanz, ‘Nuclear analysis of Torus Cryopump Port,’ ITER Report ITER_D_WEPL87 v1.4, 2018”.
- [114] V. Barabash, “Chemical composition and impurity requirements for materials,” ITER Report ITER_D_REYV5V v2.3, 2016.
- [115] “PCR-439 - Equatorial and Upper Port Plug Handling and Dogleg Configuration,” ITER_D_ETJB4Q, 2015.
- [116] “PCR-644 - Dimensions of Dog Leg between Blankets and Equatorial Ports 5.5 & 5.6,” ITER_D_PJDS6X, 2014.
- [117] E. Polunovskiy, “Nuclear heating in in-vessel components and vacuum vessel,” ITER Report ITER_D_N3J7NR v1.3, 2014.
- [118] M. Fabbri, D. Leichtle, A. Martin, R. Pampin, and E. Polunovskiy, “Nuclear heat analysis for the ITER Vacuum Vessel regular sector,” *Fusion Eng. Des.*, vol. 137, pp. 435–439, Dec. 2018, doi: 10.1016/j.fusengdes.2018.04.022.
- [119] A. Serikov, L. Bertalot, U. Fischer, J. Guirao, E. Polunovskiy, and R. Pampin, “Neutronic effects of the ITER Upper Port environment update in C-model,” *Fusion Eng. Des.*, vol. 146, pp. 2586–2591, Sep. 2019, doi: 10.1016/j.fusengdes.2019.04.048.
- [120] R. Juárez, R. Pampin, B. Levesy, F. Moro, A. Suarez, and J. Sanz, “Shutdown dose rates at ITER equatorial ports considering radiation

-
- cross-talk from torus cryopump lower port,” *Fusion Eng. Des.*, vol. 100, pp. 501–506, Nov. 2015, doi: 10.1016/j.fusengdes.2015.07.027.
- [121] P. Sauvan, J. P. Catalan, F. Ogando, R. Juarez, and J. Sanz, “Development of the R2SUNED Code System for Shutdown Dose Rate Calculations,” *IEEE Trans. Nucl. Sci.*, vol. 63, no. 1, pp. 375–384, Feb. 2016, doi: 10.1109/TNS.2015.2507138.
- [122] A. Davis and R. Pampin, “Benchmarking the MCR2S system for high-resolution activation dose analysis in ITER,” *Fusion Eng. Des.*, vol. 85, no. 1, pp. 87–92, Jan. 2010, doi: 10.1016/j.fusengdes.2009.07.002.
- [123] Y. Chen and U. Fischer, “Rigorous mcnp based shutdown dose rate calculations: computational scheme, verification calculations and application to ITER,” *Fusion Eng. Des.*, vol. 63–64, pp. 107–114, Dec. 2002, doi: 10.1016/S0920-3796(02)00144-8.
- [124] J. W. Kim, C. W. Lee, and Y.-O. Lee, “Shutdown dose rate analysis with unstructured tetrahedral element based R2S method using deterministic transport solver AETIUS,” *Fusion Eng. Des.*, vol. 131, pp. 156–165, Jun. 2018, doi: 10.1016/j.fusengdes.2018.05.007.
- [125] M. Z. Youssef and R. E. Feder, “Global dose rate assessment in ITER diagnostics ports based on the 3-D FEM ATILA code,” *Fusion Eng. Des.*, vol. 87, no. 7–8, pp. 1101–1110, Aug. 2012, doi: 10.1016/j.fusengdes.2012.02.079.
- [126] D. Valenza, H. Iida, R. Plenteda, and R. T. Santoro, “Proposal of shutdown dose estimation method by Monte Carlo code,” *Fusion Eng. Des.*, vol. 55, no. 4, pp. 411–418, Sep. 2001, doi: 10.1016/S0920-3796(01)00188-0.
- [127] R. Villari *et al.*, “Shutdown dose rate assessment with the Advanced D1S method: Development, applications and validation,” *Fusion Eng. Des.*, vol. 89, no. 9–10, pp. 2083–2087, Oct. 2014, doi: 10.1016/j.fusengdes.2014.01.071.
- [128] P. Lu *et al.*, “Hybrid Monte Carlo approach for accurate and efficient shutdown dose rate calculation,” *Fusion Eng. Des.*, vol. 136, pp. 498–502, Nov. 2018, doi: 10.1016/j.fusengdes.2018.03.005.
- [129] R. Juarez *et al.*, “Shielding proposal to reduce cross-talk from ITER lower port to equatorial port,” *Fusion Eng. Des.*, vol. 101, pp. 67–72, Dec. 2015,
-

- doi: 10.1016/j.fusengdes.2015.10.005.
- [130] R. Juarez, A. Lopez, G. Pedroche, A. Kolsek, “Deliverable D3 - Global MCNP of EP#16. Nuclear analysis of EPP#16 and PI up to bio-shield during plasma shutdown,” F4E Report F4E_D_29DBNF v1.3, 2017.
- [131] R. Juarez, A. Kolsek, M. De Pietri, “D11-7 - Demonstration of the ALARA implementation in EP n11 as per Section 6.4,” ITER Report ITER_D_Y86VFC v1.0, 2020.
- [132] R. Juarez, A. Kolsek, M. De Pietri, “D12-7 - Demonstration of the ALARA implementation in EP n12 as per Section 6.2,” ITER Report ITER_D_Y873L9 v1.0, 2020.
- [133] A. Turner *et al.*, “Nuclear analysis and shielding optimisation in support of the ITER In-Vessel Viewing System design,” *Fusion Eng. Des.*, vol. 89, no. 9–10, pp. 1949–1953, Oct. 2014, doi: 10.1016/j.fusengdes.2014.01.066.
- [134] A. Travleev *et al.*, “Nuclear analysis of the ITER In-Vessel viewing system,” *Fusion Eng. Des.*, vol. 136, pp. 247–251, Nov. 2018, doi: 10.1016/j.fusengdes.2018.01.073.
- [135] “Y. Le Tonqueze, ‘Rad map Task force - NIU domain 1.1 Building – PIM-466 - Status report,’ ITER Report ITER_D_29HS2U v2.0, 2020”.
- [136] N. Taylor, S. Ciattaglia, P. Cortes, M. Iseli, S. Rosanvallon, and L. Topilski, “ITER safety and licensing update,” *Fusion Eng. Des.*, vol. 87, no. 5–6, pp. 476–481, Aug. 2012, doi: 10.1016/j.fusengdes.2012.01.001.
- [137] R. Juarez, J.P. Catalan, F. Ogando, A. Lopez, J. Sanz, “Radiation maps in the Tokamak Complex due to plasma source excepting the NBI,” ITER Report ITER_D_SXRSHE v1.4, 2016.
- [138] Z. Ghani *et al.*, “Radiation levels in the ITER tokamak complex during and after plasma operation,” *Fusion Eng. Des.*, vol. 96–97, pp. 261–264, Oct. 2015, doi: 10.1016/j.fusengdes.2015.05.019.
- [139] R. Juárez *et al.*, “ITER plasma source and building modelling to produce radiation maps,” *Nucl. Fusion*, vol. 58, no. 12, p. 126012, Dec. 2018, doi: 10.1088/1741-4326/aadf9c.
- [140] J. P. Catalan, R. Juarez, F. Ogando, J. Sanz, “Radiation Source for the

- MCNP tokamak building model,” ITER Report ITER_D_TU9NKF v2.1, 2016.
- [141] L. Bertalot *et al.*, “Present Status of ITER Neutron Diagnostics Development,” *J. Fusion Energy*, vol. 38, no. 3–4, pp. 283–290, Aug. 2019, doi: 10.1007/s10894-019-00220-w.
- [142] P. Batistoni *et al.*, “Calibration of neutron detectors on the Joint European Torus,” *Rev. Sci. Instrum.*, vol. 88, no. 10, p. 103505, Oct. 2017, doi: 10.1063/1.4991780.
- [143] D. B. Syme *et al.*, “Fusion yield measurements on JET and their calibration,” *Fusion Eng. Des.*, vol. 89, no. 11, pp. 2766–2775, Nov. 2014, doi: 10.1016/j.fusengdes.2014.07.019.
- [144] P. Batistoni *et al.*, “14 MeV calibration of JET neutron detectors—phase 1: calibration and characterization of the neutron source,” *Nucl. Fusion*, vol. 58, no. 2, p. 026012, Feb. 2018, doi: 10.1088/1741-4326/aa98f6.
- [145] P. Batistoni *et al.*, “14 MeV calibration of JET neutron detectors—phase 2: in-vessel calibration,” *Nucl. Fusion*, vol. 58, no. 10, p. 106016, Oct. 2018, doi: 10.1088/1741-4326/aad4c1.
- [146] J. D. Strachan *et al.*, “Absolute calibration of TFTR helium proportional counters (abstract a),” *Rev. Sci. Instrum.*, vol. 66, no. 1, pp. 897–897, Jan. 1995, doi: 10.1063/1.1146198.
- [147] K. Stammers and M. J. Loughlin, “The calibration of the MAST neutron yield monitors,” *Nucl. Instruments Methods Phys. Res. Sect. A Accel. Spectrometers, Detect. Assoc. Equip.*, vol. 562, no. 1, pp. 521–530, Jun. 2006, doi: 10.1016/j.nima.2006.03.012.
- [148] T. Nishitani *et al.*, “Absolute calibration of the JT-60U neutron monitor using a ^{252}Cf neutron source (abstract a),” *Rev. Sci. Instrum.*, vol. 63, no. 10, pp. 4558–4558, Oct. 1992, doi: 10.1063/1.1143666.
- [149] M. Isobe *et al.*, “Neutron Diagnostics in the Large Helical Device,” *IEEE Trans. Plasma Sci.*, vol. 46, no. 6, pp. 2050–2058, 2018, doi: 10.1109/TPS.2018.2836987.
- [150] A. Čufar *et al.*, “Calculations to Support In Situ Neutron Yield Calibrations at the Joint European Torus,” *Fusion Sci. Technol.*, vol. 74, no. 4, pp. 370–386, Nov. 2018, doi: 10.1080/15361055.2018.1475163.

- [151] J. Alguacil, P. Sauvan, R. Juarez, and J. P. Catalan, “Assessment and optimization of MCNP memory management for detailed geometry of nuclear fusion facilities,” *Fusion Eng. Des.*, vol. 136, pp. 386–389, Nov. 2018, doi: 10.1016/j.fusengdes.2018.02.048.
- [152] INR-KIT/numjuggler (GitHub, 2016), <https://github.com/inr-kit/numjuggler>.
- [153] G. Pedroche, “E-lite 360° MCNP model - Model Report,” ITER Report ITER_D_2RLM3G v1.1, 2020.
- [154] G. Pedroche, “memo - Standard Tallies for E-lite R200430,” F4E Report F4E_D_2QGUP4 v1.0, 2021.
- [155] A. Kolsek, “D1 - B1 Level: Production of a computational model,” ITER Report ITER_D_Y8XCF3 v1.0, 2019.
- [156] A. Kolsek, R. Juarez, “D3 - B1 Level: Report on the results,” ITER Report ITER_D_Y8Y7G9 v1.0, 2019.
- [157] “D. Sancristobal, A. Aviles, ‘D12.04.04A EP01 Engineering analysis reports and calculations - Section A Neutronic Analysis,’ F4E Report F4E_D_2JFGR8 v1.0, 2019”.
- [158] A. Kolsek, “D07- Design of the MCNP EQ#8 Port Integration model,” ITER Report ITER_D_ITER_D_SQFJC3 v1.0, 2016.
- [159] M. Magan, A. Aviles, “EP10 Design Documentation [D4.3]. Part 10/10: Engineering Analyses Reports - Section A: Neutronic analyses,” F4E Report F4E_D_26MB7A v2.0, 2016.
- [160] R. Juarez, A. Kolsek, M. De Pietri, “D12-1 - Description of the production of the MCNP models of EP n12 as per Section 6.1.1,” ITER Report ITER_D_Y87LGP v1.0, 2020.
- [161] A. Turner, “Shielding Optimisation of the ICRH Antenna, subtask 3 and 4 report,” ITER Report ITER_D_N5349P v1.0, 2014.
- [162] K. Kajiwara, N. Kobayashi, “Interim Report_Del.5,” ITER Report ITER_D_Y3T2DG v1.0, 2019.
- [163] R. Juarez, A. Lopez, G. Pedroche, A. Kolsek, “Deliverable D1 - Technical Report: Local MCNP model of EPP #16,” F4E Report F4E_D_26UR5T v1.2, 2017.

-
- [164] D. Sancristobal, A. Aviles, "D06.04.04A UP01 Engineering analysis reports and calculations - Section A Neutronic Analysis," F4E Report F4E_D_2JK2AF v2.0, 2019.
- [165] Y. An, "Neutron Analysis and SDDR Assessment for UP18," ITER Report ITER_D_Q7EMF9 v1.3, 2018.
- [166] D. Sancristobal, A. Aviles, "D08.04.04A UP03 Engineering analysis reports and calculations - Section A Neutronic Analysis," F4E Report F4E_D_2JK87G v1.0, 2019.
- [167] A. Lopez, R. Juarez, "D5_Upper Launcher SDDR calculations (final)," ITER Report ITER_D_23BNQG v1.0, 2019.
- [168] M. Magan, A. Aviles, "UP17 Design Documentation [D6.4]. Part 10/10: Engineering Analyses Reports - Section A: Neutronic Analyses," F4E Report F4E_D_27JJH7 v1.0, 2016.
- [169] M. B. Chadwick *et al.*, "ENDF/B-VII.1 Nuclear Data for Science and Technology: Cross Sections, Covariances, Fission Product Yields and Decay Data," *Nucl. Data Sheets*, vol. 112, no. 12, pp. 2887–2996, Dec. 2011, doi: 10.1016/j.nds.2011.11.002.
- [170] "TENDL-2015: TALYS-based evaluated nuclear data library," A.J. Koning, D. Rochman, J. Kopecky, J. Ch. Sublet, E. Bauge, S. Hilaire, P. Romain, B. Morillon, H. Duarte, S. van der Marck, S. Pomp, H. Sjostrand, R. Forrest, H. Henriksson, O. Cabellos, S. Gori.
- [171] M. Fabbri, "MEMORANDUM - From FENDL2.1 to 3.1d," F4E Report F4E_D_26Z9ZV v1.1, 2018.
- [172] A. J. van Wijk, G. Van den Eynde, and J. E. Hoogenboom, "An easy to implement global variance reduction procedure for MCNP," *Ann. Nucl. Energy*, vol. 38, no. 11, pp. 2496–2503, Nov. 2011, doi: 10.1016/j.anucene.2011.07.037.
- [173] M. Loughlin, N. Taylor, "Recommendation on Plasma scenarios," ITER Report ITER_D_2V3V8G v1.2, 2009.
- [174] M. C. White, "Further Notes on MCPLIB03/04 and New MCPLIB63/84 Compton Broadening Data For All Versions of MCNP5," LA-UR-12-00018, 2012.

- [175] M Loughlin, “Recommendations on Computation of Dose from Flux Estimates,” ITER Report ITER_D_29PJCT v1.0, 2008.
- [176] R. Juárez *et al.*, “A full and heterogeneous model of the ITER tokamak for comprehensive nuclear analyses,” *Nat. Energy*, vol. 6, no. 2, pp. 150–157, Feb. 2021, doi: 10.1038/s41560-020-00753-x.
- [177] R. Juárez, G. Pedroche, P. Martinez, M. De Pietri, A. Lopez-Revelles, A. Kolšek, J. Alguacil, “Biological dose rate maps in mode 0,” ITER Report ITER_D_3QBAPQ v1.6, 2021.
- [178] R. Juárez, G. Pedroche, P. Martinez, M. De Pietri, A. Lopez-Revelles, A. Kolšek, J. Alguacil, “Radiation environment for equipment during operations,” ITER Report ITER_D_3FM52L v1.1, 2020.
- [179] G. Pedroche, “Plasma Radiation Source for Radiation Maps,” ITER Report ITER_D_2YBFY3 v1.2, 2020.
- [180] Y. Le Tonqueze, M. Battaglia, R. Brown, M. Loughlin, M. Regad, G. Tarasewicz, “Nuclear Integrated Engineering contract,” ITER Report ITER_D_WTAD57 v2.4, 2018.
- [181] R. Juárez, “Definitive Maps for Phase I Areas,” ITER Report ITER_D_3GS3KM v1.1, 2020.
- [182] R. Pampin, M. Fabbri, “C74TD23FE D7 Report on radiation maps mode-1 inside bioshield,” F4E Report F4E_D_2QERK5 v1.1, 2021.
- [183] M. Fabbri, “C74TD23FE D3 Report on MCNP model for mode-1 radiation maps,” F4E Report F4E_D_2NRKNV v1.1, 2021.
- [184] R. Juárez *et al.*, “Scoping studies of shielding to reduce the shutdown dose rates in the ITER ports,” *Nucl. Fusion*, vol. 58, no. 7, p. 076018, Jul. 2018, doi: 10.1088/1741-4326/aac1c5.
- [185] R. Juárez *et al.*, “The use of the long modular diagnostics shield module to mitigate shutdown dose rates in the ITER diagnostics equatorial ports,” *Nucl. Fusion*, vol. 58, no. 5, p. 056015, May 2018, doi: 10.1088/1741-4326/aaadce.
- [186] A. Kolšek *et al.*, “Shutdown dose rate mitigation in the ITER upper ports,” *Fusion Eng. Des.*, vol. 136, pp. 228–232, Nov. 2018, doi: 10.1016/j.fusengdes.2018.01.070.

-
- [187] M. Loughlin, "Qualification of D1S code," ITER Report ITER_D_V55RBS v1.0, 2017.
- [188] G. Pedroche, R. Juarez, P. Sauvan, J. Sanz, "D2-3. Assumptions, errors and uncertainties of D1SUNED v3.1.2," ITER Report ITER_D_WDQLMX v1.0, 2018.
- [189] R. Juarez, G. Pedroche, P. Sauvan, J. Sanz, "D2-4. Benchmark validation cases of D1SUNED v3.1.2," ITER Report ITER_D_WQEZWK v1.0, 2018.
- [190] G. Pedroche, R. Juarez, P. Sauvan, J. Sanz "D1-3. Activation study and D1SUNED v3.1.2 nuclear data set," ITER Report ITER_D_WDQR2F v1.0, 2018.
- [191] P. Martinez, G. Pedroche, A. Lopez, M. De Pietri, R. Juarez, "Full MCNP Model Report," ITER Report ITER_D_3FJW3M v1.3, 2020.
- [192] P. Martinez, G. Pedroche, A. Lopez, M. De Pietri, R. Juarez, "Tokamak Complex MCNP Model Report," ITER Report ITER_D_3FEA8J v1.1, 2020.
- [193] G. Pedroche, P. Martinez, M. De Pietri, A. Lopez, R. Juarez, "Auxiliary Buildings Report - MCNP models," ITER Report ITER_D_2SA24Q v1.3, 2020.
- [194] G. Pedroche, P. Martinez, A. Lopez, M. De Pietri, R. Garcia, R. Juarez, "NB Cell & HV Deck - MCNP model," ITER Report ITER_D_2SGT5W v1.0, 2020.
- [195] A. Kolsek, R. Juarez, G. Pedroche, A. Lopez, "D05 - Modelling and calculations of new modular EP#12," ITER Report ITER_D_VDMBFZ v1.1, 2018.
- [196] G. Pedroche, R. Juarez, A. Kolsek, P. Sauvan, J. P. Catalan, A. Lopez, J. Sanz, "Mode 1 Radiation Maps Building Contribution," ITER Report ITER_D_V96MHG v1.3, 2017.
- [197] R. Juarez, G. Pedroche, A. Lopez, "Nuclear analysis for the evaluation of modifications proposed in SDR#295 and SDR #508," ITER Report ITER_D_7K7SAJ v1.6, 2019.
- [198] M. Fabbri, "memo - Preliminary review of the new 2019 NB tokamak sector MCNP model embed within E-lite_200403_R1," F4E Report F4E_D_2H7GQW v2.2, 2020.
- [199] J. García, J. P. Catalán, and J. Sanz, "Development of the automatic void

generation module in GEOUNED conversion tool,” *Fusion Eng. Des.*, vol. 168, p. 112366, Jul. 2021, doi: 10.1016/j.fusengdes.2021.112366.

APPENDIX I – RELATIVE ERRORS

In Figure 0-1 and Figure 0-2, I show relative error maps of the neutron flux maps shown in Figure 4-5 and Figure 4-6 (section 4.1.3).

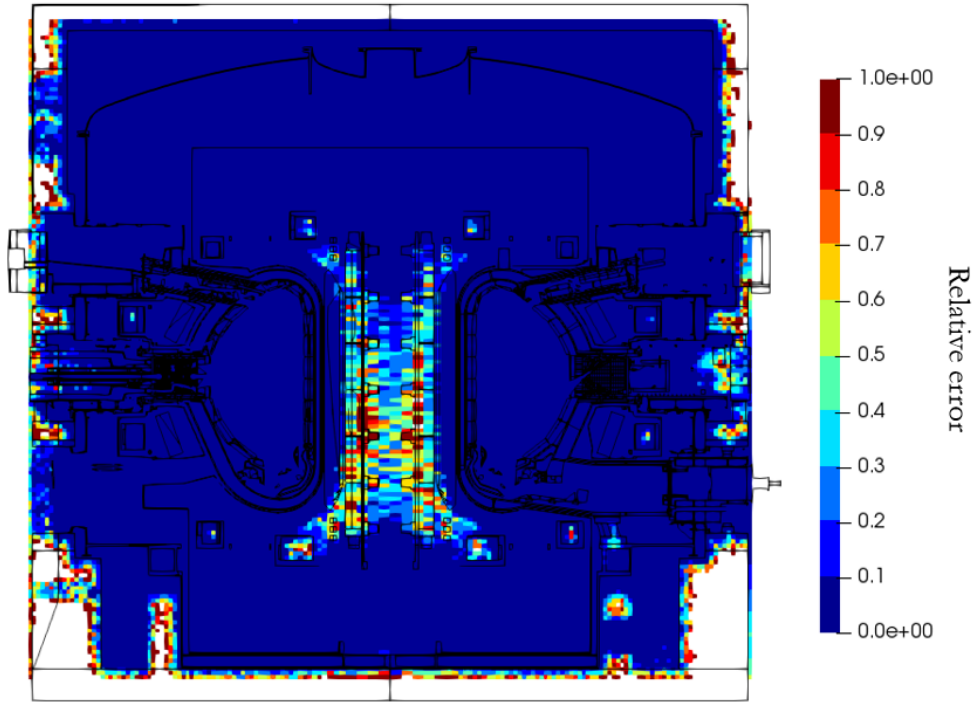


Figure 0-1. Relative error map of the neutron flux map shown in Figure 4-5.

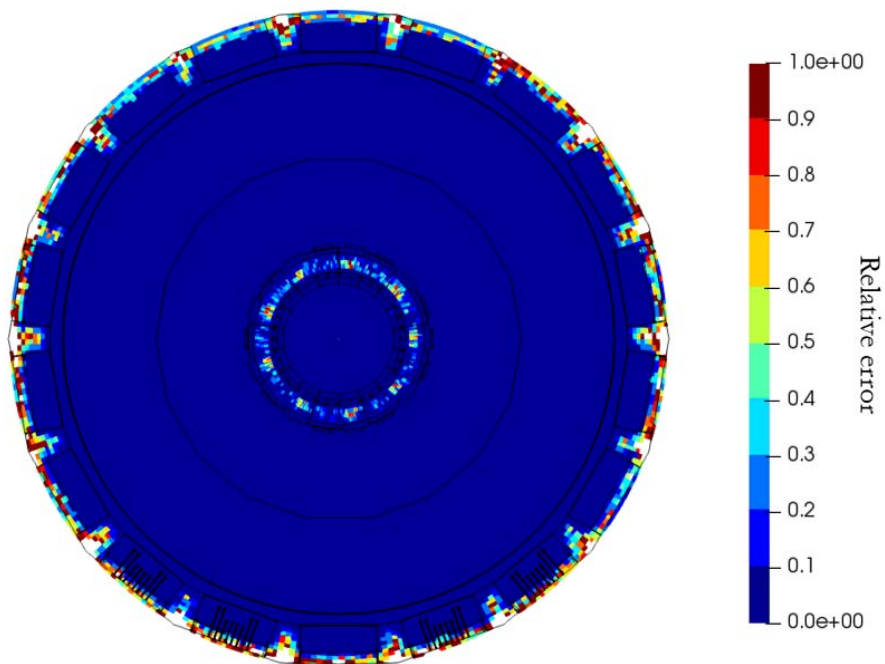


Figure 0-2. Relative error map of the neutron flux map shown in Figure 4-6.

In Figure 0-3, I show relative error maps of the neutron flux maps shown in Figure 4-7 (section 4.2.3).

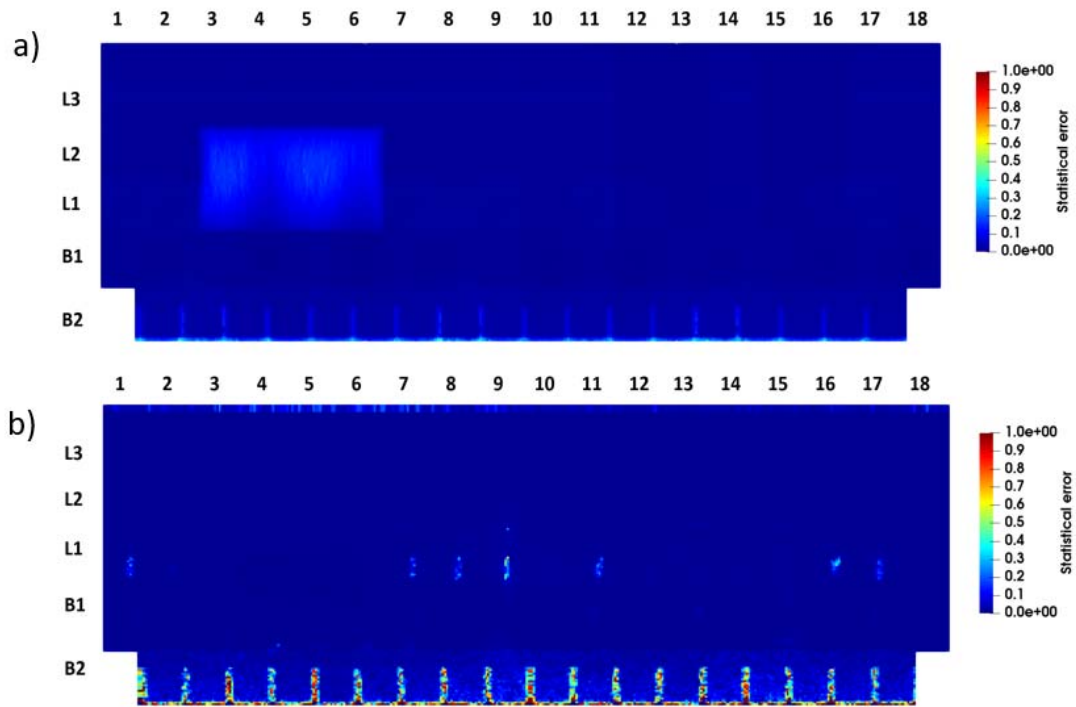


Figure 0-3. Relative error maps of the neutron flux maps shown in Figure 4-7.